Geophysical Measurements on Glacial Soils - A Challenge in the Detection, Identification and Reconstruction of Archaeological Targets

Dissertation
zur Erlangung des Doktorgrades
der Mathematisch-Naturwissenschaftlichen Fakultät
der Christian-Albrechts-Universität zu Kiel

vorgelegt von
Diana Panning

Kiel, March 2023

Referent:	Prof. Dr. Wolfgang Rabbel
Koreferent:	Assoz. Prof. Dr. Immo Trinks, PD
Tag der mündlichen Prüfung:	June 5, 2023

Zusammenfassung

Die archäo-geophysikalische Untersuchung von bronzezeitlichen Befunden in glazialen Böden stellt eine große Herausforderung dar, der in dieser Arbeit begegnet werden soll. Glaziale Böden zeichnen sich durch einen hohen Anteil an Feldsteinen aus aber auch durch das Vorkommen von Eisenoxidkonkretionen und sind somit sehr heterogen. Die Herausforderung besteht unter anderem darin steinige archäologische Befunde in der steinigen Umgebung zu identifizieren. Dazu werden in drei aufeinander aufbauenden Teilen unterschiedliche Aspekte beleuchtet, die thematisch der Detektion, Identifikation und Rekonstruktion zuzuordnen sind. Die ersten beiden Teile beschäftigen sich mit der Verbesserung der Detektion und Identifikation von archäologischen Befunden in Radar- und Magnetikdaten. Gegenstand der Untersuchungen sind Grabhügel und deren nahes Umfeld, wozu unter anderem Urnen, Kochsteingruben, Körperbestattungen und Gruben aber auch Gräben gehören. Im ersten Teil der Arbeit werden steinige archäologische Befunde untersucht und unter anderem mit Hilfe einer Bodenradar-Amplitudenklassifizierung ein Unterscheidungsmerkmal zu geologischen Strukturen herausgearbeitet. Darüber hinaus werden Porosität und Wassergehalt des Bodens abgeleitet, um die Bodenverhältnisse, die eine Detektion von steinigen archäologischen Befunden ermöglichen, zu beschreiben. In einem zweiten Teil wird untersucht, unter welchen Bodenbedingungen Gruben in Bodenradar und Magnetikdaten erkannt werden können. Der Fokus des letzten Teils liegt auf die Rekonstruktion und Höhenabschätzung eines fast vollständig erodierten Grabhügels.

Bislang gibt es verschiedene Ansätze die Identifikation von archäologischen Befunden in Radardaten zu verbessern. Jedoch liegt der Fokus zumeist auf große leicht zu identifizierende archäologische Befunde aus jüngeren Zeiten, wie Mauerstrukturen. Die vorliegende Arbeit leistet einen Beitrag bei der Verbesserung der Identifizierung von kleineren Befunden mit Ausmaßen von wenigen Metern zwischen 0.3 m (Urnen) und 2 m (Körperbestattung). Gruben sind ebenso selten im Fokus von Auswertungen von Bodenradardaten. Zumeist sind Gruben oder Gräben Gegenstand von magnetischen Untersuchungen. Aber grubenähnliche Strukturen sind durchaus im Radar zu erkennen, nur ist es wichtig zu verstehen, unter welchen Bedingungen diese vom Radar detektiert werden. Diese Frage wird im zweiten Teil der Arbeit diskutiert. Mit dem dritten Teil der Arbeit wird ebenso versucht eine Untersuchungslücke zu füllen, in dem ein fast erodierter Grabhügel versucht wird in Form und Höhe zu rekonstruieren. Die meisten Studien, die versuchen einen Grabhügel zu rekonstruieren, haben zumeist ein sehr gut erhaltenes Exemplar zur Grundlage, bei welchem sie versuchen, die verschiedenen Nutzungsphasen herauszuarbeiten.

Die vorliegende Arbeit an einen Fragenkatalog zu jedem Thema zur Grundlage. Zum Thema Detektion beschäftigt sich die Arbeit mit der Frage, ob die Erkennungsrate von steinigen archäologischen Befunden verbessert werden kann, wenn die Radardaten mit den magnetischen verglichen werden. Auch wurde die

Signalstärke (vom GPR) von steinigen Befunden (archäologischer und geologischer Herkunft) analysiert, um festzustellen, ob dadurch die Detektierbarkeit erhöht werden kann. Außerdem wird die Frage diskutiert, welche Bodeneigenschaften Gruben haben müssen, um in den magnetischen und Radardaten erkannt zu werden. Um die Identifikation archäologischer Befunde zu erleichtern, wurde untersucht, warum einige archäologische Befunde in den magnetischen und Radardaten identifizierbar sind und andere nicht. Weiterhin wurde die Frage diskutiert, ob Bodenanalysen helfen, im Vorhinein Aussagen zur Identifizierbarkeit von archäologischen Befunden zu treffen. Am Beispiel des Grabhügels LA 117 (Bornhöved), konnte ein Versuch der Rekonstruktion gestartet werden. Aufgrund der Schwierigkeit, dass der Grabhügel bis auf wenige Zehner Zentimeter wegerodiert war, einen Ansatz zu finden, die Rekonstruktion umzusetzen. Daher stellte sich die Frage, ob mit Hilfe des Volumens des Füllmaterials aus dem Graben, der den Grabhügel umgibt, die ehemalige Höhe abgeschätzt werden kann. Dazu wurde auch der Schüttwinkel als Stabilitätskriterium berücksichtigt. Zum anderen stellten sich die Frage, ob der Grabhügel auch für Mehrfachbestattungen genutzt worden ist und ob das Grabenmaterial pro Grabenphase ausgereicht hätte, um weitere Bestattungen zu überdecken.

Die Datenerhebung erfolgte in großskaligen geophysikalischen Messkampagnen. Der Schwerpunkt lag auf den Messmethoden Radar und Magnetik. Um einschätzen zu können, wieviel archäologische Befunde erkannt bzw. nicht erkannt werden, wurde zusätzlich die archäologische Dokumentation berücksichtigt. Bodenanalysen wurden ebenso herangezogen, um mit Hilfe von numerischen Modellierungen die Bodenbedingungen einzuschätzen. Für die Abschätzung der Höhe des ehemaligen Grabhügels wurden zunächst die Grabenphasen in den Radardaten gepickt, um basierend darauf das Volumen pro Grabenphase abzuschätzen. Die Höhe wurde mit Hilfe von geometrischen Formen, wie Glockenform, Kegel und Kugelsegment, abgeschätzt.

Die Untersuchung zeigt, dass eine kombinierte Betrachtung von Radar- und magnetischen Daten hilft, steinige archäologische Befunde von steinigen geologischen Strukturen aber auch von Eisenoxidkonkretionen zu unterscheiden. Auch können bestimmte archäologische Befunde, wie Kochsteingruben oder Bestattungen, aber auch Eisenoxidkonreationen eindeutig identifiziert werden. Die Analyse der Signalstärken kann durch Umsetzung in ein Werkzeug zur Mustererkennung die Detektierbarkeit erhöhen. Mit Hilfe der Bodenanalysen und Modellierungen konnte festgestellt werden, dass eine Messkampagne in den feuchten Monaten hilfreich ist, um steinige archäologische Befunde zu detektieren und zu identifizieren. Gruben hingegen können besser erkannt werden, wenn die Grubenfüllung trockener ist und einen etwas höheren Sandgehalt als die Umgebung aufweist (rund 5 %). Bei Gruben trägt die Form ebenso dazu bei, zu welchem Grad die Grubenwände erkannt werden können. Es konnte festgestellt werden, dass eine eingehende Bodenanalyse vor einer Messkampagne dazu beiträgt, die Erkennungsrate zu beeinflussen, vorausgesetzt, dass neben Bodenzusammensetzung, auch mindestens der Wassergehalt bestimmt wird.

Mit Hilfe des Rekonstruktionsansatzes anhand von geometrischen Formen, konnte gezeigt werden, dass wenn die ehemalige Form des Grabhügels glockenförmig war, war mindestens eine weitere Bestattung möglich, die mit Grabenmaterial abgedeckt werden konnte. Je konischer die Form ist, desto wahrscheinlicher ist eine dritte Bestattung. Da nur eine Bestattung archäologisch beobachtet wurde, wurde die Bestattung der Phase 2 wahrscheinlich erodiert. Die ehemalige Höhe des Grabhügels konnte anhand der Grabenphasen abgeschätzt

werden. Die Mindesthöhe, die sich aus der Verwendung des Grabenmaterials der einzelnen Phasen insgesamt ergibt, läge zwischen 2,1 m (unter Annahme eines Kugelsegmentes) und 3,4 m (unter Annahme der Kegelform). Dieses Ergebnis steht in Übereinstimmung mit anderen dokumentierten und gut erhaltenen Grabhügeln.

Die vorliegende Arbeit leistet einen Beitrag zur Verbesserung der Detektion und Identifikation kleinerer steinhaltiger archäologischer Befunde, wie Urnen oder Kochsteingruben, aber auch grubenähnlicher Strukturen in Magnetik- und Radardaten. Die Untersuchung zur Rekonstruktion eines erodierten Grabhügels ist in ihrer Form einzigartig, da zumeist nur gut erhaltene Grabhügel untersucht werden, weshalb eine Rekonstruktion ihrer ehemaligen Form und Höhe nicht notwendig ist.

Abstract

The archaeological investigation of Bronze Age features in glacial soils in geophysical data is a great challenge and will be the focus of this thesis. Glacial soils are characterised by a high proportion of boulder stones but also by the occurrence of iron oxide concretions and are thus very heterogeneous. One of the challenges is to identify stony archaeological features in the stony environment. For this purpose, different aspects are examined in three distinct chapters, which can be thematically assigned to detection, identification, and reconstruction of archaeological features in geophysical data. The first two chapters deal with the improvement of the detection and identification of archaeological features in radar and magnetic data. Subject of the investigations are burial mounds and their near surroundings, which include urns, cooking pits, inhumations and pits as well as ditches. So far, there are several approaches to improve the identification of archaeological features in radar data, such as the usage of neuronal networks or the analysis of GPR attributes. However, their focus is mostly on large and easily identifiable archaeological features from more recent times (e.g. wall structures). This thesis contributes to the improvement of the identification of smaller features with dimensions of a few meters (0.3 m for urns and 2 m for inhumations). Previously, pits and ditches are rarely the focus of ground penetrating radar (GPR) studies but rather subject of magnetic investigations. However, pit-like features can be detected by radar, if the conditions under which those are detected are understand. Therefore, in the first chapter of the thesis, stony archaeological features are investigated, such as urns, cooking pits and inhumations. A ground penetrating radar amplitude classification is used to distinguish these from geological structures. Additionally, porosity and water content of the soil are derived to describe the soil conditions that allow the detection of stony archaeological features in the GPR data. In the second chapter, the soil conditions are investigated, under which pits can be detected in both GPR and magnetic data.

The third chapter attempts to reconstruct the shape and height of an almost eroded burial mound. Previous studies, which reconstructed burial mounds are mainly based on very well preserved specimens to identify the most useful phases. This work focuses on the reconstruction and the height estimation of an almost completely eroded burial mound. The possible shape of the former burial mound is reconstructed, and the geometrical dimensions are described.

This work is based on a set of questions for each topic. On the topic of detection, the thesis addresses the question of whether the detection rate of stony archaeological features can be improved if radar data is compared to magnetic data. Additionally, the GPR signal strength of stony features with archaeological and geological origin was analysed to determine if GPR signal strength can increase the detectability of those features. Furthermore, which soil characteristics are required to detect pits in radar and magnetic data is discussed. To facilitate the identification of archaeological features, it was investigated why some archaeological features

are identifiable in the magnetic and radar data, while others are not. Furthermore, the general question of whether soil analyses help to make statements about the identifiability of archaeological features in advance was discussed.

Since the burial mound is almost completely eroded except for a few decimeters, the question arose as to whether the former height can be estimated using the volume of fill material from the ditch surrounding the burial mound. For this purpose, the angle of repose was considered as a stability criterion. Subsequently, the question arose whether the burial mound had been used for multiple burials and whether the ditch material per ditch phase would have been sufficient to cover further burials.

The data collection was carried out within the framework of the interdisciplinary Collaborative Research Center (CRC) 1266 "Scales of Transformation". Extensive geophysical measurement campaigns were carried out over Bronze Age sites in the region of northern Germany, with a strong focus on radar and magnetic measurements. To be able to estimate how much archaeological features are detected in the geophysical data the archaeological documentation was included in the evaluation of the geophysical data. Soil analyses were used to estimate soil conditions with the help of numerical modelling. To estimate the height of the former mound, the ditch phases were picked in the radar data to estimate the volume for each ditch phase. The height was estimated using geometric shapes, such as bell shape, cone, and spherical section.

This study demonstrates that a combined view of radar and magnetic data improves the distinguishability between stony archaeological features from stony geological structures, and also from iron oxide concretions. Certain archaeological features, such as cooking pits or burials and furthermore iron oxide concretions can be clearly identified. The analysis of signal strengths can increase the detectability through implementation in a pattern recognition tool. The soil analyses and modelling demonstrated that a measurement campaign in the wet months is helpful to detect and identify stony archaeological features. While pits can be better identified when the pit filling is drier and has a slightly higher sand content than the surrounding subsoil (around 5 %). The pit shape has additionally a strong influence on the detectability. This study demonstrates that a detailed soil analysis prior to a measurement campaign improve the detection rate, if at least the water content is also determined.

Using the reconstruction approach based on geometric shapes, it could be shown that a former bell-shaped form of the burial mound would have allowed at least one additional burial, which could be covered with ditch material. The likelihood of a third burial increases the more conical the shape of the burial mound is. Since only one burial was archaeologically observed, the burial of phase 2 was probably eroded. The former height of the burial mound could be estimated from the ditch phases. The minimum height, based on the usage of the ditch material from each phase as a whole, would range from 2.1 m (assuming a spherical section) to 3.4 m (assuming a conical shape). This result is in good agreement with other documented and well-preserved burial mounds.

The presented work contributes to the improvement of the detection and identification of smaller stone-bearing archaeological features, such as urns or cooking pits, but also pit-like features in magnetic and radar

data. The investigation for the reconstruction of an eroded burial mound is unique in its form, since mostly only well-preserved burial mounds are investigated, therefore a reconstruction of their former shape and height is not necessary.

Contents

List of Figures

i Introduction

i.1 Detection, Identification and Reconstruction of Archaeological Targets

Detection, identification and reconstruction are three major tasks and challenges for archaeo-geophysical projects. The ability to detect features often depends on the prospection method used, on the kind of feature in question and/or on soil conditions. Often, the prospector needs a priori information to decide which geophysical method is likely to be best suited to detecting the salient features. If the measurement was successful, evaluation can begin. The task of the data analyst is to identify features. Identification depends on the needs of the customer. An archaeologist, for example, requires the identification of archaeological features. Archaeological features differ widely in terms of geometry, kind, depth, age and other aspects. The point of age is the most critical one. Most common archaeological features of prehistoric times are characterised by several pits, pit houses or postholes. The younger the archaeological epoch, the more likely there are to be archaeological features involving the use of stones, such as ovens, cooking pits, urns etc.

For the Bronze Age, which is the archaeological epoch of interest in this thesis, the most common archaeological features are pits, post holes, urns in a stone package, cooking pits, burial mounds with a burial embedded of a stone package, stone circles or ditches surrounding the burial mound, to name the most important. In collaboration with the CRC 1266 "Scales of Transformation" sub-project D3, two sites in Bornhöved were explored: Mang de Bargen (MdB) and the burial mound LA 117 in Bornhöved (BH). The archaeological investigation is focussed on two different points of time. The most important archaeological times are the transition from the early to mid-Bronze Age around 1500 BC and the transition from the mid to late Bronze Age around 1300 BC. Both periods are characterised by transformation processes. The first period is characterised by a change in the settlement practices. Until 1500 BC the region between Elbe and Warta was settled continuously, with a break of about 150 years after 1500 BC. The second transformation process was characterised by the transition from burial to cremation (Kneisel, Brinkmann, et al. 2018). Because of the few settlements of the Bronze Age studied so far, the CRC 1266 "Scales of Transformation" examines mainly funerals, of which burial mounds are characteristic features.

Sandy rather than loamy soils were preferred for the establishment of Bronze Age settlements and burial mounds. The documentation of Bronze Age settlements of Northern Germany and Denmark is fragmentary in comparison to the one of burial mounds and urn grave fields. Settlements are located in a plane area. Therefore, it is often by chance that settlements can be discovered and investigated. Furthermore, Schleswig-Holstein is characterised by a high degree of agricultural activity, which may contribute to the destruction of archaeological sites. The Bronze Age inhabitants of this region preferred to build their settlements close

to the shore. For their burial mounds, which were arranged along the end moraine in groups, they display a preference for natural elevations. The cemetery of Mang de Bargen shows the largest concentration of burial mounds in the region between the Grimmelsberg and the Bornhöveder Rinne. In this thesis the focus is on burial mounds. The site Mang de Bargen is 3 km from the Belauer See and is the basis for the investigation of the transformation around 1500 BC and 1300 BC as well, since urn graves were set next to the burial mounds (Schaefer-Di Maida 2019).

With regard to soil conditions, we may expect glacial soils characterised by large amounts of gravel. Therefore, the site of Mang de Bargen is of interest for gravel mining, which is why several burial mounds were already destroyed before they could be investigated (Schaefer-Di Maida 2019). Due to scattering of the surrounding of archaeological features, this soil situation is challenging for geophysical questions, leading to ambiguous or faulty findings. An advantage of using geophysics in archaeology is the ability to conduct investigations on a large scale. With magnetics, it is possible to examine several hectares per day. A multichannel radar likewise makes it possible to examine large areas in a single day. Smaller daily areas can be examined by means of electrics (electrical resistivity tomography – ERT) and seismics. The latter two methods are preferable if the examination needs to be taken to greater depths. Bronze Age features are located in depths up to 1 m. Due to the heterogeneity of the subsoil, the combination of different geophysical methods promises the most comprehensive results. To improve the detection rate and identification of archaeological features, an interdisciplinary approach was used, consisting of the combination of magnetics and ground-penetrating radar (GPR) together with the archaeological documentation and soil analyses. The identification of archaeological features as well as their differentiation from geological features or the glacial subsoil is a challenge in interpreting geophysical data. This is the task of the first part of this thesis.

The features of interest are urns, burials and cooking pits. Since these features mainly consist of boulder stones in an environment rich in boulders, the differentiation is often difficult. Therefore, the aim of this study is to refine interpretation by addressing single archaeological or geological features and estimating the potential of a classification of the signal strength per feature.

Since the focus of part I is on stony features, pit-like features will be presented in the second part. The results of the archaeological investigations at the site BH (LA 117) will be shown together with the results of the soil analyses and the geophysical investigations performed by means of magnetics and GPR. The focus will be on the main features: the central grave and the ditch surrounding barrow LA 117. In addition to the examinations of part I, the complexity of pit modelling with GPR will be highlighted. Furthermore the difficulty of the identification of steep dipping layers with a low contrast to the surrounding subsoil will be discussed.

The third challenge is reconstruction, on which the third part of this thesis will focus. A reconstruction helps to understand the conditions and transformation processes of archaeological times. This may take the form of a climatic reconstruction on the basis of sediments (e.g. Seguin et al. 2019), the analysis of pollen to understand the vegetation at a particular point in time (e.g. Zanon et al. 2018, Mariotti Lippi et al. 2010)

or a 3D reconstruction of a lake full of inhabited islands (e.g. Corradini, Wilken, et al. 2020, Guidi et al. 2013). The basis of any reconstruction in a geophysical context is clear prior to identification. In the third part of this thesis a burial mound is reconstructed on the basis of a 3D GPR data set and archaeological documentation. Most studies of burial mounds focus on the identification of archaeological features inside the barrow (e. g. the burial chamber) as well as on stratigraphy to identify the archaeological utilisation phases of the mound (e.g. Forte & Pipan 2008). However, a barrow must be preserved if its stratigraphy is to be analysed. The object of interest is eroded up to a remaining height of about 0.1 m (artificial part of the barrow). To reconstruct its stratigraphy and estimate its former height necessitates a close collaboration between archaeology and geophysics.

i.2 The Importance of Ground Truthing

Identification and interpretation are crucial aspects of analysing geophysical data. Without them, reconstruction would not be possible. The task of ground truthing is to support the interpretation of geophysical data and guard against misinterpretation. It may be performed, for example, by a test trench to understand magnetic anomalies in a magnetic map. Comparing the results of the test trench with the magnetic map can help to interpret the rest of the magnetic map with greater certainty (Hargrave 2006). This is important for many reasons. On the one hand, there is often not enough time and/or money to excavate large areas. From the point of view of conservation, large excavations are not desirable. The aim is to preserve historical monuments. On the other hand, archaeologists need information to decide which area is the most important. Therefore, non-destructive methods are often required to support archaeological investigations.

The second point is the most crucial. It is not helpful to make a test trench to support the interpretation of geophysical data for the purpose of using this interpretation to choose the right position for an excavation area. In the best case, researchers' knowledge of the soils and the archaeology allow them to interpret the data. The archaeological knowledge can be provided by an archaeologist, but the geophysicist should know what kind of signal with what strength a certain archaeological feature produces. For magnetic measurements, it is known that archaeological features cause anomalies in a small nanotesla range (e.g. 5-20 nT [Schaefer-Di Maida 2019]). The advantage of the evaluation of magnetic data is to play with the range of signal strength. So far, nothing comparable exists for GPR measurements. GPR is more complex. The quality of data depends on soil conditions. Therefore, soil analyses are very important.

The soils in Bornhöved are glacial and characterised by a high gravel content and massive iron oxide concretions. Also, the Bronze Age archaeological features contain boulder stones, which makes for a high potential for misinterpretations. In this thesis, ground truthing was performed alongside the archaeological documentation and soil analyses. The aim was to document the detection rate per applied geophysical method, i.e. magnetics and GPR measurement. In a second step, the signal strength caused by the feature was classified to predict the potential archaeological feature on the basis of the signal strength in further data sets. The archaeological documentation was used to extract the geophysical data at the position of the archaeological or geological feature in order to analyse it with regard to shape and signal strength. The soil analysis was used to

estimate its porosity, water content and susceptibility. The global aim of this investigation is to improve the detection rate – not only by combining magnetic and GPR measurements, but also by analysing soil samples.

i.3 Motivation and Objective

With these considerations in mind, a variety of challenges is faced. First, the detection rate shall be increased by using additional information from archaeological excavations and soil analysis. Second, misinterpretation shall be prevented in a surrounding soil similar to the components of an archeological feature. Third, the identification shall be improved in order to clearly address the kind of feature we are faced with, whether archaeological or geological. The solutions to these challenges form the basis for reconstructing archaeological features or sites.

Therefore the research questions are the following:
considering detection:

1. Will the recognition rate be better if GPR is compared with magnetic data?
2. Will the detection rate be improved if the information about the signal strength is also taken into account?
3. Which soil properties pits must have to be detected in the geophysical data?
4. Do soil analyses offer an additional gain of information to improve the detection rate?

considering identification:

1. Why are some archaeological features identifiable in the magnetic and/or GPR data and some are not?
2. Is it possible to make predictions regarding the identification of archaeological features on the basis of soil analyses?

considering reconstruction:

1. Is it possible to reconstruct the former height on the basis of the volume of the ditch phases by considering the angle of repose for typical soil materials?
2. Is it possible that the material of the ditch phases was used to cover up a further inhumation?

i.4 Structure of the Thesis

The thesis consists of three consecutive parts, each looking at three different aspects of the sites MdB and BH. The first discusses the difficulties of detecting and identifying (stony) archaeological features in glacial soils. In addition, porosity values and water content are determined to get an impression of the soil conditions. Furthermore, an attempt is made to classify the GPR amplitude. The second part investigates the soil condition of the pit filling with the help of a modelling study. Additionally, the position of the pits will be verified.

The resulting porosity and water content of part I of the thesis is used to derive a starting model. In the third part of the thesis the former height will be estimated by using the volume of the material of the ditch phases. The ditch phases are seen as phases of usage of the burial mound. The investigations of the pits in part II and the verification of the position of the three ditch phases allow the identification of them in the GPR data, so that the ditch phases can be picked.

In part I the archaeological documentation of the years 2005, 2017 and 2018 will be studied systematically. These data will be compared with the geophysical data. Data were gathered mainly by magnetics and GPR, conducted in each of these years on selected areas which, taken together, largely cover the excavation areas. First the archaeological and geological features were classified by their kind, size, depth of occurrence and recognition in GPR and magnetics, in order to determine a threshold of identification for each geophysical method regarding size and depth of the feature. After sorting, the features were counted and compared with magnetic and GPR data. A statistic was created, showing the kinds of features and their detectability in magnetics and GPR. To explain these statistics, the features were numerically modeled. The modelling was supported by soil analyses, which provides information about permittivity of the soil matrix and susceptibility. For the analysis, e.g. modelling, key targets were chosen. Furthermore, the glacial surroundings are characterised by boulder stones. Therefore, urn graves, cooking pits, burials and one iron oxide concretion (as representative for geological features) were chosen as key targets. They were compared in pairs to explain the differences in detection and in data quality. First, two different objects that caused similar anomalies in the GPR data (burial and iron oxide concretion) were compared, then the same features (urns and cooking pits) were compared in different soils. The modelling together with the soil analysis helped to estimate the soil parameters of porosity, water content, permittivity contrast and reflection coefficient, which have a high influence on the quality of the GPR data. Magnetic modelling was used to estimate stone susceptibility. Based on the results of the modelling and the soil parameters measured, the signal strength of the GPR data was classified by feature (both archaeological and geological) by assuming a mean porosity and three different water contents.

In part II of this thesis, the geophysical data from the 2018 measurements will be presented. Magnetic and 3D GPR measurements were made in advance of the excavation as part of the CRC 1266 “Scales of Transformation”. In contrast to part I, pit-like features are analysed. Archaeologically, the most important pit-like features are the central grave as well as the ditch surrounding the barrow. In this part of the thesis, the soil conditions of the pit filling will be analysed and the position of the pits are verified due to modelling. Furthermore the complexity of pit modelling is discussed. It is demonstrated that if the pit filling is drier than the surrounding the pits can be recognized easier.

The topic of part III is the reconstruction of a burial mound which has been nearly completely eroded by agricultural activities. In this part its previous height is determined together with the amount of material used to construct the barrow. The information on the basement of each filling phase yielded by the 3D GPR data set was the basis for selecting the layers. Then the volume of the ditch phases was determined. Two of the opening phases – the most recent ones – could be detected in the GPR data. Since it was common

burial practice in the Bronze Age to put the coffin at the surface and cover it with soil material, the question arose whether the material from each ditch phase could have been used to cover a secondary burial. Since the ditch shows three opening phases and the barrow three erecting phases, the assumption was that the material of the ditch per opening phase was used to erect the burial mound. The aim of this study was therefore to estimate its previous height, including the height after each opening phase and the volume of the material of the barrow.

Archaeologists used to estimate volume and height by assuming a hemisphere, although they know that typical burial mounds were in fact bell-shaped. This is the fastest and easiest way, but it is prone to lead to an overestimation of the volume. The approach of this part is to estimate the mound's previous height by assuming a spherical, bell-shaped and conical form, respectively, and using the volume of the ditch material. The bell-shaped form was defined by three mathematical functions: parable, modified generalised bell-shaped membership function and bump function. These theoretical approaches were complemented by investigating the stability of the slope by considering the angle of repose for chosen materials and the assumption of a conical shape.

Finally, a summary will present the findings of this thesis along with its conclusion.

ii Contributions

This thesis emerged from the collaboration with subproject D3 of the CRC 1266 “Scales of Transformation” as well as with the Institute for Ecosystem Research at the University of Kiel, which took and evaluated the soil samples. I ought therefore to identify the contributions of the various people involved.

Measurements; soil samples and excavations at the sites Mang de Bargen and Bornhöved:
I was part of the GPR and ERT measurements in Mang de Bargen. The GPR data of LA 58, LA 59 and LA 60 was conducted by Harald Stümpel and Christina Klein as part of her thesis (Klein 2006). LA 57 was also measured with GPR by Harald Stümpel and Christina Klein in 2005. In 2017 a further GPR measurement was conducted before and during the excavations. The measurements were conducted by Erica Corradini, Natalie Pickartz and me and supported by Ercan Erkul. In 2018 a GPR measurement was conducted by Ercan Erkul, Simon Fischer und Detlef Schulte-Kortnack crossing burial mound LA 117. I evaluated the GPR data of the sites Mang de Bargen (re-evaluation of the 2005 data sets and evaluation of the 2017 data set) and Bornhöved (LA 117). The ERT measurements of 2017 were conducted by Erica Corradini, Natalie Pickartz and me and evaluated by Erica Corradini. The conductivity values were used in the modelling study. The magnetic measurements at the site Mang de Bargen were conducted by Harald Stümpel and Christina Klein. At the Bornhöved site, the magnetic measurements were conducted by Stefanie Schaefer and others (see acknowledgements). Stefanie Schaefer-Di Maida also evaluated the data in her thesis (Schaefer-Di Maida 2019). The soil samples at both sites were taken and evaluated by Stefan Dreibrodt. The data were provided by Stefan Dreibrodt, too and were the basis for the numerical modelling. The archaeological excavation was conducted by Stefanie Schaefer-Di Maida (Mang de Bargen) and Jutta Kneisel (Bornhöved). They provided the archaeological documentation for LA 117 (Kneisel, Schaefer-Di Maida, et al. (in prep.)) and LA 57 (Schaefer 2017), which was the basis for the comparison with the geophysical data. The documentation of LA 58, 59 and 60 was provided by Lütjens (Lütjens 2013a-2013e). Furthermore, the archaeological documentation was the basis for digitizing the archaeological features for the modelling studies.

Part I:
I created all the figures and maps by myself. Photographs were provided by Kneisel, Schaefer-Di Maida and Dreibrodt. I conducted all numerical modellings and calculations. Jutta Kneisel provided the text of section I.2.2. Stefan Dreibrodt provided the text and the data set of section I.3.1. The rest was written by me. Except of the mentioned sections the text was written by me. The visualisation of the data was conducted by me. The results of the soil analysis are the basis for section I.4.1.1 and its subsections. The data of the soil analysis are also basis for estimating the porosity, water content and permittivity. These are also an integral part of the modelling study. The data of the surveyed features during the excavation were provided by Jutta

Kneisel and formed the basis of the QGIS maps. For comparing the geophysical data with the archaeological documentation, I digitized the documentation that was provided by Jutta Kneisel. The idea of conducting this study arose in the regular technical meetings between Jutta Kneisel, Stefanie Schaefer-Di Maida, Wolfgang Rabbel and me.

Part II:
I created all the figures and maps by myself. Photographs and archaeological documentation were provided by Jutta Kneisel. The text of sections II.2.2 and II.4.1 was provided by Jutta Kneisel. The text of section II.2.3 was written by me, checked by Jutta Kneisel and modified and expanded by me. Also the sections II.2.2 and II.4.1 were checked by Jutta Kneisel to, but modified and expanded by me. Stefan Dreibrodt provided the text and the data set of section II.3.3. The results of the soil analysis were the basis for the results presented in sections II.4.2 and II.4.4.1. The visualisation of the data werde conducted by me. The data of the soil analysis are also basis for estimating the porosity, water content and permittivity. Except of the mentioned sections the text was written by me. The data of the surveyed features during the excavation were provided by Jutta Kneisel and formed the basis of the QGIS maps. For comparing the geophysical data with the archaeological documentation, I digitized the documentation that was provided by Jutta Kneisel. The idea for conducting the modelling study and sensitivity analysis are mine.

Part III:
I created all the figures and maps by myself. Photographs were provided by Kneisel and Schaefer-Di Maida. The picking of the GPR data was conducted by myself. The text was written by myself. The idea for conducting this study as well as the calculations are mine.

iii Contributions to Other Publications

Corradini, Wilken, et al. 2020

Corradini, Eriksen, et al. 2020

Corradini, Dreibrodt, et al. 2020

I contributed to these papers as a participant in the measurement campaigns.

Groß et al. 2019

I contributed to this paper as a participant in the measurement campaigns.

Kneisel, Brinkmann, et al. 2018

I contributed to this paper by processing the data and creating figure 3.

Pickartz, Corradini, et al. 2020

I contributed to this paper by writing the sections "Methods – Ground Penetrating Radar", "Results – Ground Penetrating Radar" and processing the GPR data and creating figures 2C, 3B and 3C.

Part I

GPR and Magnetic Measurements of Burial Mounds on Glacial and Glaciofluvial Deposits in Bornhöved (N Germany) – A Comparison

I.1 Introduction

This study investigates Bronze Age archaeological features in glacial soils. Common Bronze Age features are pits, post holes, urns (enclosed by stone packages), cooking pits, burials (embedded in stone packages) and stone concentrations. Typical glacial soils are characterized by sand, clay, loam and gravel that are heterogeneously distributed as well as remains of stones transported by the abrasion processes of the glacial sheets. The complexity of the glacial soils produces numerous anomalies in magnetic and GPR measurements, which complicate the interpretation of the data and can therefore lead to misinterpretations (Trinks 2015, Viberg et al. 2011). Difficulties in magnetic prospection may be posed by shallow bedrock overlying potential archaeological features (Trinks 2015, Viberg et al. 2011). A problem in GPR measurements can be the occurrence of clay, which leads to high damping of the GPR waves (Trinks 2015, Viberg et al. 2011).

The challenge of interpreting radar data is its complexity. Time slice and profile always need to be considered together and, if possible, in combination with other geophysical methods. Therefore, there are many approaches to make radar data interpretable in such a way that even beginners can easily interpret it. There are more recent approaches via neuronal networks, such as Green & Cheetham (2019) or Küçükdemirci & Sarris (2019), to name some of the most recent studies. They are using neuronal networks for the identification of graves (Green & Cheetham 2019) or anomaly detection (Küçükdemirci & Sarris 2019). Other approaches are to analyze GPR attributes such as amplitude, frequency, coherence, etc. to highlight specific lateral or vertical discontinuities (Zhao, Forte, Pipan, et al. 2013, Zhao, Forte, Levi, et al. 2015, Boeniger & Tronicke 2010). This applies in particular to the identification of brick walls. There are also approaches to improve the interpretation of magnetic data, such as the classification of anomalies by using automatic approaches, such as pattern recognition (e.g. Trinks 2015, Pregesbauer et al. 2014). These approaches are commonly applied to ditch systems.

A further challenge in interpreting geophysical data for archaeologists are the differences in archaeological settings (e.g. sites, kinds of feature) depending on their archaeological time. In protohistoric times archaeological features are commonly massive, whereas remains of prehistoric times (e.g. the Iron, Bronze and Stone Ages) are mainly pits, post holes, ditch systems, urns, cooking pits, stone concentrations and graves. As e.g. Trinks 2015 has observed, pits, graves and stone concentrations are not arranged in geometric patterns, like post holes. An advantage of the study of Bronze Age remains in northern Germany is that archaeological features are commonly arranged around the burial mounds we are looking for.

The intention of this part of the thesis is to develop a statement regarding the recognition rate of archaeological features of different types and sizes in geophysical data, in order to be able to give more reliable

statements about the archaeological subsurface in future geophysical prospections. Usually, with conservation in mind, excavation of archaeological monuments is limited, which is why it is accompanied or supported by geophysical measurements. This makes it difficult to make a reliable statement regarding the recognition of archaeological features in geophysical measurements. The advantage of the measurement and excavation campaign in Bornhöved is that extensive excavations, geophysical measurements (GPR, magnetics and susceptibility measurements) and soil analyses have been conducted, allowing a statistical analysis regarding the identification of archaeological features in the geophysical measurements as well as a classification of their signal strengths.

The focus of the investigations in this part of the thesis will be on two main tasks: First, to find out if the recognition rate will be improved by combining magnetic and radar measurements as well as by including the signal strength of the features. Second, the question will be answered why some archaeological features are identifiable in the magnetic and/or radar measurements and others are not. The hypothesis is that the soil conditions influence the measurement results. In this framework, the question is addressed whether it is possible to make predictions regarding the recognition rate based on soil conditions and parameters.

The main archaeological features to be studied in the study area of Bornhöved are Early Neolithic to Bronze Age burial mounds, urns, cooking pits and burials with stone packages, which, like the subsoil, consist of boulder stones. Geologically, a lot of gravel and boulders as well as concrete iron oxide layers can be expected in the study area, whose occurrence in the radar time slices may be misinterpreted as man-made. The study area consists of two sites: Mang de Bargen (MdB) and Bornhöved (BH). Therefore, the following examples are used: an inhumation burial (MdB-IB) and an iron oxide concretion (MdB-FeO) to discuss the potential of a comparative investigation of magnetics and radar in contributing to better differentiation and therefore interpretation. Furthermore, one example of the urn graves (MdB-U and BH-U) and one of the cooking pits (MdB-CP and BH-CP) of the two sites is investigated, to address the question of the influence soil and measurement conditions have on the geophysical data

I.2 A Priori Information

I.2.1 Geological Setting

Bornhöved is located in Schleswig-Holstein, northern Germany (fig. I.2.1a) in the transition zone from glacial till to glaciofluvial outwash sands. The landscape was mainly formed by the events of the Weichselian glacial. Burial mound LA 117, site BH, is located in the till, which consists mainly of boulder clay (fig. I.2.1b). The mound is situated on an island of silty, clayey, sandy and gravelly till deposits upon sand. The east of Bornhöved is characterized by the so-called Trappenkamper Sander, the glaciofluvial outwash sands. The site Mang de Bargen (MdB) is located on the northeastern end of these outwash sands (fig. I.2.1b). Mainly even, the Trappenkamper Sander locally shows a strong relief. The sediments are mainly characterized by sand and gravel. The Bornhöveder See, a lake in the north of Bornhöved, is part of the so called Bornhöveder Zungenbecken which probably developed in the older or younger Dryas (Landesamt für Landwirtschaft 2012 Barsch 1978a; Barsch 1978b). From the soil analyses it is known that the soils in MdB are Cambisols and Luvisols (Dreibrodt, Nelle, et al. 2009).

Figures I.2.1c and I.2.1d show the deposition of archaeological features in the subsoil in MdB (fig. I.2.1c) and BH (fig. I.2.1d). MdB's subsoil is more gravelly with smaller stones in the first 0.3 m beneath the topsoil and larger boulder stones beneath. The subsoil of BH is more homogeneous, whereas smaller stones can be also found around the archaeological feature and beneath. Additionally, a lot of boulder stones are inside the soils. These stones were brought with the glaciers from northern Europe. In northern Germany one can expect magmatic (in particular granite and porphyry), metamorphic (in particular gneiss and amphibolite) and sedimentary stones (in particular limestone) (Smed & Ehlers 2002). Iron oxide layers, which can be seen in figure I.2.1d (red brown layer marked with black arrow) occur in both sites. In Bornhöved, large areas of iron oxide concretions occurred directly beneath the topsoil (fig. I.4.10a (MdB), fig. I.2.1d (BH)). Iron oxide concretions develop in porous soils by iron oxide precipitation through pH changes, bacteria activity and oxidation conditions (Parry 2011). There are several types of iron oxides or hydroxides, such as magnetite (Fe3O4), haematite (α-Fe2O3), goethite (α-FeOOH), maghemite (γ-Fe2O3) or lepidocrocite (γ-FeOOH), which are stable under certain conditions, like their chemical stability, solubility and precipitation mechanism (Parry 2011, Guo & Barnard 2013). Goethite and haematite are the most common (Blume et al. 2016). Maghemite and magnetite are ferrimagnetic, goethite and Lepidocrocite are antiferromagnetic, ferrihydrite is speromagnetic and haematite is weakly ferromagnetic (Chesworth et al. 2008). Considering the magnetic anomaly between -0.5 and 0.5 nT, the absence of charcoal and the fact that the soils in MdB are luvisols, magnetite and maghemite can be excluded as potential iron oxide representatives for the found concretion. Due to the occurrence of lepidocrocite in soils with slack water and ferrihydrite in podzol, we

can also exclude these iron oxide minerals. Regarding the occurrence of the other iron oxides, it is known, that goethite is common in soils of all climate zones and causes a yellow-brown colour of the soils. Haematite can occur together with goethite in soils of the tropic and sub-tropic zones and causes the red soil colour. Haematite needs high temperature conditions and small water contents of the soils. In moderate climate zones as well as in cooler zones goethite is more common than haematite. Moreover, the wetter the soils, the more likely we are to find goethite. It was also observed that soils in topographically higher areas are drier and redder due to the presence of haematite. Lower-layered soils are wetter and more yellow due to the presence of goethite. Lepidocrocite develops in carbonate-poor environments, in clayey soils with slack water. It is a metastable mineral compared to goethite, into which it tends to transform. In moderate climatic zones, lepidocrocite occurs in a reduced carbonate-free environment. Ferrihydrite occurs by oxidation of Fe^{2+}-containing waters or by the presence of organic compounds in B horizons of podzol soils. Magnetite developed by bacteria is found in soils influenced by groundwater. Maghemite developed by oxidation of lithogenous magnetite through burning processes (Blume et al. 2016).

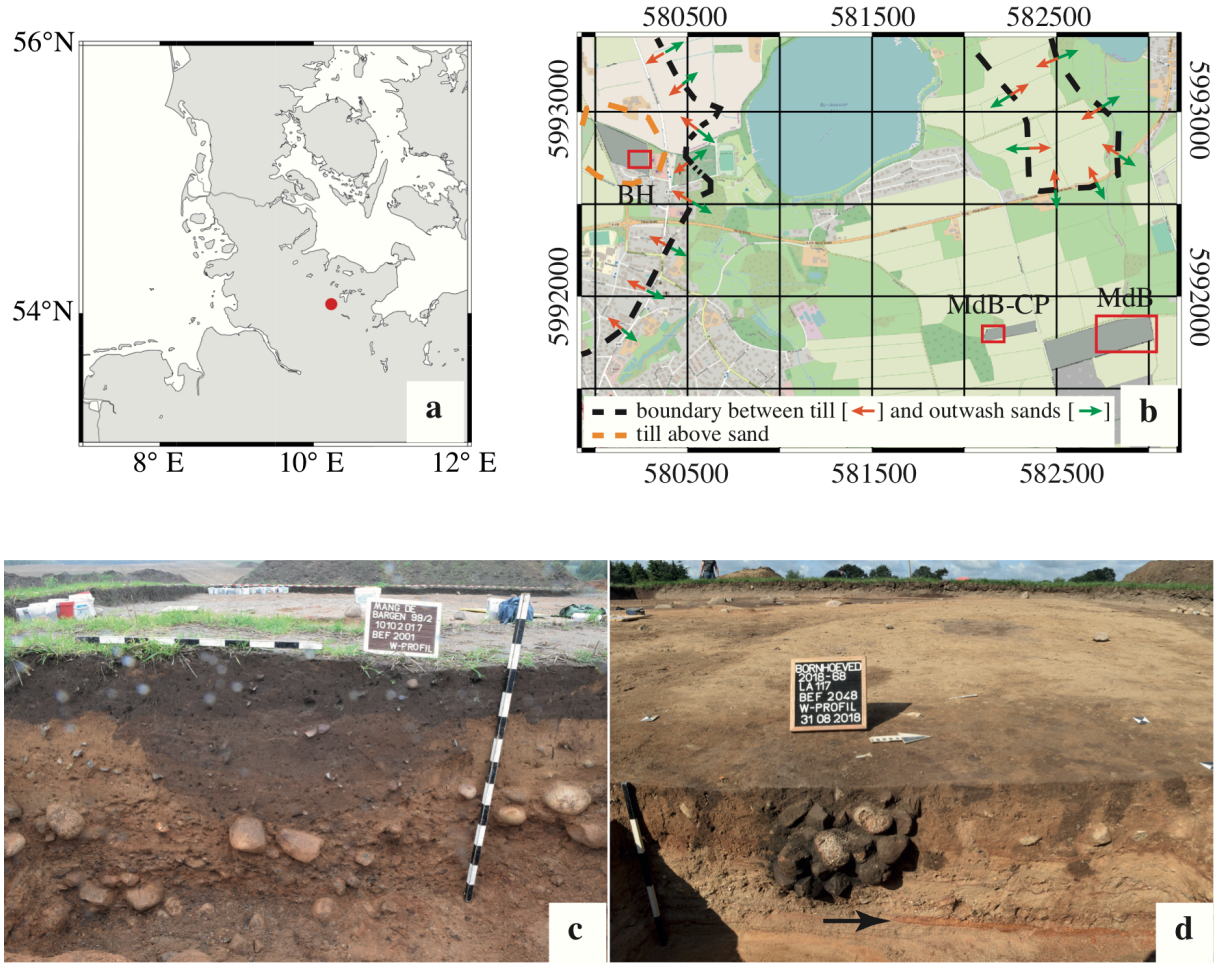

Fig. I.2.1: Location of the study sites (in WGS 84 coordinates)) (a) and geophysically investigated sites (in UTM zone N32 coordinates) (b). Fig. I.2.1a was created with GMT (Wessel & Smith 1991). The red boxes indicate the sections that are shown in Figs. I.2.3 – I.2.5. Fig. I.2.1c shows a photography of the inhumation MdB-U (by Schaefer-Di Maida). Fig. I.2.1d is a photograph of the cooking pits BH-CP (by Kneisel).

I.2.2 Archaeological Background

In the Bronze Age (1750-500 BC) Schleswig-Holstein belonged to the southern border zone of the Nordic Circle, which included southern Scandinavia, northern Germany and Poland. The Early Bronze Age (1500-1100 BC) is characterised by barrows which are usually situated on the edges of the glacial moraine hilltops. In the rural district of Segeberg, between the village of Trappenkamp and the Plöner See, there is such a SW-NE oriented moraine hilltop (fig. I.2.2) at the edges of which about 280 known burial mounds are grouped. The plateaus, on the other hand, are free of burial mounds, with the exception of the Grimmelsberg, whose highest elevation is dominated by a Bronze Age barrow (Krosigk 1976). One of the largest groups is located on the "Mang de Bargen" corridor (fig. I.2.2), consisting of about 18 burial mounds, all of which were investigated to document the human remains before destruction by gravel mining (Schaefer-Di Maida 2019). One of them was investigated as part of the CRC 1266 "Scales of Transformation" to finalise the documentation of all burial mounds of the Mang de Bargen corridor. The archaeological question addressed by the evaluation of the archaeological documentation of all MdB burial mounds concerns the development of the Bronze Age population on the basis of the graves, since little so far is known about Bronze Age settlements.

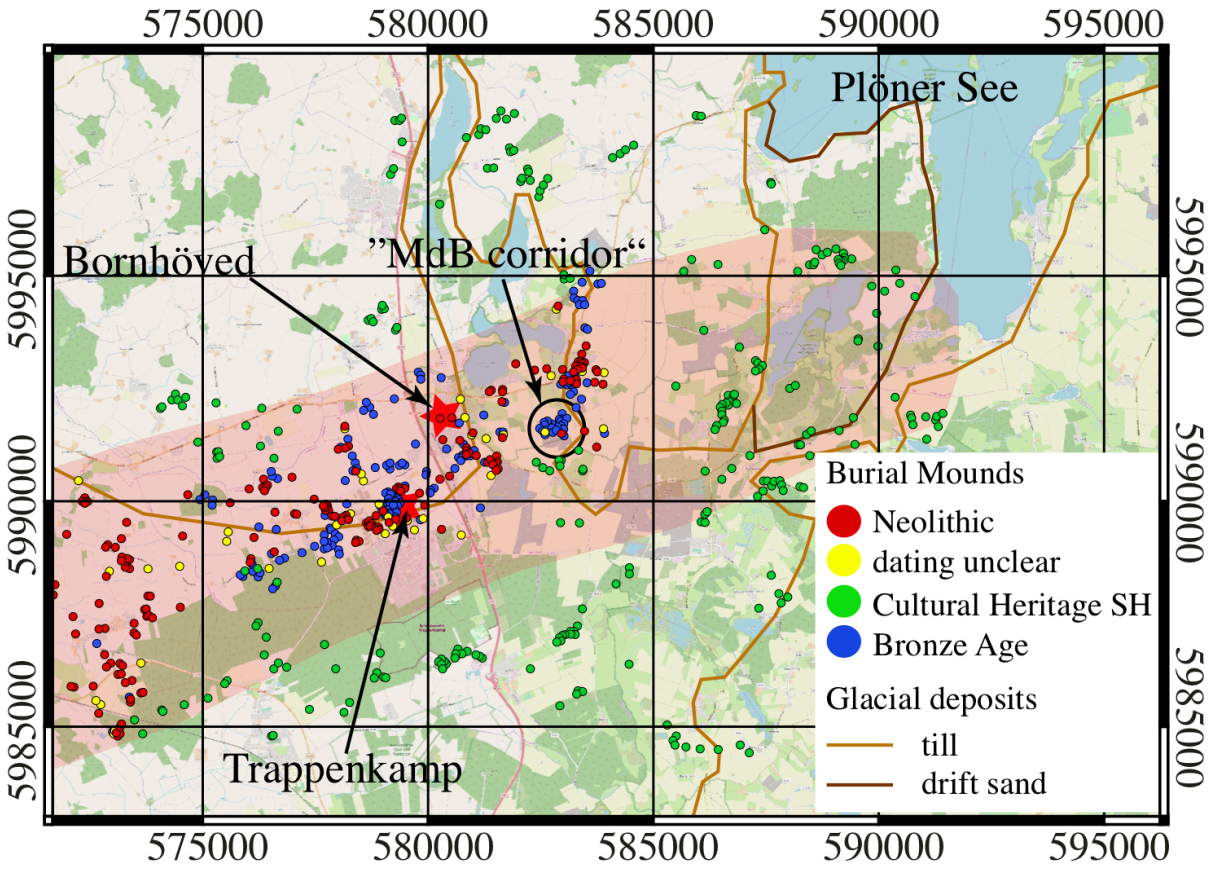

Fig. I.2.2: Distribution of the burial mounds in the area around Bornhöved. The red shaded area highlights the barrows at the edges of the moraine hilltop. The black circle marks the position of the "Mang de Bargen corridor". The red dots represent burial mounds dated to the Neolithic, whereas the blue ones may date from the Bronze Age. There are some barrows whose dating is still unclear and which are represented by a yellow dot. Green represent additional burial mounds, also dating from the neolithic to the bronze age, as documented by the conservation authorities. The documentation of the barrows was part of an investigation by Krosigk (1976).

The younger Bronze Age (1100-500 BC) was marked by a change in burial customs. Instead of newly erected burial mounds, urn graves were now buried in the barrows or at their edge, as it was done in Mang de Bargen. The burial mound LA117 at Bornhöved, about 3 km to the northwest of Mang de Bargen, is a special feature of the region, due to its henge of posts and the circular ditch surrounding the barrow. From about 1400 BC, cooking pits appear, which are regularly found in the landscape, both near settlements and near burial mounds. Due to their regular arrangement (linear or in groups) and the fact that they consist of burnt stones, they are easily recognisable in magnetic investigations.

I.2.3 Previous Geophysical Measurements

Due to gravel mining, geophysical measurements using GPR and magnetic gradiometry were conducted by geophysicists from the University of Kiel at the site Mang de Bargen in 2005. GPR measurements have so far focused on the burial mounds LA 17, 18, 57, 58, 59 and 60 (fig. I.2.3).

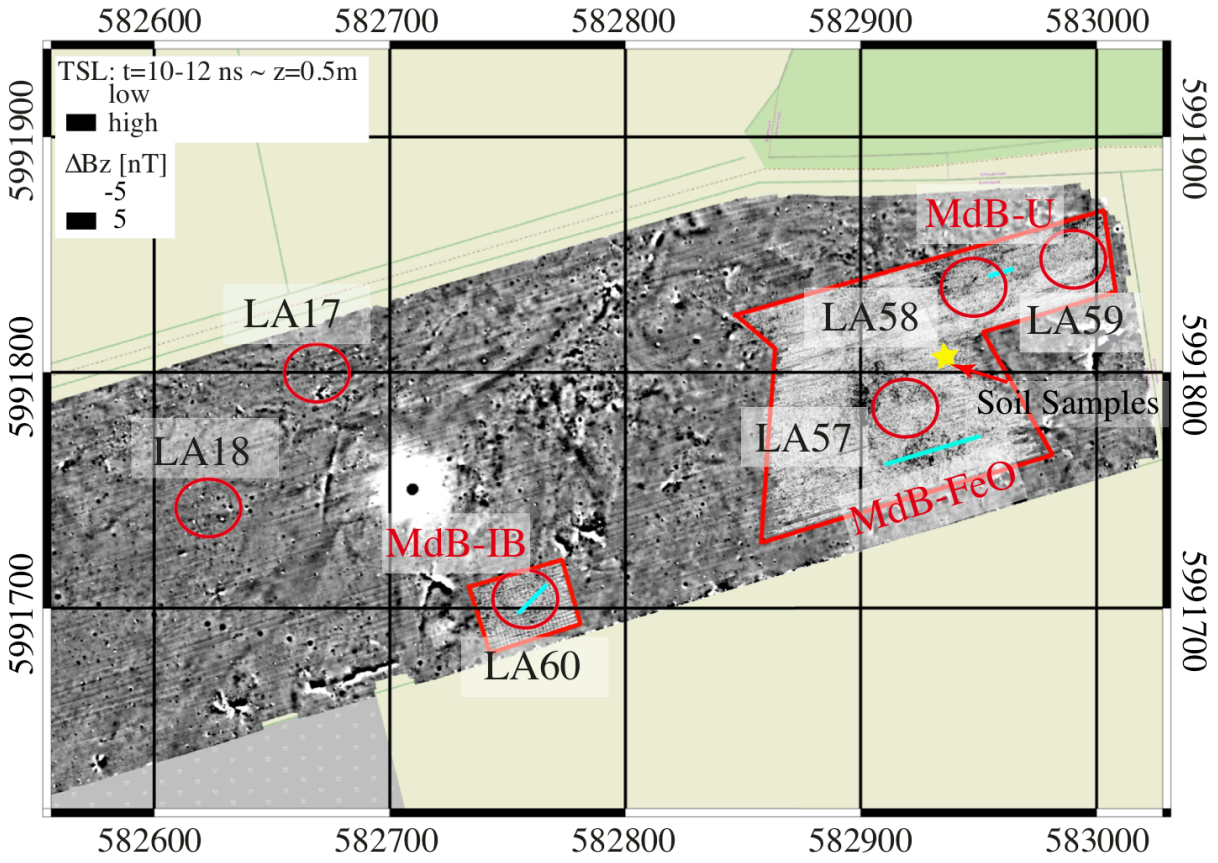

Fig. I.2.3: Locations of already geophysically investigated burial mounds. Magnetic map and GPR time slice at about 0.5m of depth of the measurements in MdB. The blue line indicates the position of the discussed features in the results. The yellow star marks the position of the soil samples taken.

Additionally, a large-scale magnetic prospection was conducted (Klein 2006). The aim of these investigations was to plan archaeological trenches, since the excavations of LA 17, 18, 58, 59 and 60 started in 2005 (Lütjens 2013a, Lütjens 2013b, Lütjens 2013c, Lütjens 2013d, Lütjens 2013e). The geophysical results of LA 17 and 18, as well as those of LA 57, 58 and 59, remain unpublished to date. The burial mound LA 57 was excavated in 2017 as part of the CRC 1266 "Scales of Transformation" (Schaefer 2017; Schaefer-Di Maida 2019). A magnetic measurement 500 m to the west of the cemetery of Mang de Bargen showed an assemblage of cooking pits (fig. I.2.4), whose magnetic signature is very clear. A few cooking pits were excavated in test trenches by Schaefer in 2017 (Schaefer-Di Maida 2019).

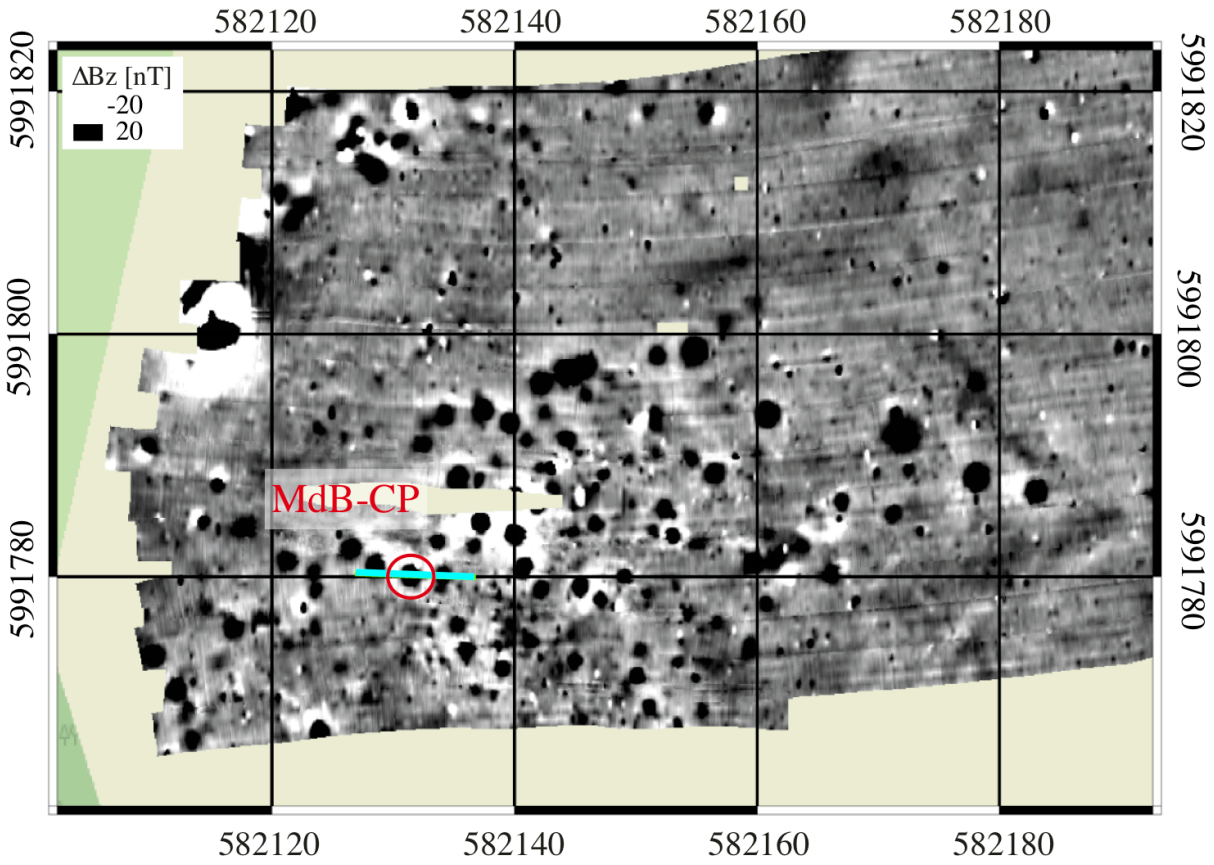

Fig. I.2.4: Magnetic map of the cooking pit complex in MdB. Blue line indicates the position of the discussed profile or feature respectively in the results. The investigated cooking pit is highlighted by a red circle.

LA 117, at the Bornhöved site, was magnetically prospected (fig. I.2.5) and excavated by archaeologists from the University of Kiel in 2018. Kiel geophysicists were able to conduct GPR measurements beforehand. All the investigations were part of the CRC 1266 “Scales of Transformation” (fig. I.2.5).

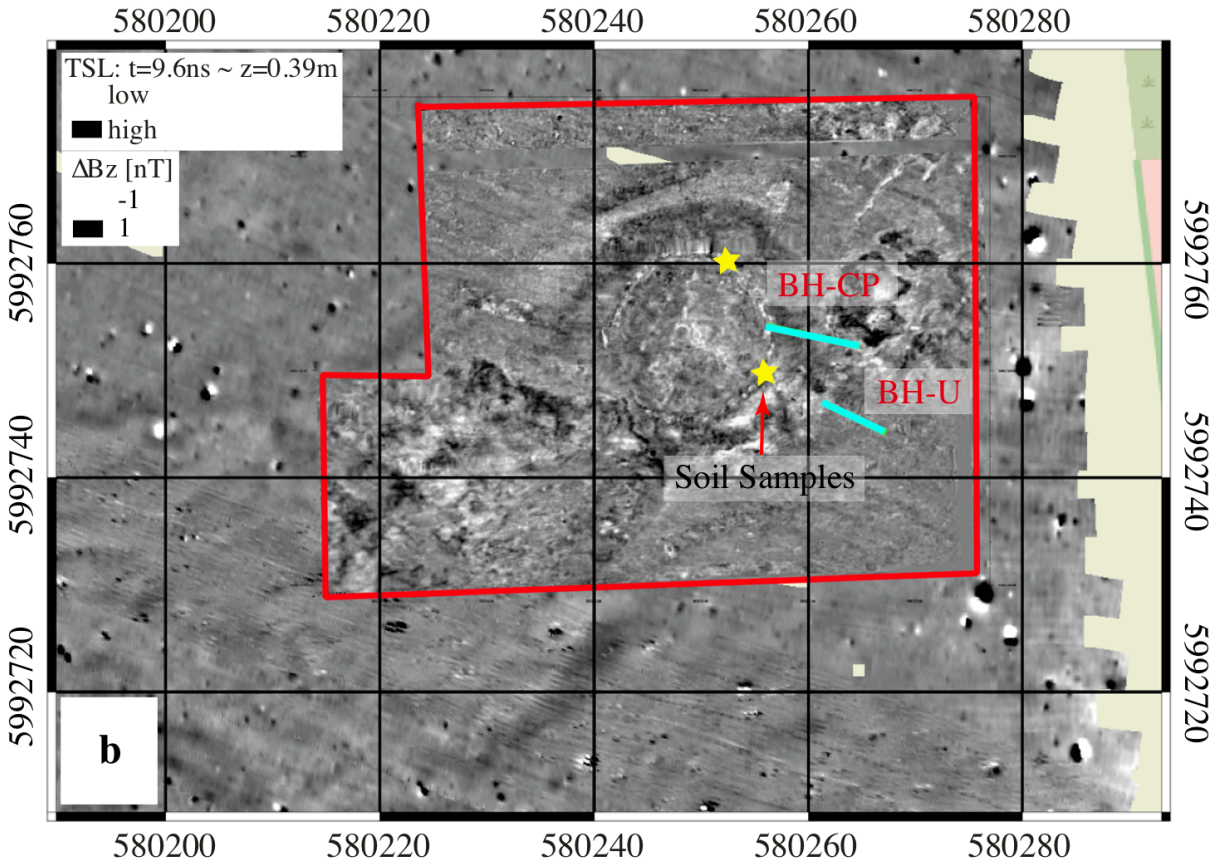

Fig. I.2.5: Magnetic map and GPR time slice at about 0.5m of depth of the measurements in BH. Blue lines indicate the position of the profiles or features discussed in the results. The yellow stars mark the position of the soil samples taken.

I.3 Methods

This part of the thesis deals with the possibility of a differentiation between geological and archaeological features in geophysical data and a clear identification of single archaeological features (e.g. urns, cooking pits) in GPR and magnetics. For that purpose, geophysical data is being collected at two different sites through large-scale GPR and magnetic measurements, which have been completed with archaeological excavation and documentation. The geophysical data are analysed and classified with regard to the most common Bronze Age archaeological and geological features.

Since the surrounding soil (soil composition, physical properties) influences the appearance of the features in the radar or magnetic measurements, soil conditions are investigated as well. From the soil composition the permittivity of the soil matrix is derived. By varying the relative permittivity, the porosity and volumetric water content of the soil are derived to understand the behaviour of GPR wave propagation through modelling. This information is used to get an impression of the shape of the signal. From the susceptibility measurements, the detection of common archaeological and geological features can be assessed through magnetic modelling.

Since GPR and magnetic measurements depend on the distance between sensor/receiver and feature, it was necessary to eliminate depth dependence in the signals of GPR and magnetic data, in order to correct the data to a common level. The necessary corrections for GPR are spreading correction and correction for attenuation, those for magnetic data are down- or upward continuation to enable a comparison. Additionally, numerical modelling is used and the modeled signal is compared with the measured signal, to assess the physical properties (in particular permittivity and susceptibility). Soil analyses are used to evaluate the influence of the geological surroundings of the features.

I.3.1 Soil Analysis

Soil analysis was conducted to obtain information about soil composition, content of organic matter, magnetic susceptibility and frequency-dependent susceptibility. Organic matter is related to soil moisture (Gustavsen et al. 2018). Magnetic susceptibility is a material-dependent parameter and describes how magnetizable the material is in an externally-applied magnetic field (Blakely 1996). The frequency-dependent susceptibility of a material reflects the size of its magnetic components. Low-frequency measurements allow small magnetic crystals (close to 0.3 μm) to contribute to the susceptibility of a material; high-frequency measurements do not (Dearing et al. 1996; O. A. Clark & A. Clark 1996). There are grains of small size, e.g. ultra-fine secondary iron oxides, which show a relatively high frequency dependency. These grains are often the product of human

activity. Either they can be precipitated by well-drained topsoils, e.g. through cultivation, or originated by firing processes (O. A. Clark & A. Clark 1996).

Two archaeological profiles were selected for geoarchaeological analyses: one crossing the ditch of BH and one in MdB outside an archaeological feature, but within a sequence of cultural layers ranging from modern times (at the top), early medieval, pre-Roman Iron Age until the late Neolithic at its base. The samples were taken vertically, following the chronostratigraphic order identified in the field. The profile as well as the sampling positions were documented in scaled drawings and digital photographs. In addition, the position of the samples was documented with the help of a total station. In the laboratory the samples were dried for two weeks at 35 °C. The preparation for further measurements included their careful disintegration with a mortar and pestle and the extraction of the < 2 mm fraction via dry sieving. Any further analysis continued on the < 2 mm fraction. Loss on Ignition (LOI) measurements were carried out to estimate the content of organic matter (550 °C) and carbonates (940 °C) (Dean 1974). The grain size distribution of the samples was carried out by a combination of wet sieving and sedimentation in Atterberg-cylinders after removal of organic matter and carbonates (Roderick 1972).

I.3.2 Ground Penetrating Radar (GPR)

I.3.2.1 Data Acquisition and Processing

In 2005, the areas in MdB were measured with 2 combined 400 MHz GSSI antennas with SIR-20 (GSSI) and a profile distance of 0.4 m. The distance between the two antennas measured 0.3 m. In 2018, at BH, a 16 channel MALA Mira antenna was used (Guideline Geo AM MALA & ABEM), which can collect a 3D data set due to its channel distance of 8 cm. A RTK-DGPS was used for positioning. Processing steps applied were:

(a) time zero shift,

(b) correction for spherical divergence and attenuation,

(c) subtraction of a mean trace to remove horizontal lines,

(d) in the case of the BH data: band pass filtering and applying a gain function and

(e) topographic migration (Wilken et al. 2016)

The correction of spherical divergence and attenuation was applied to ensure the comparison of different data sets. The parameter of interest for correcting the attenuation are conductivity and permittivity (Davis & Annan 1989; Neal 2004). At MdB electrical resistivity (ERT) could be measured at 4 profiles crossing LA 57. Conductivity for the MdB data set was determined by using the average conductivity values of the first 2 m. To determine the permittivity for the topsoil and subsoil of Mang de Bargen, the velocity is determined through hyperbola fitting and used the equation $\epsilon_r = \frac{c^2}{v^2}$ (Davis & Annan 1989; Neal 2004). For BH there were no ERT measurements available and also almost no hyperbolas. The conductivity and permittivity values

of MdB are used as an estimate, while the conductivity values for the subsoil (0.3 to 2 m of depth) were used for attenuation.

To enhance reflections of the data set of 2018, a bandpass filter and a gain function were applied. Velocities for migration were determined by hyperbola fitting and test migrations. The final parameters can be found in table I.3.1.

Table I.3.1: Parameters for processing

processing steps	location	parameters
time zero shift		
correction for spherical divergence and attenuation	MdB BH	σ=1.23 mS/m; ϵ_r=14 σ=0.9 mS/m; ϵ_r=14.1
bandpass filter	BH	start frequency=100 MHz; end frequency = 700 MHz
gain	BH	trace $*\sqrt{t}$
subtraction of a mean trace to remove horizontal lines		
topographic migration	MdB BH	v=0.09 m/ns v=0.08 m/ns

I.3.2.2 Modelling

To get a better understanding of the signals' origin and to verify the measurements, GPR data was modeled. For GPR modelling, the Matlab-based program by Irving & Knight (2006) was used. This is a finite difference time-domain modelling of GPR data in 2D. For avoiding edge effects, they implemented absorbing boundaries, and the second derivative of a gaussian pulse was used as the source pulse (Warren & Giannopoulos 2012).

The parameters used for modelling can be found in table I.3.4. Since the transition from topsoil to subsoil is always clear, it was necessary to determine permittivity and conductivity for top and sub soil separately. For modelling the GPR data of MdB, conductivity values are derived from the ERT measurements and the permittivity values by hyperbolas present in the data due to a large quantity of gravel and boulder stones in the soil. The permittivity values for MdB were calculated by using velocity as determined by hyperbola tests. Conductivity was determined from the results of the Wenner Alpha configuration for the topsoil (first 0.3m) as well as the subsoil (0.3 to 2m).

At BH, only magnetic and GPR measurements were conducted. Therefore, no information about the conductivity of the soil is available. Therefore, the conductivity values for the topsoil of BH are adapted from MdB. For the subsoil of BH, the conductivity values are calculated with the generalized Archie's law after

Shah and Singh (2005) for the archaeologically documented soil textures (loam, loamy sand and sand) by assuming a volumetric water content between 10% and 20% (parameters are summarized in table I.3.4).

Due to the lack of hyperbolas, it was also not possible to derive permittivity values for the BH soils. But the soil analyses of BH allows the estimation of the permittivity using the soil composition by using Birchak's equation (1974) for a three-phase system. The soil analysis was used to determine the clay (C), silt (U) and sand content (S). From Daniels & Utsi (2013) and Davis & Annan (1989), the bulk dielectric constants of clay, silt and sand are collected in table I.3.2. This information was used to determine the permittivity of the soil matrix:

$$\epsilon_{soilmatrix} = (C * \sqrt{\epsilon_C} + U * \sqrt{\epsilon_U} + S * \sqrt{\epsilon_S})^2 \tag{I.3.1}$$

Table I.3.2: Bulk dielectric constants (ϵ_r measured at 100 MHz) of clay, silt and sand

Material (symbol)	ϵ_r after Davis & Annan 1989	ϵ_r after Daniels & Utsi 2013
Clays (C)	5-40	
Clay (C), wet		15-40
Clay (C), dry		2-6
Silts (U)	5-30	
Sand (S), wet	20-30	10-30
Sand (S), dry	3-5	4-6

Since the soil consists of the soil matrix, porosity and water content, there is another three-phase system of relevance, defined as follows

$$\epsilon_{soil} = (\theta * \sqrt{\epsilon_w} + (\theta - \phi) * \sqrt{\epsilon_{air}} + (1 - \phi) * \sqrt{\epsilon_{soilmatrix}})^2 \tag{I.3.2}$$

The variation of porosity (ϕ) and volumetric water content (θ) in a GPR modelling study allows an estimate to be made of the soil conditions during the measurement.

Since it was not possible to obtain permittivity values for the site BH by using (for instance) GPR velocity, the relative permittivity of the soil was calculated by using equation I.3.2. By doing this, a water content of 10 to 20% was established. From Blume et al.(2016) we can expect porosity values between 30 and 55% (see table I.3.3). By applying equation I.3.2, the permittivity was varied between 7 and 16 (representing velocities between 0.075 and 0.113 m/ns – compare table I.3.4) during modelling of the BH-features.

From Birchak's equation, it is known that permittivity increases with the water content, whereas it decreases with increasing porosity. it was also tried to estimate porosity and volumetric water content from permittivity using Birchak's equation (1974).

Table I.3.3: Typical porosity values for mineral soils (Blume et al. 2016)

mineral soils	porosity [%]
sands	36-56
silts	38-56
loams	30-55
clays	35-65

The conductivity and permittivity values for the most common archaeologically observed materials (e.g. iron oxide, ceramics, bones and stones) were extracted from literature (see table I.3.4). Since a range of permittivity values of stones is given, different values were tested and the amplitudes were compared with the signal of measured data. For the permittivity value of bones, the averaged value of bone fat and bone meal was used to obtain an average value. The conductivity values for bones and ceramics are estimates drawn from the studies mentioned in table I.3.4. An "estimate" in this context means that the averaged values of all the measurement results of these studies for each material was used.

Due to the heterogeneous shape of the iron oxide concretion (see photograph Fig. I.4.10a), up to three layers of iron oxide with thin layers of sand in between were assumed. The number (number of layers to be varied: 1-3) and thickness of these three layers (thickness of MdB-FeO layers: 8-12 cm) were then varied during modelling. In the case of the inhumation, both the approximate depth and the geometry of the stone package were known. To simulate the space between the stones, up to three stone layers were created, with a thin sand layer in between. The number (number of layers to be varied: 1-3) and thickness of these three layers (thickness of MdB-IB layers: 8-14 cm) were then varied during modelling. Since the urn BH-U was situated at a depth of more than 1 m, additional layers of random thickness were inserted. The permittivity of the filling was varied between 12 and 15, assuming intruded soil caused by small cracks in the pottery (Kneisel in prep.). In contrast to BH-U, the model of MdB-U was based only on the photographs of the archaeological documentation (Fig. I.4.18a). Therefore not only the permittivity values were changed but also the height of the urn (and thus the height of the stone package) as well the depth of the urn complex. From the documentation of the urn, it is known that the urn contained a mixture of bone and sand (Fig. I.4.18a). The depth was varied between 0.28 m and 0.35 m. Since it was not obvious how much damage the urn and sustained, it was necessary to vary the height of the urn, too, between 4 and 8 cm.

For comparison of the modeled and measured signal, the amplitudes are normalized by the direct wave to obtain an idea of the strength of the amplitudes of the subsurface. Additionally to that, the reflection coefficients are calculated, which are defined as follows

$$R = \frac{\sqrt{\epsilon_{r2}} - \sqrt{\epsilon_{r1}}}{\sqrt{\epsilon_{r2}} + \sqrt{\epsilon_{r1}}} \tag{I.3.3}$$

$$R = \frac{\sqrt{v_2} - \sqrt{v_1}}{\sqrt{v_2} + \sqrt{v_1}} \tag{I.3.4}$$

The reflection coefficient describes the amount of reflected energy at layer boundaries, where one can expect abrupt changes in dielectric properties and velocities with respect to the dominant radar wavelength (Kirsch et al. 2006; Neal 2004)

Table I.3.4: Parameters for modelling

location	feature	material	parameter	range
MdB		top soil	ϵ_r	6.05
MdB		top soil	σ [mS/m]	1.83
MdB		sub soil	ϵ_r	14 - 20
MdB		sub soil	σ [mS/m]	0.9
BH		top soil	ϵ_r	6.05
BH		top soil	σ [mS/m]	1.83
BH		sandy loam	ϵ_r	7-16
BH		sandy loam	σ [mS/m]	0.7-2.07
BH		sand	ϵ_r	7-16
BH		sand	σ [mS/m]	0.76-1.97
BH		loam	ϵ_r	7-16
BH		loam	σ [mS/m]	0.68-2.09
		stone (Cassidy & Jol 2009)	ϵ_r	5-10
		stone (Cassidy & Jol 2009)	σ [mS/m]	1
		iron oxide	ϵ_r	1.9 (KG n.d.)
		iron oxide	σ [mS/m]	6.25e-6 (goethite); 5e-5 (haematite) (Guskos et al. 2002)
		ceramics	ϵ_r	17 (KG n.d.)
		ceramics	σ [mS/m]	1e-5 (Hirata et al. 1993)
		bones	ϵ_r	2.3 (KG n.d.)
		bones	σ [mS/m]	6.5 (Williams & Saha 1996)
MdB	FeO	iron oxide concretion	number of layers	1-3
MdB	FeO	iron oxide concretion	thickness of layers [m]	0.08-0.12
MdB	IB	stones	number of layers	1-3
MdB	IB	stones	thickness of layers [m]	0.08-0.14
MdB	U	urn	position in depth [m]	0.28-0.35
MdB	U	urn	height of the urn [m]	0.04-0.08
BH	U	urn filling	ϵ_r	12-15

I.3.3 Magnetics

I.3.3.1 Data Acquisition and Processing

In 2005, the field at the site Mang de Bargen was measured with an 8-channel data logger (HESlab) with 6 to 8 fluxgate gradiometers (0.5 m horizontal probe spacing) measuring the vertical difference of the vertical component of the Earth's magnetic field. In 2018, at BH the magnetic measurements were conducted with a device by Sensys with 12 fluxgate gradiometers (0.25 m horizontal probe spacing). All measurement devices are equipped with an RTK-DGPS positioning system. The data was processed by subtracting a mean value over each profile and interpolation onto a 0.2 x 0.2 m grid.

Since the magnetic signal is also dependent on the depth of the magnetic source and the geological and archaeological features appearing in different depths, correction to a common level is necessary to eliminate depth dependence. The depths of the archaeological features are known from the archaeological documentation, the ones of the geological features from the radar data, which required prior depth correction. To ensure a comparison of features at different depths, the magnetic field was continued to a constant level above the source (0.3m above the archaeological feature) using the program REGCONT by Pašteka et al. (2012). In nearly all cases (with one exception) the magnetic field was continued downwards. In the figures the downward continuation of the magnetic field is abbreviated as DC, the one that is continued upwards as UC. REGCONT uses Tikhonov regularization as a low-pass filter.

For magnetic modelling, the susceptibility was measured in situ inside and outside of archaeological features. The soil samples were analysed in the laboratory. Magnetic susceptibility was measured on 10 ml material using a Bartington MS2B susceptibility meter (resolution 2*10-6 [SI], measuring range 1-9999*10-5 [SI], systematic error 10%). Measurements were carried out at both low (0.465 kHz) and high (4.65 kHz) frequency. Three sub-samples were measured in each case to allow an average and a standard deviation to be determined.

I.3.3.2 Modelling

For magnetic modelling Fatiando a Terra (Uieda et al. 2013) was used, which is an open source inversion and modelling software for geophysical methods. It is available as a python library. The process begins with determining the object, which means defining its geometry and depth as well as its susceptibility. Then the grid in which the vertical component of the magnetic induction will be calculated is defined (Uieda 2010-2016). For this modelling the declination was set to D = 3°, the inclination to I = 69° and the magnetic field strength to B = 49800 nT. As a result of spatial variations of the total magnetization of the soil, archaeological features can be mapped as magnetic anomalies. The total magnetization is the sum of induced and remanent magnetization.

$$M_T = M_R + M_I \tag{I.3.5}$$

with

$$M_I = \mathcal{X} * H \tag{I.3.6}$$

H is the earth magnetic field and $\mathcal{X}$ the isotropic volume susceptibility, which was measured in the field. Remanent and induced magnetization relate to one another according to the Koenigsberger ratio (Koenigsberger 1930; Koenigsberger 1934; Koenigsberger 1936).

$$Q = \frac{M_R}{M_I} \tag{I.3.7}$$

Several studies have shown that the Koenigsberger ratio Q strongly depends on how strongly the material has been heated (e.g. Schnepp et al. 2004, Hanson et al. 2015, Pickartz, Rabbel, et al. 2020). For strongly heated archaeological features such as ovens or pottery kilns, the values vary between 0.1 and larger than 100 (Schnepp et al. 2004). For partly or not heated soils, the values are lower with 0.1-10 (Pickartz, Rabbel, et al. 2020). There are also studies that have dealt with the Koenigsberger ratio Q in connection with sediments without human influence (Hanson et al. 2015). In the study of Hanson et al. (2015) the Koenigsberger ratio Q was investigated for lake sediments. They found the values for silt and sand vary between 0.2 and 4. Table I.3.5 provides a compilation of the values for the Koenigsberger ratio and the associated literature references. For the present thesis, the value for the Königsberger ratio Q was selected with the help of the literature in comparison to the modeling result of an intensively analysed archaeological feature, which is presented in part II of this thesis (see chapter II.4.4.1). A Koenigsberger ratio of $Q = 5$ is assumed for magnetic forward calculation.

Table I.3.5: Literature values of the Koenigsberger ratio

Material	Q	Reference
bread oven, burnt clay floor, fire places, pottery kilns, hearth, open fire place and others	0.1 – >100	Schnepp et al. 2004
partly or not heated soils and sediments with loess as parent material	0.1 – 10	Pickartz, Rabbel, et al. 2020
glacial Lake Missoula lacustrine and flood sediments	0.2 – 4	Hanson et al. 2015

The magnetic field gradient was modeled in 3D by assuming the upper sensor at a height of 1 m and the lower one at a height of 0.35 m. The grid spacing was 0.25 m or 0.5 m, depending on the measurement device used. Spheres were assumed for the urns and rectangles for pits (post hole or cooking pit), burials or the iron oxide concretion. The parameters for extension and depth were drawn from the archaeological documentation. The susceptibility values of the soils were taken from the in situ susceptibility measurements. Since no susceptibility measurements were taken from stones or pottery, the relevant information had to be obtained from the literature. For the pottery typical values for Bronze Age pottery of the 'nordic circle'

(Kneisel et al. in prep.) were ectracted from the literature. There is a study of Bronze Age pottery in Denmark (Rasmussen et al. 2012), which is considered to be adequate on the assumption, based on spatial proximity, that the material and techniques used to make ceramics in Denmark were similar to those used in Northern Germany in the Bronze Age. For stones, a wide range in several papers was found (see table I.3.6). For the stones used in burials, urns and cooking pits, the susceptibility values were varied during modelling, since the types of stone were not documented. Therefore, table I.3.6 shows susceptibility values for magmatic, metamorphic and sedimentary rocks. It can be seen that the range for magmatic rocks alone is very large at $\mathcal{X}$=0-27,000 * 1e-5 SI, making the modelling of these rocks challenging. The same applies for metamorphic or sedimentary rocks, although their susceptibility range is much smaller than that of magmatic rocks. Based on the documentation and the observed stones in the field, the presence of magmatic and/or metamorphic stones was assumed.

Table I.3.6: Magnetic susceptibility values [SI]

Kind of feature	values by literature [*1e-5 SI]	measured in situ [*1e-5 SI]
soil (BH)		50
soil (MdB)		90
granite	1,300 (Carmichael 2017; Thompson 2012) 0-5000 (Hunt et al. 1995)	
gabbro	2,500 (Carmichael 2017; Thompson 2012) 100-9000 (Hunt et al. 1995)	
syenite	1,500 (Carmichael 2017; Thompson 2012)	
diorite	150 (Carmichael 2017; Thompson 2012) 63-13000 (Hunt et al. 1995)	
igneous rocks	270-27,000 (Hunt et al. 1995)	
average acidic igneous rocks	3.8 - 8,200 (Hunt et al. 1995)	
average basic igneous rocks	55-12,000 (Hunt et al. 1995)	
average metamorphic rocks	0-7,300 (Hunt et al. 1995)	
average sedimentary rocks	0-5,000 (Hunt et al. 1995)	
pottery	1,000 (Rasmussen et al. 2012)	
iron oxide	12.5 (Carmichael 2017; Thompson 2012)	
lepidocrocite	170-290 (Hunt et al. 1995)	
goethite	110-1,200 (Hunt et al. 1995)	
haematite	50-4,000 (Hunt et al. 1995)	
ilmenite	220-380,000 (Hunt et al. 1995)	
maghemite	200,000 - 250,000 (Hunt et al. 1995)	
magnetite	100,000-570,000 (Hunt et al. 1995)	
soil of the post hole (MdB)		84

I.3.4 Archaeological Documentation

Most of the burial mounds were excavated and documented in excavation reports (Lütjens 2013c, Lütjens 2013d, Lütjens 2013e). Schaefer-di Maida excavated LA 57 in 2017 (Schaefer 2017) and Kneisel excavated

LA 117 in 2019 (in prep.). These last two excavations were conducted in cooperation with the Schleswig-Holstein conservation authorities and as part of the CRC 1266 "Scales of Transformation". In all cases, the topsoil was removed by an excavator and the barrows divided into four quadrants. These quadrants were excavated using the planum method and documented by photography, photogrammetry and drawings (scale 1:50). Features were excavated in profiles and documented by photographs and drawings (scale 1:10 or 1:20). Owing to time constraints, LA 58 and 60 were excavated mainly with an excavator.

The results of the magnetic and GPR data will be compared with archaeological documentation and form the basis for the statistics showing the detection rate. For modelling the GPR and magnetic data, the archaeological drawings or the geometry of the documented archaeological features were used. The drawings of BH and the MdB CP-complex were digitized (see Fig. I.4.19b & c, I.4.25b & c, I.4.17b & c, I.4.23b & c and I.4.24b & c) and for MdB features the photographs were used to create the model (see Fig. I.4.10a, I.4.11a , I.4.18a).

Furthermore, the archaeological documentation was used to create a statistical breakdown of the recognition of archaeological features in GPR and magnetics. This allowed us to feed the excavation plans as well as the magnetic and GPR data into QGIS for comparison. Typical Bronze Age archaeological features were then chosen: urns, cooking pits, stone concentrations, burials, settlement pits and postholes. Pits lacking any archaeological significance – for instance, tree pits or pits left by the removal of stones – were selected, since they are also found in archaeological settings. Since the geological background is defined by gravel and bolder stones, geological features were also chosen, in order to have a direct comparison with the archaeological features, thereby allowing archaeological features to be distinguished from geological ones in geophysical data. Each archaeological feature was checked in the magnetic and GPR data if they are detected or not. Additionally, their average size and depth as well as the occurrences of each feature was recorded according to the archaeological documentation (see tables I.3.7 and A.1 – A.4).

Table I.3.7: Total number of features

feature	total number
urns	23
cooking pit	8
stone concentration	12
burial	7
geology	8
settlement pit	45
posthole	83
tree pit	11
pit left by moved stones	100

I.4 Results

I.4.1 Setting the Frame

I.4.1.1 What to Expect from the Soil Analyses

I.4.1.1.1 Soil Composition, Permittivity and Susceptibility

To explain the difference in the appearance in the GPR data per archaeological site, several soil samples were taken and analysed them by soil composition. Considering the composition of clay, sand and silt, the soils of both sites are sandy loam, with that of MdB more sandy and that of BH more loamy. Additionally, the percentage of gravel is larger in MdB than in BH (see fig. I.4.1b-I.4.3b). Based on the percentage of sand, silt and clay, Birchak's equation (1974) was used to calculate the relative permittivity (see equation I.3.1). For BH a mean permittivity of 7.6±3.3 was expected and for MdB a mean permittivity of 6.9±3.0 (see fig. I.4.1c-I.4.3c) based on the soil composition without considering water content and porosity. These values are the result of drying the soil probes before analysing them. Therefore the expecting velocities range between 10.9 cm/ns for BH and 11.4 cm/ns for MdB. In comparison to the hyperbola test of MdB it can be concluded, that a velocity of about 11 cm/ns is too high. Due to missing hyperbolas in the data set of BH and missing common midpoint (CMP) measurements, there is no reference to compare with.[1] The final migration with 8 cm/ns (for the BH data set) was the result of testing different velocities and compare the migrated data sets based on the different migration velocities.

The susceptibility measurements provide information about the ability of the soil to be magnetized. The samples of MdB were taken in a vertical profile of the excavation trench outside an archaeological feature but within a sequence of Pre-Roman, Early Medieval and modern cultural layers. to estimate the susceptibility values of the stones, also the average susceptibility values were taken for modelling the features from the susceptibility measurements of the soil samples. To obtain an independent susceptibility value for the BH soils the average of the topsoil were taken and the last four samples of the east profile of the BH ditch, since it is to be assumed that the ditch was naturally refilled with the same material after the first opening phase. For BH an averaged susceptibility of 50 * 1e-5 [SI] is assumed for MdB 90 * 1e-5 [SI] (see fig. I.4.1d-I.4.3d).

1 Unfortunately, there are no in-situ velocity measurements to match the derived relative permittivities of the dried soil samples with the CMP measurements. For the site MdB the data set of 2005 was used. From this year no CMP measurements are available. Since the site BH was measured in 2018 with 3D GPR, no CMP measurements were conducted.

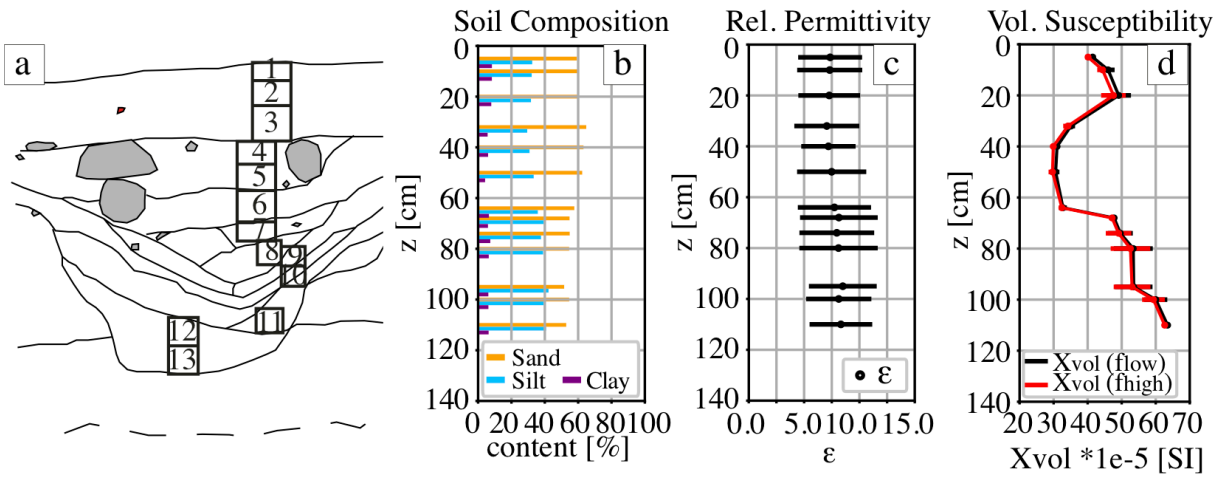

Fig. I.4.1: Soil analysis of a profile crossing the ditch in the north (a). (b) shows the soil composition, (c) the permittivity derived using Birchak's equation (1974), (d) shows the susceptibility measured at low (red solid line) and high (black solid line) and (e) the volume susceptibility.

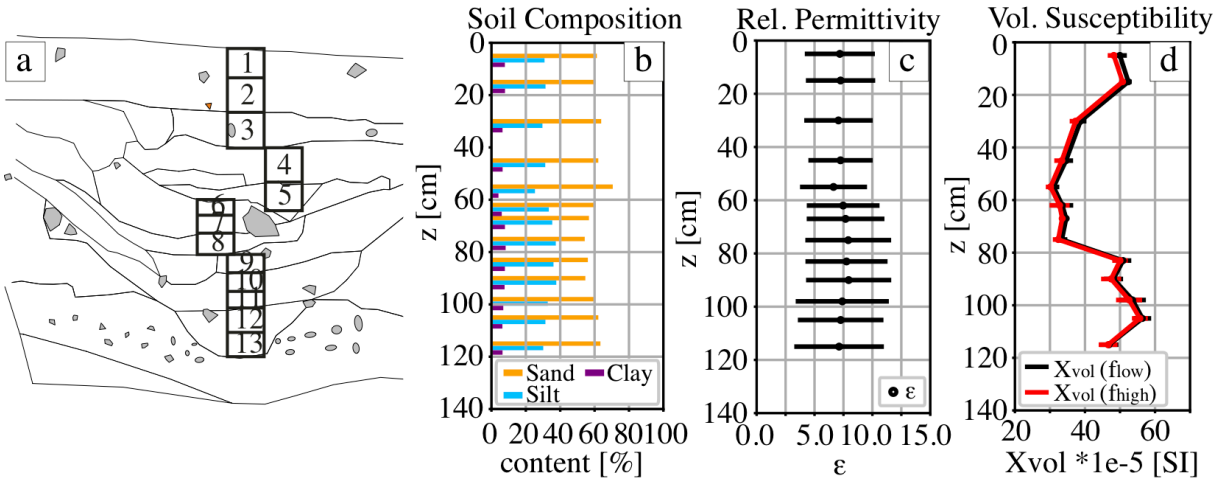

Fig. I.4.2: Soil analysis of a profile crossing the ditch in the east (a). (b) shows the soil composition, (c) the permittivity derived using Birchak's equation (1974), (d) shows the susceptibility measured at low (red solid line) and high (black solid line) and (e) the volume susceptibility.

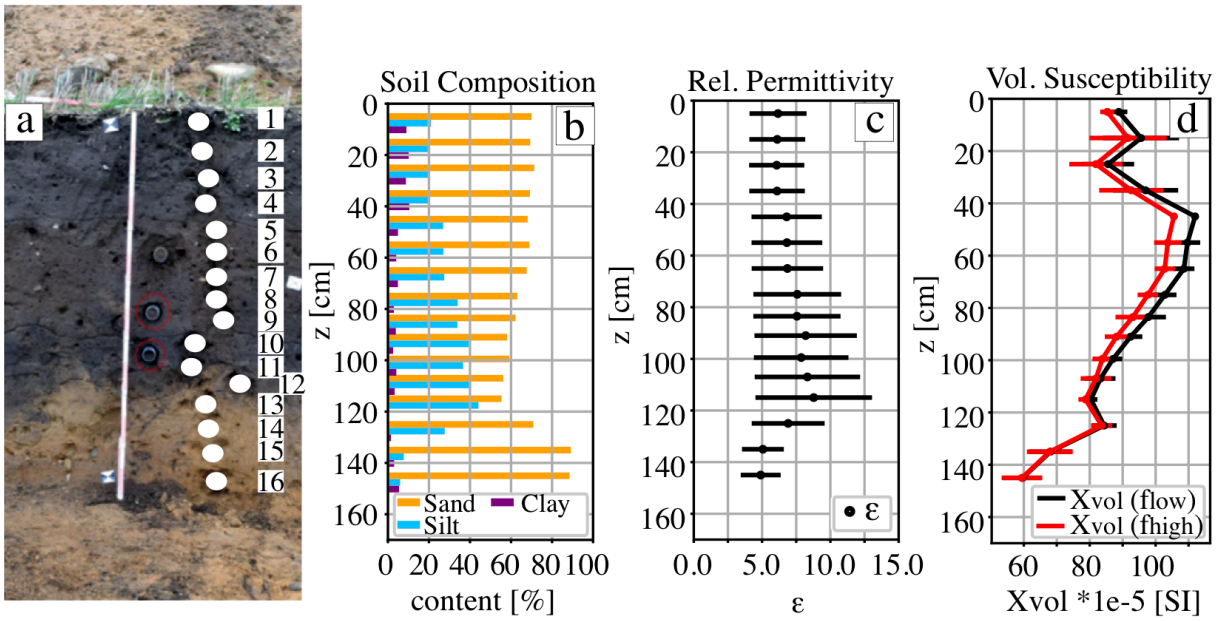

Fig. I.4.3: Soil analysis of a profile of the excavation in MdB (a). (b) shows the soil composition, (c) the permittivity derived using Birchak's equation (1974), (d) shows the susceptibility measured at low (red solid line) and high (black solid line) and (e) the volume susceptibility.

I.4.1.1.2 Moisture and Human Impact on the Soil

From Birchak's equation, it is known that permittivity is influenced by soil composition, porosity and volumetric water content. Since it was not possible to directly extract the water content from the soil analysis, the content of organic matter was taken as a qualitative estimation, which in turn was obtained from the loss on ignition at a temperature of 550°C. In fig. I.4.4b and fig. I.4.5b it can be seen that the topsoil of both sites has a similar amount of organic matter, which means a more or less similar moisture. Considering the depths of the documented archaeological features it is known that the layers of archaeological interest lie at depths of between 0.3 m and 0.7 m in MdB and 0.3 m and 1.3 m in BH. By comparing the content of organic matter in this region it can be concluded that the content of organic matter is about 33% higher in MdB than in BH, which means the soils in the region of archaeological interest are more moist in MdB than in BH. Since a higher water content increases permittivity, it may be concluded higher permittivity values of the MdB soils than the BH soils in the region of archaeological interest (fig. I.4.4b and fig. I.4.5b).

Additionally, besides the volume susceptibility of the soil, its frequency dependent susceptibility (Xdf) is analysed (fig. I.4.4c,I.4.5c) providing information about soil magnetization as a proxy of human cultivated activity. The frequency-dependent susceptibility is at about 2% larger in MdB than in BH. Since the frequency-dependent susceptibility is larger in MdB, it may be assumed that the amount of small magnetic particles is larger in MdB, meaning a larger human impact (O. A. Clark & A. Clark 1996).

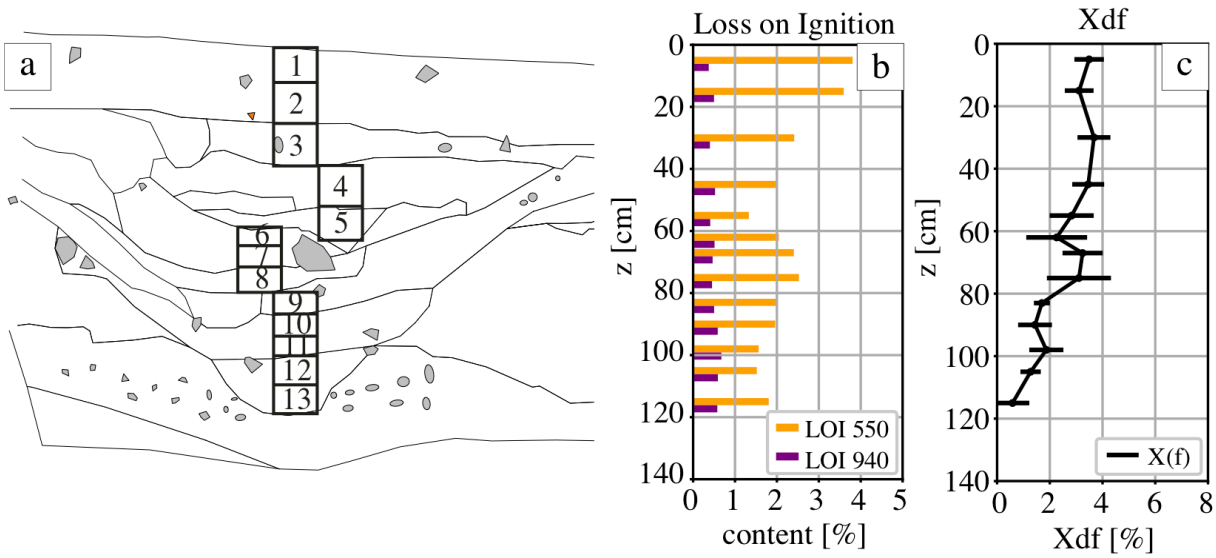

Fig. I.4.4: Comparison of geoarchaeological data of the east profile of BH. Digitized archaeological drawing (a) with the positions where the soil samples were taken. (b) shows the loss on ignition (indicating the proportion of organic matter) and (c) the frequency dependent susceptibility (indicating human activity).

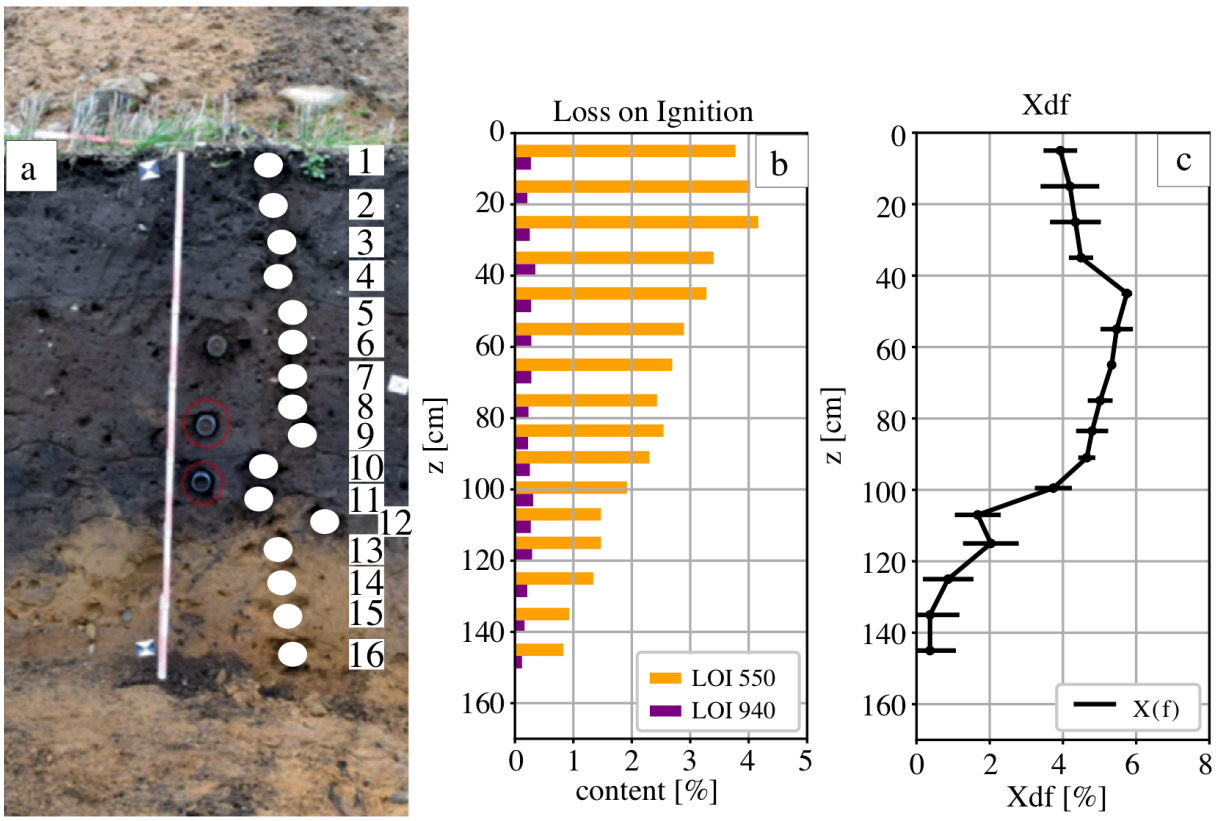

Fig. I.4.5: Comparison of geoarchaeological data of MdB. Digitized archaeological drawing (a) with the position of the taken soil samples. (b) shows the loss on ignition (indicating the proportion of organic matter) and (c) the frequency dependent susceptibility (indicating human activity).

I.4.1.2 Classification of Archaeological and Geological Features

The number of features commonly found in archaeological excavations – and in Bronze Age sites in particular – is analysed considering their real size, depth and appearance in GPR and magnetics, taking the sites MdB and BH as our case study. These features are pits, post holes, urns, burials embedded in stone packages or in pits, stone concentrations, urns embedded in stone packages, cooking pits consisting of stones, pits left by the removal of stones (e.g. in the course of agricultural activities), tree pits, a ditch (in one case) and iron oxide layers, sometimes concretized to a massive concretion. 57 stony features could be observed in excavation. 7% of these are burials embedded in stone packages, 12% are geological features, 16% cooking pits, 25% stone concentrations and 40% are urns. Besides the stony features, 240 pits are documented. Almost 5% of them are tree pits, 19% settlement pits, 35% post holes and 42% pits left by the removal of stones.

The appendix contains two tables showing the most common features (urns, cooking pit, stone concentration, burial, settlement, post hole, tree pit, geology and pit left by moved stones) found in archaeological excavations and their recognition in GPR or magnetics respectively (tables A.1 and A.2). Table A.3 and A.4 summarise these findings and are displayed in I.4.6 and I.4.7.

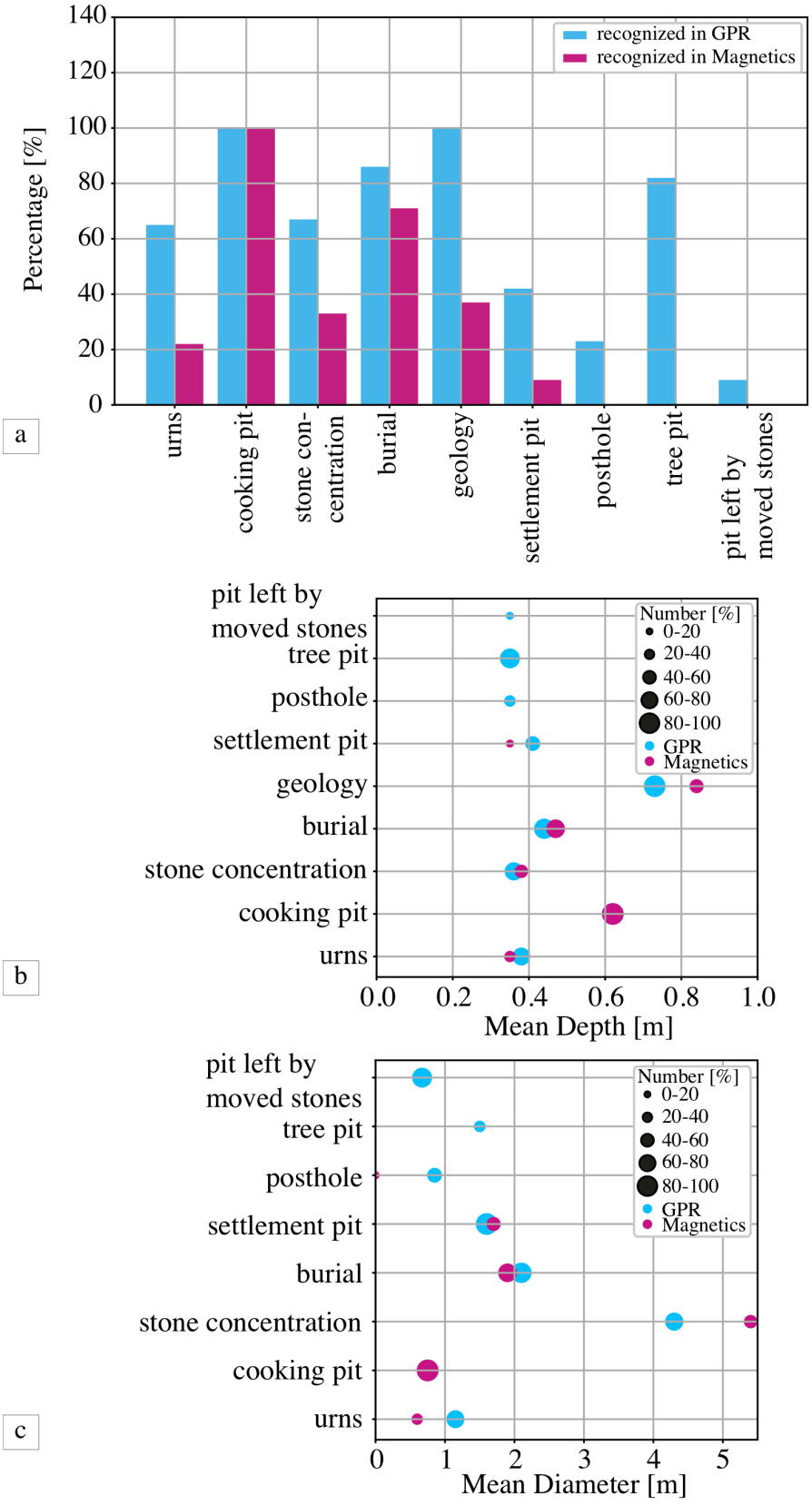

Fig. I.4.6: Visualisation of the statistics relating to the recognition of archaeological features (of both sites, MdB and BH) in GPR and Magnetics. (a) shows the recognition rate in comparison between GPR and magnetics. (b) shows the kind of feature in dependance on depth, whereas (c) shows it in dependence on the area without geology, since this would distort the figure because of the large size (288.24 m^2) of the features. The size of the symbols represents the number of detected features.

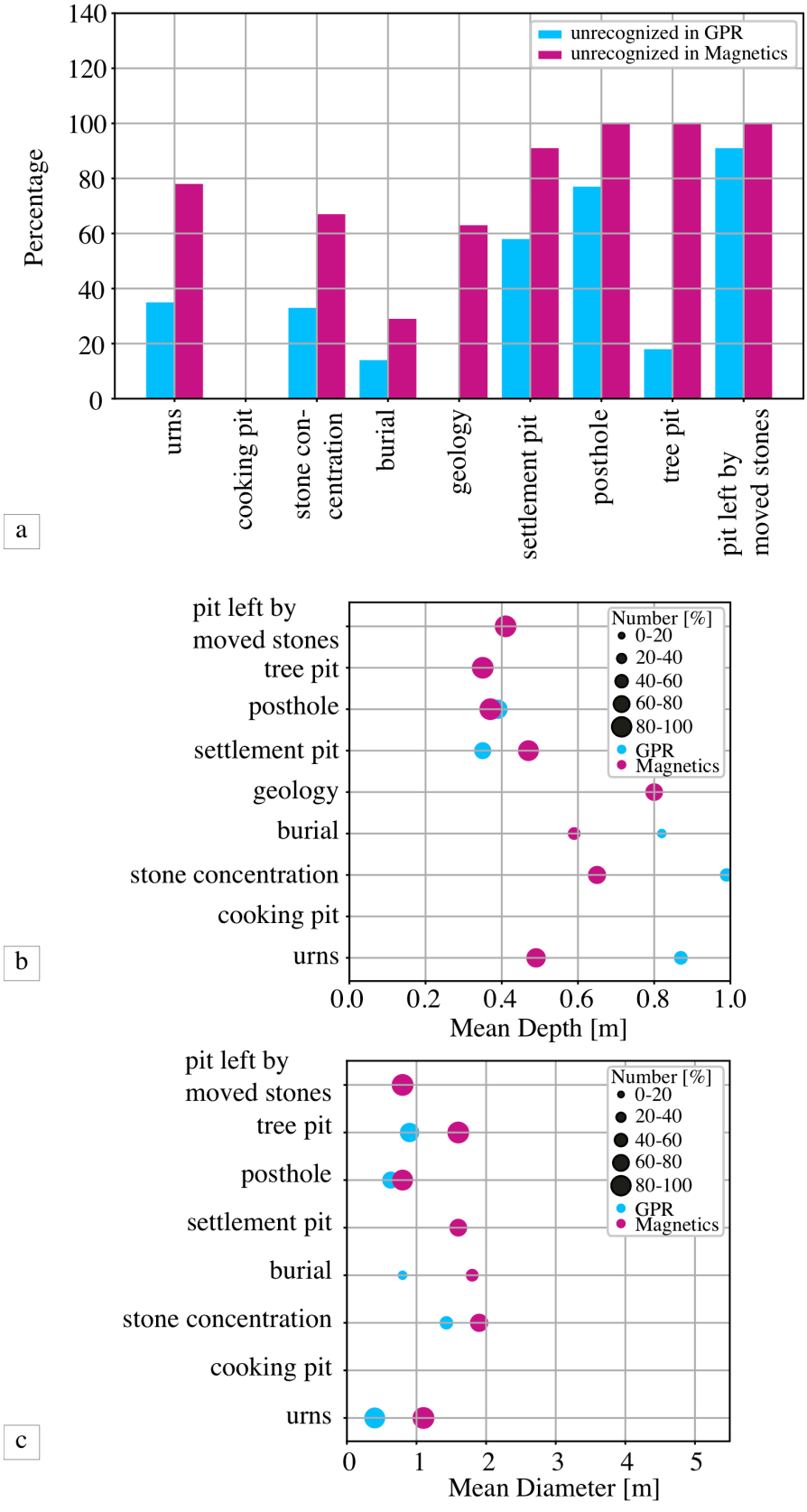

Fig. I.4.7: Visualisation of the statistics relating to the non-recognition of archaeological features (of both sites, MdB and BH) in GPR and Magnetics. (a) shows the percentage of features that could not be recognised in comparison between GPR and magnetics. (b) shows the kind of feature in dependance on depth, whereas (c) shows it in dependance on the area without geology, since this would distort the figure because of the large size (352.24 m^2) of the feature. The size of the symbols represents the number of non-detected features.

As expected a correlation between size and recognition in GPR and magnetics is obvious. Generally speaking, the larger the size of the archaeological feature, the more likely it is to be recognised in GPR and magnetics (see figure I.4.6c). The smallest feature to be recognised in GPR has a mean diameter larger than 0.3 m (area[2] of about 0.1 m^2 – pit left by moved stones). In magnetics the smallest feature to be recognised has a mean diameter larger than 0.5 m (area of about 0.25 m^2 – urn). The averaged diameter of the recognised features in magnetics is about 2 m and in GPR 1.3 m (area of about 1.5 m^2) – not inclusing geological features (see also tables A.1 and A.2). It emerges that most of the features, that could be recognised are located in an averaged depth of about 0.4 m (fig. I.4.6b). In larger depths it becomes increasingly unlikely that features will be detected (fig. I.4.7b).

GPR

Stony features that could be detected by GPR are at averaged depths between 0.3 and 0.75 m. Cooking pits are always detected by GPR. Almost 65% of the urns could be recognised by GPR and 86% of the burials. Also 67% of the stone concentrations could be identified.

The urns found at the MdB site are between 0.5 and 0.6 m in diameter (area of about 0.4 m^2). The BH urns are somewhat smaller (between 0.3 and 0.5 m in diameter and having an are of about 0.14 m^2). Just two of the seven BH urns could be recognised in GPR with knowledge of their position. Comparing the cooking pits at both sites, it can be found that the cooking pits of MdB are larger than those of BH. The ones at MdB have a diameter of 0.87 m (area of about 0.8 m^2) and are situated at an average depth of 0.35 m. The average depth of the MdB cooking pits is 0.4 m. Additionally, the number of stones is higher in MdB cooking pits than those in BH.

Regarding pits, the reverse applies. Most of the pits were not recognised by GPR, particularly post holes and pits left by moved stones, with the exception of tree pits of about 1.5 m in diameter (area > 3 m^2). 82% of them were recognised. Pits that are recognised by GPR appear at an averaged depth of 0.35 and 0.4 m, with an averaged diameter of 1.5 m (area of about 4 m^2). The ones unrecognised in GPR are smaller with 0.4 m as mean diameter (area of about 0.6 m^2) and are located at the same averaged depth. 42% of the settlement pits were recognised. In some of them a larger content of organic matter could be observed during the excavations, recognizable by the dark brown colour.

Magnetics

When dealing with magnetics, caution must be applied before analysing the results. This is because whether a feature can be detected or not depends on the presence of magnetizable or magnetized elements within the features. Therefore, the kind of feature is more important. If one considers the kind of feature, it becomes clear that pits in particular (also in an averaged depth of 0.4 m) are not detected very well by magnetics. None of the post holes, tree pits or pits left by moved stones could be detected by magnetics and almost all of the settlement pits (about 91%) went unrecognised.

2 The area is related to the area in the archaeological documentation.

With stony features, the matter is somewhat different. 71% of the burials and all cooking pits are recognised, whereas urns, stone concentrations and also geological features are not (< 40%). This can be explained by the lack of magnetizable or magnetized elements in stone concentrations or geological features. One reason for not recognizing urns can be their size in combination with their depth. The averaged diameter of detected and undetected urns is about 0.6 m (averaged area of 0.34 m^2), whereas the urns recognised in magnetics are at a depth of 0.35 m and the ones unrecognised in magnetics at a depth of 0.5 m. Another reason why urns go undetected may be the superposition of heterogeneous glacial soil. Stone concentrations that are detected have an averaged diameter of 3.8 m (area of about 40 m^2) and are located at a depth of about 0.4 m. The undetected ones are located at an averaged depth of 0.65 m and have a mean diameter of about 1.7 m (area of about 3 m^2).

I.4.1.3 GPR Modelling Study on the Basis of the Soil Analyses

To describe the archaeological transformation in Bronze Age Schleswig-Holstein, the most relevant features burials, inurned cremations and cooking pits. Furthermore, 12% of the features are geological features and were misinterpreted. Therefore, it was decided to limit GPR modelling to stony archaeological features. No pits, were chosen since, due to their weak amplitudes, they could not be recognised without knowledge of their position. Additionally, one iron oxide concretion was chosen to represent the geological features, because at the site MdB it turned out that they appear at depths of archaeological relevance between 0.3 m and 0.7 m. In BH there are also iron oxide layers, but these are not concretized. Most of the stony geological features appear at depths between 0.7 m and 1.8 m.

For permittivity values the derived ones shown in figs. I.4.1c – I.4.3c were used, whereas the value for the topsoil is the averaged one of the first 0.3 m and for the subsoil the averaged one for greater depths. For MdB it is ϵ_r=6.1 for the topsoil and ϵ_r=7.2 for the subsoil. For BH it is ϵ_r=7.2 for the topsoil and ϵ_r=7.7 for the subsoil. Since there were no permittivity values for the stones, they were drew from the literature (ϵ_r=5 for MdB and ϵ_r=10 for BH).

By applying the permittivity values for numerical modelling, the signals were found to be too weak in most cases, in comparison to the measured GPR profiles (see fig. I.4.8). This result support, that the found permittivity values based on the soil analyses on dried soil samples are too small. This is not surprising since the soil property is not only influenced by the soil matrix but also by water content and porosity.

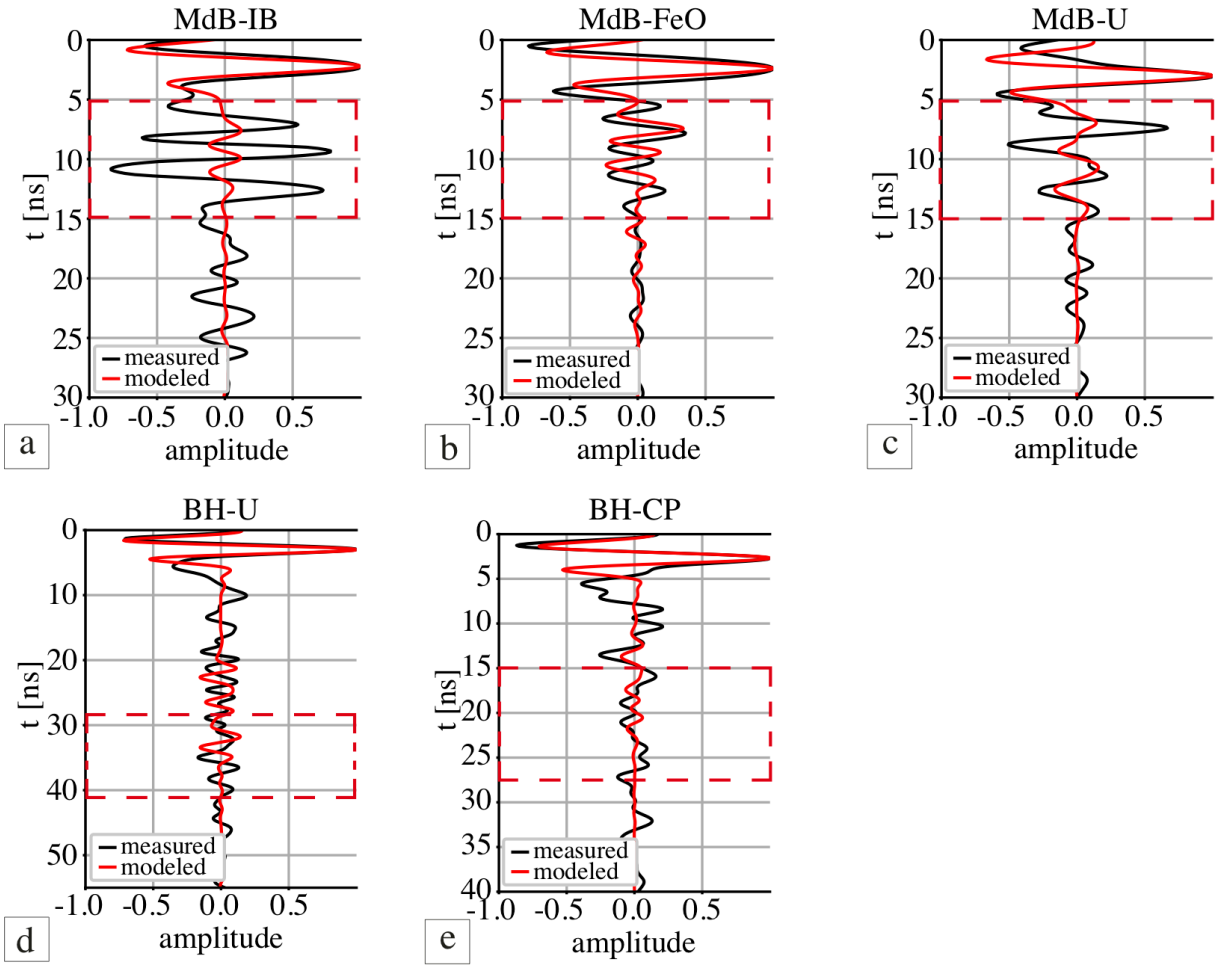

Fig. I.4.8: Trace comparison of the modelling study of selected archaeological key targets. (a) shows the resulting mid trace of the burial (MdB-IB – model can be found in I.4.11), (b) the mid trace of the iron oxide concretion (MdB-FeO – model can be found in I.4.10), (c) the mid trace of the inurned cremation (MdB-U – model can be found in I.4.18), (d) the mid trace of the inurned cremation of BH (BH-U – model can be found in I.4.17) and (e) the mid trace of the cooking pit of BH (BH-CP – model can be found in I.4.23). The features BH-CP and BH-U could be recognised in GPR by comparing with the archaeological maps. MdB-IB, MdB-FeO and MdB-U could be detected by GPR very well, whereas MdB-FeO was interpreted as house structure. In the magnetics the features BH-CP and MdB-IB could be detected.

I.4.2 Comparison of Selected Key Features in Geophysical Data

In the following, the question shall be answered whether the signal strength can provide more information. Furthermore, the influence of soil conditions is analysed. Both, information about the signal strength and the soil conditions aim to improve the recognition rate. To this end, the data of selected key features are going to be analysed in pairs: (a) MdB-FeO and MdB-IB, (b) BH-U and MdB-U and (c) BH-CP and MdB-CP. These three pairs are characterized by features that generate the same anomalies (pair (a)) but also by features of the same kind but in different soils (pairs (b) and (c)). Urns and cooking pits are two typical key targets of Bronze Age archaeology in northern Germany. Here, they are situated in a glacial environment

characterized by grain sizes ranging from clay to boulder stones. Stone concentrations, stone packages (urn graves), stone pits (cooking pits) as well as naturally distributed stone accumulations may be heterogeneously distributed. Therefore, stony archaeological features provide a potential source to be analysed with regard to their identification by combining magnetic and GPR measurements.

I.4.2.1 Iron Oxide Concretion (MdB-FeO) and Burial (MdB-IB)

As already mentioned, iron oxide concretions can occur at depths between 0.3 m and 0.7 m. They are very massive and thick, causing strong reflections in the GPR. While boulder stones may also be expected in clusters in the subsoil, they occur at depths beyond those of archaeological relevance. Therefore an iron oxide concretion and an inhumation embedded in a stone package are chosen as key targets.

I.4.2.1.1 Appearance in Geophysical Data

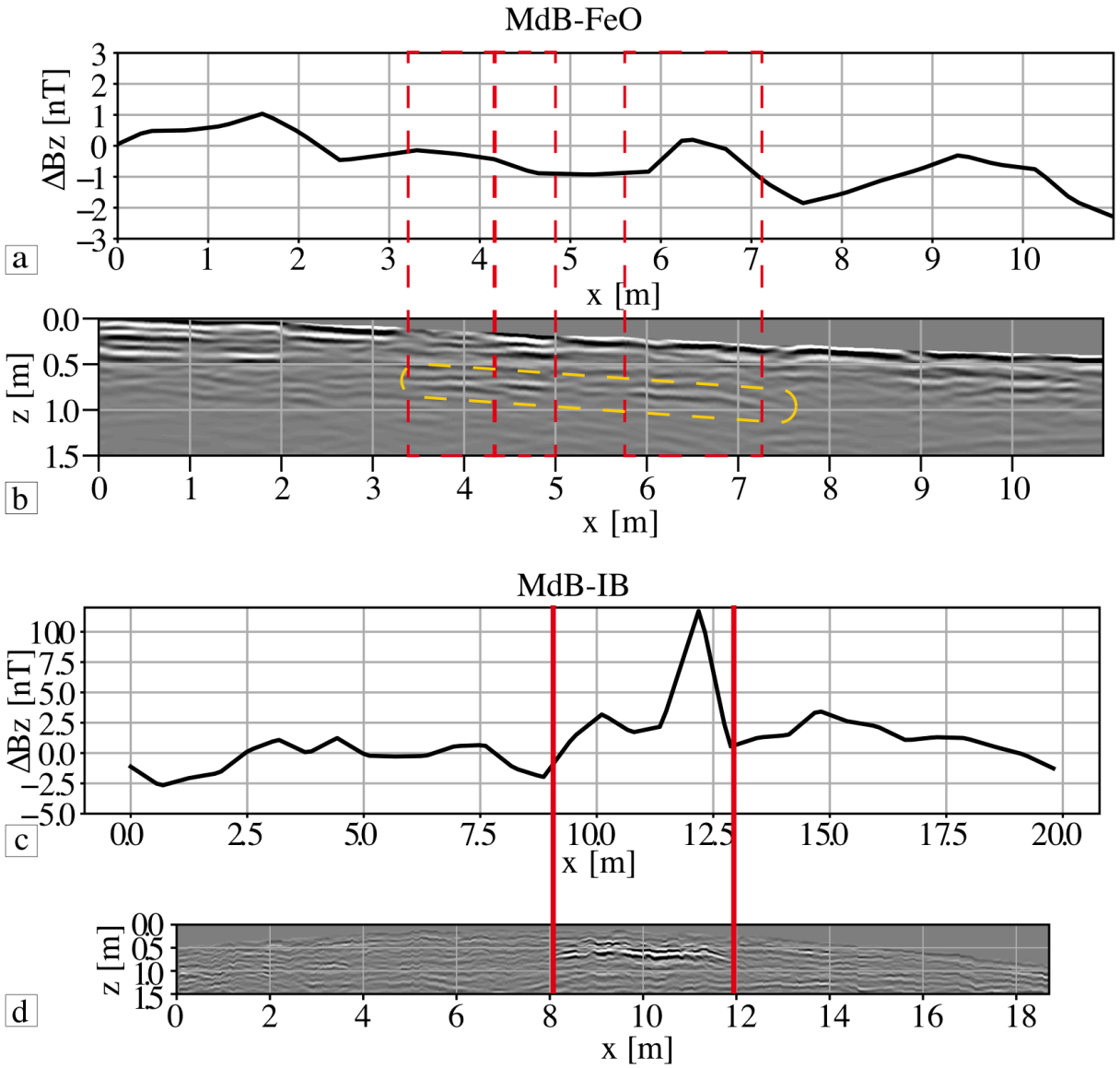

Fig. I.4.9: Comparison of magnetic (a,c) and GPR data (b,d) of MdB-FeO and MdB-IB. Magnetic data shown as profile (a,c) crossing the feature at the position of the GPR profile; (b,d) shows the GPR data as profile (black: positive, white: negative amplitude). Relevant features in the profile are marked as red vertical lines (dashed: (a & b); solid: (c & d)). The orange dashed rectangle marks the position of the geological feature. The position of the profile can be found in figures A.1 (MdB-FeO) and A.4 (MdB-IB).

The comparison of the GPR profiles of the iron oxide concretion (fig. I.4.9b) and the inhumation (fig. I.4.9d) show how similar the reflections of both features, with their sequence of strong-low-strong reflection energy, appear at first sight in the GPR profile. Due to the rectangular shape of the geological feature (MdB-FeO) (fig. A.1a), it was initially interpreted as a house structure. The excavation showed a heterogeneous, very hard structure, which turned out to be an iron oxide concretion (see photograph in fig. I.4.10a, GPR time slice

fig. A.1a). The GPR profile (fig. I.4.9b) shows the iron oxide layer as a more or less flat reflection.

By way of comparison, the magnetic data are also considered (fig. A.1b, I.4.9a). It is apparent that the iron oxide concretion is not magnetized. The amplitudes of the magnetic anomaly of the iron oxide layer range from -1 to 0.5 nT (fig. I.4.9a).

The inhumation (MdB-IB) shown for comparison is embedded in a stone package. The corresponding GPR reflection appears scattered at the edges of the stone package in the GPR profile (fig. I.4.9d) and flat in its middle part. For comparison the magnetic data are considered (fig. A.4b, I.4.9c). It is apparent that the stone package of the inhumation is highly magnetized. The amplitudes of the magnetic anomaly of the archaeological feature range from -2 to 12 nT (fig. I.4.9c). Also the other burials show magnetic amplitudes in the same range.

I.4.2.1.2 Modelling the Features

GPR

To determine the relevant subsurface physical parameters, synthetic radargrams are computed for both features and the modeled and measured signals are compared. The subsurface model of MdB-IB was created using the archaeological documentation. Due to its archaeological irrelevance, the iron oxide concretion was not excavated, but its depth was known. The final model with permittivity (fig. I.4.10b) and conductivity (fig. I.4.10c) is shown in fig. I.4.10 for MdB-FeO. The final model of MdB-IB can be found in fig. I.4.11.

The parameters of the subsurface model of MdB-FeO were first estimated using literature values and then varied in a predefined range (as already described in the methods) to obtain a good fit between measured and modeled data (the parameters as well as the geometry of the model can be found in fig. I.4.10b,c and table I.4.1). As already mentioned, some iron oxide minerals – magnetite, hematite, goethite, lepidocrocite, maghemite and ferrihydrite – are very common, with goethite and haematite the most common (Blume et al. 2016). Haematite and goethite are the most probable representatives of the iron oxide minerals in moderate temperatures. Therefore, conductivity and permittivity values were tested for goethite and haematite (table I.4.1). Final parameters can be found in table I.4.1.

Table I.4.1: Dielectric Permittivity and electrical conductivity values used for modelling of MdB-IB and MdB-FeO

Material	Feature	Parameter	Value
Top soil	MdB-FeO	ϵ_r	2.97
Top soil	MdB-FeO	σ [mS/m]	1.83
Top soil	MdB-IB	ϵ_r	6.17
Top soil	MdB-IB	σ [mS/m]	1.83
Sub soil	MdB-FeO	ϵ_r	14.1
Sub soil	MdB-FeO	σ [mS/m]	0.9
Sub soil	MdB-IB	ϵ_r	19.5
Sub soil	MdB-IB	σ [mS/m]	0.9
iron(III) oxide	MdB-FeO	ϵ_r	1.9
iron(III) oxide	MdB-FeO	σ [mS/m]	6.25e-6 (goethite); 5e-5 (haematite)
stone	MdB-IB	ϵ_r	5
stone	MdB-IB	σ [mS/m]	1
	MdB-FeO	number of layers	2
	MdB-IB	number of layers	2
	MdB-FeO	total thickness of layers [m]	0.2
	MdB-IB	total thickness of layers [m]	0.2
	MdB-FeO	depth of feature [m]	0.36
	MdB-IB	depth of feature [m]	0.36

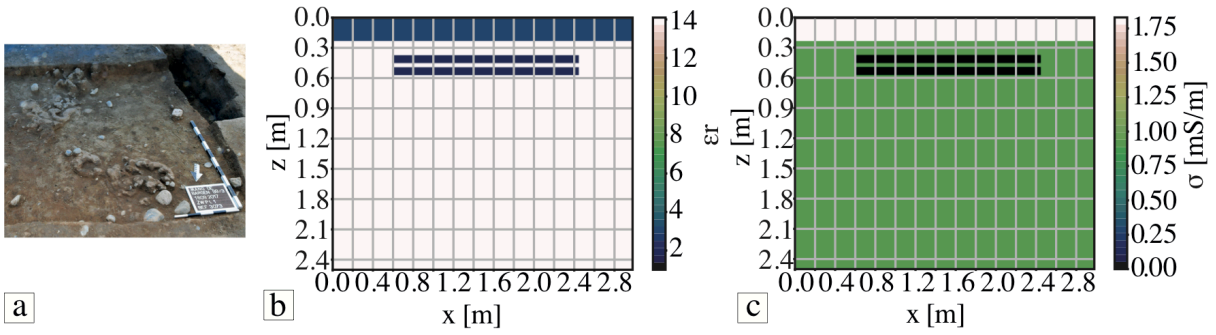

Fig. I.4.10: Photograph (Schaefer-di Maida) showing iron oxide concretion (a) and the model of MdB-FeO (b,c). (b) shows permittivity and (c) conductivity subsurface models.

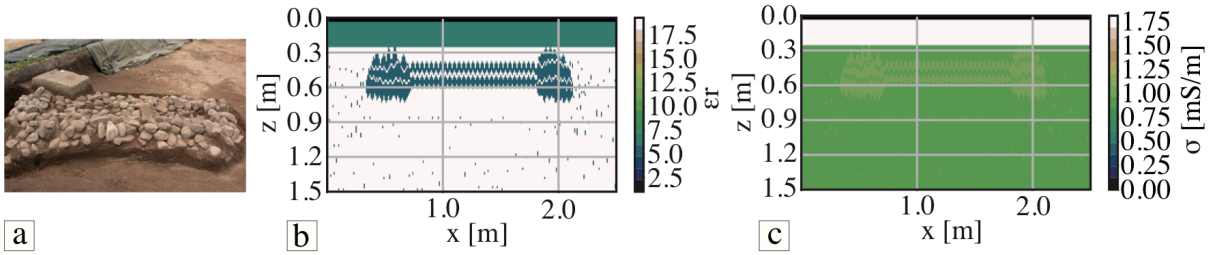

Fig. I.4.11: Photograph (Lütjens) showing the inhumation (a) and model of the inhumation burial of LA 60 (MdB-IB) (b,c). (b) shows permittivity and (c) conductivity subsurface models.

A good match for the feature MdB-FeO in the GPR modelling for both minerals was found (fig. I.4.12c, I.4.13c). The comparison of modeled and measured trace shows that the large amplitude of the radargram can be explained by a comparably simple stratigraphic model. The target depth of 0.36 m established by modelling agrees well with the excavation documentation. Unfortunately, information about the thickness of the stone package was not available. The modelling, however, showed a thickness of about 0.2 m. The reflection amplitudes of the iron oxide layer – normalized by the direct wave – range from -0.3 to 0.3.

The source of reflection for the inhumation (MdB-IB) is an accumulation of stones (see fig. I.4.11a). The types of stone were not documented, but it may be assumed that the stones were magmatic and/or metamorphic. The modelling shows the feature to lie at a depth of 0.36 m and to be about 0.2 m thick (fig. 7.14d). The amplitudes, normalized by the direct wave, ranging from -0.6 to 0.6 for the modeled trace and -0.8 to 0.8 for that measured at the depth of the stone package. The stronger amplitude of the measured data can be explained by interference with other materials in the surrounding area, while the shape of the stones also influences the shape of the signal. Additionally, the distribution of permittivity values in the model is an influencing factor and does not provide a unique result.

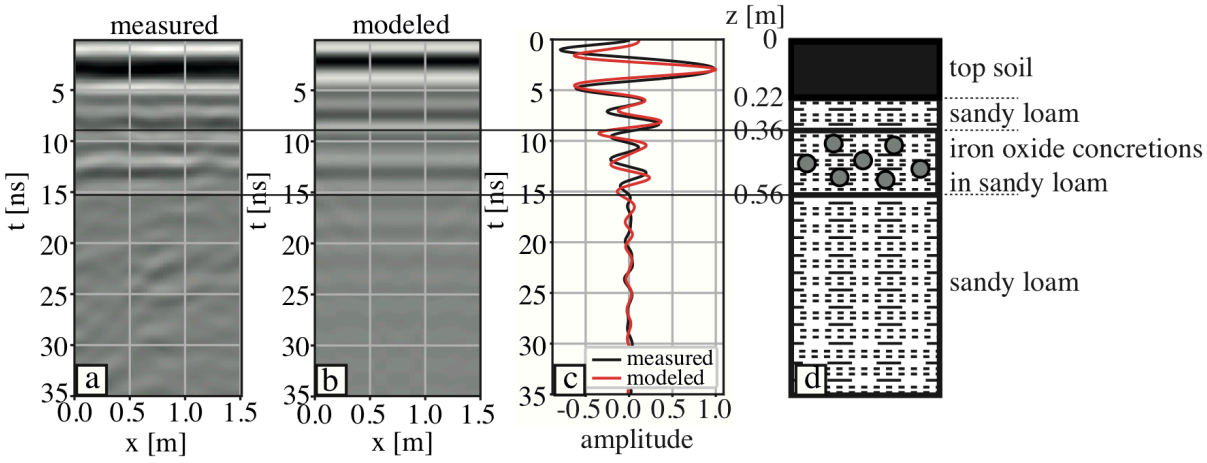

Fig. I.4.12: Comparison of measured and modeled data of MdB-FeO (by using the conductivity for the iron-bearing mineral goethite). a) and b): Measured and modeled GPR profile showing a section of the archaeological feature. c): trace comparison of measured and modeled data (traces are the summed traces of the shown GPR profile section on the left). All amplitudes are normalized to the largest amplitude of the direct wave. d): schematic stratigraphic column.

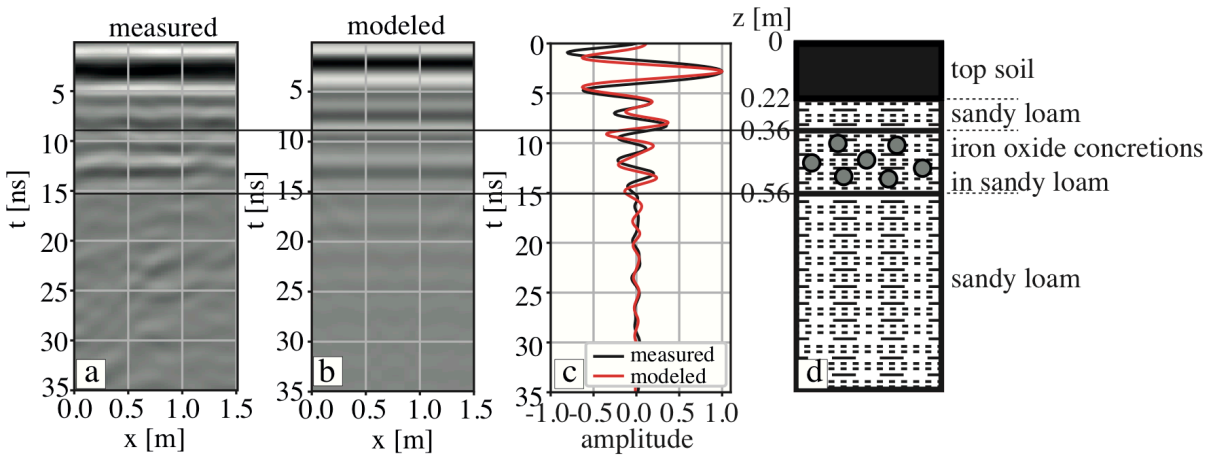

Fig. I.4.13: Comparison of measured and modeled data of MdB-FeO (by using the conductivity for the iron-bearing mineral haematite). a) and b): Measured and modeled GPR profile showing a section of the archaeological feature. c): trace comparison of measured and modeled data (traces are the summed traces of the shown GPR profile section on the left). All amplitudes are normalized to the largest amplitude of the direct wave. d): schematic stratigraphic column

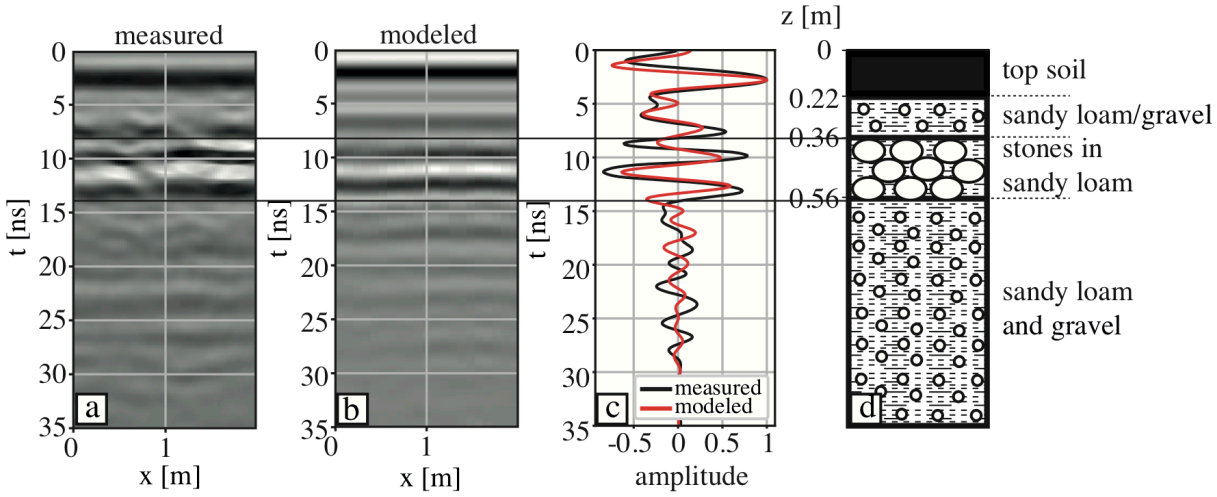

Fig. I.4.14: Comparison of measured and modeled data of MdB-IB. a) and b): Measured and modeled GPR profile showing a section of the archaeological feature. c): trace comparison of measured and modeled data (traces are the summed traces of the shown GPR profile section to the left). All amplitudes are normalized to the largest amplitude of the direct wave. d): schematic stratigraphic column.

Table I.4.2: Derived reflection coefficients

Feature	Transition	Reflection coefficient
MdB-FeO	iron to soil	0.46
MdB-IB	stone to soil	0.33

Table I.4.3: Estimated porosity and water content on the basis of the found permittivity values (see table A.5

Feature	Permittivity	Porosity [ϕ in %]	Water Content [θ in %]	Reflection coefficient
MdB-FeO	14	46	28	0.46 [iron to soil]
MdB-IB	19.5	38-44	32-34	0.33 [stone to soil]
mean MdB-FeO		**46**	**28**	
mean MdB-IB		**41**	**33**	

From Table I.4.1 it is known there is a permittivity contrast of about $\Delta\epsilon_r$=12 between subsoil and iron oxide concretion and $\Delta\epsilon_r$=14 between the stones and soils of MdB-IB. One can expect a mean porosity of 41% for MdB-IB and 46% for MdB-FeO and a mean water content of 33% for MdB-IB and 28% for MdB-FeO. By analysing the reflection coefficient on the basis of permittivity, a larger reflection coefficient was found for MdB-FeO than for MdB-IB (see tables I.4.3 and I.4.2).

Magnetics

The magnetic modelling of the iron oxide concretion (MdB-FeO) showed a wide range of possible susceptibility values. By varying the susceptibility values between 12.5*1e-5 [SI] and 500*1e-5 [SI], the average anomaly is found to lie between 0 and 0.5 nT. Due to the heterogeneity of the real feature and the homogeneous model, the anomalies look quite different. The modelling showed that all susceptibility values seem to be realistic. Fig. I.4.15 shows the best fit with a susceptibility value of 400*1e-5 [SI] representing goethite, haematite and ilmenite.

While the modelling would not allow for a direct identification of the mineral, but according to the occurrence the range of possibilities can be reduced to haematite and goethite, with goethite the more probable mineral (see fig. I.4.15).

Since the magnetic profile crosses the feature at the north-western edge in the case of MdB-IB (see fig. A.4b) the anomaly of about 4nT between 5 and 7 m applies only to the northern edge of the western half of the anomaly. The anomaly of about 12 nT between 7 and 9 m crosses the eastern half of the anomaly closer to the centre. The magnetic modelling of the burial shows that susceptibility values between 1,000 and 1,300*1e-5 [SI] are capable of causing an anomaly of about 12 nT. The burial was modeled by having a rectangular shape with a susceptibility that was varied during the fitting process (fig. I.4.15c). The susceptibility values are in the range of granite, gabbro or syenite (see again table I.3.6). Figure I.4.15 shows the best fit with a susceptibility value of 1,200*1e-5 [SI]. Table I.4.4 summarizes the parameters applied for modelling.

Table I.4.4: Susceptibility values for the model of an iron oxide concretion MdB-FeO (see fig. I.4.15a) and the burial MdB-IB (see fig. I.4.15c)

Material	Susceptibility (1e-5 [SI])
Soil	90
iron(III) oxide concretion	12.5 - 500 (see fig. I.4.15b)
Stones	1,000-1,500 (see fig. I.4.15d)

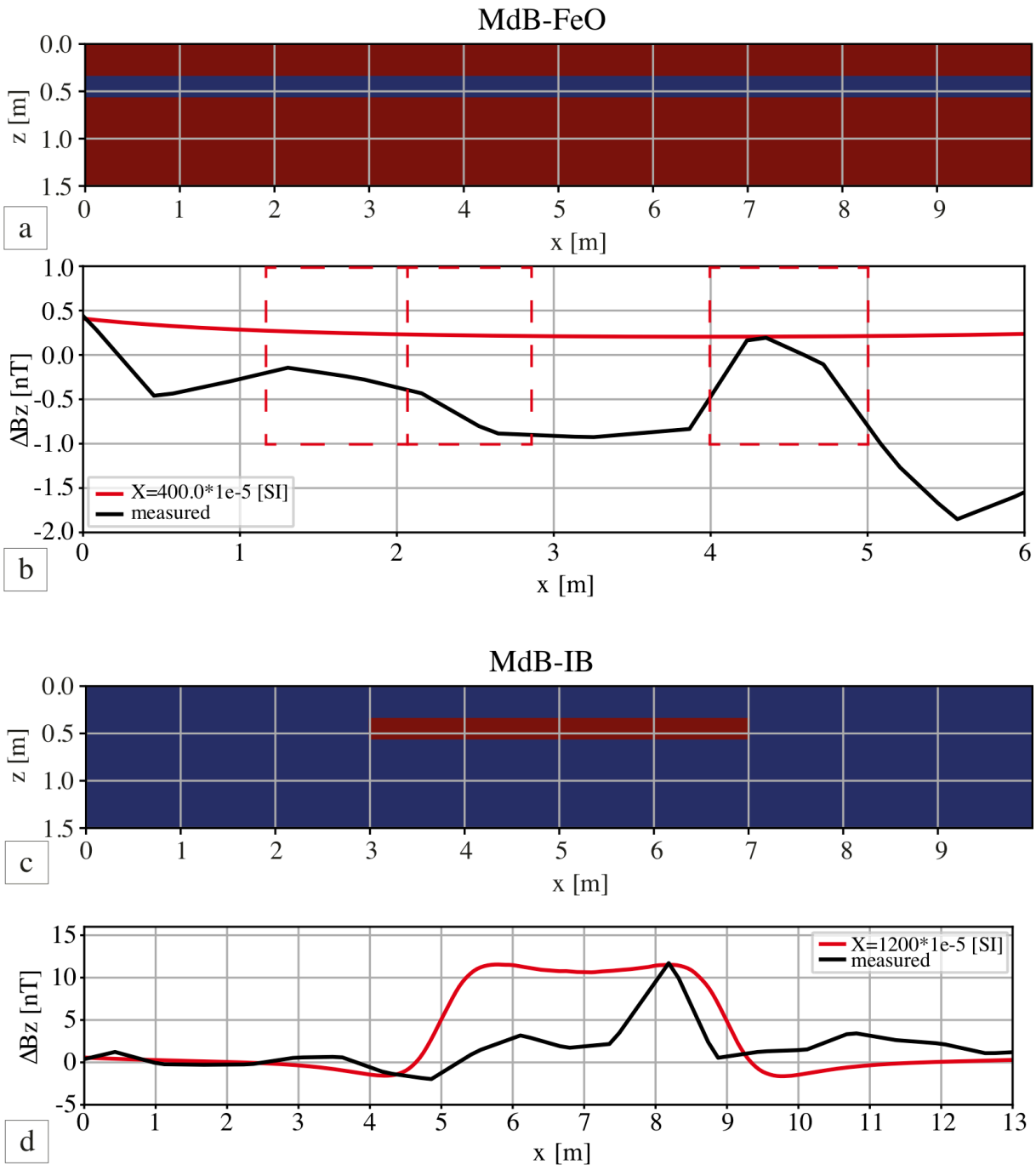

Fig. I.4.15: Magnetic model (a,c) and results of the magnetic modelling of MdB-FeO and MdB-IB. (b.d) shows the magnetic profile of MdB-FeO and MdB-IB as black (measured) and red (modeled) solid line.

I.4.2.1.3 Summary

In the case of the iron oxide concretion of MdB, a direct comparison of GPR and magnetics is helpful to differentiate between archaeological feature and the iron oxide concretion. Both features appear at the same depth. As expected, the iron oxide concretion provides anomalies of about 0nT (between -0.5 and 0.5 nT). This suggests the presence of iron oxide minerals with low susceptibility values as the modelling showed.

Magmatic and metamorphic stones provide anomalies between 8 and 15 nT, assuming susceptibility values between 1,000*1e-5 [SI] and 1,500*1e-5 [SI].

In the GPR data, both the iron oxide concretion and the stone package of the burial show a clear reflection amplitude. The data as well as the modelling show that there is potential to differentiate, with the help of magnetics the stone package of the burial from the iron oxide concretion, both of which occur at depths of archaeological interest (0.3–0.7m). Furthermore, it was found that, although the reflection coefficient of the iron oxide concretion is larger than that of the stones, the amplitudes caused by the reflection from the stones are larger than those of the iron oxide concretion. It was found, that a higher volumetric water content as well as a lower porosity of MdB-IB cause larger amplitudes.

I.4.2.2 Inurned Cremation (BH-U and MdB-U)

The identifiability of these features is investigated by comparing the magnetic and GPR data of excavated examples from our two investigation sites (BH and MdB) in two different soil conditions. The geophysical appearances of the urns (BH-U and MdB-U) and cooking pits (MdB-CP and BH-CP) will be discussed with respect to the influence of soil conditions on the measurement results.

There are several urn graves in MdB, but only a few were recognised by GPR due to the profile distance of about 0.4 m during the measurement. MdB-U is one example in which GPR crosses the urn directly in the centre. Additionally, this example is one of the good preserved ones, although the upper part of the urn was damaged. In BH seven urn graves were documented, with five completely intact, BH-U among them. Since not all BH urns could be clearly identified in magnetics and GPR, one urn was chosen randomly.

I.4.2.2.1 Appearance in Geophysical Data

BH-U, an example of an inurned cremation, is visible neither in the magnetic map nor in the GPR time slice and depth section (fig. A.5a,b, I.4.16b). BH-U was found in a large-area excavation in a loamy channel between gravel layers at a depth of about 1.1 m beneath the colluvium. In contrast, the urn MdB-U is clearly visible as a strong reflection in the radar profile as well as in the time slice (fig. A.3a, I.4.16d). As in the case of BH, MdB-U is not visible in the magnetic map, although it was found at a depth of 0.3 m depth, just beneath the topsoil, with no gravel layers whose magnetic signals might have covered the urn signal.

Since the GPR data were corrected for attenuation and damping, they are comparable for both sites. The different depths cannot therefore be the explanation for the failure of detection in BH. To explain this difference and to investigate the influence of the surrounding soil, numerical modelling was performed on the GPR data. Since geometrical spreading and absorption can be compensated, the crucial role here is played by the reflection coefficient, which is basically the permittivity contrast (Davis & Annan 1989; Neal 2004). In the following the role of porosity and water content influencing permittivity was investigated for both sites.

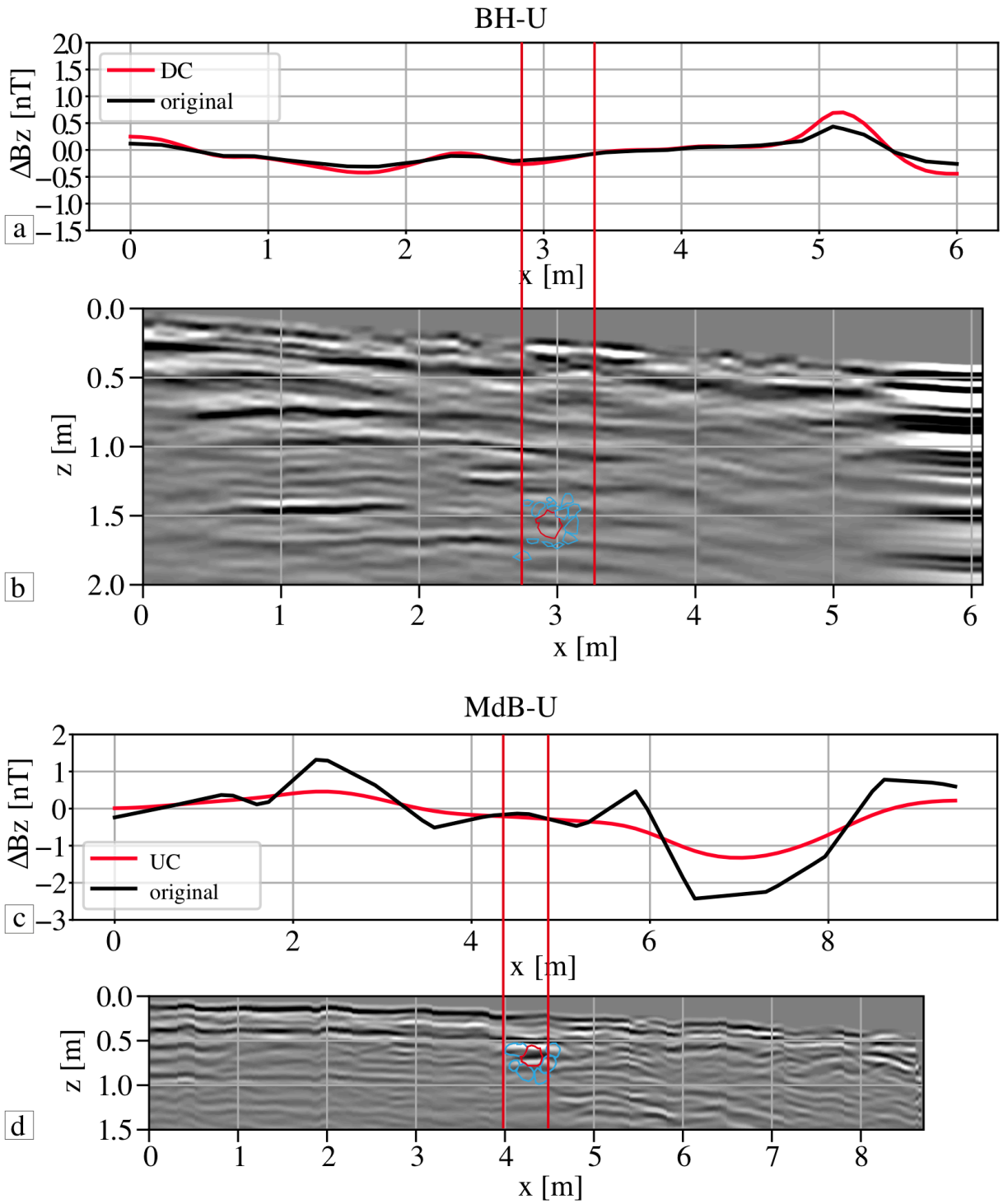

Fig. I.4.16: Comparison of magnetic (a,c) and GPR data (b,d) of BH-U and MdB-U. Magnetic data shown as profile (a,c) crossing the urn at the position of the GPR profile (b,d). The black line shows the magnetic amplitudes measured directly at the surface, the red line represents the downward (DC) or upward (UC) continuation. (b,d) show the GPR data as profile (black: positive, white: negative amplitude). The drawing of the archaeological documentation is inserted in the GPR profile (red represents the urn, blue represents stones). The red lines mark the position of the archaeological target. The urn MdB-U was digitized on the basis of the photography of fig. I.4.18a. Stones were also covering the urn, but were already removed for the photography and therefore not in this figure. BH-U was digitized on the basis of the archaeological drawings. The position of the profile can be found in figures A.5 (BH-U) and A.3 (MdB-U).

I.4.2.2.2 Modelling the Features

GPR

Both urns (MdB-U and BH-U) were placed inside a stone package consisting of boulder stones. The model of BH-U was created by digitizing the archaeological drawings (fig. I.4.17a). The model of MdB-U was based solely on the photographs of the archaeological documentation (fig. I.4.18a). Its depth, size and shape were therefore not exactly known. The parameters for the filling of BH-U and MdB-U as well as the final depth and height of the urn MdB-U were found during the modelling and trace comparison process and were compared with the archaeological documentation afterwards. After each modelling process the middle trace of the synthetic GPR profile was compared with the middle trace of the measured profile and afterwards the model was manually adjusted. The final parameters for permittivity and conductivity can be found in table I.4.5.

Table I.4.5: Dielectric Permittivity and electrical conductivity values used for modelling of BH-U and MdB-U

Material	Feature	Parameter	Value
Top soil	BH-U	ϵ_r	6.05 (layer 1 [fig. I.4.17b])
Top soil	BH-U	σ [mS/m]	1.83 (layer 1 [fig. I.4.17b])
Top soil	MdB-U	ϵ_r	6.05
Top soil	MdB-U	σ [mS/m]	1.83
Sub soil	BH-U	ϵ_r	16 (layers 2, 5 [fig. I.4.17b])
Sub soil	BH-U	σ [mS/m]	1.11 (layers 2, 5 [fig. I.4.17b])
Sub soil	BH-U	ϵ_r	15 (layers 3, 6 [fig. I.4.17b])
Sub soil	BH-U	σ [mS/m]	1.04 (layers 3, 6 [fig. I.4.17b])
Sub soil	BH-U	ϵ_r	14 (layer 4 [fig. I.4.17b])
Sub soil	BH-U	σ [mS/m]	1.07 (layer 4 [fig. I.4.17b])
Sub soil	MdB-U	ϵ_r	14.1
Sub soil	MdB-U	σ [mS/m]	0.9
urn filling	BH-U	ϵ_r	12
urn filling	BH-U	σ [mS/m]	1.11
ceramics	BH-U	ϵ_r	17 (layer 10 [fig. I.4.17b])
ceramics	BH-U	σ [mS/m]	1e-5 (layer 10 [fig. I.4.17b])
ceramics	MdB-U	ϵ_r	17
ceramics	MdB-U	σ [mS/m]	1e-5
stone	BH-U	ϵ_r	10 (layer 8 [fig. I.4.17b])
stone	BH-U	σ [mS/m]	1 (layer 8 [fig. I.4.17b])
stone	MdB-U	ϵ_r	5
stone	MdB-U	σ [mS/m]	1
bone	MdB-U	ϵ_r	2.3
bone	MdB-U	σ [mS/m]	6.5
gravel	BH-U	ϵ_r	8 (layer 9 [fig. I.4.17b])
gravel	BH-U	σ [mS/m]	1 (layer 9 [fig. I.4.17b])
	MdB-U	depth [m]	0.27
	MdB-U	remaining height of the urn [m]	0.04

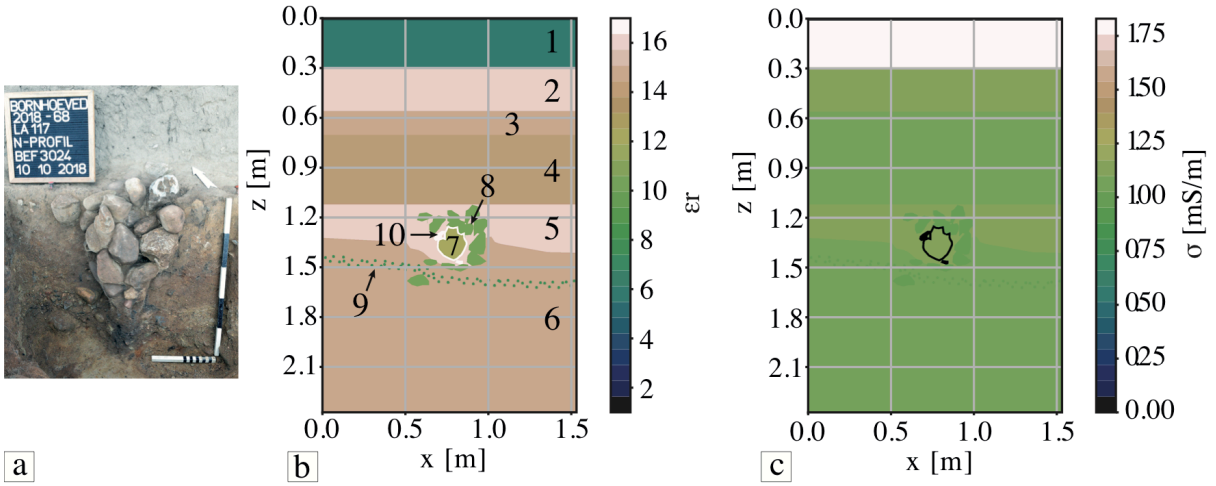

Fig. I.4.17: Photograph (Kneisel) of one of the urns of LA117 (a) and model of inurned cremation of LA 117 (BH-U) (b,c). (b) shows permittivity and (c) conductivity.

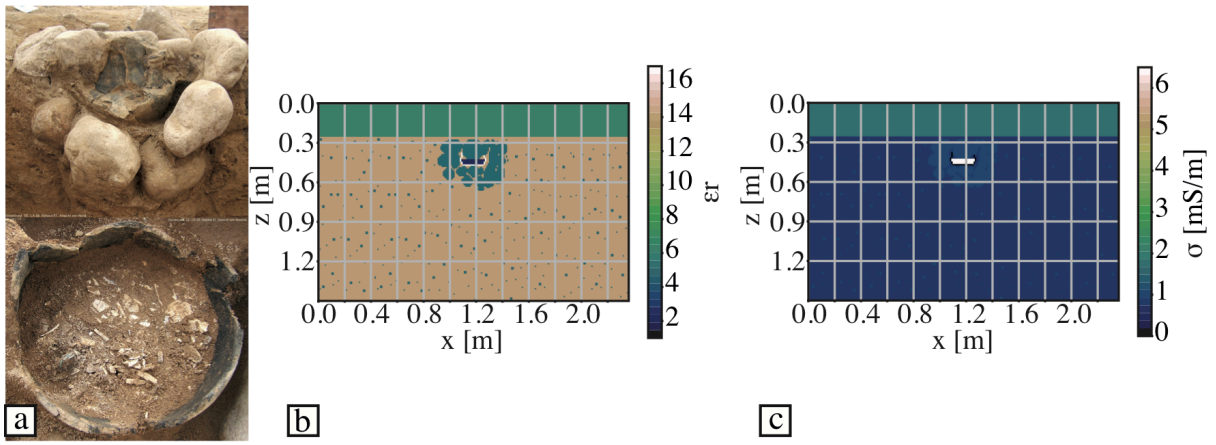

Fig. I.4.18: Photograph (Lütjens) showing one of the urns of LA 58 (a) and model of inurned cremation of LA 58 (MdB-U) (b,c). (b) shows permittivity and (c) conductivity.

Comparing the traces in the model results (fig. I.4.19c) shows that the amplitudes caused by the urn BH-U are very small, whereas those of the stones at the bottom are large. The parameters resulting from modelling show that the permittivity contrasts between stone and surrounding soil is $\Delta\epsilon_r$=6 (see table I.4.5). The reflection coefficient is at about 0.11 for the transition of soil to stone. The contrast between pottery and filling is $\Delta\epsilon_r$=5 and the contrast between stone and pottery is $\Delta\epsilon_r$=7. For the transition of stone to pottery one can expect a reflection coefficient of -0.13 and for the last transition between pottery and filling a coefficient of about 0.09.

Comparing the traces in both model results (fig. I.4.20c), it can be seen, that the amplitudes caused by the urn MdB-U are larger than those of BH-U. Looking at the reflection coefficients, it is clear, that the reflection coefficients of the transitions from soil to stone and stone to ceramics are twice as large in the case of MdB-U

than in that of BH-U. The largest reflection coefficient can be found at the transition from ceramics to filling in the case of MdB-U (see table I.4.6).

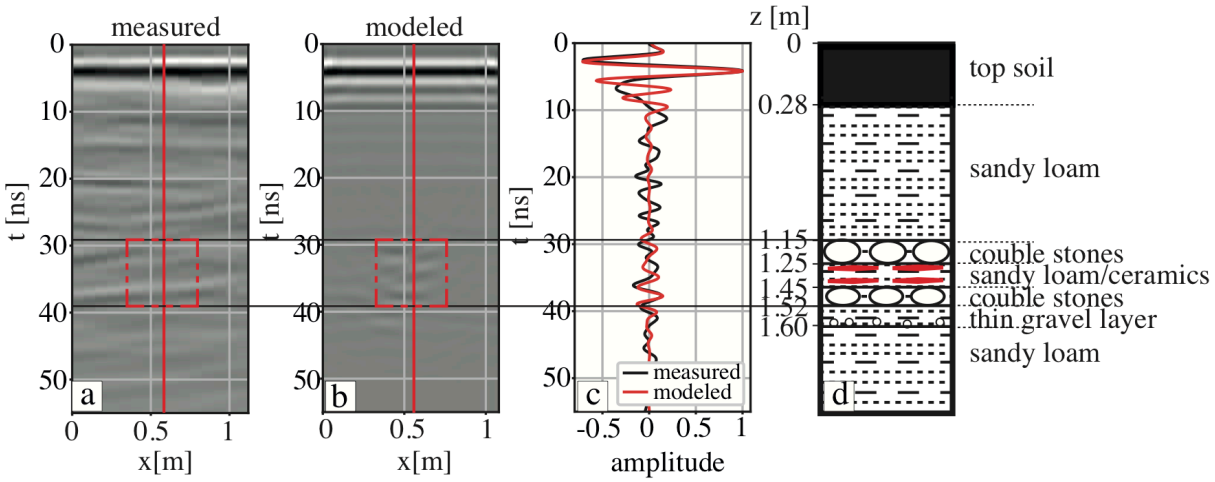

Fig. I.4.19: Comparison of measured and modeled data of BH-U. a) and b): measured and modeled GPR profile. The dashed red rectangle highlights the position of the archaeological feature. BH-U was not recognised in the GPR data at first sight. c): trace comparison of measured and modeled data. All amplitudes are normalized to the largest amplitude of the direct wave. d): Schematic stratigraphic column.

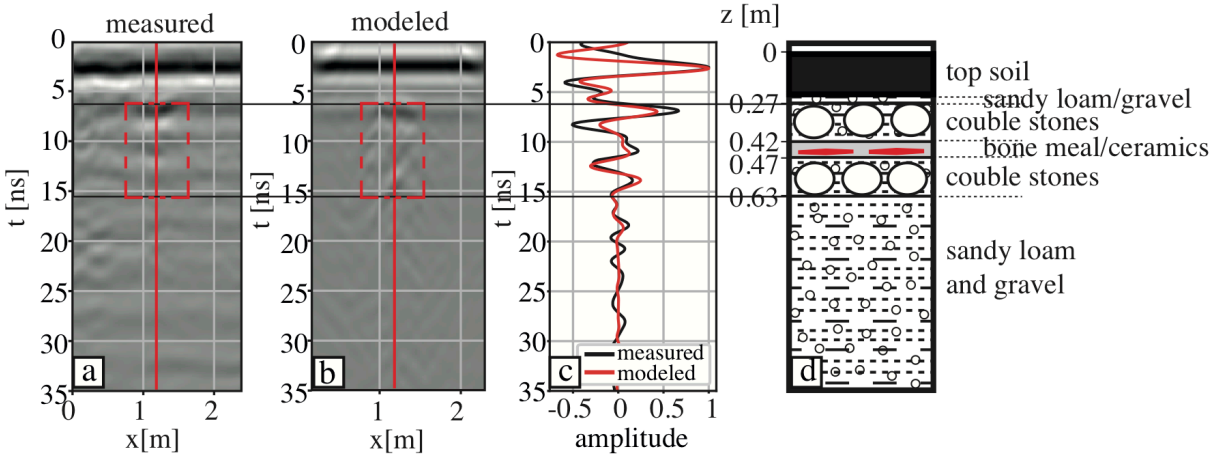

Fig. I.4.20: Comparison of measured and modeled data of MdB-U. a) and b): measured and modeled GPR profile. The dashed red rectangle highlights the position of the archaeological feature. MdB-U was recognised very well in the GPR data. c): trace comparison of measured and modeled data. All amplitudes are normalized to the largest amplitude of the direct wave. d): schematic stratigraphic column.

Table I.4.6: Derived reflection coefficients

Feature	Transition	Reflection coefficient
BH-U	soil to stone	0.11
BH-U	stone to ceramics	0.13
BH-U	ceramics to filling	0.09
MdB-U	soil to stone	0.25
MdB-U	stone to ceramics	0.29
MdB-U	ceramics to filling	0.46

Table I.4.7: Estimated porosity and water content on the basis of the found permittivity values

Feature	Permittivity	Porosity [ϕ in %]	Water Content [θ in %]
BH-U	16 [layer 2,5]	46	30
BH-U	15 [layer 3,6]	44	28
BH-U	14 [layer 4]	32-42	22-26
MdB-U	14.1	40	26
mean BH-U		**41**	**26.5**
mean MdB-U		**40**	**26**

Now one can estimate the porosity and water content on the basis of the permittivity values according to Birchaks equation (table A.5 and A.6). By looking at the mean porosity and mean water content of MdB-U and BH-U, similar values for both sites and features are found (see table I.4.7). A mean porosity of 40% for MdB and 41% for BH and a mean water content of 26% for MdB and 26.5% for BH was found.

Magnetics

For purposes of magnetic modelling, two spheres were assumed for both urn models, one consisting of pottery inside another one consisting of stones (see fig. I.4.17a/I.4.21a). The magnetic model of MdB-U is similar to the BH-U model. Two circles were created, one with the susceptibility values of the stones (red) and an inner circle (blue) with susceptibility values of pottery, both drawn from literature (see fig. I.4.21).

Only the susceptibility values for stones were varied, although it is expected that if we also varied the susceptibility values of the ceramics, one would obtain results similar to fig. I.4.21b, but with different susceptibility values for the stones. Susceptibility values for stones in the range of 10,000*1e-5 [SI] to 30,000*1e-5 [SI] were found, causing an anomaly of about -0.2nT for BH-U by a constant susceptibility of ceramics, which is consistent with values for igneous rocks (Hunt et al. 1995). For MdB-U susceptibility values between 100*1e-5 [SI] and 300*1e-5 [SI] were found, causing an anomaly of about -0.2nT. This agrees with the range of magmatic (e.g. granite, rhyolite (Hunt et al. 1995)), metamorphic (e.g. gneiss, schist, slate (Hunt et al.

1995)) and sedimentary (e.g. dolomite, limestone, sandstone, shale (Hunt et al. 1995)) rocks, as well. Final parameters can be found in table I.4.8.

By comparing the magnetically modeled urns, one can conclude, that the anomalies of typical urns are at about -0.2 nT. In comparison to the surrounding, the urns do not show a clear differentiation. It is obvious that the susceptibility contrast between the subsoil of BH and the urn BH-U is very low. Additionally, the urn is located at a depth of more than 1 m. Also, the urn itself has a diameter of only 20 cm, together with the surrounding stone package the diameter is about 30 cm. In the case of MdB-U, a greater contrast can be seen compared to the surrounding soil, but overall very small. It is noticeable that effectively only the pottery of the urn contributes to the anomaly, as the stone package has a similar susceptibility to the surrounding soil. The modeled pottery has a diameter of about 20 cm, and together with the surrounding stone package the diameter is about 45 cm. In addition, the soils of MdB have a higher proportion of gravel and stones, which likewise superimpose the magnetic signal of the urn.

Table I.4.8: Susceptibility values for the magnetic modelling of the urn BH-U (see fig. I.4.21a) and MdB-U (see fig. I.4.21c)

Material	Feature	Susceptibility (1e-5 [SI])
Soil	BH-U	50
	MdB-U	90
Stones	BH-U	1,843-100,000 (see fig. I.4.21b)
	MdB-U	100-1,843 (see fig. I.4.21d)
Pottery	BH-U	1,000
	MdB-U	1,000

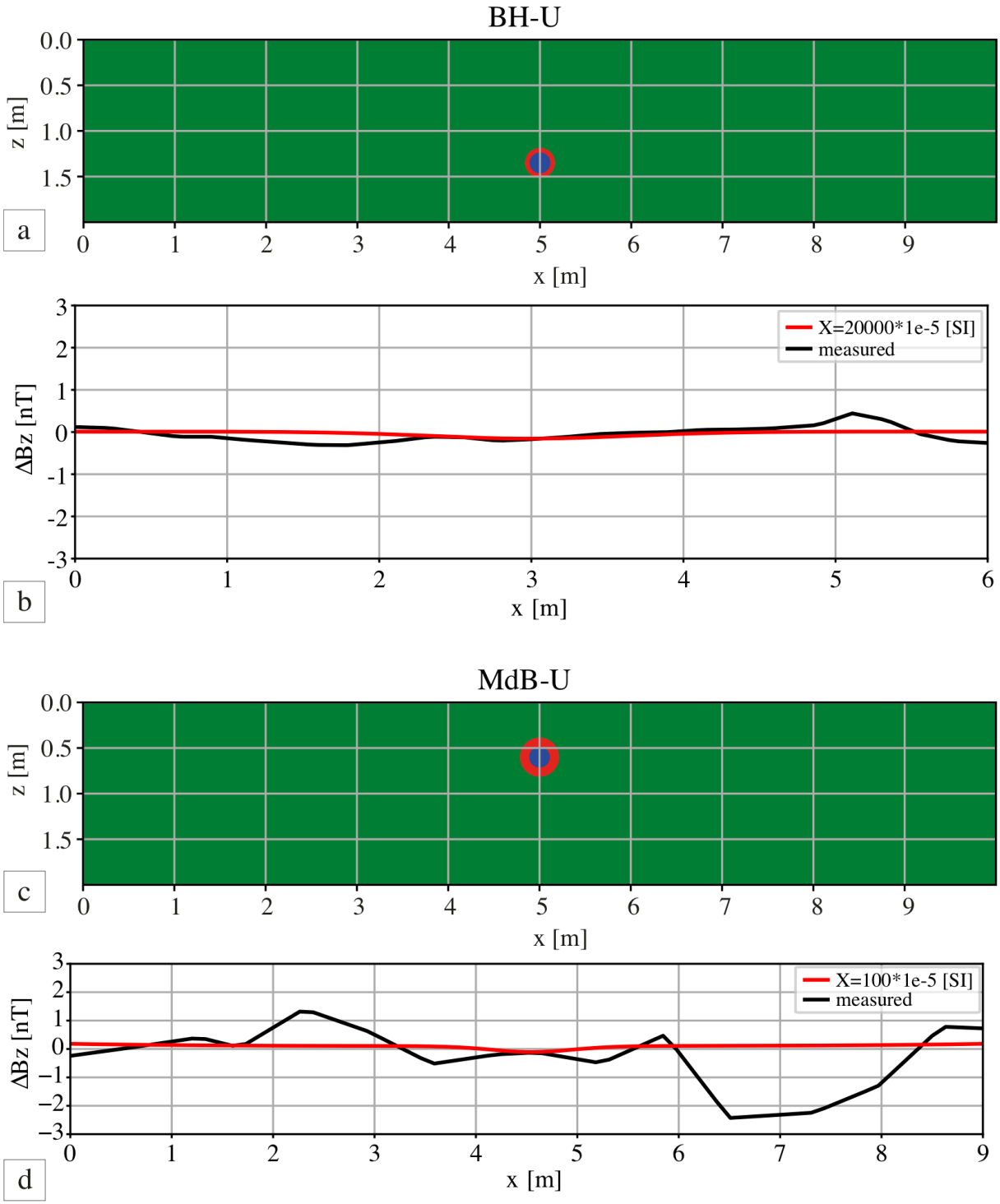

Fig. I.4.21: Magnetic model (a,c) and results of the magnetic modelling of BH-U and MdB-U. (b,d) shows the magnetic profile by varying the susceptibility values of the stones (black: measured; red: modeled). The red circle represents the stone package, the blue one the pottery. The diameter of the red circle of BH-U is 35 cm, the one of MdB-U is 45 cm. Susceptibility value of the pottery is X=1000*e-5 [SI].

I.4.2.2.3 Summary

To sum up the most important results obtained by comparing the urn graves and their surrounding areas in both sites, higher reflection coefficients could be identified for MdB than for BH, with the former twice as large as the latter. The mean porosity as well as the water content is similar for both sites. From the magnetic modelling a susceptibility of about 200*1e-5 [SI] for MdB-U and 20000*1e-5 [SI] for BH was found, whose affiliation of the kind of stones is not unique.

I.4.2.3 Cooking Pit (BH-CP and MdB-CP)

In the following BH-CP will be discussed, which shows the strongest magnetic amplitudes and displays the largest amount of stones of the BH cooking pits, and MdB-CP, which displays magnetic amplitudes in the middle range in comparison to the other cooking pits in the cooking pit complex of MdB. This cooking pit is one of the two excavated pits at the site MdB, with magnetic data also taken from the surrounding area. Therefore, it was decided to use this example. Both cooking pits differ in the amount of stones and in terms of depth, size and magnetic amplitude. Soil conditions are also different at both sites.

Cooking pits are often recognisable in the magnetic map by their large positive circular anomalies (fig. A.5). The maximum amplitudes of the magnetic anomaly have a wide range. The MdB cooking pits between the burial mounds display amplitudes between 2 and 8 nT, those of the MdB cooking pit complex range from 50 to 550 nT and those of BH from 0.1 to 4 nT. One example of BH-CP can be found in fig. I.4.23a, one of the MdB cooking pits in fig. I.4.24a. Further differences in the size of the magnetic anomaly may also be attributable to the duration and intensity of usage and even the type of the stones inside the pit.

I.4.2.3.1 Appearance in Geophysical Data

For the purpose of comparison of MdB-CP and BH-CP, the magnetic data were downward continued (DC). The maximum amplitude is at about 5 nT for BH-CP and 300 nT for MdB-CP (fig. I.4.22a,c). In comparison to the magnetics, the cooking pit BH-CP does not stand out from its surrounding in the GPR profile (fig. I.4.22b). In the GPR time slice (fig. A.5b) BH-CP appears as a circular feature and shows a clear reflection from its top in the vertical section. The reflections are too weak to be identified without knowing its position. But the GPR enables the determination of the position and therefore the depth of the feature once it is recognised on the magnetic map. To understand the weak appearance of BH-CP in the GPR data numerical modelling was applied.

Since no GPR data of the MdB cooking pit are available, the GPR data was modeled by using the mean relative permittivity values for MdB (fig. I.4.22d). Additionally, the relative permittivity values were used, which were found during the modelling of MdB-IB and MdB-U of section I.4.2.1.2 and I.4.2.2.2, which means ϵ_r=14.1 and ϵ_r=20 for the soil in the surrounding of the feature (see fig. I.4.22e,f). It is obvious that the amplitudes increase if the soil permittivity is larger. The details concerning the reflection coefficient, water content and porosity will follow in the next section.

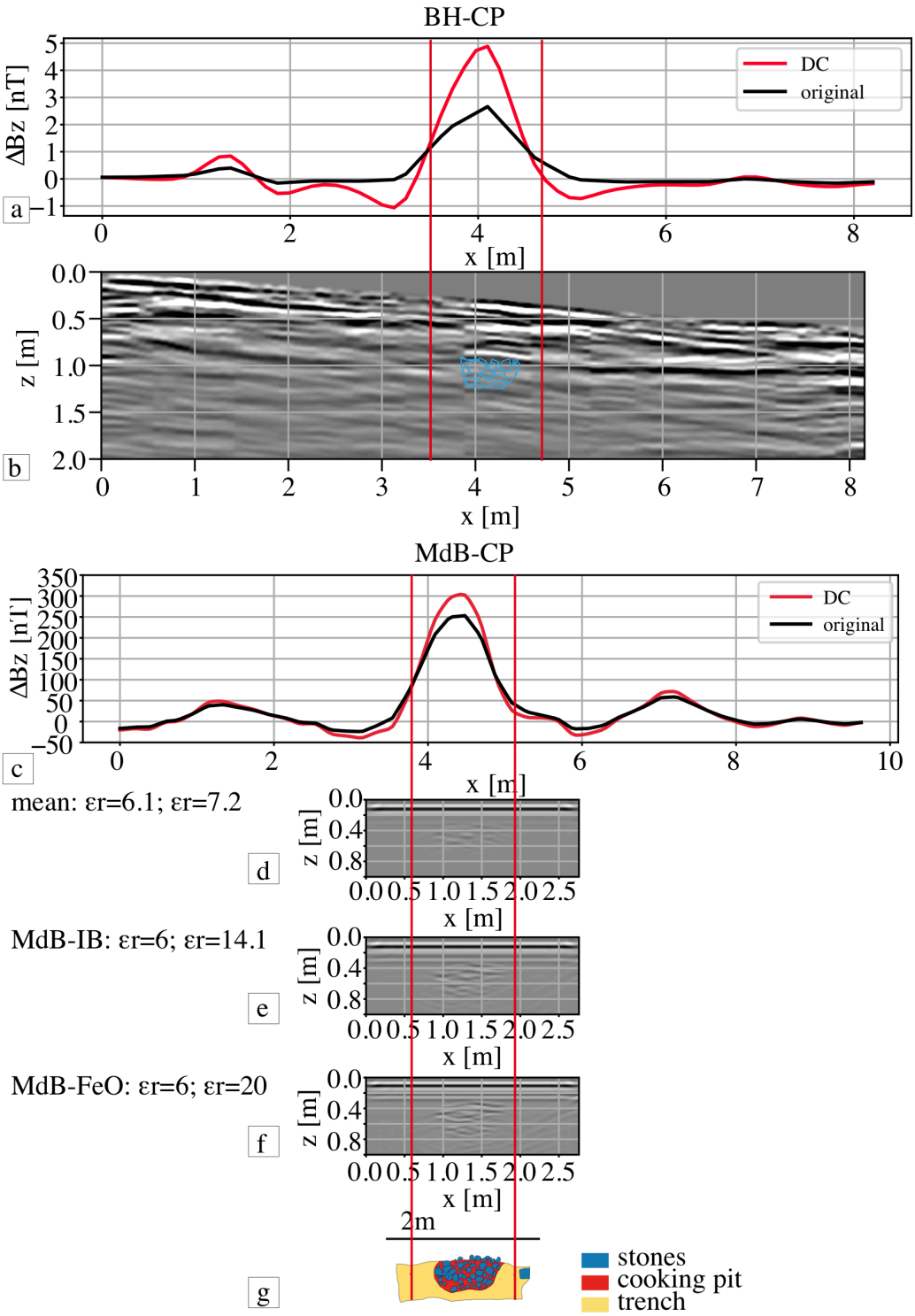

Fig. I.4.22: Comparison of magnetic (a,c) and GPR data (b,d) of BH-CP. Magnetic data shown as profile (b,d) crossing the centre of the cooking pit. The black line reflects the measured data. The red solid line represents the downward continuation (DC). GPR data shown as profile (black: positive, white: negative amplitude) in b, d, e and f. The drawing of the archaeological documentation (by Kneisel) is inserted in the GPR profile of BH-CP. The red vertical lines mark the position of the cooking pit. (d), (e) and (f) show the modeled GPR profile by applying the mean permittivity (d), as well as the permittivities used for the subsoil of MdB-U (e) and MdB-IB (f). (g) is the archaeological documentation provided by Schaefer-Di Maida (blue: stones; red: soil of the pit; yellow: surrounding soil). The position of the profile of BH-CP can be found in figure A.5. The profile of MdB-CP, which was measured only with magnetics cam be found in figure I.2.4.

I.4.2.3.2 Modelling the Features

GPR

The models of BH-CP and MdB-CP were created by digitizing the archaeological drawings. Since nothing is known about the layers above in the case of BH-CP, it was tried to insert suitable layers to provide a signal similar to that which was measured. In particular, the strong negative amplitude on top of the cooking pit indicates a large negative reflection coefficient. The measured GPR profile also allows some layers above the pit to be identified. The arrangement of the layers was varied, as well. To decide which layers and inherent permittivity values are the most suitable, the middle traces of the modeled and measured GPR trace were manually compared after each modelling step. From the archaeological documentation, the depth of the cooking pit is known to be about 0.65 m. The final stage of the model can be found in figs. I.4.23b and I.4.23c.

For MdB the permittivity of the stones was kept constant at ϵ_r=5. The soil of the cooking pit was set to ϵ_r=9 for a soil permittivity of ϵ_r=7.2, ϵ_r=16 for a soil permittivity of ϵ_r=14.1 and ϵ_r=22 for a soil permittivity of ϵ_r=20. The values of ϵ_r=9, 22 and 16 for the cooking pit are assumptions based on the theory that the soil of the cooking pit contains a higher content of organic matter (Gustavsen et al. 2018). Final parameters for BH-CP and MdB-CP can be found in table I.4.9.

Table I.4.9: Dielectric Permittivity and electrical conductivity values used for modelling of BH-CP and MdB-CP

Material	Feature	Relative Permittivity	Electrical Conductivity [mS/m]
Top soil	BH-CP	6.05 (layer 1, [I.4.23b])	1.83
	MdB-CP	6.1	1.83
Sub soil	BH-CP	15 (layer 2, [I.4.23b])	0.9
	BH-CP	8 (layer 3, [I.4.23b])	0.9
	BH-CP	12 (layer 4, [I.4.23b])	0.9
Sub soil	MdB-CP	7.2, 14.1, 20	0.9
cooking pit	BH-CP	12 (layer 5, [I.4.23c])	1.11
	MdB-CP	9, 16, 22	0.9
stone	BH-CP	10 (layer 6, [I.4.23b])	1
	MdB-CP	5	1

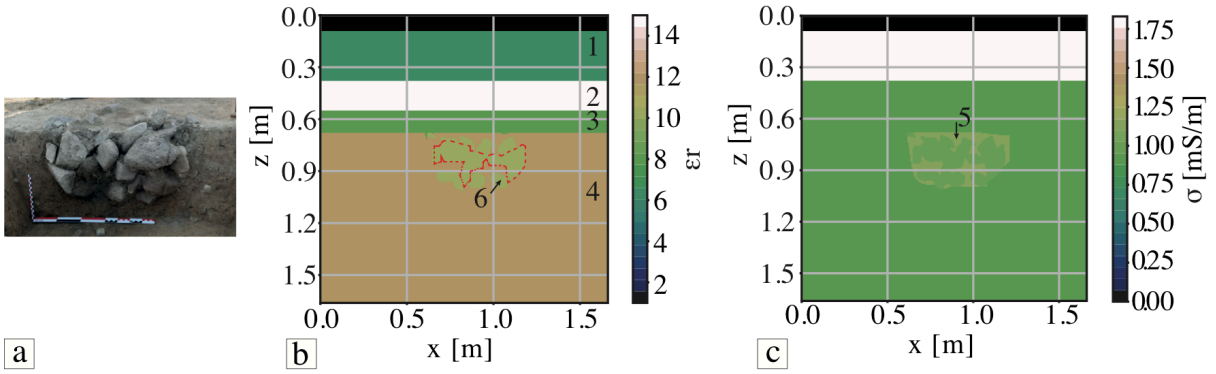

Fig. I.4.23: Photograph (Kneisel) of the cooking pit BH-CP of LA117 (a) and the model of it (b,c). (b) shows permittivity and (c) conductivity.

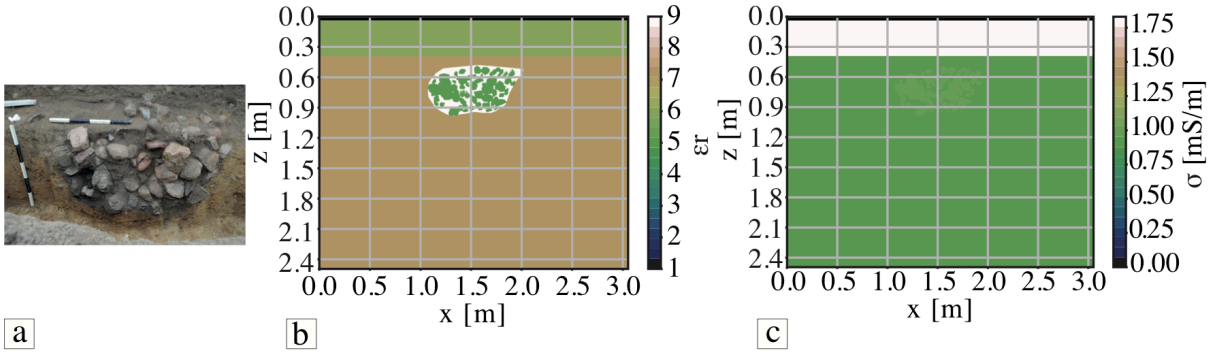

Fig. I.4.24: Photograph (Schaefer-Di Maida) of the cooking pit MdB-CP (a) and model of it (b,c). (b) shows permittivity and (c) conductivity.

The comparison of the measured and modeled traces of BH-CP (fig. I.4.25c) fits quite well in a qualitative sense, showing amplitudes between -0.2 and 0.2 with respect to the direct wave. These low amplitudes imply a small permittivity contrast between the stones and surrounding soil of the cooking pit. The modelling showed that a permittivity contrast of $\Delta\epsilon_r$=2 has to be assumed for matching the observed reflection amplitudes (table I.4.9). For the transition from soil to stone a reflection coefficient of 0.05 can be expected. Against the assumption of a higher water content inside the cooking pit, its permittivity is the same as that of the surrounding soil.

Furthermore, the middle traces of all the modeled GPR profiles of MdB-CP is compared (fig. I.4.26). As expected the mean permittivity values provide a GPR profile with small relative amplitudes due to the small permittivity contrast of $\Delta\epsilon_r$=2 between subsoil and stones (fig. I.4.22d). But from MdB-IB, MdB-FeO and MdB-U one would expect the feature to be recognised quite well due to a high permittivity contrast between stones and surrounding soil. By using the permittivity values of the modelling of MdB-IB and MdB-U of sections I.4.2.1.2 and I.4.2.2.2 one would expect amplitudes of reflection between -0.3 and 0.3 with relation to the direct wave. The corresponding reflection coefficients between the soil of the cooking pit and the stone are about 0.15 (for ϵ_r=9 of the soil of the cooking pit), 0.28 (for ϵ_r=16 of the soil of the cooking pit) and

0.35 (for ϵ_r=22 of the soil of the cooking pit). All these coefficients are larger than those of BH (see table 7.10). The difference in the maximum amplitude caused by the stones, obtained by varying soil permittivity, is between 16% (difference between soil permittivity of ϵ_r=20 and ϵ_r=14.1) and 73% (difference between soil permittivity of ϵ_r=20 and ϵ_r=7.2) (fig. I.4.22).

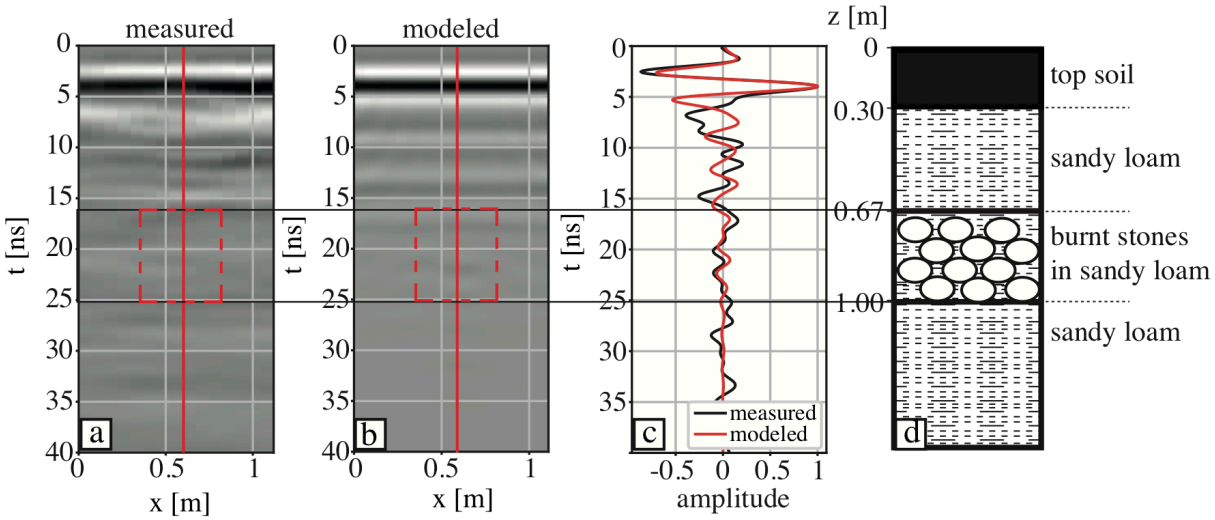

Fig. I.4.25: Comparison of measured and modeled data of BH-CP. a) and b): measured and modeled GPR profile. The dashed red rectangle highlights the position of the archaeological feature. BH-CP was not recognised in the GPR at first sight. c): trace comparison of measured and modeled data. All amplitudes are normalized to the largest amplitude of the direct wave. d): schematic stratigraphic column.

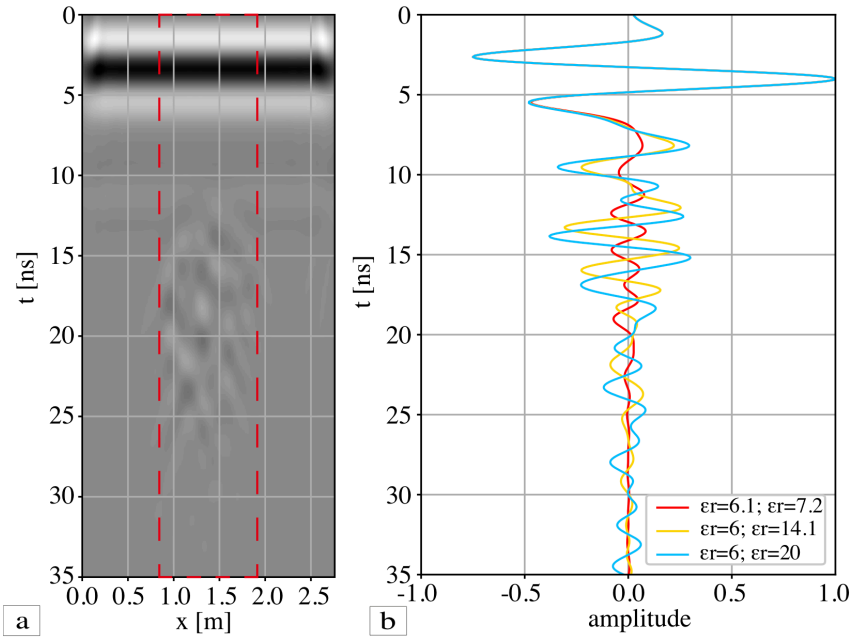

Fig. I.4.26: Example of the GPR profile of fig. I.4.22d with the mean permittivity of MdB (a). The dashed red rectangle highlights the position of the archaeological feature.(b) shows the comparison of the mid traces of the GPR profiles of fig. I.4.22d,e and f normalized by the direct wave. The legend of (b) shows the permittivity values used for the topsoil (first) and the soil beneath (second).

Table I.4.10: Derived reflection coefficients

Feature	Transition	Reflection coefficient
MdB-CP	soil of the pit [ϵ_r=9] to stone	0.15
MdB-CP	soil of the pit [ϵ_r=16] to stone	0.28
MdB-CP	soil of the pit [ϵ_r=22] to stone	0.35
MdB-CP	soil [ϵ_r=7.2] to soil of the pit [ϵ_r=9]	-0.06
MdB-CP	soil [ϵ_r=14.1] to soil of the pit [ϵ_r=16]	-0.03
MdB-CP	soil [ϵ_r=20] to soil of the pit [ϵ_r=22]	-0.02
BH-CP	soil to stone	0.05

Table I.4.11: Estimated porosity and water content on the basis of the found permittivity values

Feature	Permittivity	Porosity [ϕ in %]	Water Content [θ in %]
BH-CP	15 [layer 2]	44	28
BH-CP	8 [layer 3]	40	16
BH-CP	12 [layer 4]	34-43	20-24
MdB-CP	7.2	48	18
MdB-CP	14.1	46	28
MdB-CP	20	48	36
mean BH-CP		**40.5**	**22**
mean MdB-CP		**47**	**32**

By looking at permittivity one can estimate the porosity and water content of the features BH-CP and MdB-CP. A mean porosity of about 47% for MdB and 40.5% for BH can be found. For the volumetric water content a mean water content of 32% for MdB and 22% for BH can be found (see tab. I.4.11).

Magnetics

Considering the magnetics, a modelling study of the cooking pit BH-CP was conducted (fig. I.4.27). The magnetic amplitude of BH-CP at a depth of 0.65 m is at about 2.6 nT. A susceptibility of 50*1e-5 [SI] of the soil was taken and the susceptibility of the stones was varied between 1000*1e-5 [SI] and 1500*1e-5 [SI]. A susceptibility was found ranging between 1100*1e-5 [SI] and 1300*1e-5 [SI] to fit the measured anomaly quite well. This range falls within the range for granite or for average metamorphic rocks.

The anomaly of MdB-CP was also modeled to find the susceptibility values for the stones. A susceptibility of 90*1e-5 [SI] was assumed for the soils and the values of the stones were varied between 2,000 and 20,000*1e-5 [SI]. It was found that the susceptibility of 20,000*1e-5 [SI] fit the measured anomaly of 250 nT quite well (fig. I.4.27). This value falls within the susceptibility values of igneous rocks.

Table I.4.12: Susceptibility values for the magnetic modelling of the urn BH-CP (see fig. I.4.27a) and MdB-CP (see fig. I.4.27c)

Material	Feature	Susceptibility (1e-5 [SI])
Soil	BH-CP	50
Soil	MdB-CP	90
Stones	BH-CP	1,000-1,500 (see fig. I.4.27b)
Stones	MdB-CP	1,843-20,000 (see fig. I.4.27d)

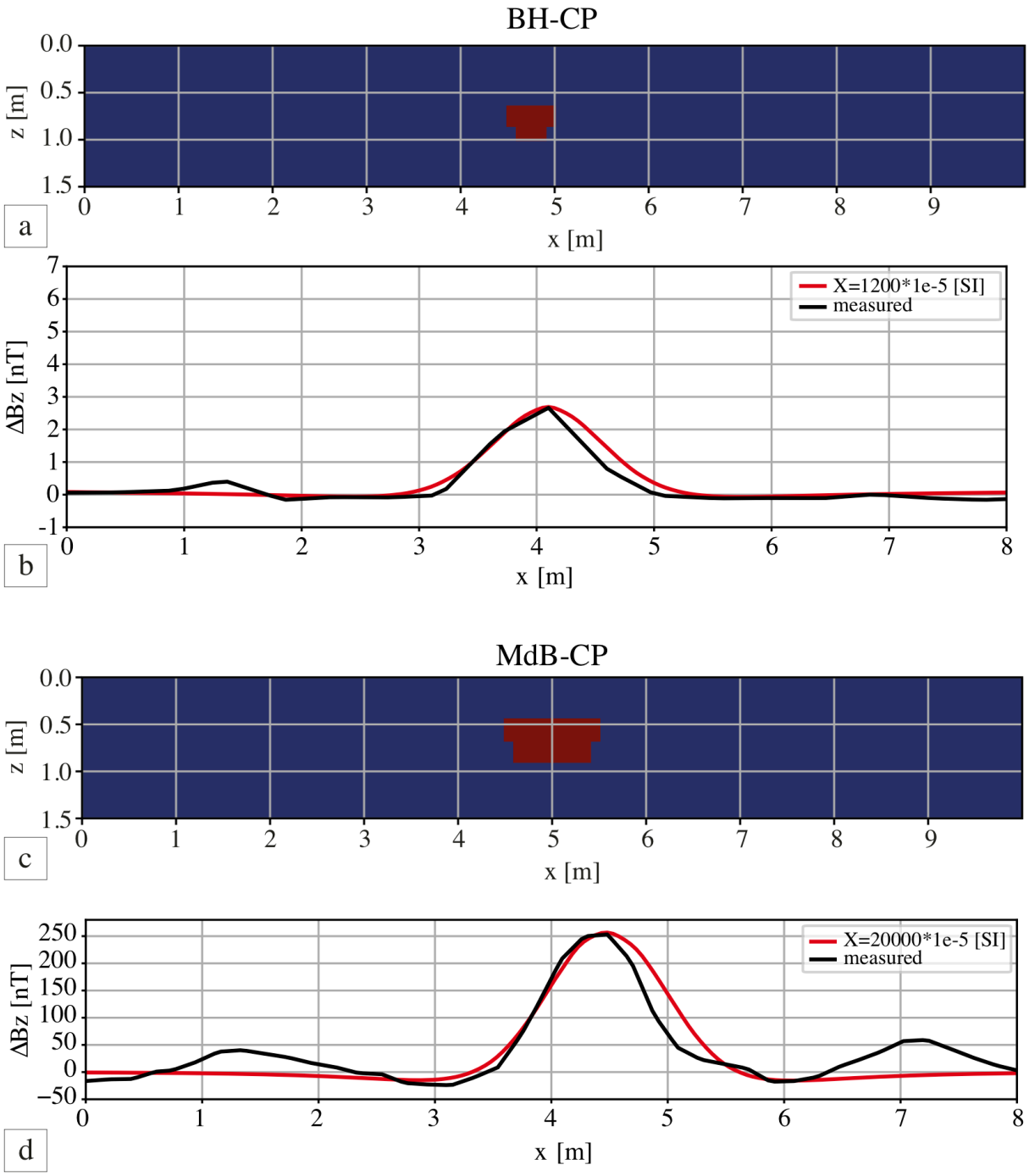

Fig. I.4.27: Magnetic model (a,c) and results of the magnetic modelling of BH-CP and MdB-CP. (b,d) shows the profile of BH-CP and MdB-CP (black line: measured; red line: modeled profile).

I.4.2.3.3 Summary

Cooking pits are always recognised by magnetics. If they are not directly recognised by GPR, a comparison with magnetic data will serve to identify their position. The MdB cooking pits are larger and therefore show a stronger magnetic anomaly. The number of stones they contain is also larger. The main difference in the detection by applying GPR is the permittivity contrast between soil and stone of $\Delta\epsilon_r$=2 for BH and $\Delta\epsilon_r$=9 for MdB. The reflection coefficients of MdB-CP are larger than those of BH-CP. The mean porosity of the

soils in BH is at about 40.5% with a mean volumetric water content of about 22%. For MdB one can expect a mean porosity of about 47% with a mean volumetric water content of about 32%.

I.4.3 Attempted Classification of Signal Strength

Based on the previously obtained results, some general conclusions shall be drawn before continuing. The chosen features (urn graves, stony features: cooking pits and stone package of the burial, iron oxide concretion) were modeled with a mean porosity of 42.1% and a water content of 25%, 30% and 35%, respectively. Since the porosity values are similar for both sites, it was decided to assume an average porosity. The volumetric water content was selected based on the mean water content of BH – about 24.3%. From the excavation documentation, it is known that excavation and geophysical measurements took place under warm conditions of around 40 °C. A water content of 25% hence represents glacial soils under dry conditions.

From studying the weather conditions of the year 2005, it is known that the precipitation rate was about 33% higher than in 2018 (Deutscher Wetterdienst. Climate Data Center). Therefore, we assumed 30% as a medium water content. Additionally, an additional 5% water content is assumed, to represent a very wet year. For a water content of 25% a soil permittivity of ϵ_r=13.09 is calculated, for a water content of 30% a soil permittivity of ϵ_r=16.94 and finally for 35% represent a soil permittivity of $\Delta\epsilon_r$=21.28, all on the basis of a mean permittivity of the soil matrix of 7.2±3.1. For the topsoil a permittivity value of ϵ_r=6.1 was assumed, since this was the most commonly used value across all examples. Furthermore, the features were set at three different depths (0.35m, 0.7m and 1.1m). In MdB most of the features appear at a depth between 0.35m and 0.7m, whereas in BH depths of 1.1m are also possible

After modelling all features, the mid trace of each profile was taken to compare the maximum amplitude from the reflection caused by the feature. This is shown in fig. I.4.28. The reflection amplitudes of the BH and MdB urn graves are compared, since both have different fillings – soil (BH-U) and bone (MdB-U) (fig. I.4.28a). It was assumed that the stone package of the burial may also represent a stone concentration or a geological stone accumulation, since it was assumed that the same stones are part of the glacial soils (fig. I.4.28b). The iron oxide concretion is separated due to its nature (fig. I.4.28c).

For the urn graves one can expect a relative (to the normalized direct wave) amplitude of 0.4±0.2 at a depth of 0.35m. At 0.7m one can expect a relative amplitude of 0.32±0.15 and at 1.1m 0.32±0.13. For stony features one can expect similar signal strengths at all depths. At 0.35m the relative amplitude is 0.37±0.21, at 0.7m 0.37±0.23 and at 1.1m 0.36±0.20. Higher amplitude values can be expected for the iron oxide concretion. At 0.35m the relative amplitude is 0.73m±0.10m, at 0.7m 0.66±0.12 and at 1.1m 0.72±0.13.

Relatively high standard deviations were found for the relative amplitudes at all three depths, particularly for the urn graves and stony features. Concerning the standard deviation of stony features, one need to consider the different permittivity values for stones between ϵ_r=5 (stone package of the burial) and ϵ_r=10 (cooking pit).

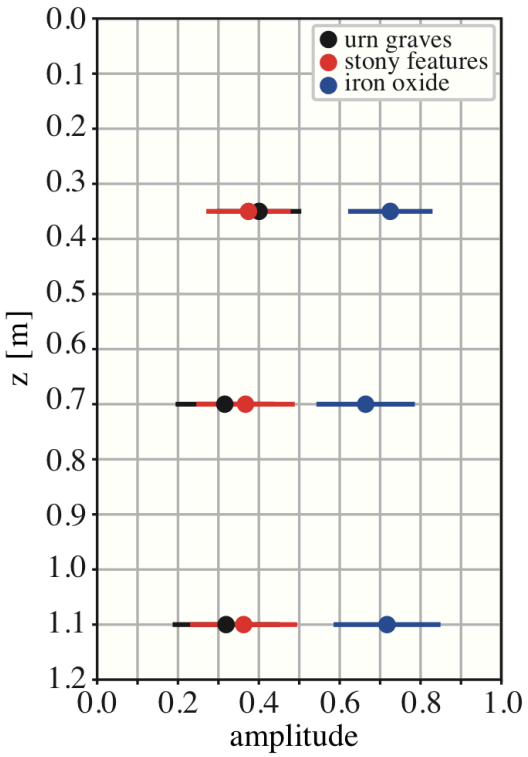

Fig. I.4.28: Comparison of the maximum amplitude of the reflection caused by the features at three different depths (0.35m, 0.7m and 1.1m). The amplitudes are relative to the normalized direct wave. Black dots represent the urn graves, red the stony features (cooking pits and burials embedded in stones) and blue the iron oxide concretions.

To summarize, it is possible to differentiate stony features from naturally occurring features such as iron oxide concretions in the GPR data on the basis of the GPR signal strength, because the GPR amplitudes of the concretions are twice as large as those of the stony features. To differentiate between archaeological and geological stony features is not possible with GPR alone. To do so requires magnetic data as additional tool to differentiate between them. This will be discussed in the following section.

I.5 Discussion

I.5.1 Influence of Soil Conditions on Detectability of Objects

I.5.1.1 GPR

From the soil analysis, the permittivity of the (dried) soil matrix was derived, which is 7.56±3.26 for BH and 6.88±3.03 for MdB. The modelling study of section I.4.1.3 showed that these permittivity values provide reflection amplitudes smaller than would be expected from the measurements. Permittivity contrasts were found between soil and stones ranging from $\Delta\epsilon_r$=2 to $\Delta\epsilon_r$=6 for BH and $\Delta\epsilon_r$=9 to $\Delta\epsilon_r$=14 for MdB, with reflection coefficients from R=0.05 to R=0.11 for BH and R=0.25 to R=0.46 for MdB.

The research presented in section I.4.2 has shown that one can assume a mean porosity of 43.6%±3.88% for MdB and 40.6%±5.0% for BH. The mean volumetric water content of MdB is about 30.6%±3.9% and that of BH about 24.3%±4.7%. This leads to a mean permittivity of about 16.34±3.12 for MdB and 13.33±2.94 for BH. The content of organic matter confirmed the result of a higher soil moisture in MdB than in BH.

To draw generalized conclusions, the results of both sites are summarized. One can expect a mean permittivity of 7.2±3.1for Bornhöved's soils. By considering a mean porosity of 42.1±4.44% and a volumetric water content of 27.5±4.3% one can expect a mean permittivity of 14.95±4.63. These findings result from analysing the modelling results of the chosen features. It is known that modelling provides results that are not unique. One should therefore keep in mind that other results are possible and that the choice of the features also influences the result.

It was also found that the soil properties are strongly influenced by water and porosity. This fact was used to derive a generalized statement about GPR signal strength for urn graves, stony features and iron oxide concretions. Figure I.5.1a shows the amplitude strength in its relation water content with a fixed porosity. It can be seen that the amplitude is larger if the water content is smaller. This is shown in I.5.1b. It is equally clear that with smaller water content but fixed porosity, relative permittivity is smaller. In such cases, one can expect a smaller permittivity contrast and consequently smaller amplitudes. It is also obvious that relative permittivity changes more slowly with a fixed water content but varying porosity and faster with fixed porosity and varying water content. Therefore, one can conclude that the influence of water content on relative permittivity is stronger than that of porosity.

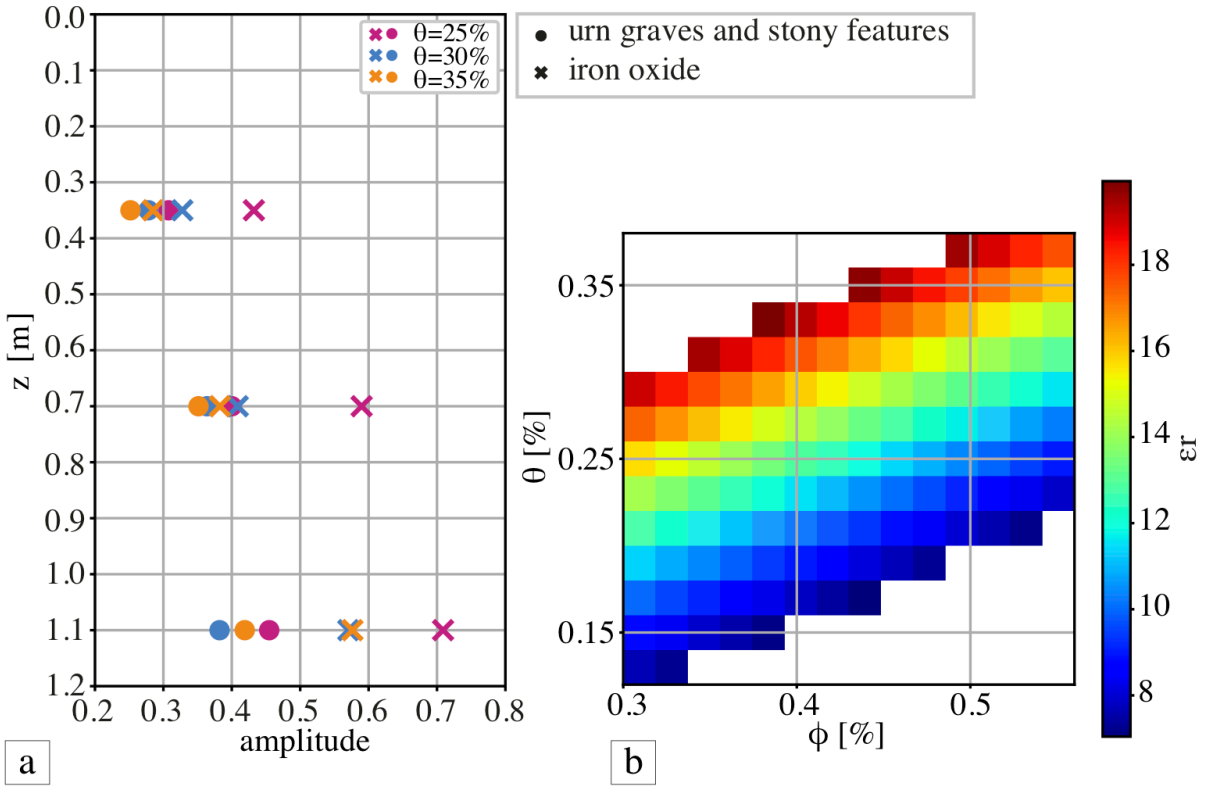

Fig. I.5.1: a) Comparison of the maximum amplitude of the reflection caused by the features at three different depths (0.35m, 0.7m and 1.1m) considering the water content. The amplitudes are evaluated relative to the normalized direct wave. b) Relative permittivity depending on porosity and water content. The shown range of porosity between 30 and 55% corresponds to that of mineral soils (sand, silt, loam and clay).

I.5.1.2 Magnetics

The soil magnetization differs for both sites with susceptibility values between 50±6*1e-5 [SI] for BH and 90±14*1e-5 [SI] for MdB. One could observe that the magnetic data from MdB are more heterogeneous than those of BH. As already mentioned, soils can be magnetized due to the development of magnetite in soil-forming processes (Faßbinder 1994; Blume et al. 2016). Climate conditions also play a role. It is known that weather phenomena such as lightning, human activity and other factors may also influence soil magnetization. In the case of MdB, a high incidence of lightning could be observed, but the magnetic imprint is very local and distinct (Klein 2006). They can be excluded, as a reason for a heterogeneous magnetic response. By considering the frequency dependent susceptibility, one could find a more intense human activity in MdB than in BH. Human activity can be expressed, for example, by pottery shards that may have been left in the ground over time. This may have been either intentional (urn burials or garbage pits) or unintentional in the form of loss (in which case no complete ceramic objects). On the other hand, stones worked by fire in historical times (e.g. in the form of the cooking stone pits) may also be evidence of human activity.

During the analysis of the features, it was also found, that there are stony features (e.g. urns, stone concentrations, geological features) that could not be identified by magnetics. The problem here may be the

superposition of heterogeneous surrounding matter or even the type of the stones themselves.

I.5.2 Combining Magnetics and GPR for Better Identification of Archaeological Targets

In the results chapter, archaeological and geological features were classified with regard to their size and and depth of occurrence as well as their recognition in GPR and magnetics. It was found that cooking pits are often recognized by GPR and magnetics regardless of their size and depth of occurrence. The urns, stone concentrations and burials could be recognized at a mean depth of 0.4 m. Geological features occur at an averaged depth of 0.73 m measured over a large area (> 200 m^2).

The basis for all these results was the analysis of the archaeological documentation of two sites situated approximately 3 km apart. A more representative analysis might have been obtained by also using data from other sites and from other periods within the Bronze Age. The features may occur at different depths and glacial soils are also very heterogeneous (sandy, clayey and loamy). Therefore, one might also expect other thresholds for recognition in GPR and magnetics, since human activity also influences the degree of heterogeneity in the magnetic data. And as was found, the MdB magnetic data are more heterogeneous than those recorded for BH.

I.5.2.1 Pits

Pits are difficult to identify, since their reflection amplitudes in the GPR profile are too weak to be, identified at first sight. If they contain organic matter, their amplitudes become stronger. Nevertheless, in the next part of the thesis we show examples of pits that could be detected very good in the GPR. These form the basis for understanding, with the help of a modelling study and parameter variation, how pits or pit filling have to be composed so that they can be well detected with GPR.

Most pits are not visible in the magnetics, either. Those that were recognised (only 9%) occur at a depth of 0.35m and are larger than 3 m^2. The pits that were recognised were probably refilled in later times or with different soil. From Faßbinder (1994) it is known that ferrimagnetic minerals can be developed by natural soil-forming processes and in under the influence of climatic conditions in the past. Therefore, comparing magnetics with GPR will not produce a higher recognition rate.

I.5.2.2 Stony Archaeological Features

Cooking pits are easily identified using both GPR and magnetics. A direct comparison of GPR and magnetic data helps to identify them in the GPR data if they are not identifiable at first sight. Cooking pits occur randomly but also in lines or clusters, as was found in the MdB cooking pit complex or in the study of Gustavsen et al. (2018). Here a tool for pattern recognition would be helpful.

A combination of GPR and magnetics will also help to identify burials. Furthermore, since they do not have a magnetic signature, it can help to distinguish them from iron oxide concretions.

Identifying urns in glacial soils is more difficult. They show strong reflections in the GPR if the filling contains organic material. Identification by means of GPR is also difficult when the filling consists more or less of the surrounding soil. Urns could also not be detected with magnetics. One might expect pottery to be recognised, since it is magnetized in the process of firing. It is likely that the surroundings are too heterogeneous and overlie the magnetic signal. Therefore, one conclusion of this study is that detectability of the urns will not be improved by combining GPR and magnetics in glacial soils.

I.5.2.3 Geological Features

For geological features there is no threshold for either the depth of occurrence or the area. As has already been discussed, antiferromagnetic iron oxide concretions can occur in the soils of MdB and at the same depth as archaeological features. It was found that haematite and goethite are among their potential representatives, with goethite as the most likely. Nevertheless, both minerals show a similar amplitude range in GPR and magnetics. In comparison to stone accumulations in the form of either or stone concentrations (man-made or natural), they can be identified by additionally considering the magnetics.

The combination of magnetics and GPR is helpful to identify archaeological and geological features. In GPR these features show strong reflections by covering a large area. In the magnetics they are mostly not recognised. If the geological feature is an iron oxide concretion, the combination with magnetics is indeed helpful in distinguish it from archaeological stony features (e.g. cooking pits or burials).

I.5.2.4 Differentiation Between Stony Archaeological and Geological Features

Stony archaeological features are identifiable by considering the depth at which they occur: smaller than 0.5 m, whereas geological features occur at an averaged depth of larger than 0.7 m. This depth range is sufficient to be recognized by magnetics and GPR. It is also known that geological features often have an averaged diameter larger than 10 m (area of about 200 m^2).

In addition, there are stony geological features and iron oxide concretions that occur at depths of archaeological interest directly beneath the topsoil. The combination of magnetics and GPR can be useful in some cases to distinguish them from archaeological features. Concerning the iron oxide concretions, the natural occurrence of goethite was discussed as a probable representative of an iron-bearing but antiferromagnetic mineral in our moderate and cooler regions. Here, differentiation is possible by combining GPR with magnetics. This is different in the case of naturally occurring stone accumulations in the same depth range as archaeological features. If geological and archaeological stony features are not magnetized, an attempt at distinguishing them by combining GPR with magnetics will not be helpful. A likely distinguishing feature is size (naturally occurring stone concentrations: diameter > 10 m; archaeological stone concentrations: diameter < 5 m). It is known that burials are often embedded in magnetizable stones. Moreover, cooking pits display a clear magnetic anomaly due to the fact that the stones are magnetized by use. Here, the further expertise of the GPR interpreter will be helpful.

Nevertheless, one also needs to consider that there are stony features that GPR is unable to detect. To discuss this phenomenon, one needs to keep an eye on the permittivity contrast between stone and soil, because a large profile distance during measurement cannot account for features of large sizes, such as stone concentrations with a mean diameter of about 1.4 m. Due to the fact that stones in northern Germany were carried there by the glaciers in the last ice ages and are therefore of a different nature, permittivity values were found between ϵ_r=5 and ϵ_r=10. From modelling the cooking pit with a permittivity of ϵ_r=10 and different water contents it was found that the reflection amplitudes are in any case small (between 0.1 and 0.3) relative to the direct wave. In a heterogeneous environment these amplitudes can be superposed. As was found, the glacial character of the soils in northern Germany is very heterogeneous, causing noise and scattering.

Finally, one must bear in mind that only a small amount of geological features (n=8) were part of the analysis. This is due to the small measurement areas in MdB and BH and the large extent of the geological features. For a more representative statement, it would have been useful to have a larger amount of geological features.

I.5.2.5 Influence of Scattering on the GPR Amplitude

GPR amplitude is influenced by several factors. There are damping and attenuation, which cause a decrease in amplitude by depth. The permittivity contrast determines the size of the amplitude just by looking at a homogeneous soil without any damping. Furthermore, one must consider the presence of features which influence the amplitude by superposition. Scattering due to the presence of features also influences amplitude by decreasing it. In the following, two selected archaeological features were examined with regard to the scattering effect.

I.5.2.5.1 Urn Graves

First, we modified the model of BH-U (fig. I.4.17b,c, table I.4.5). We removed the layers of different permittivity and created a homogeneous subsoil of ϵ_r=14. The resulting GPR profile can be found in fig. I.5.2a. Furthermore, we removed the pottery (fig. I.5.2b) and the stones (fig. I.5.2c). Comparison of the traces shows a large influence of the layers with different permittivities (see fig. I.5.2d). The relative amplitudes remain more or less the same, but the reflection resulting from the permittivity contrast between stone and pottery (red line in fig. I.5.2d) as well as stone and subsoil (yellow line in fig. I.5.2d) is recorded a little earlier. It is also obvious that the influence of the pottery is very small. At about 34 ns one can see that the reflection amplitude without pottery is 25% smaller than with. The reflection resulting from the gravel layer is not separable from the stones of the package at the bottom of the urn (fig. I.5.2).

By looking at the GPR traces, one can conclude that neither the absence or presence of stones or ceramics influences the amplitude in a significant way. So the difference in the amplitudes must be mainly influenced by water content and porosity.

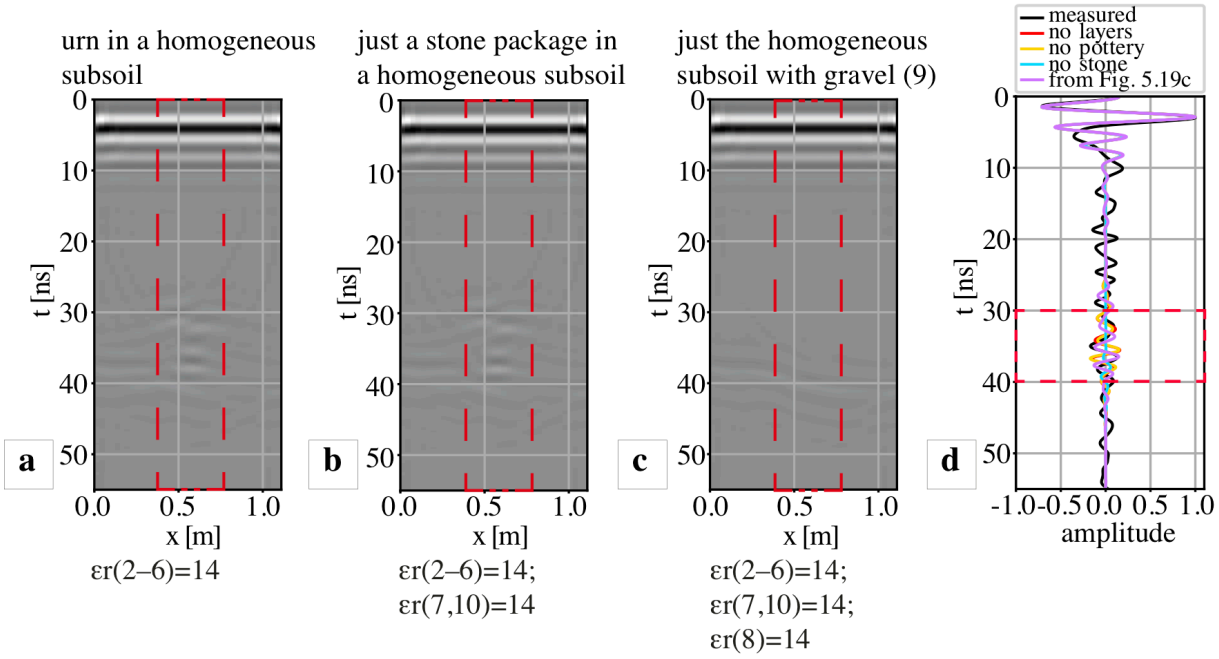

Fig. I.5.2: Comparison of the modeled GPR profiles of three different modifications of the urn package and its surroundings. (a) is the result of the documented urn BH-U within a homogeneous subsoil, (b) that of the feature consisting of just the stone package without the pottery inside in a homogeneous subsoil and (c) that of the homogeneous subsoil without the feature but with the gravel layer at its bottom. The permittivity of the subsoil is ϵ_r=14; conductivity is σ=0.9 mS/m. The dashed red rectangles highlight the position of the archaeological feature. (d) shows the mid trace comparison of the three profiles (a) in red, (b) in yellow and (c) in blue together with the mid trace of that already modeled in fig. I.4.19b (violet) and the measured profile of fig. I.4.19a (black).

I.5.2.5.2 Cooking Pits

To investigate the scattering also modifications of the model of fig. I.4.23 was modeled. The same model of fig. I.4.23 was tested (first) without layers 2 and 3 (fig. I.4.23a) and (second) the model of fig. I.4.23 was modified by removing the stones within the red dashed line in fig. I.4.23b while retaining layers 2 and 3 above. Soil permittivity was assumed to be ϵ_r=14. Similarly to the modelling study of the urn, it emerges that the missing layers above the archaeological feature do not have a strong influence. Comparison of the middle traces of all the models shows that the proportion of removed stones does not have a significant influence on the shape of the signal and amplitude. The comparison of all the three models show similar relative amplitudes (fig. I.5.3).

This modelling study also shows that the absence or presence of stones does not have a significant influence on amplitude.

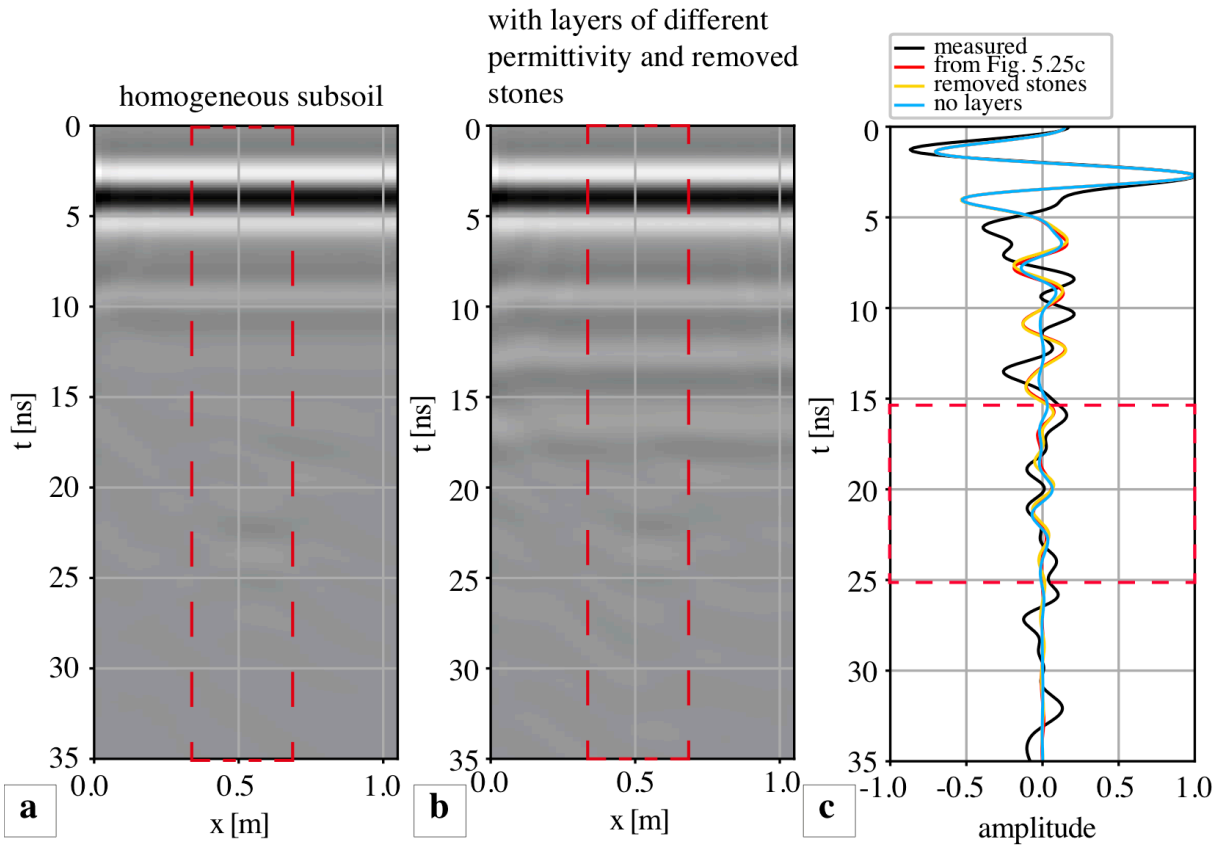

Fig. I.5.3: Comparison of the modeled GPR profiles of two different modifications of the cooking pit BH-CP and its surrounding. (a) is the result of the cooking pit BH-CP within a homogeneous subsoil (see fig. I.4.25b), (b) that of the cooking pit with some removed stones (within the red dashed line in fig. I.4.23b). The dashed red rectangles highlight the position of the archaeological feature. (c) shows the resulting mid traces of the measured GPR profile (black) of fig. I.4.25, that modeled one in fig. I.4.25b (red) as well as the mid traces of (a, blue) and (b, yellow).

In addition to the variation of a model of an existing cooking pit, a model of a cooking pit was created to examine the influence of the permittivity of the stones, assuming a constant permittivity and conductivity of the soil (fig. I.5.4; the parameters used can be found in table I.5.1). The model is not part of the archaeological documentation and was created only for testing purposes. In fig. I.5.5a the GPR profile of the modeled cooking pit with ϵ_r=5 for stones is shown together with the comparison of the middle trace of the GPR profiles with permittivity values between ϵ_r=5 and ϵ_r=10 for stones (fig. I.5.5b). The amplitudes of the strongest reflection caused by the stones differ in the range of 27% (between ϵ_r=5 and ϵ_r=10 for stones) relative to the normalized direct wave. The reflection coefficient varies between 0.09 for ϵ_r=10 and 0.25 for ϵ_r=5. The strongest reflection can also be expected in the upper half of the cooking pit. Furthermore, the reflections of the stone are recorded earlier if the permittivity of the stones is low.

Now one can compare two modelling studies of a cooking pit model to identify the most influential factor. The first is the modelling of the cooking pit of fig. I.4.26 with a fixed permittivity of stones but varying soil permittivity; the second the cooking pit of fig. I.5.4 (varying permittivity of stones and fixed soil permittivity).

By considering the maximum amplitude of the reflection caused by the stones of the cooking pit, it was found that the influence of varying soil permittivity but constant stone permittivity on the amplitudes of the reflections is larger than the influence of varying stone permittivity and constant soil permittivity.

It is also known that the influence of water content is larger on soil permittivity than on rock permittivity. This is due to the small porosity of rocks in comparison to that of soils (sedimentary rocks <30% porosity; magmatic rocks <5% porosity and metamorphic rocks <5% porosity (Šperl & Trčková 2008)). It must therefore be assumed that the cause of the differing permittivity contrasts is basically the difference in soil parameters rather than differences in rock parameters.

Table I.5.1: Dielectric Permittivity and electrical conductivity values used for the modelling study of fig I.5.4

Material	Relative Permittivity	Electrical Conductivity [mS/m]
Top soil	6.05	1.83
Sub soil	14.1	0.9
stone	5 - 10	1

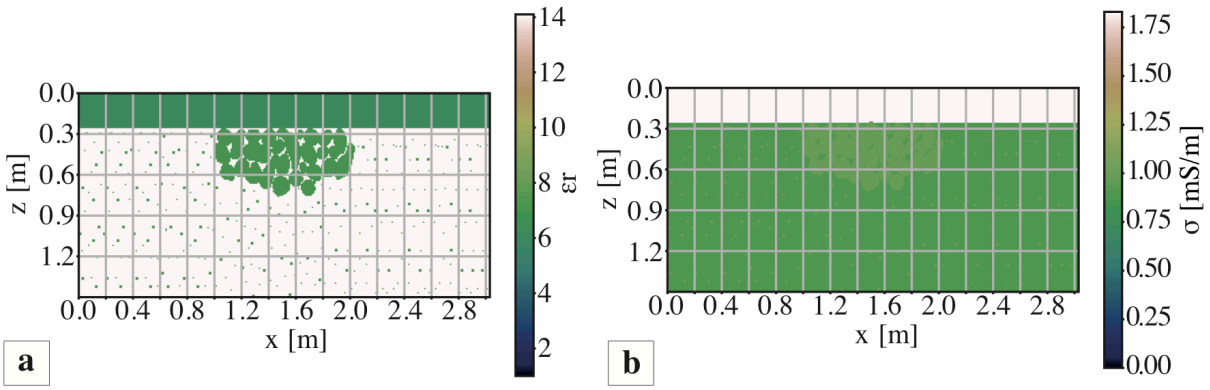

Fig. I.5.4: Model of a cooking pit, created for varying the permittivity of the stones between 5 and 10.

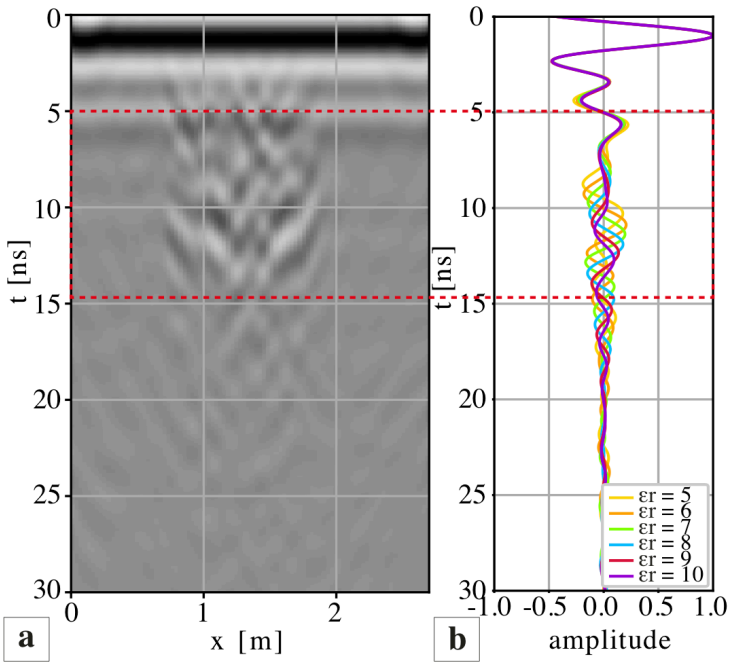

Fig. I.5.5: Modeled GPR profile of the cooking pit (fig. I.5.4) by using a relative permittivity of the stones of ϵ_r=5 (a) together with the trace comparison of the mid traces of the GPR profiles resulting by assuming a relative permittivity of ϵ_r=5, 6, 7, 8, 9 and 10.

I.5.2.6 Potential for Classification using Signal Strength

I.5.2.6.1 GPR

The modelling study on the basis of the shown models for MdB-FeO, MdB-IB, MdB-U, BH-U and BH-CP with average values for porosity and permittivity of the soil matrix (fig. I.4.28) shows that the relative amplitudes for the urn graves and stony features are similar for all three depths, at about 0.36±0.16 for urn graves and 0.37±0.21 for stony features (cooking pits, stone packages, stone concentrations (man-made or geological)). For the iron oxide concretion, they were twice as large as for the stony features before, at about 0.7±0.12. It was found that at least the iron oxide concretions can be differentiated from the archaeological features by the GPR amplitude. Stony geological features cannot be differentiated from the archaeological ones at the same depth range by GPR signal strength alone and, as was found, it is also not possible to differentiate them with magnetics.

Nevertheless, in order to test these findings, it would be a worthwhile future project to develop a recognition tool at least for urn graves, cooking pits and burials. As was mentioned in the introduction, there are already some approaches for anomaly detection in GPR by using neuronal networks (Green & Cheetham 2019 or Küçükdemirci & Sarris 2019). The additional information that were established regarding signal strength would probably be a useful contribution to such a project.

I.5.2.6.2 Magnetics

Regarding the classification of magnetic amplitudes, no clear result was found. Due to the nature of the stones that were carried from northern Europe to northern Germany, they are differently magnetized, since magmatic and metamorphic as well as sedimentary stones are mixed, whereas sedimentary stones are underrepresented (Smed & Ehlers 2002). For both sites susceptibility values between 100*1e-5 [SI] and 20,000*1e-5 [SI] were found (see section I.4.2). The found susceptibility values of the stones reflect the heterogeneity of the occurrence of stones, highlighting the difficult situation we have to deal with in glacial soils. This is a problematic fact, since a modelling with such a fairly high susceptibility range will always give a plausible result. Another insight is that we cannot use magnetic amplitude for classification, because the amplitude range of the cooking pits is also quite high, ranging from 2 to more than 500 nT. For other sites, the range may be even larger.

That the anomalies of the cooking pits show such a wide range may have several reasons. First, they differ in terms of size, degree of use and number of stones. It is probably worth attempting a classification in terms of size and signal strength. For this one need more excavations and a comparison with the signal strength. To discuss this, in addition to the excavation, the number and type of stones per pit must be determined, and probably their use too. But no such analysis has hitherto been conducted.

I.6 Conclusion

To improve the interpretability of geophysical data in glacial environments, a classification of GPR signal strength for stony features, such as stone concentrations of different kinds, iron oxide concretions and urns, was developed. Furthermore, a threshold for the detection with magnetics and GPR was worked out depending on the size and depth of Bronze Age features. Additionally, the potential for an improved interpretation of geophysical data was evaluated by comparing magnetics with GPR. All this was supported by soil analysis, which was used first to assess the soil conditions for GPR by extracting the permittivity of the soil matrix and estimating the porosity and water content and second to assess the degree of magnetization of the soils and human activity by using susceptibility and frequency-dependent susceptibility. Furthermore, our investigations with GPR and magnetics were accompanied by many modelling studies. Numerical modelling of GPR was used to determine porosity, water content, permittivity contrasts and reflection coefficients. Magnetic modelling was used to estimate the susceptibility of stones, in order to clarify the complexity of boulder stone distribution in glacial soils.

In summary, may draw the following conclusions: With regard to our first set of questions – Will the detection rate for archaeological features be improved if the analysis of GPR data is combined with magnetics data? And will the detection rate be improved if the information about the signal strength is also taken into account? – it was found that

1. By looking on the GPR amplitudes, those of iron oxide concretions are twice as large as those of stony features.

2. The signal strength of stony features is similar. A differentiation between cooking pits, burials and urns, and geological stone accumulations is not possible. This means that it is generally not possible to distinguish between stony archaeological and stony geological features.

3. The combination of GPR and magnetics is helpful to identify cooking pits and burials. This information can be combined with signal strength to develop a pattern recognition tool with additional information about signal strength.

4. This combination also helps to distinguish between stony archaeological features and iron oxide concretions and between stony archaeological features and stony geological features in the same depth range. Naturally occurring features are not magnetized and therefore not recognizable with magnetics.

5. The combination is particularly helpful in identifying iron oxide concretions.

6. Due to the heterogeneous nature of glacial soils, the combination of magnetics and GPR is not helpful in identifying urn graves. A further study may be required to classify the urns themselves, due to their complex structure (stone, pottery and filling of different kinds). This may contribute to the development of a pattern recognition tool for detecting urns.

7. The identification of pits is difficult. The conditions, under which a detection with GPR is possible will be discussed in the next part of the thesis.

8. Regarding stony features, it was found that the signal strength of the magnetic data covers a wide range, reflecting the heterogeneity of glacial soils and the difficulty of detecting archaeological features in these soils.

Considering the second set of questions – Why are there archaeological features that are recognized and others that are not? Is it possible to make predictions regarding the recognition rate based on soil conditions? – the following conclusions can be drawn:

Considering GPR:

1. A strong influence of water content and porosity was found. The influence of water content on permittivity is larger than that of porosity.

2. Information about the permittivity of the soil matrix alone is not sufficient, providing signals with amplitudes smaller than those measured.

3. The soil analyses must at least provide information as to water content directly. Then predictions are indeed possible.

4. It was found that some stony features could be recognized and others not. It was found, that detection is difficult if the permittivity contrast between soil and stone is too small. This also reflects the difficulty of analysing GPR data in a glacial environment.

Considering magnetics:

1. Knowing the susceptibility of each object and soil enables archaeological features to be predicted.

2. Furthermore, the analysis of the frequency-dependent susceptibility allows statements to made on the magnetic heterogeneity of the soil, which enables predictions on the quality of the magnetic data and of the potential for the detection of archaeological features in general.

Finally, the following procedure can be recommended to increase the hit rate:
Before a GPR measurement, soil samples must be taken and analyzed in order to be able to assess the geophysical result. Sensible sampling points for soil samples must be located on the basis of the magnetic measurements. Soil parameters that have to be determined are: Soil composition, porosity (see Danielson &

Sutherland 1986) and water content (see Gardner 1986) to get a realistic estimation of the relative permittivity. A good estimate of relative permittivity eliminates the need for a detailed modelling study, but it can verify the measurement results along with matching the archaeological documentation. Once the amplitude strengths from the radar are known, a pattern search in the time slices can be started.

The frequency dependent susceptibility provide an impression of the magnetic heterogeneity. For the interpretation of the magnetic data, it is better to set different amplitude ranks to address specific archaeological features. For example, cooking pits mostly show amplitudes in the range of 2 to >500 nT. Body burials bedded on a stone pack also show conspicuous magnetic amplitudes in the range of -2 to 12 nT, so that one can set the range to about -5 to 20 nT. Bronze Age urns do not show noticeable magnetic amplitudes in contrast to the glacial soils.

To better detect Bronze Age stony features in a glacial environment with GPR, the soil should have a soil moisture content of at least 30%. It is best to take measurements in the fall or (warmer) spring (April-June).

When evaluating GPR, the archaeologically relevant depth of max. 1 m must be taken into account to avoid misinterpretation of geological structures. Iron oxide concretions have to be matched with the magnetic signature to identify them as such in the radar. Cooking pits have a prominent signature in the magnetic map and should be identified from this and verified in the GPR data (time slice and profile). In order to detect urns more reliably, it should be investigated why they are rarely detected in the magnetics. Their extent is too small to be detected at the first sight in a large GPR area. Pits should be identified primarily in the GPR data. For this to succeed, the moisture of the pit filling should be different from the surrounding, e.g. by a higher content of organic matter. However, this does not depend on the evaluator, but on the type of pit.

The next part of this thesis focusses on the investigation of pits to understand the composition of the pit filling. From this part we can use the following results and knowledge:

1. A mean porosity of about 41 % and a mean water content of about 24% of the site BH
2. A mean porosity of about 44 % and a mean water content of about 30% of the site MdB
3. The combined investigation of soil analysis, GPR and magnetic data and modelling to derive porosity and water content from the permittvity.

Part II

On the Detectability of Pits in Glacial Soils – A Modelling Study of Bronze Age Pits located at the Site Bornhöved, Germany

II.1 Introduction

Burial mounds bear witness to a burial culture that began in the Neolithic period in northern Europe and peaked in the Bronze Age (e.g. Schaefer-Di Maida 2019, Hingst 1976, Hingst 1979, Holst et al. 2001). Many burial mounds were situated in topographical dominant positions (e.g. Schaefer-Di Maida 2019). From an archaeological perspective, information about the lifestyle of Bronze Age people is hard to obtain, since little is known about Bronze Age settlements. This is because Bronze Age settlements were built on flatlands while burial mounds were erected on local hilltops. Since burial mounds are often located close to settlement sites, they indicated an increased probability of finding settlement remains in the surrounding plains. Accordingly, not only the burial mound LA 117, but also its closer surroundings were investigated as part of the CRC 1266 "Scales of Transformation" in the subprojects D3 (archaeological subproject) and G2 (geophysical subproject).

This part of the thesis focuses on the most important structures for the burial mound LA 117 of the site Bornhöved (BH), namely the ditch surrounding the burial mound and the burial pit. Both are pit-like features. The identification of pits in the GPR data is mostly difficult and depends on various factors, such as soil characteristics, i.e. soil type, porosity and water content, but also the nature of the pit filling, with loose material or heterogeneous material consisting of pottery, burnt clay or other material of non-natural origin. In previous studies, pit-like structures are mostly explored magnetically, such as in Neubauer, Melichar, et al. (1996), Neubauer & Eder-Hinterleitner (1997) and Eder-Hinterleitner et al. (1999). Thereby settlement pits play an important role, because through them one gets an impression about the way of life of the people at that time. Studies that deal with the investigation of settlement pits are e.g. Chapman et al. (2014) and Nowaczinski et al. (2015). In this part, however, the exploration with GPR shall be in the foreground, because it ist important to understand under which conditions pits are recognised in the radar. The question to be answered in this part is, which soil properties pits must have to be detected in the geophysical data.

To answer the question, again soil analyses are essential. A modelling study is started. For this a starting model will be created based on the resulting mean porosity and mean water content of the first part of this thesis. In a second step this starting model will be refined by considering the sand content. Objects of the modelling study will be, one profile crossing the ditch and the east profile of the burial in the centre of the barrow. Both features are archaeological seen important features to understand the burial mound and to get an impression of its chronological classification. Furthermore, the ditch is the basis for trying to understand the phases of use of the burial mound as well as to estimate the former height in the following part III of this thesis.

In this part of the thesis, the geophysical data are merged and presented with the archaeological documentation and soil sampling results. The focus is on the site BH with the burial mound called LA 117, a Late Neolithic burial mound with three archaeologically documented phases of usage, an enclosing ditch and posts. Since part I mainly considered archaeological features with a high stone content, the focus in this part is exclusively on pit-like features, such as the central burial or the ditch. In the first part of the thesis, we found the soil of the site BH to be so low in contrast, that the interpretation of the GPR data is difficult. This was mainly the reason why pits, postholes or ditches were excluded for the purposes of the amplitude classification approach (part I of this thesis).

First, the results of the archaeological investigation and the soil analyses are presented. Than the results of the geophysical data of the whole investigation area will be presented. Afterwards the geophysical data of the key features will be shown: the central burial and the ditch. Since the permittivity contrast of the site BH is so low, that it is difficult for many archaeological features to be detected by magnetics or GPR, a detailed modelling study will be started by using pit-like features. The modelling study is the basis for answering the question. In the discussion chapter the difficulty to model pit-like features will be discussed by conducting a sensibility analysis. Finally a conclusion will follow.

II.2 The Site of LA 117 - BH

II.2.1 Geographical Setting

The site BH is located at the Bornhöved chain of lakes in northern Germany (Bornhöveder See, Schmalensee, Belauer See, Schiersee, Stolper See), which was formed during the repeated glacial erosion processes. The subsoil of the site area is composed by glacier-accumulated substrate made up of sand, gravel and clay lenses covered by luvisol, cambisol and colluvisol soil layers (Dreibrodt & Wiethold 2015, Piotrowski 1991). The base of slopes is covered by colluvisols (Piotrowski 1991). Along the lakes, the soils are mainly characterized by gleys and peat. Today, the site area is used for agriculture (Schaefer-Di Maida 2019).

II.2.2 Archaeological Classification of the Site LA117 (BH)

Bronze Age burial mounds are mostly located at the edges of the moraines mapped by Krosigk in 1976 (Schaefer-Di Maida 2019, Krosigk 1976). They were often arranged in clusters of 3-30 mounds (Feeser et al. 2022). The burial mound known as LA 117 is located close to the group of burial mounds of Mang de Bargen, a sight which shows one of the highest concentrations of burial mounds (Schaefer-Di Maida 2019). The investigated barrow LA 117 belongs to a group of three mounds from the older Bronze Age (1750-1100 BC). It is located in the north of Bornhöved (fig. II.2.1a,b) and deposited on a local southwest-northeast-running elevation that was first used as a burial mound in the late Neolithic (Fig. II.2.1c). The south-eastern and eastern slopes of this elevation are steeper; those in the west and southwest more moderate. The ancient people used the natural elevation as a barrow, adding to its height artificially. The barrow's total preserved height (natural and artificial) is 0.7 m, of which the preserved part of the artificial height makes up about 0.1 m. Its diameter is about 12 to 13 m.

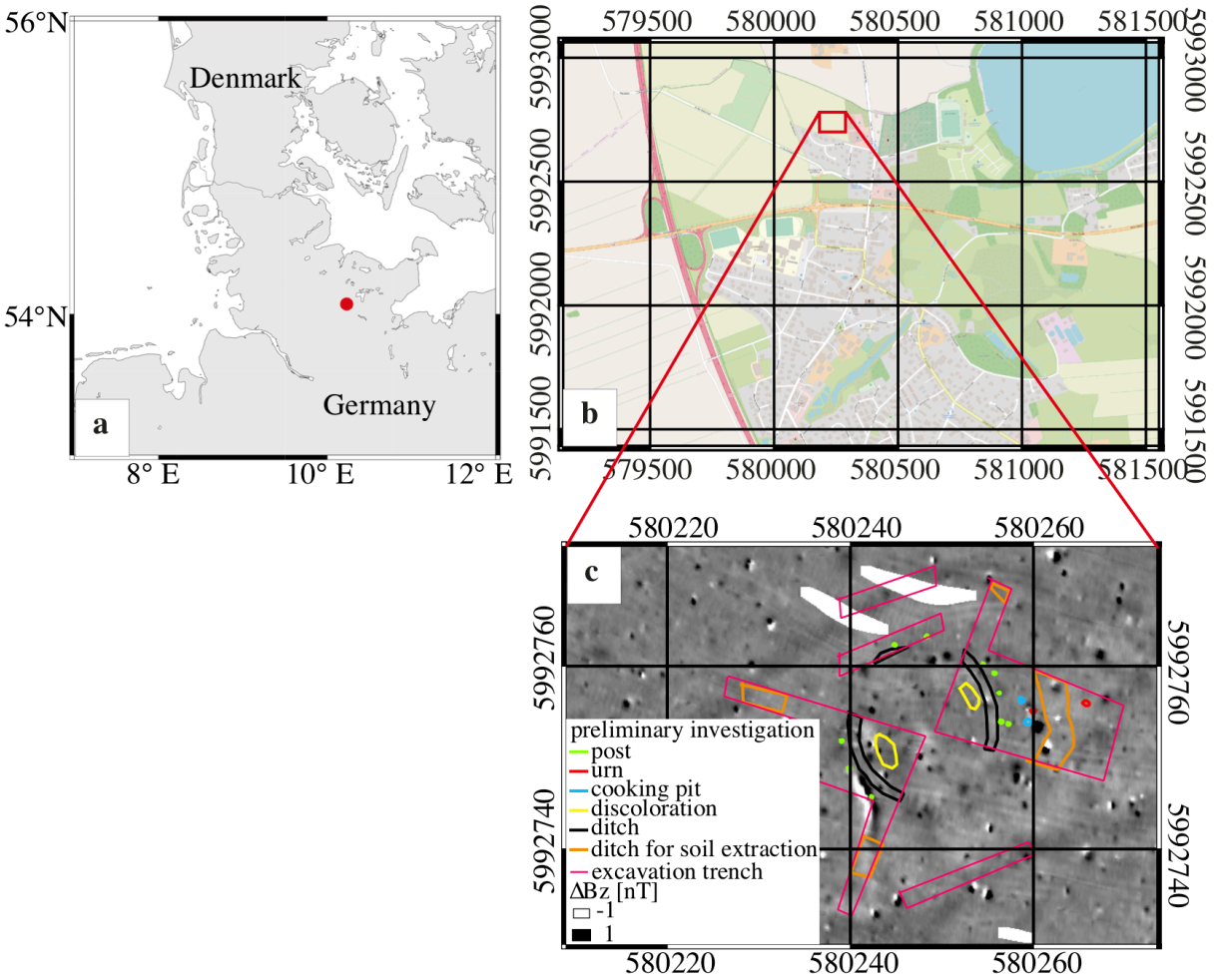

Fig. II.2.1: Location of Bornhöved (a) and LA 117 ((b), within the red rectangle) together with the position of the preliminary investigations of 2017 (c). The pink solid line shows the extent of the excavation trenches directly at the position of the burial mound (LA 117). The ditch (black solid line) surrounded by posts (green solid line) and at a distance of 4-7m also a ditch for the extraction of material (according to archaeological interpretation) to raise the barrow (orange solid line) was observed. In the east of the barrow two cooking pits (blue solid line) and two urns (red solid line) were found.

II.2.3 Current State of Research

There was a preliminary investigation in 2017 before excavation began in the following year. The aim was to identify archaeological structures directly beneath the topsoil and to evaluate the necessity of an excavation to document any remains of historical significance, since the field containing the barrow was to be given over to construction. The investigation of 2017 showed a ditch at the edge of the barrow (black solid line in Fig. II.2.1c) with posts surrounding the ditch (green solid line in Fig. II.2.1c). Within the ditch, two features showing different soil colour were found but not interpreted (yellow solid line in Fig. II.2.1c). In the west two urns (red solid line in Fig. II.2.1c) and two cooking pits (blue solid line in Fig. II.2.1c) were found. Also, at a distance of 4 to 7 m from the burial mound, a feature with a different soil colour was observed and interpreted as a ditch for soil extraction to raise the barrow (orange solid line in Fig. II.2.1c).

Prior to the excavation in 2018, which took place as part of the CRC 1266 “Scales of Transformation”, geophysical measurements (magnetic and GPR) were conducted to investigate the vicinity of the burial mound.

II.3 Methods

II.3.1 Ground Penetrating Radar (GPR)

II.3.1.1 Data Acquisition and Processing

In 2018, at BH, a 16-channel MALA Mira antenna was used (Guideline Geo AM (Publ) MALA & ABEM), which can collect a 3D data set due to its channel distance of 8 cm. An RTK-DGPS was used for positioning. The processing steps applied were:

(a) time zero shift,

(b) correction for spherical divergence and attenuation,

(c) subtraction of a mean trace to remove horizontal lines,

(d) band pass filtering and applying a gain function and

(e) topographic migration (Wilken et al. 2016)

To enhance reflections of the data set of 2018, a bandpass filter and a gain function were applied. Velocities for migration were determined by hyperbola fitting and test migrations. The final parameters can be found in table II.3.1.

Table II.3.1: Parameters for processing

processing steps	parameters
time zero shift	
correction for spherical divergence and attenuation	σ=0.9 mS/m; ϵ_r=14.1
bandpass filter	start frequency=100 MHz; end frequency = 700 MHz
gain	trace $*\sqrt{t}$
subtraction of a mean trace to remove horizontal lines	
topographic migration	v=0.08 m/ns

II.3.1.2 Modelling

To get a better understanding of the signals' origin and to verify the measurements, GPR data was modeled. For GPR modelling, the Matlab-based program by Irving & Knight (2006) was used. This is a finite difference time-domain modelling of GPR data in 2D. For avoiding edge effects, they implemented absorbing boundaries, and the second derivative of a gaussian pulse was used as the source pulse (Warren & Giannopoulos 2012).

On the basis of the soil analyses of BH an estimation of the permittivity can be reached using the soil composition by using Birchak's equation (1974) for a three-phase system. The content of sand, clay and silt was determined by the soil analysis and used to determine the permittivity of the soil matrix by using the following equation:

$$\epsilon_{soilmatrix} = (C * \sqrt{\epsilon_C} + U * \sqrt{\epsilon_U} + S * \sqrt{\epsilon_S})^2 \tag{II.3.1}$$

Since the soil consists of the soil matrix, porosity (ϕ) and water content (θ), there is another three-phase system of relevance, defined as follows

$$\epsilon_{soil} = (\theta * \sqrt{\epsilon_w} + (\theta - \phi) * \sqrt{\epsilon_{air}} + (1 - \phi) * \sqrt{\epsilon_{soilmatrix}})^2 \tag{II.3.2}$$

The values of porosity and water content for BH are provided by the results of part I. This is $\phi = 41\%$ for porosity and $\theta = 24\%$ for water content.

II.3.2 Magnetics

II.3.2.1 Data Acquisition and Processing

The magnetic measurements were conducted with a device by Sensys with 12 fluxgate gradiometers (0.25 m horizontal probe spacing). All measurement devices were equipped with an RTK-DGPS positioning system. The data were processed by subtracting a mean value over each profile and interpolation onto a 0.2 x 0.2 m grid.

For magnetic modelling, also the susceptibility was measured in situ inside of archaeological features. Soil samples were taken for analysis in the laboratory. Magnetic susceptibility was measured on 10 ml material using a Bartington MS2B susceptibility meter (resolution 2*10-6 [SI], measuring range 1-9999*10-5 [SI], systematic error 10%). Measurements were carried out at both low (0.465 kHz) and high (4.65 kHz) frequency. Three sub-samples were measured in each case to allow both average and standard deviations to be determined.

II.3.2.2 Modelling

For magnetic modelling Fatiando a Terra (Uieda et al. 2013) was used and was introduced in section I.3.3.2 of part I of this thesis. First, the object (e.g. geometry and susceptibility) is determined, then the grid in

which the vertical component of the magnetic induction will be calculated is defined (Uieda 2010-2016). For modelling the declination was set to D = 3°, the inclination to I = 69° and magnetic field strength to B = 49800 nT. The total magnetization is the sum of induced and remanent magnetization. Remanent (M_R) and induced (M_I) magnetization are related by the Koenigsberger ratio (Q) (Koenigsberger 1930; Koenigsberger 1934; Koenigsberger 1936).

$$Q = \frac{M_R}{M_I} \tag{II.3.3}$$

Several studies have shown that the Koenigsberger ratio Q strongly depends on how strongly the material has been heated (e.g. Schnepp et al. 2004, Hanson et al. 2015, Pickartz, Rabbel, et al. 2020). For strongly heated archaeological features such as ovens or pottery kilns, the values vary between 0.1 and larger than 100 (Schnepp et al. 2004). For partly or not heated soils, the values are lower with 0.1 to 10 (Pickartz, Rabbel, et al. 2020). There are also studies that have dealt with the Koenigsberger ratio Q in connection with sediments without human influence (Hanson et al. 2015). In the study of Hanson et al. (2015) the Koenigsberger ratio Q was investigated for lake sediments. They found the values for silt and sand vary between 0.2 and 4. Table II.3.2 provides a compilation of the values for the Koenigsberger ratio and the associated literature references. For the present thesis, the value for the Königsberger ratio Q was selected with the help of the literature in comparison to the modeling result of an intensively analysed archaeological feature, which is presented in chapter II.4.4.1 of this part of the thesis. A Koenigsberger ratio of $Q = 5$ was used for magnetic forward calculation.

Table II.3.2: Literature values of the Koenigsberger ratio

Material	Q	Reference
bread oven, burnt clay floor, fire places, pottery kilns, hearth, open fire place and others	0.1 – >100	Schnepp et al. 2004
partly or not heated soils and sediments with loess as parent material	0.1 – 10	Pickartz, Rabbel, et al. 2020
glacial Lake Missoula lacustrine and flood sediments	0.2 – 4	Hanson et al. 2015

The magnetic field gradient was modeled in 3D by assuming the upper sensor at a height of 1 m and the lower one at a height of 0.35 m. Depending on the measurement device used, grid spacing was set at 0.25 m or 0.5 m. The parameters regarding extension and depth were drawn from the archaeological documentation. The susceptibility values of the soils were taken from in situ susceptibility measurements.

II.3.3 Soil Analysis

Soil analysis was conducted to obtain information about soil composition, content of organic matter, magnetic susceptibility and frequency-dependent susceptibility. Organic matter is related to soil moisture (Gustavsen et al. 2018). Magnetic susceptibility is a material-dependent parameter and describes how magnetizable the material is in an external applied magnetic field (Blakely 1996). The frequency-dependent susceptibility of a material reflects the size of its magnetic components. For further explanations see section I.3.1 of the first part of this thesis.

Two archaeological profiles were selected for geoarchaeological analyses: one crossing the ditch in the north, the other one crossing it in the east. The samples were taken vertically, following the chronostratigraphic order identified in the field. The profile as well as the sampling positions were documented in scaled drawings and digital photographs. In addition, the position of the samples was documented with the help of a total station. In the laboratory, the samples were dried for two weeks at 35°C. The preparation for further measurements included their careful disintegration with a mortar and pestle and the extraction of the < 2 mm fraction via dry sieving. The grain size distribution of the samples was carried out by a combination of wet sieving and sedimentation in Atterberg-cylinders after removal of organic matter and carbonates (Roderick 1972).

II.3.4 Archaeological Documentation

Kneisel excavated LA 117 in 2019 (in prep.). This excavation was conducted in cooperation with the Schleswig-Holstein conservation authorities and as part of the CRC 1266 "Scales of Transformation". First the top soil was removed by an excavator and the barrows divided into four quadrants. Afterwards the quadrants were dug up using the planum method and documented by photography, photogrammetry and drawings (1:50). Features were excavated in profiles and documented by photography and drawings (1:10 or 1:20).

The results of the magnetic and GPR data will be compared with archaeological documentation. For modelling, the magnetic data, the archaeological drawings or the geometry of the documented archaeological features were used.

Furthermore, the archaeological documentation of the ditch was the basis for determining the angle of the ditch walls of each ditch phase.

II.4 Results of the Comparison of the Archaeological Documentation with GPR and Magnetics

II.4.1 Results of the Archaeological Excavation

The barrow was erected in the late Neolithic and used until the end of the older Bronze Age. A common feature of Bronze Age barrows is that they set the tree-coffin upon the surface and cover it with soil to form a barrow (Kneisel, Schaefer-Di Maida, et al. (in prep.)). In contrast to that, the late Neolithic ritual still consisted of grave pits dug deep into the ground. Additionally, it was common that after each phase, a secondary burial was covered up with soil, thereby raising the mound (Schaefer-Di Maida 2019, Lütjens 2013a, Lütjens 2013b, Lütjens 2013c, Lütjens 2013d, Lütjens 2013e).

Archaeologically, this barrow is unusual due to its ditch structure and a henge of 16 posts. The central burial is a deep pit of 1.2 m with an inhumation with a few stones at the northern end. The continuous use of the burial mound can be followed stratigraphically, in particular in the ditch's reopening process (see fig. II.4.1). The ditch measures 17 m in diameter, 2–2.5 m in width and is about 1.2 m deep. It was reopened in three phases (fig. II.4.1b,c&e). The barrow has a diameter of about 12 to 13m. The C-14 (radiocarbon) dates prove the inhumation to be the oldest feature, dating back to the late Neolithic (fig. II.4.1a). In Neolithic times it was typical to dig a pit for the burial. Afterwards the burial mound was raised and a ditch was dug, first in a U-shape and then in a V-shape (fig. II.4.1b). The excavation showed eroded material of the barrow to fill in the ditch. In phase 2 the ditch was reopened, now with a sharper shape (fig. II.4.1c). Many archaeological profiles show a thin iron oxide layer at its basis indicating the boundary between phase 2 and phase 3. Phase 2 ended with a partly naturally refilling on top of which burning oak planks were deposited (fig. II.4.1d,e). This is dated to the beginning of the older Bronze Age (the earliest to the mid-17th century BC). The ditch of the last phase was flat (fig. II.4.1e) and at the end of this phase covered by a dense pack of cobblestones (fig. II.4.1f). The wood henge surrounding the ditch can be dated to the end of the older Bronze Age (fig. II.4.1g; 14-12th century BC). From the 11th to 6th century BC, the barrow was reused by burying urns at its edge (fig. II.4.1h). In medieval and modern times the mound was eroded by agricultural activities, causing the urns to be covered by an approx. 0.7 m colluvial layer (fig. II.4.1i) (Kneisel, Schaefer-Di Maida, et al. (in prep.)).

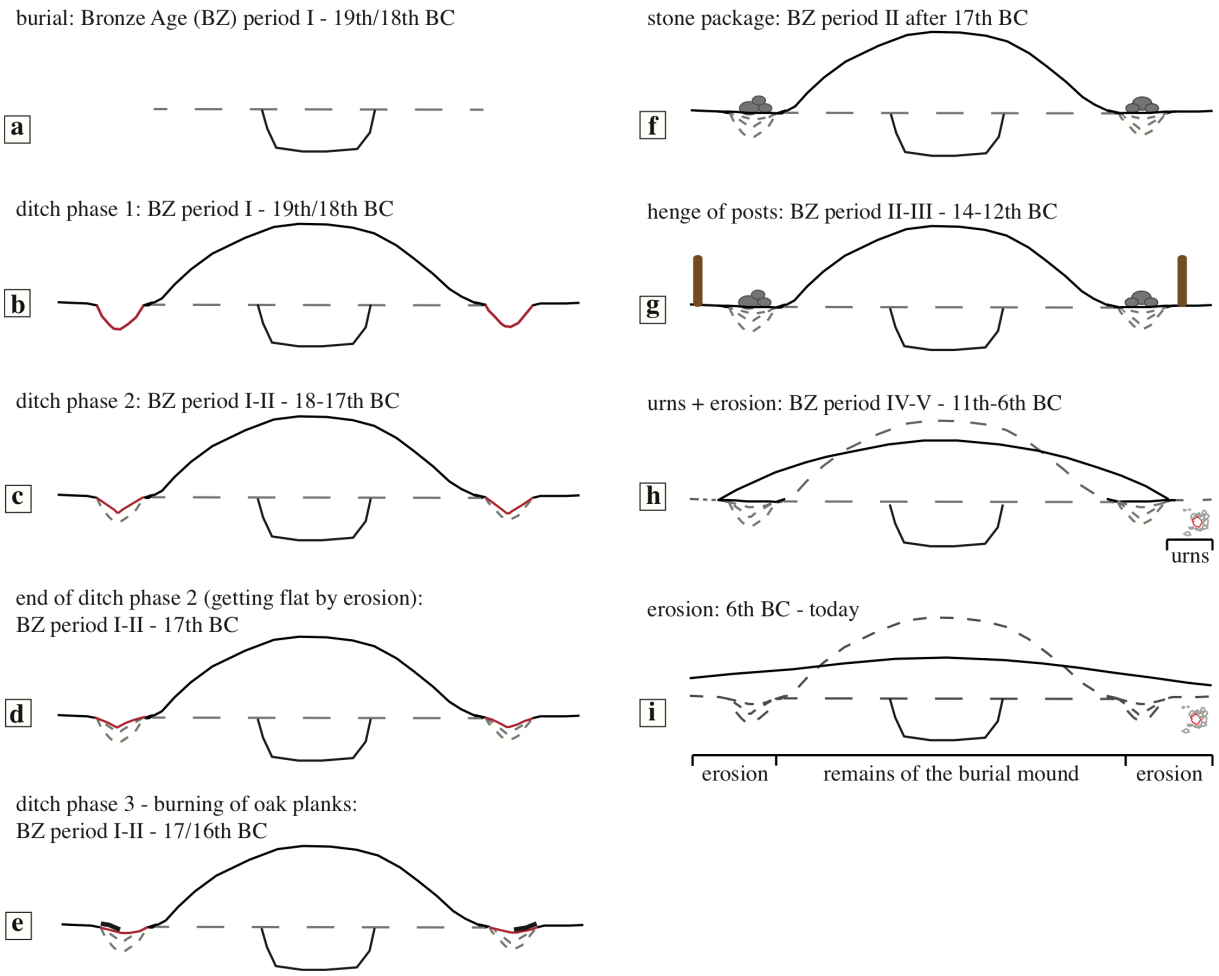

Fig. II.4.1: Scheme of the development of the burial mound on the basis of the archaeological observations. Dimensions do not correspond to reality.

II.4.2 Results of the Soil Analyses - Soil Composition, Permittivity and Susceptibility

The results of the soil analysis were used to explain the appearance of the ditch in the geophysical data. Since the ditch shows three phases of usage, the soil was evaluated with respect to these phases. The same samples have already been discussed, in more general terms, in part I, section I.4.1.1. Figure II.4.2 shows the position of the profiles, where the soil samples were taken from. In black dashed lines the archeological ditch profiles are shown. The two profiles shown as green dashed lines are presented and discussed in this part of the thesis. The pink stars represent the position of the soil samples, which will be discussed here.

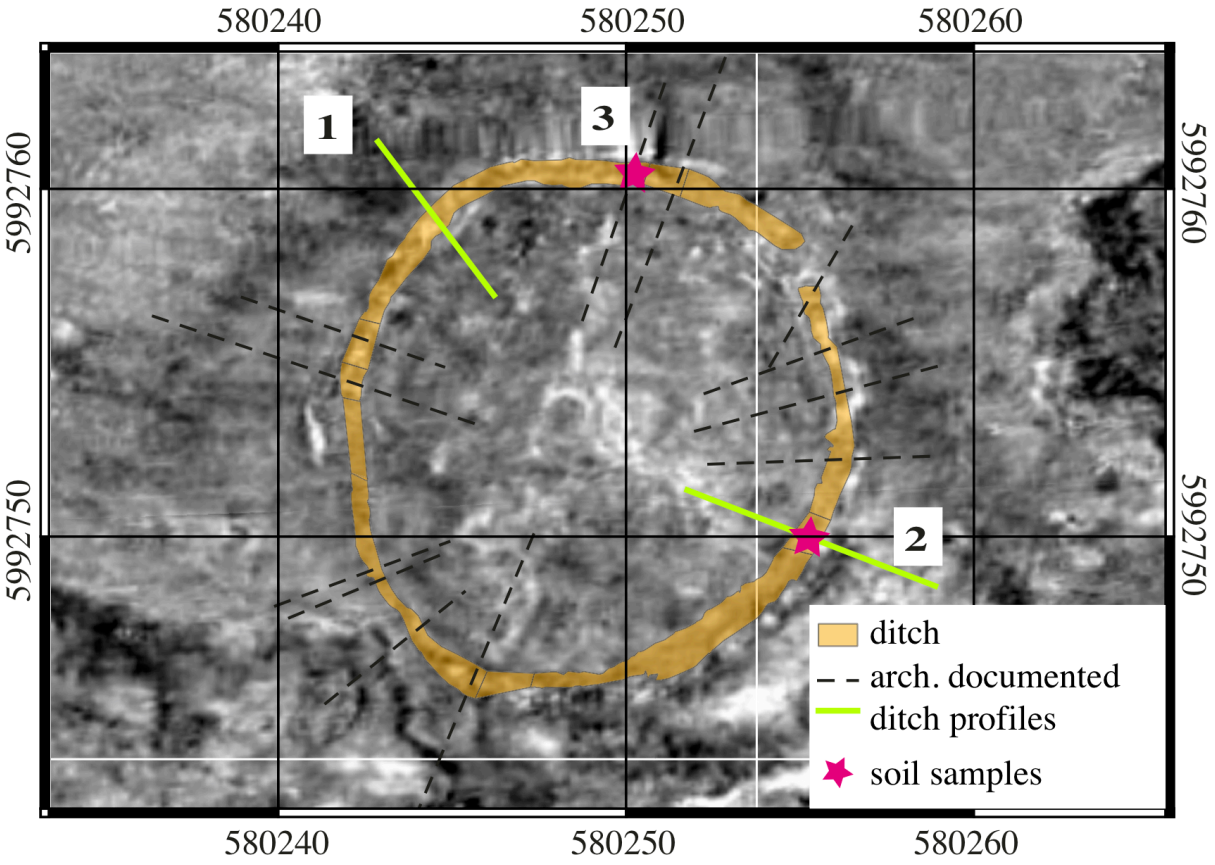

Fig. II.4.2: GPR time slice at about 0.54 m with the archaeologically documented bottom of the ditch. The black dashed lines and green solid lines present the profiles, that were documented by the archaeologists. The two green profiles will be discussed in the following sections. The pink stars represent the position of the soil samples.

Figures II.4.3 and II.4.4 show soil composition, calculated relative permittivity based on soil composition, volumetric susceptibility, loss on ignition and frequency-dependent susceptibility. The tables II.4.1 to II.4.6 break down the results by ditch phase.

Tables II.4.1 and II.4.2 show that the sand content is highest in ditch phase 3 in both profiles (3 and 2; see fig. II.4.2) at about 65%. The humus layer shows the highest clay content in both profiles at about 8%. The ditch phases 2 and 1 show a relatively high silt content ranging from 35 to 40%. Concerning the clay content, it can be seen that in profile 2 the clay content is about 1% higher in the humus layer and ditch phases 1 and 2 than in profile 3.

The calculated relative permittivity on the basis of the soil matrix (means dried soil sample) shows similar values for the humus layer and phase 3 (tab. II.4.3). The permittivity of profile 3 increases with depth from ditch phase 3 to 1, whereas in profile 2 one can observe a slight decrease of permittivity from ditch phase 2 to 1. Nevertheless, the permittivity values of the humus layer and ditch phases 3 and 2 are similar in both profiles.

The analysis of the volumetric susceptibility shows (tables II.4.4 and II.4.5) that phases 2 and 3 have the lowest volumetric susceptibility in both profiles. In profile 3, the susceptibility of phase 3 is smaller than that of phase 2. In profile 2, the susceptibility of phase 2 and 3 is more or less the same.

Frequency-dependent susceptibility decrease with depth (see tables II.4.4 and II.4.5). It is clear that phase 3 shows similar values than the lower ditch phases. Bearing in mind our theoretical knowledge, this means that human activity is highest in phase 3 and the humus layer as well.

Loss on ignition is an indicator of organic matter, from which one can derive a qualitative statement about the soil moisture. Table II.4.6 shows a decreasing content of organic matter (and therefore also moisture) with depth. In profile 2 the soils of phase 1 and 3 show a similar content of organic matter. The content of organic matter of the soil of phase 2 is a bit higher than in the soils of phase 1 and 3.

Table II.4.1: Results of the determined content of clay, silt and sand in the soil sample of profile 3

phase	clay [%]	silt [%]	sand [%]
humus layer	8	32	60
ditch phase 3	6	30	64
ditch phase 2	6	37	58
ditch phase 1	6	40	53

Table II.4.2: Results of the determined content of clay, silt and sand in the soil sample of profile 2

phase	clay [%]	silt [%]	sand [%]
humus layer	8	31	61
ditch phase 3	6	29	66
ditch phase 2	7	35	57
ditch phase 1	7	34	59

Table II.4.3: Permittivity detemined from the soil composition of profiles 3 and 2

phase	ϵ_r profile 3	ϵ_r profile 2
humus layer	7.3	7.2
ditch phase 3	7.1	7.1
ditch phase 2	7.8	7.8
ditch phase 1	8.3	7.4

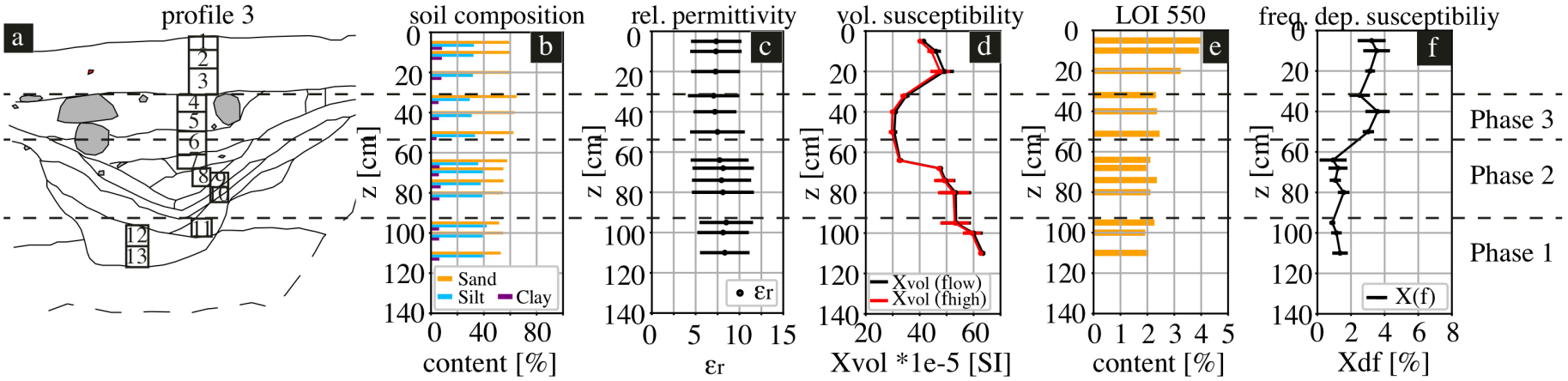

Fig. II.4.3: Comparison of the archaeological documentation of the ditch of profile 3 (a) together with the results of the soil analysis. b) shows the soil composition and c) the relative permittivity ϵ_r, d) the volumetric susceptibility, e) loss on ignition and f) the frequency dependent susceptibility. The black dashed lines highlight the three opening or refilling phases of the ditch.

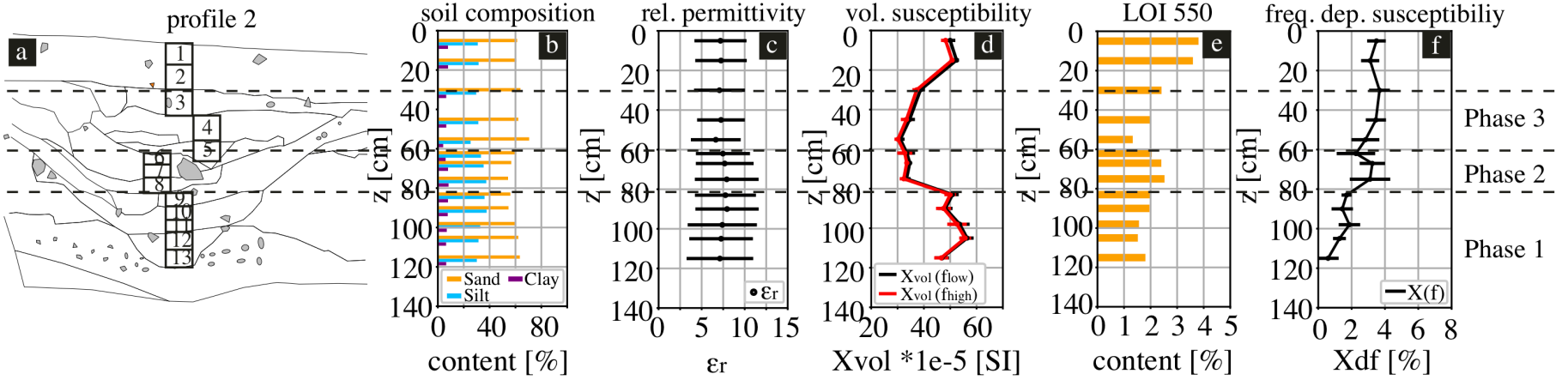

Fig. II.4.4: Comparison of the archaeological documentation of the ditch of profile 2 (a) together with the results of the soil analysis. b) shows the soil composition and c) the relative permittivity ϵ_r, d) the volumetric susceptibility, e) loss on ignition and f) the frequency dependent susceptibility. The black dashed lines highlight the three opening or refilling phases of the ditch.

Table II.4.4: Determined volumetric susceptibility measured with low and high susceptibility (f_{low} and f_{high}) and frequency dependent susceptibility in the soil sample of profile 3

phase	volumetric susceptibility [f_{low}]	standard deviation	volumetric susceptibility [f_{high}]	standard deviation	freq. dependent susceptibility	standard deviation
humus layer	45.5	2.1	44.0	2.0	3.3	0.6
ditch phase 3	33.0	0.7	32.1	0.9	3.0	0.7
ditch phase 2	40.2	1.6	39.6	1.7	1.6	0.5
ditch phase 1	57.6	3.8	56.9	3.8	1.2	0.3

Table II.4.5: Determined volumetric susceptibility measured with low and high susceptibility (f_{low} and f_{high}) and frequency dependent susceptibility in the soil sample of profile 2

phase	volumetric susceptibility [f_{low}]	standard deviation	volumetric susceptibility [f_{high}]	standard deviation	freq. dependent susceptibility	standard deviation
humus layer	51.2	1.5	49.5	1.2	3.3	0.6
ditch phase 3	34.8	1.6	33.6	1.7	3.3	0.7
ditch phase 2	33.8	1.6	32.9	1.6	2.9	1.0
ditch phase 1	51.2	2.8	50.5	2.7	1.4	0.5

Table II.4.6: Loss on ignition (loi) based on the soil material of profiles 3 and 2

phase	loi 550 (profile 2)	loi 550 (profile 4)
humus layer	4	4
ditch phase 3	3	2
ditch phase 2	2	2
ditch phase 1	2	2

II.4.3 Results of the Large-Scale Geophysical Measurements

Figure II.4.5 shows the comparison of the archaeological documentation and the results of the magnetic and GPR measurements. It is clear that only the 'big' structures are visible in the geophysical data, such as the ditch or the burial in the centre of the barrow (see table II.4.7). Two of the five urns were detected by GPR, none by magnetics. The documented cooking pits were detected by both geophysical methods. Urn graves and cooking pits were already presented in part I, where the focus is more on stony features. Here, in part II, pit-like features will be presented. In none of the surveyed areas were archaeological features discovered in the geophysical data alone that were not detected during excavation or were detected only at second glance. In part I of the thesis also the soil conditions of the site LA 117 were discussed and a found small permittivity contrast between the soil and the archaeological features. That is why only 14% of the archaeological features were detected by magnetics and 19% by GPR. The geophysical interpretation provided no further feature, that was not considered by the archaeologists. It is worth mentioning that only 4% of the archaeological features filled with soil (pits, burial pits, pits left by moved stones or post holes) were detected by magnetics and 7% by GPR. Therefore, the focus is on this type of feature in the following sections.

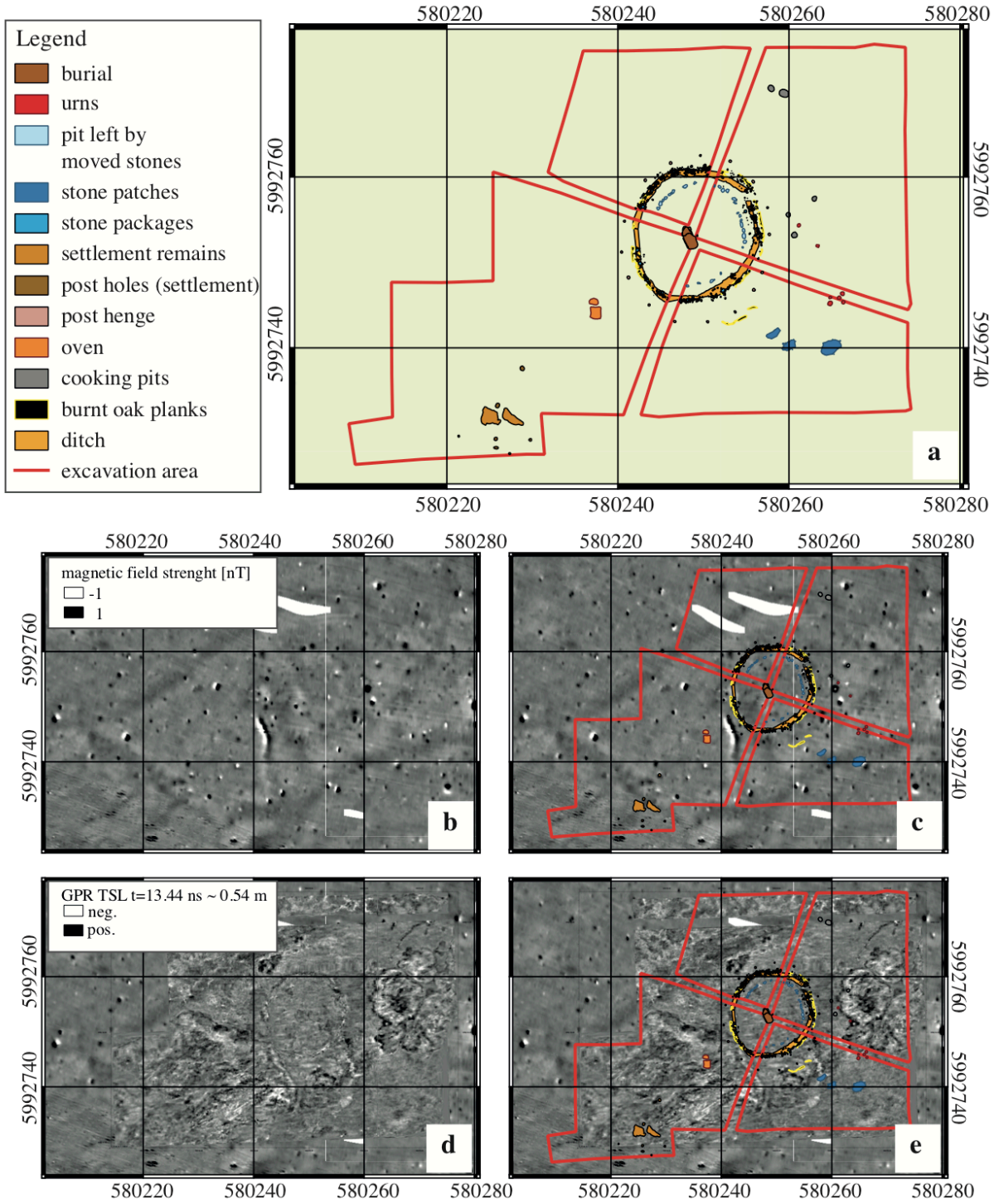

Fig. II.4.5: Result of the archaeological excavation (a) in comparison with magnetics (b) and (c) and GPR (d) and (e). In subfigures (d) and (e), the magnetic map is placed in the background behind the GPR data. In subfigures (c) and (e) display the excavation area.

Table II.4.7: Number of features and their detectability by magnetics and GPR

feature	total number	detected with GPR	detected with magnetics
urns	7	2	0
cooking pit	5	5	5
stone concentration	4	1	1
oven	1	1	1
burial	2	1	1
settlement pit	1	1	0
posthole	16	0	0
ditch	1	1	1
pit left by moved stones	26	0	0

The position of the barrow is detectable due to the weak positive anomaly in the magnetic map, including small spots showing strong positive amplitudes (see fig. II.4.6b [within the red dashed circles] and II.4.6c). The ditch surrounding the barrow appears as a weak negative anomaly, particularly in the eastern half (fig. II.4.6b,c – weak negative anomaly in the eastern half of the small red dashed circle). In the GPR time slices the ditch is visible as a thin circular structure (fig. II.4.6d-f, highlighted as a red dashed circular line), showing strong reflection energy in the first 0.4 m beneath the topsoil (fig. II.4.6d,e) and getting weaker in deeper parts (fig. II.4.6f). The burial in the centre is also visible as light negative magnetic anomaly (fig. II.4.6b,c). In the GPR time slice at about 0.4 m the burial shows low reflection energy (fig. II.4.6d).

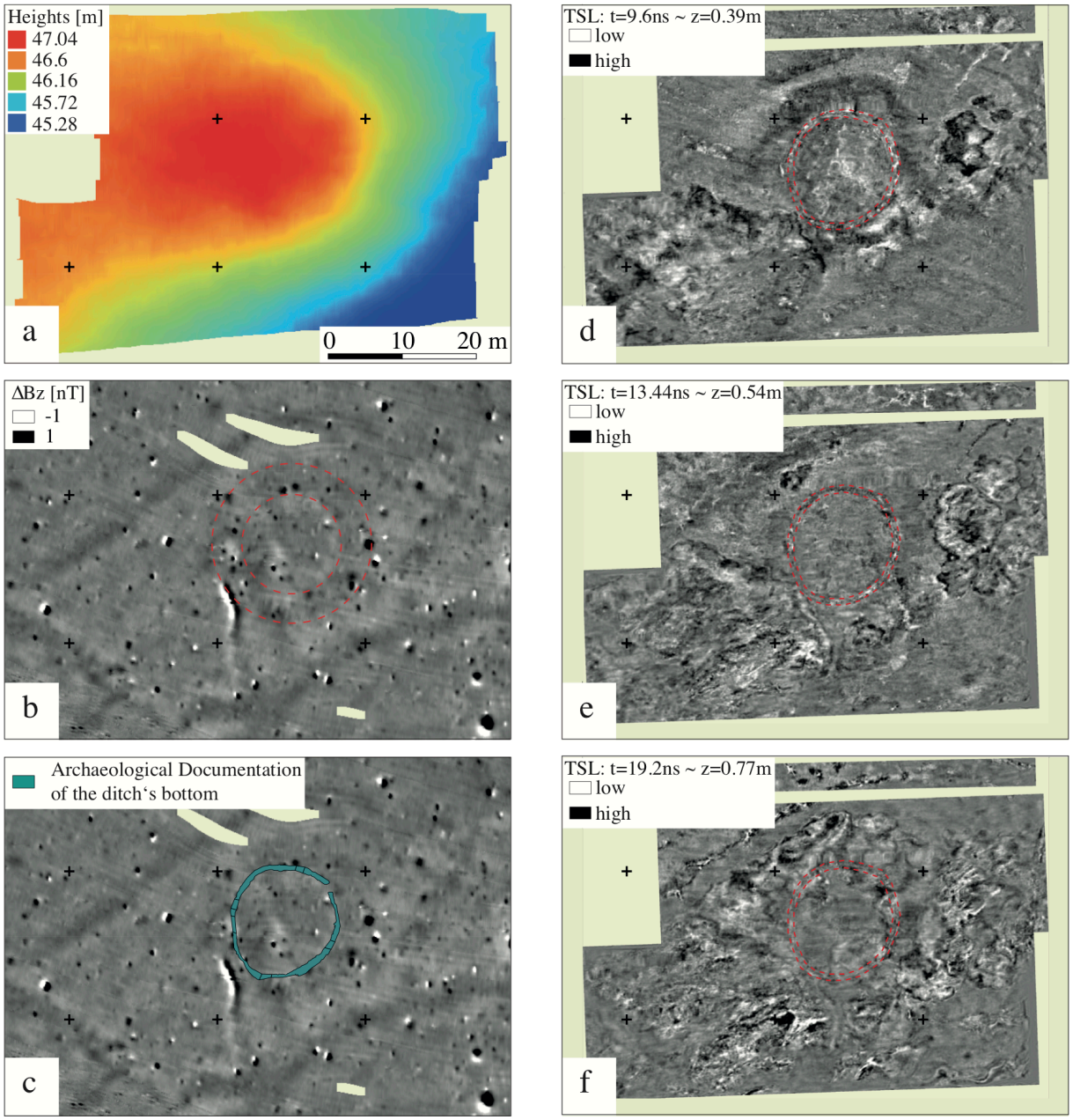

Fig. II.4.6: Local topography of the burial mound (a) together with the magnetic map in (b). Within the magnetic map the ditch is highlighted by two red dashed circles, which highlight an area with slight positive magnetic amplitudes. The archaeological documentation of the ditch's bottom is shown in (c) and three selected GPR time slices in about 0.39 m (d), 0.54 m (e) and 0.77 m (f) depth. The red dashed circles in (d-f) indicate the position of the ditch.

II.4.4 Appearance of the Pit-like Features in the Geophysical Data

II.4.4.1 Ditch – In General

In this section the results of the geophysical data of the ditch will be presented. Figure II.4.7 shows the appearance of the ditch in the magnetic map (a,c) and GPR time slice (b,d). In the magnetic map the ditch can be seen, particularly in the east, as a light negative anomaly. This is highlighted by yellow dashed lines

in figure II.4.7a. In the GPR time slices the ditch is visible up to a depth of about 1.3 m. In figure II.4.7d 14 lines are inserted, corresponding to the position of the archaeologically documented profiles. The two stars indicate the position of the soil samples. The soil samples help to understand the geophysical results. The geophysical data of profile 1 is discussed in the following section. This is also the example profile for the modelling of the ditch. Profile 2 is the basis for the magnetic considerations (for profile numbering see figure II.4.2).

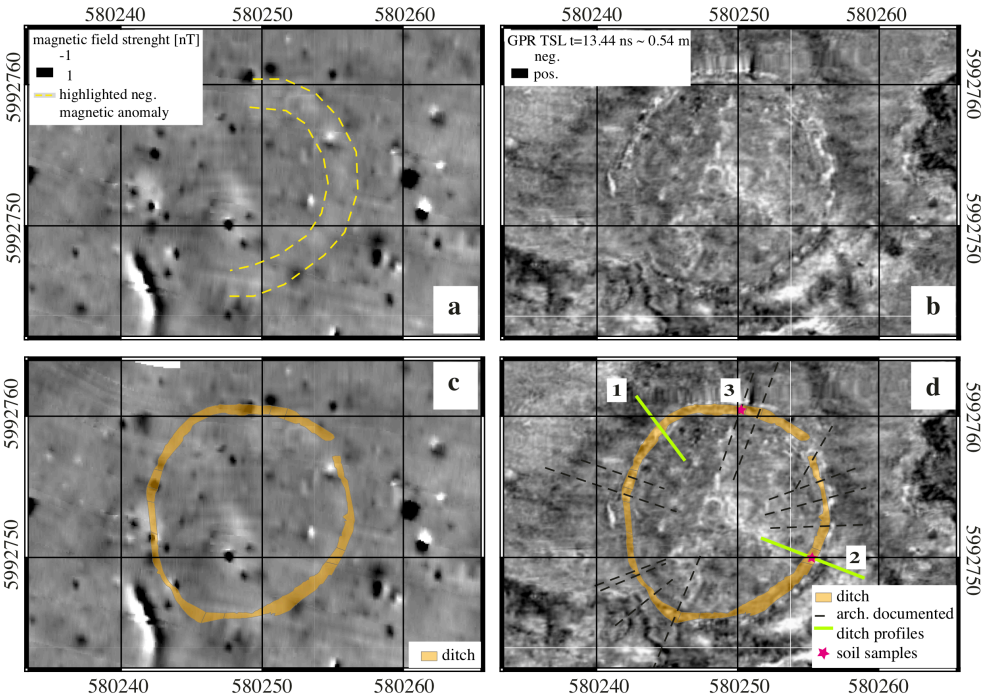

Fig. II.4.7: Comparison of magnetics (a,c) and GPR (b,d) together with the archaeological documentation (c,d). Green dashed lines mark the position of the archaeological profiles.

Figure II.4.8 shows the comparison of the archaeological documentation, the GPR and the magnetic profile of profile 2 in figure II.4.7d. The magnetic profile supports the first impression of a light negative anomaly in the magnetic map of fig. II.4.7a,c in the area of the ditch. In the GPR profile there are two distinct reflections between 2.5 and 3.5 m at depths of 0.5 and 0.7 m beneath the surface. The upper one shows strong reflection energy at the position where a charcoal-bearing layer was documented (brown solid line). The relative permittivity of charcoal is $\epsilon_r = 1.3$ (KG n.d.). This is smaller than the averaged soil permittivity of about $\epsilon_r = 12 - 16$, from which one would expect a negative reflection coefficient and therefore negative reflection amplitudes. The lower reflection is a negative one, not belonging to the strong positive reflection above. At this position a layer was documented, which is interpreted as an ancient humus horizon (yellow solid line). Due to the higher content of organic matter one can assume the soil to be wetter, resulting in a higher permittivity than the soil above.

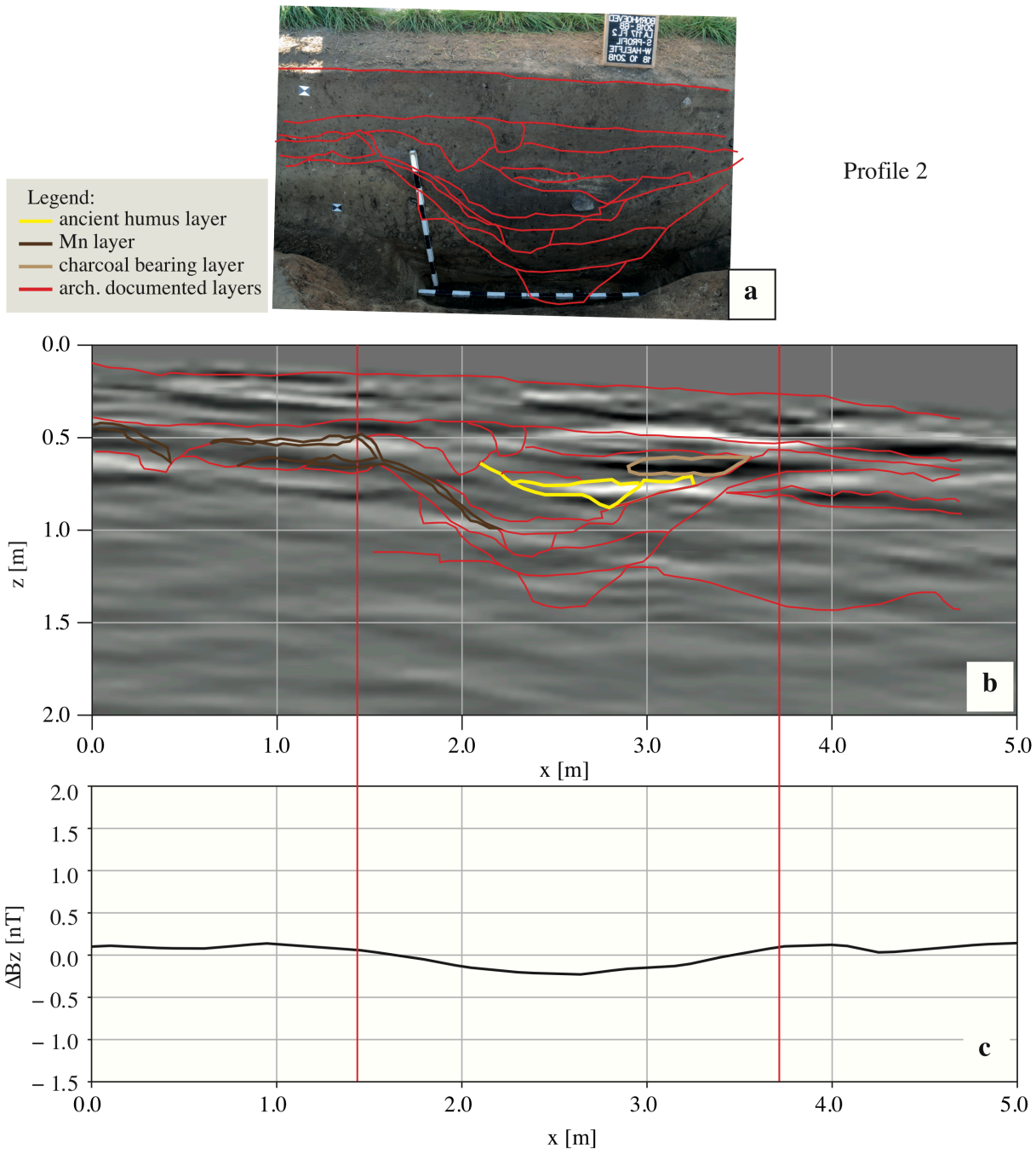

Fig. II.4.8: Comparison of the archaeological documentation in a photograph (by Kneisel, (a)) with the GPR (b) and magnetic (c) profile. Red dashed lines in the GPR profile represent the archaeological documentation, whereas the orange line highlights the iron oxide layers and yellow a distinctive negative reflection, representing the ancient humus layer. The red vertical lines mark the edges of the ditch.

II.4.4.2 Ditch Phases

During the evaluation of the GPR data, there was the problem of clearly identifying the edges of the ditch. Therefore, the GPR profiles were compared with the archaeological documentation. Phase 3 (last phase) often appears as negative amplitude together with a slight depression (fig. II.4.9a, d). The base of phase 3 can be

found at a depth of 0.5 m (beneath the surface). Phase 2 in comparison to phase 3 is more difficult to identify in the profile. In the example profile 'profile 1' (fig. II.4.9d), phase 2 appears as disturbance of the natural layers, particulary at its eastern edge. The western edge of the ditch is not clearly identifiable, since the natural layers seem to intrude into the ditch filling. This is also the case for the other profiles. The basis of phase 2 correlates with the transition of an area showing strong reflection energy to one with weak reflection energy at about 0.8 m depth (beneath the surface). But the shape of phase 2 cannot be identified clearly. In the time slices between 0.5 and 0.8 m (beneath the surface), the ditch boundaries are detectable, albeit weak (fig. II.4.9b). Phase 1, the oldest, cannot be identified in either the profile or the time slice (fig. II.4.9c,d). If one knows the ditch's position one can identify a weak circular structure in the time slice (fig. II.4.9c). But the contrast to the surrounding is not sufficiently pronounced to allow this phase to be identified in the profile. Also no further processing of the data could improve this image.

From the soil analysis, it is known that ditch phase 3 shows a higher sand content. In part I of this thesis it was found, that given a fixed water content, higher porosity leads to smaller permittivity values, causing low reflection energy. Due to a higher sand content of phase 3 one can assume a higher porosity in comparison to the humus layer. Table II.4.3 reveals lower permittivity, similar to that of the humus layer. Often the bottom of phase 2 is indicated by a negative amplitude, as is the case here in profile 1 (fig. II.4.9d). The soil samples of the two profiles (profile 2 and 3) are not unique in this case. Compared with phase 2, the relative permittivity values of phase 1 are smaller in profile 2 compared to profile 3. Low reflection energy is probably caused by a layer at the bottom of ditch phase 2.

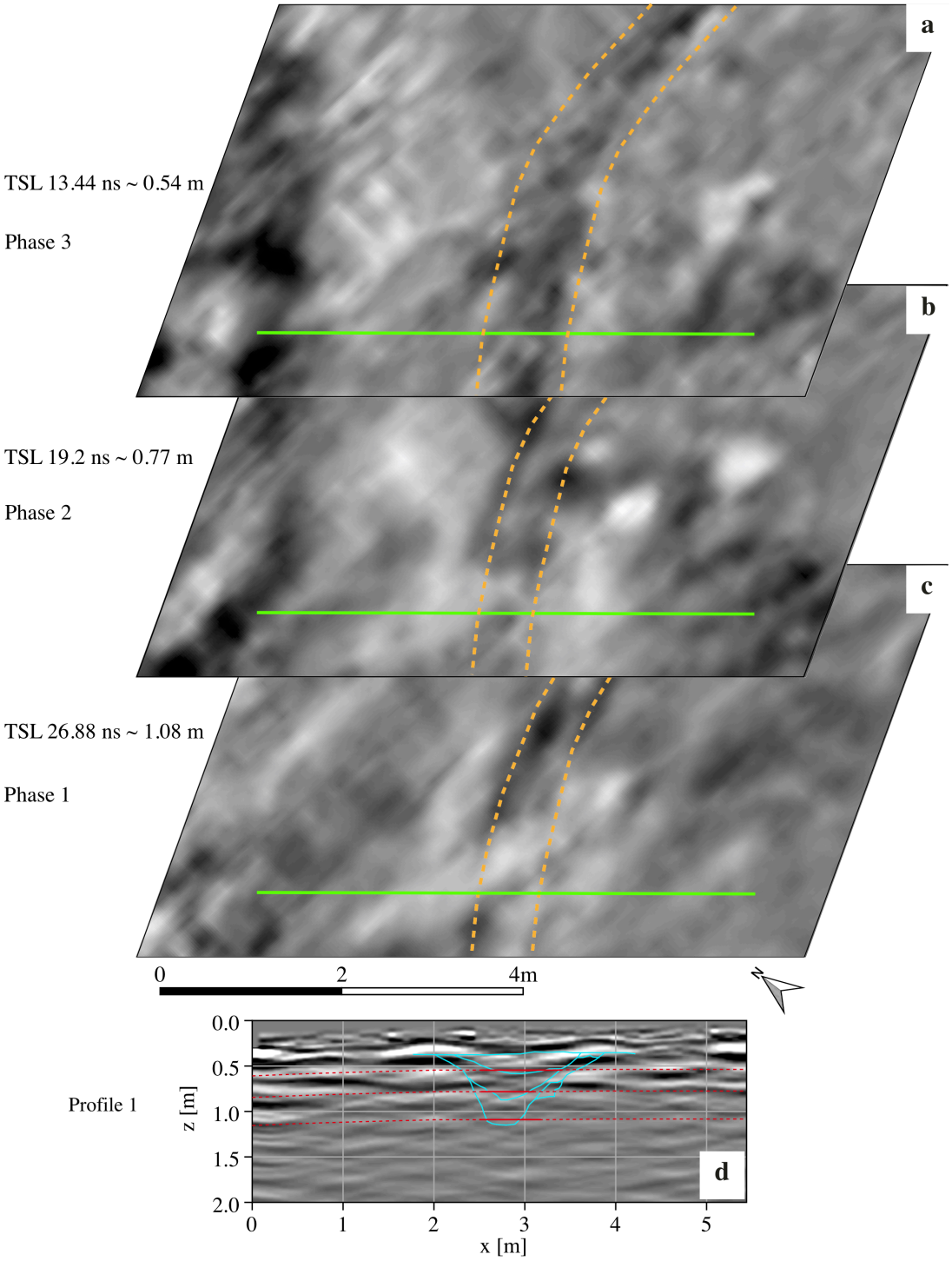

Fig. II.4.9: The appearance of the ditch in the GPR data. Three time slices were chosen (depths z=0.54 m [a], z=0.77 m [b], z=1.08 m [c]). The time slice crossing ditch phase 3 is shown in (a). The time slices in (b) cross phase 2 and (c) phase 1. In (d) the GPR profile crossing the ditch vertically is shown together with the archaeological documentation (blue solid lines) and the position of the time slices in (a), (b) and (c) (red lines). The upper red line crosses the last opening phase (phase 3), the middle one the second (phase 2) and the lower one the first opening phase (phase 1). The orange dashed lines in the time slices indicate the edges of the ditch appearing in the time slices. The red dashed lines mark the position of the time slices in the GPR profile (e), whereas the solid red lines indicate the width of the ditch recognised in the time slice.

II.4.4.3 Burial

Since the pit of the burial is visible in magnetics and GPR, three profiles were chosen for comparison (see fig. II.4.10 presented by three different lines in c) and d)). The green line marks the profile shown in fig. II.4.11. This profile was chosen to show the comparison between GPR and magnetics. The archaeological documentation is a cross profile, which is marked with a blue and a pink solid line and is presented in fig. II.4.12 in comparison with GPR.

Figure II.4.11 shows the comparison of the GPR (b) and the magnetic profile (c). (a) shows the photograph in the plane during the excavation. The magnetic profile clearly shows the negative anomaly. The GPR profile shows the pit to be clearly visible up to a depth of 0.5 m. The interpreted yellow dashed lines indicate that the burial pit reaches a depth of about 1.3 m. From the archaeological documentation, it is known, that the burial pit to have a depth of 1.1 m. At depths of 1 m and 1.3 m, there is strong reflection energy with a width of about 0.5 m (x=3-3.5m). At this depth, charcoal remains and stones were found.

Comparison with the archaeological documentation of the cross profile (see fig. II.4.12) shows that the first reflection (beneath the topsoil) correspond with the documented burial pit (light red solid line). The pit beneath the burial pit is interpreted as being formed by grave structures. This is not documented in the archaeological profile. Nevertheless, the GPR profile shows some reflections, highlighted here with yellow dashed lines. These highlighted reflections seem to belong to the burial, whereas the relation to the burial pit is clearer in the western part than in the southern part of the burial pit.

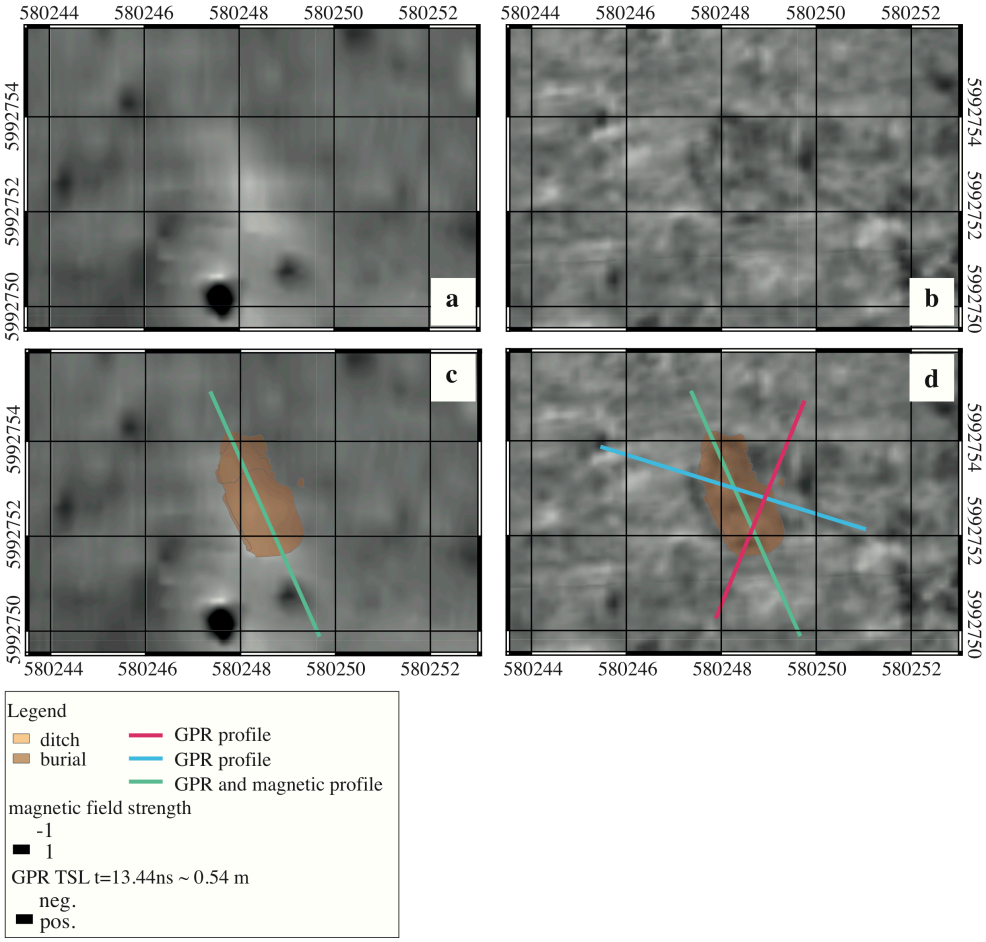

Fig. II.4.10: Comparison of the appearance of the burial in magnetics (a, c) and GPR (b,d).

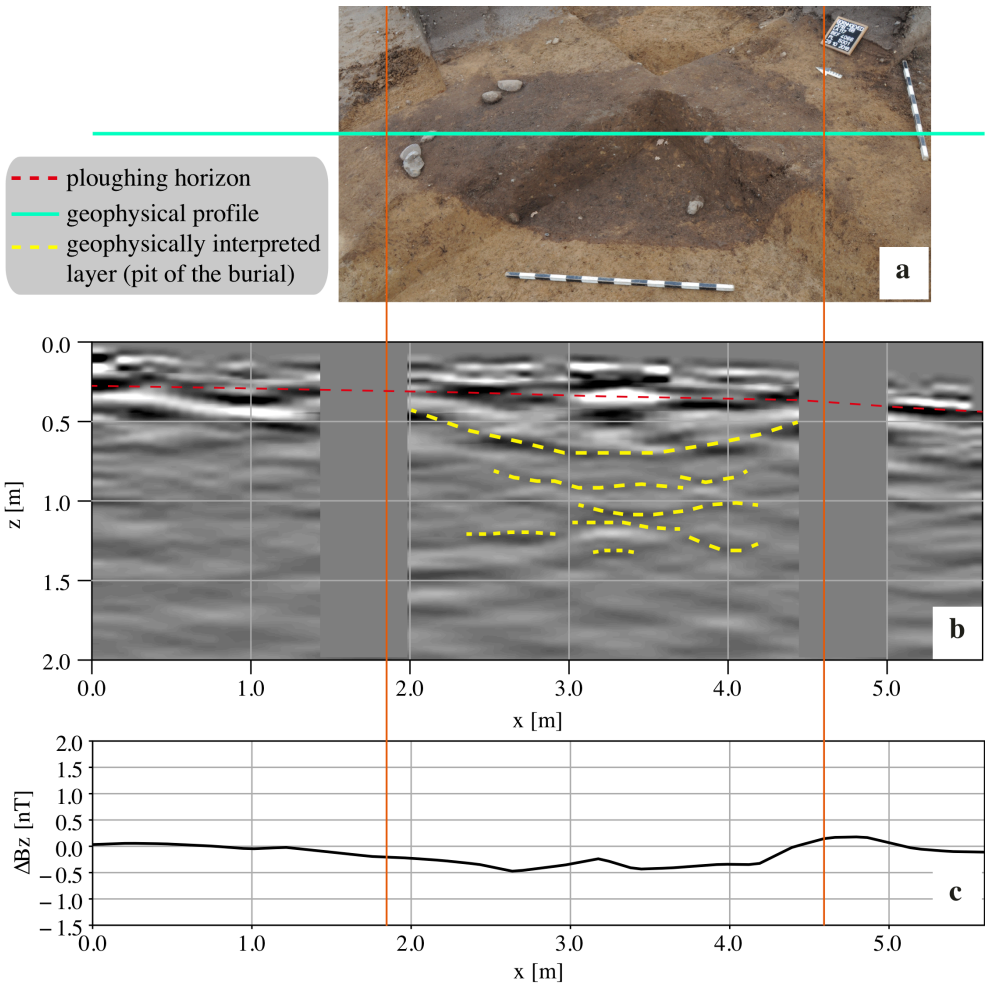

Fig. II.4.11: Comparison of the profile crossing the burial. a) Photography of the burial (by Kneisel); b) GPR profile [red dashed line = ploughing horizon; yellow dashed line = highlighted layers recognised in the GPR profile]; c) magnetic profile

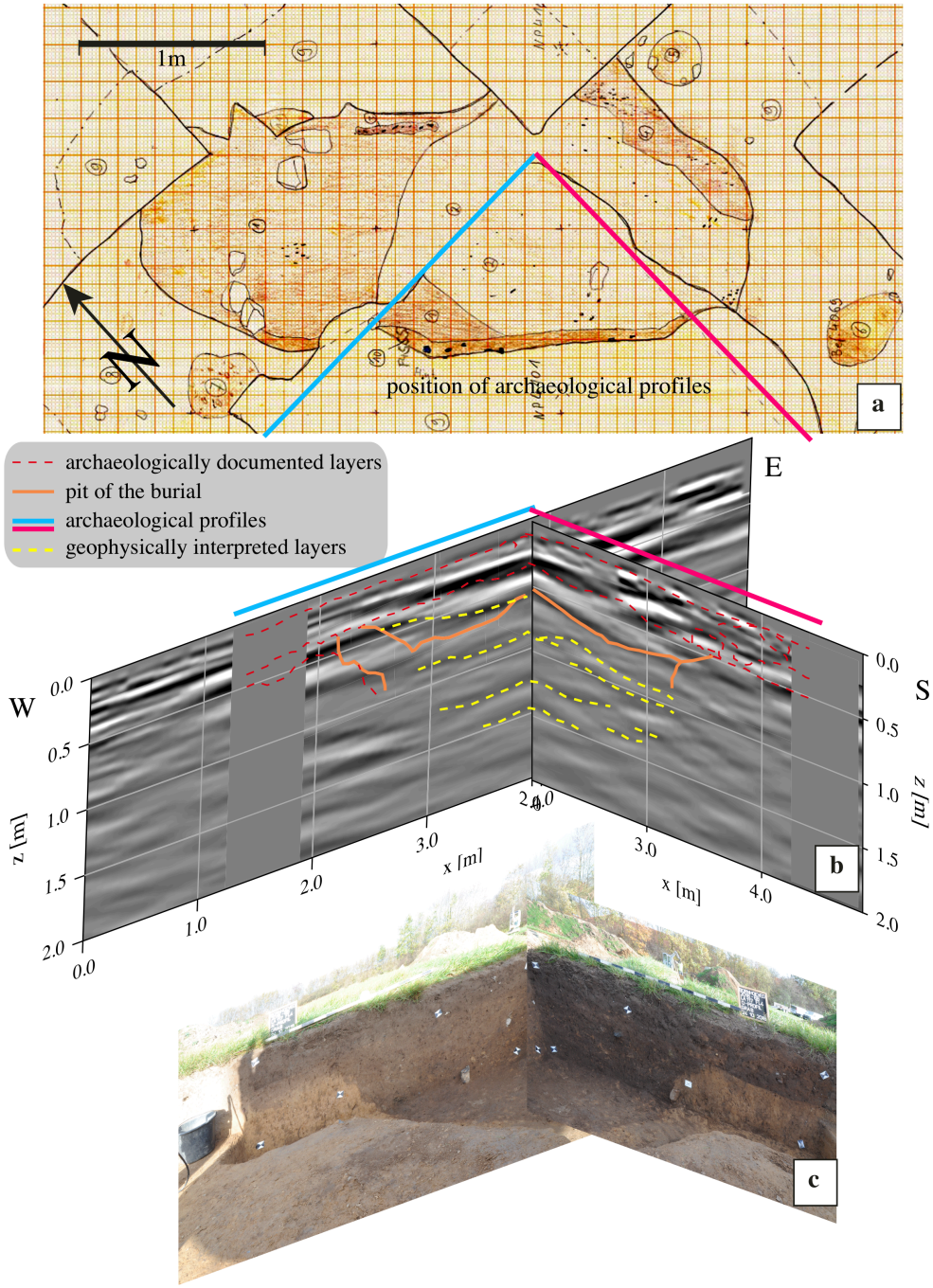

Fig. II.4.12: Archaeological (c) and GPR cross profile (b). a) shows the archaeological documentation in the plane. Blue line marks the north profile, pink line the east profile. Orange lines in the GPR profile highlight the archaeologically recognised layers of the burial pit. Yellow dashed lines mark the layers visible in the GPR profile.

II.4.5 Modelling Study to Explain the Appearance of the Pit Fillings in the Geophysical Data

As previously discussed only a few pits were detected using magnetics and GPR. The most prominent pits of the site BH are the burial and the ditch. In general, the modelling of pits is challenging because the material

that was filled in has a greater heterogeneity than, for example, stones or ceramics themselves. For example, the pit may have been filled in different "phases", initially the pit may have been filled naturally, depending on its shape (for a V-shape it is more likely), and in a second step by human hand. In this case, the degree of compaction can be significantly different. Furthermore, the sides from which the pit was backfilled may also have an influence. For example, the ditch may have been backfilled from two different sides, creating a kind of herringbone pattern in the sediments. Therefore, a set of initial parameters is required for the modelling and the model of the ditch must be kept as simple as possible. The initial set of parameters are derived from the soil analyses and from the results of part I of this thesis concerning the porosity and water content.

Soil samples were obtained from the ditch to analyze the soil composition. From those samples the relative permittivity of the (dried) soil matrix is derived by using Birchaks equation (equation II.3.1). The mean porosity and water content received from part I were than used to calculate the relative permittivity of a porous soil with a certain water content (equation II.3.2) for both sites BH and MdB. The mean porosity and mean water content are taken from site BH, which is $\phi = 41\%$ and $\theta = 24\%$ and from MdB, which is $\phi = 44\%$ and $\theta = 30\%$. In table II.4.8 the resulting values for the relative permittivity of a porous and moist soil, divided in topsoil and the ditch phases are presented.

To understand the effect which different porosity and mean water content have on the GPR response, modelling was carried out using the values from table II.4.8 columns 2 and 3. The resulting comparison of the mean traces are presented in figure II.4.13 for the ditch and figure II.4.14 for the burial. The mean trace by considering the porosity and water content of the site BH results in too small amplitudes, due to very small permittivity contrasts. Considering the porosity and water content of the site MdB lead to larger amplitudes but does not fit the measured trace. In both cases the pit filling directly beneath the topsoil shows very small amplitudes, whereas in reality, relatively large amplitudes are expected. The transition from ditch phase 3 to ditch phase 2 was not detected neither by assuming porosity and water content of BH nor that of MdB. The transition from pit to subsoil could be detected for the burial only for the model that assumed the porosity and water content of MdB. This is because a relative permittivity value of 13 for the subsoil was used in comparison to a value of about 16 for the burial pit.

Table II.4.8: Permittivity values considering a mean porosity and mean water content per site

phase	site BH ($\phi = 41\%$; $\theta = 24\%$)	site MdB ($\phi = 44\%$; $\theta = 30\%$)
humus layer	13.0	16.4
ditch phase 3/burial pit	12.8	16.2
ditch phase 2	13.4	16.8
ditch phase 1	13.4	16.9

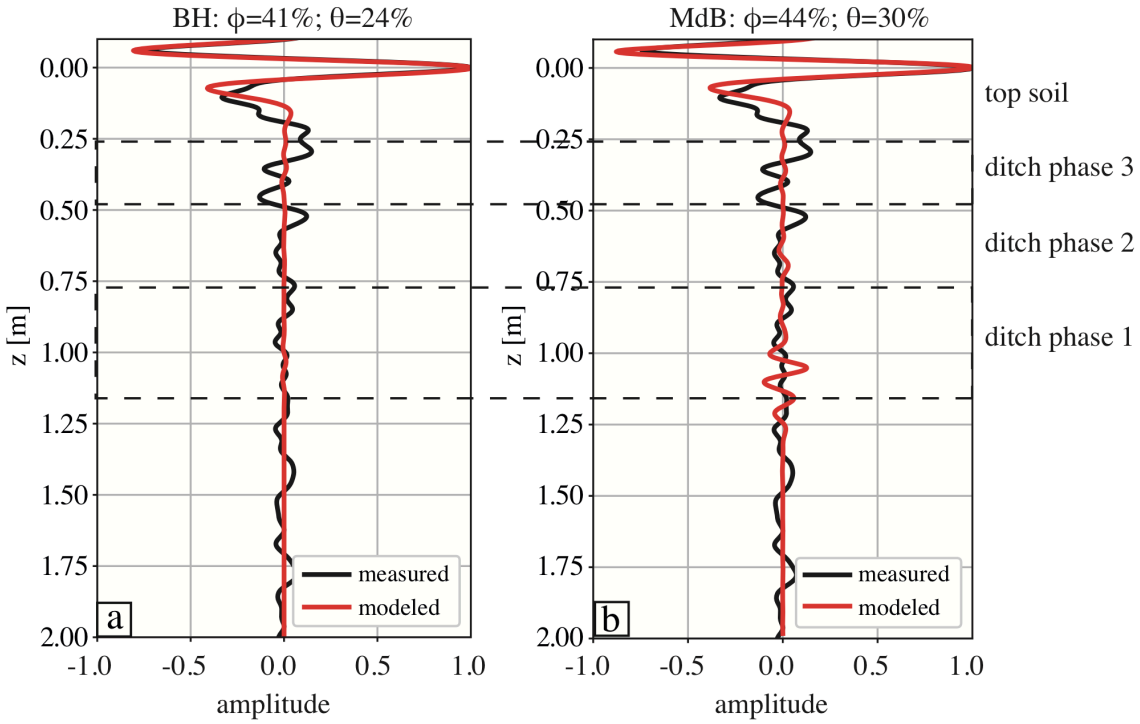

Fig. II.4.13: Comparison of the modeled and measured mean trace of the ditch. In a) the mean porosity and mean water content of the site BH was used in b) the ones derived for the site MdB.

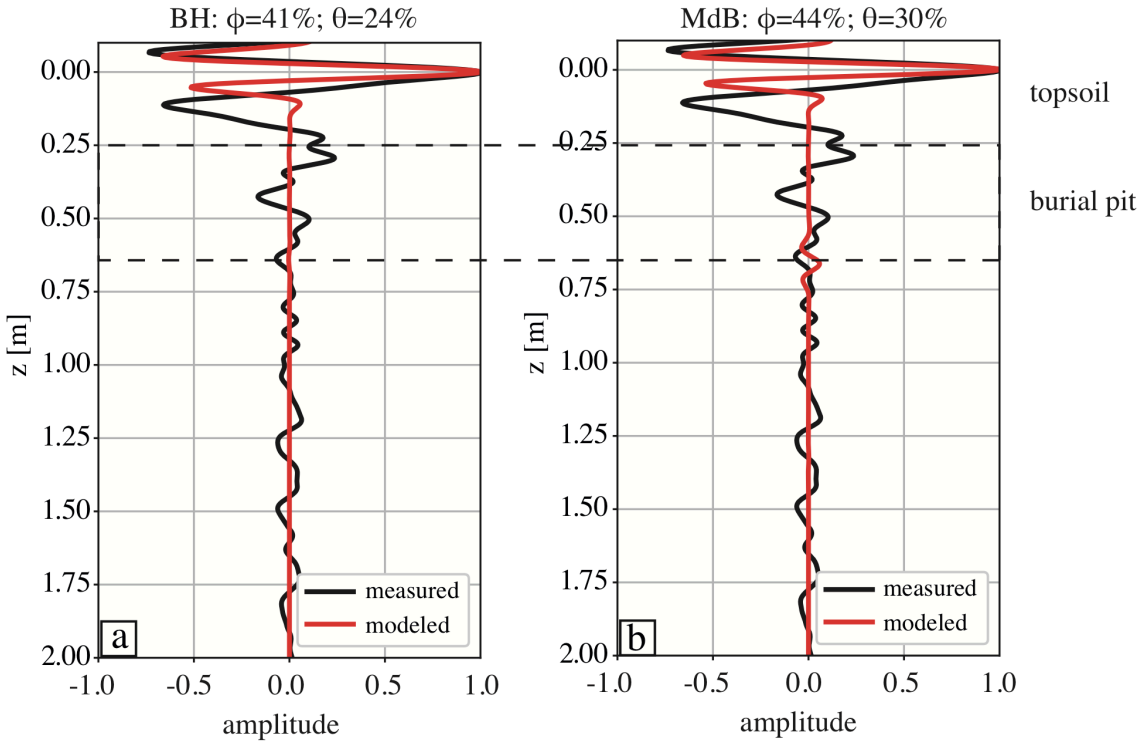

Fig. II.4.14: Comparison of the modeled and measured mean trace of the burial. In a) the mean porosity and mean water content of the site BH was used in b) the ones derived for the site MdB.

Since those models did not lead to satisfying results, the sand content is additionally considered in subsequent models. In section II.4.2 of this part it was found, that in particular ditch phase 3 shows the highest sand content, which would result in a higher porosity, than the layers above and beneath. Therefore, the new model assumes a soil with 59 % sand content with a porosity of 41 % and a mean water content of 24 % consistent with the previous modelling. 59 % is the mean value of the sand content of both ditch profiles, from which soil samples were obtained. Furthermore, the water content was modified. Since it is known from part I, that the summer of 2018 was very warm, a more porous medium is expected to be dryer, because there is more space from which the water can evaporate. The determined values are presented in table II.4.9. From them the relative permittivity was calculated again by using equation II.3.2. The resulting values can be found in table II.4.9 column 4. These values were used as initial values for the modelling, which is presented in the next sections the first for the ditch followed by the burial.

Table II.4.9: Porosity values and water content for the site BH by considering a different sand content

layer	mean porosity	mean water content	mean relative permittivity
humus layer	42	24	12.6
ditch phase 3	45	22	10.5
ditch phase 2	40	25	13.9
ditch phase 1	39	26	14.9

II.4.5.1 GPR Modelling

The purpose of this chapter is not only to lay the foundation for answering the question posed at the beginning, namely, what the pit filling must be like in order to be detected by both radar and magnetics, but also to discuss the complexities and challenges of pit modelling. First, the radar response is modeled using the ditch and the central burial. Second, the magnetic modelling of the ditch is carried out. The complexity of pit modelling is illustrated by the burial example.

II.4.5.1.1 Ditch

By applying the values of table II.4.9 column 4 the model fits the measured trace better, compared to the models using the values derived from both sites (BH and MdB) without considering the sand content. Small variations of the permittivity in some layers were necessary to get a good fit. Furthermore, an additional layer was necessary to be inserted in the topsoil. The values used for the best fit, are presented in table II.4.10 and shown in figures II.4.15a) and b).

The comparison of the modeled and measured trace are shown in figure II.4.16. Subfigures II.4.16a) and b) show a section of the ditch profile (measured (a) and modeled (b)). The archaeological documentation is

inserted in the measured and modeled GPR profile, to guide the interpretation because the amplitudes in the GPR profile are too weak.

If one looks only at the measured trace, it is noticeable that the transition from phase 3 to phase 2 is very clearly visible. The transition from phase 2 to phase 1 can be seen, but it is not as pronounced as the previous transition. The transition from phase 1 to the surrounding soil is no longer visible at first glance, only with the help of modelling. This confirms the hypothesis of the archaeologists that phase 1 has been filled with the surrounding soil by natural processes.

Looking at the modelling result, it is obvious, that the transition of phase 2 to phase 1 is more prominent in the measured trace than in the model result. The transition of phase 1 to the subsoil is deeper (about 5 cm) than expected. The size of the modeled amplitude is also slightly larger than expected. The relative bad fit of the ditch in phases 2 and 1 is because, the initial model is too simplified. Phases 1 and 2 consist only of one layer. Ditch phase 3 was separated in two distinct layers, based on the archaeological documentation. Therefore, the best fit is expected for this layer. Considering the topsoil, it was necessary to include an additional thinner layer, so that the topsoil is now consisting of two layers. Nevertheless, the transition from air to soil is quite good and the size of the amplitudes caused by the topsoil layers is very similar to the measured ones. There is a difference in a depth of 0.25 m between the measured and modeled trace, indicating that a further layer in the topsoil can be expected.

Table II.4.10 illustrates a difference in the relative permittivity values of phase 3 and phase 2 in comparison to table II.4.9. The difference for ditch in phase 3 is the result of the two assumed layers. The mean value of the relative permittivity of both layers is 10.1. The difference for ditch in phases 2 and 1 is the result of the fitting process during the modelling and the simplified assumption of the soil filling of this phase. Furthermore, the relative permittivity of the topsoil is in average $\epsilon_r = 14.9$, which is higher than expected.

Table II.4.10: Dielectric Permittivity and electrical conductivity values used for modelling of the ditch

Layer	Relative Permittivity	Electrical Conductivity [mS/m]
Top soil (1)	17 (layer 1a, [II.4.15a])	1.83
Top soil (2)	12.8 (layer 1b, [II.4.15a])	1.83
Phase 3 (1)	9.2 (layer 2, [II.4.15a])	0.9
Phase 3 (2)	11 (layer 3, [II.4.15a])	0.9
Phase 2	14.2 (layer 4, [II.4.15a])	0.9
Phase 1	14.4 (layer 5, [II.4.15a])	0.9
Sub soil	13 (layer 6, [II.4.15a])	0.9

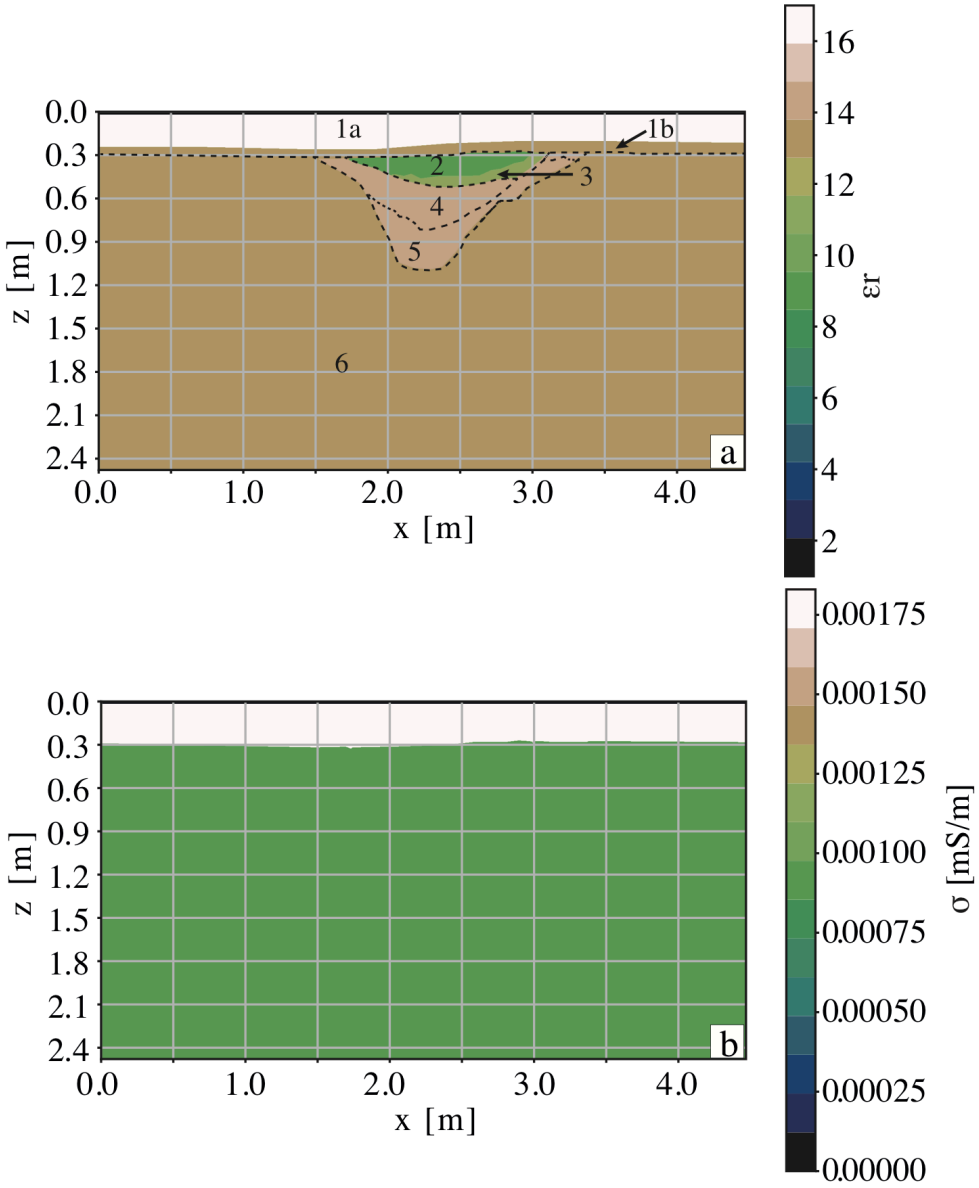

Fig. II.4.15: Permittivity (a) and conductivity (b) used for the model with the best fit. The black solid line represents the archaeological documentation and was inserted to see the position of the ditch filling of phase 2 and 1.

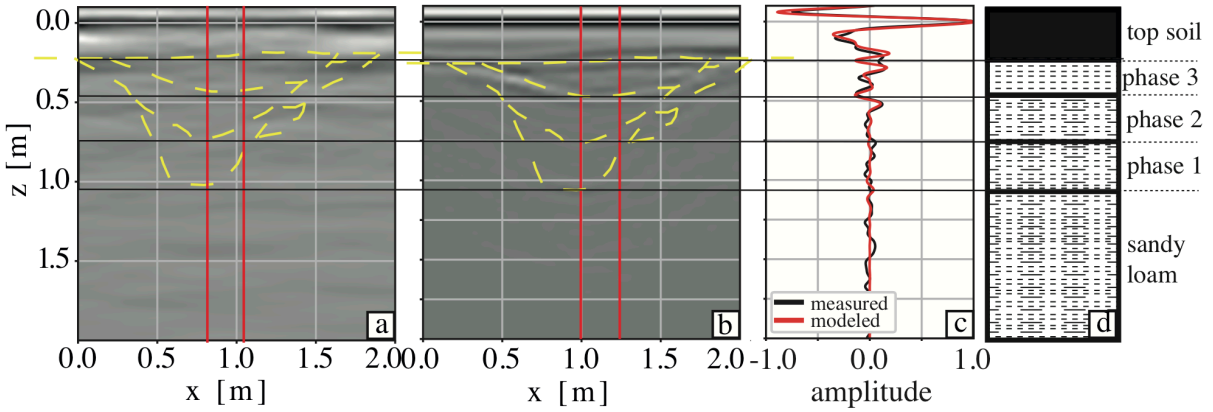

Fig. II.4.16: Comparison of measured and modeled data of the ditch profile 1. a) and b): measured and modeled GPR profile. The red vertical lines present the section, where the mean traces were extracted. The yellow dashed lines represent the archaeological documentation. c): trace comparison of measured and modeled data. All amplitudes are normalized to the largest amplitude of the direct wave. d): schematic stratigraphic column.

Table II.4.11 shows the derived porosity and water content from the modelling study. The porosity is similar in all depths and in particular the soil of ditch phase 3 shows the smallest water content, whereas the surrounding shows a similar water content of about 25.5 %.

The subsurface model implies a mean velocity of about 0.083 m/ns. This validates also the assumed velocity of 0.08 m/ns for the time-depth conversion.

Table II.4.11: Porosity values and water content for the ditch based on the modelling results

layer	mean porosity	mean water content	mean relative permittivity
humus layer	39	26	14.9
ditch phase 3	41	20	10.1
ditch phase 2	39	25	14.2
ditch phase 1	41	26	14.4
subsoil	42	25	13

II.4.5.1.2 Burial

In this section modelling of the burial is performed based on the previously derived parameters from the soil analyses. The archaeological documentation serves as the basic model. Subsequently the initial starting model from the archaeological documentation will be modified. Additionally, the parameters require adjustment in order to obtain an optimized model result.

Initial model derived from the archaeological documentation

The initial model, which is discussed here was digitized from the archaeological documentation. When using

the values of table II.4.9 column 4, the model shows a good fit in the transition from the bottom of the pit to the subsoil. The used parameters for the best fitting model can be found in table II.4.12 and the model itself is shown in figure II.4.17. The resulting modeled trace in comparison to the measured one is shown in figure II.4.18c. Once again the archaeological documentation is inserted in the measured and modeled profile section, to guide the interpretation since the amplitudes in the GPR profile are too weak (yellow dashed line in figure II.4.18).

Only the bottom of the burial pit fits perfectly the measured trace in contrast to the modelling of ditch phase 3, where only an additional layer was required. In the upper part of the burial pit at least one additional layer can be expected. During the excavation only one layer was documented as burial pit. The amplitude resulting from the transition from pit to subsoil shows, that a relative permittivity of 13 (of the subsoil) fits quite well. Considering the topsoil only one layer is not enough to obtain a satisfying model as the archaeological documentation suggests. The modeled trace does not fit the measured trace in this part. Comparing table II.4.12 with table II.4.9 it was necessary to increase the value for the relative permittivity for the topsoil to 17. This value corresponds to a mean porosity of 40 % and a mean water content of 29 %. This water content is similar to the one found at the site MdB and higher than expected (compare table II.4.9 column 4). The resulting values for porosity and water content can be found in table II.4.12. Again, the porosity of all layers is similar, but the water content of the burial pit is 5 to 10 % smaller.

The subsurface model implies a mean velocity of about 0.082 m/ns. This also confirms the assumed velocity of 0.08 m/ns with which the time-depth conversion was performed.

Table II.4.12: Dielectric Permittivity and electrical conductivity values used for modelling of the burial pit and the corresponding values for porosity and water content

Layer	Relative Permittivity	Electrical Conductivity [mS/m]	Porosity [%]	Water Content [%]
Top soil	17 (layer 1, [II.4.17b])	1.83	40	29
burial pit	10.2 (layer 2, [II.4.17a])	0.9	41	20
Sub soil	13 (layer 3, [II.4.17b])	0.9	42	25

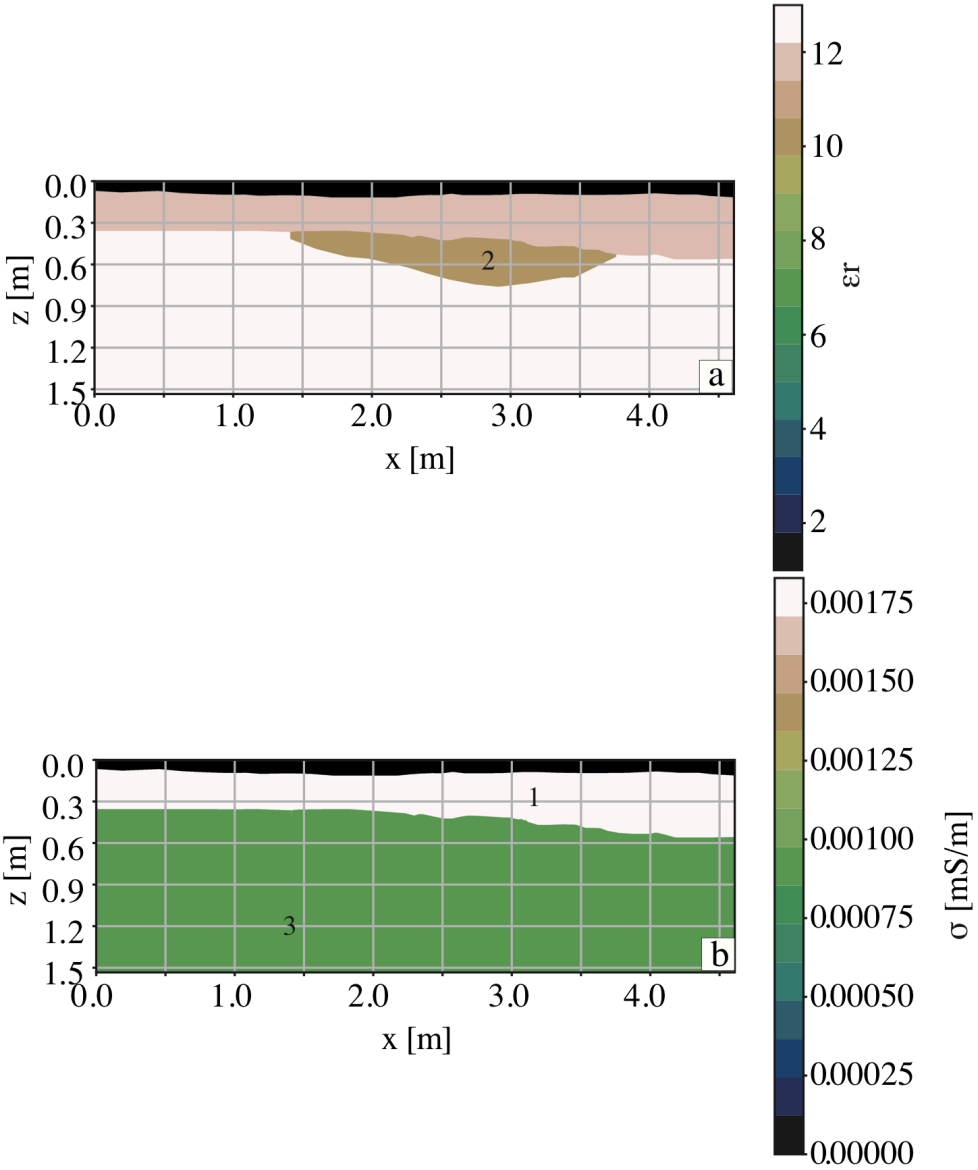

Fig. II.4.17: Permittivity (a) and conductivity (b) used for the model with the best fit.

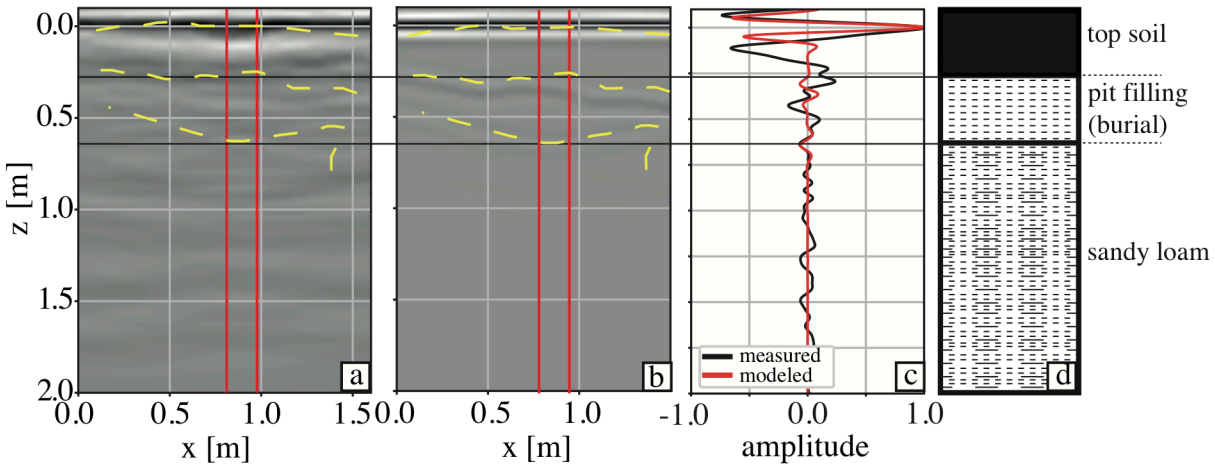

Fig. II.4.18: Comparison of measured and modeled data of the east profile of the burial. a) and b): measured and modeled GPR profile. The red vertical lines present the section, where the mean traces were extracted. c): trace comparison of measured and modeled data. All amplitudes are normalized to the largest amplitude of the direct wave. d): schematic stratigraphic column.

Refining the Model

As previously demonstrated, the model did not represent the reality very well. The heterogeneity in the soil layers of the pits could not be reproduced. Therefore, the burial pit was modeled again with a modified model to estimate how much the deviation of the parameters as well as the result from the simple model is. To obtain a good fit, two additional layers are inserted in the topsoil and burial pit. Resulting in a model setup with three topsoil layers and three layers in the pit filling. The permittivity also needed to be adjusted. The used parameters can be found in table II.4.13 and is shown in figure II.4.19. The conductivity was not changed and is the same as before. The best fit is shown as trace comparison in figure II.4.20c.

Table II.4.13: Dielectric Permittivity and electrical conductivity values used for modelling of the burial pit

Layer	Relative Permittivity	Electrical Conductivity [mS/m]
Top soil	18 (layer T1, [II.4.19])	1.83
Top soil	21 (layer T2, [II.4.19])	1.83
Top soil	9 (layer T3, [II.4.19])	1.83
burial pit	6.5 (layer B1, [II.4.19])	0.9
burial pit	12 (layer B2, [II.4.19])	0.9
burial pit	11 (layer B3, [II.4.19])	0.9
Sub soil	14 (layer S, [II.4.19])	0.9

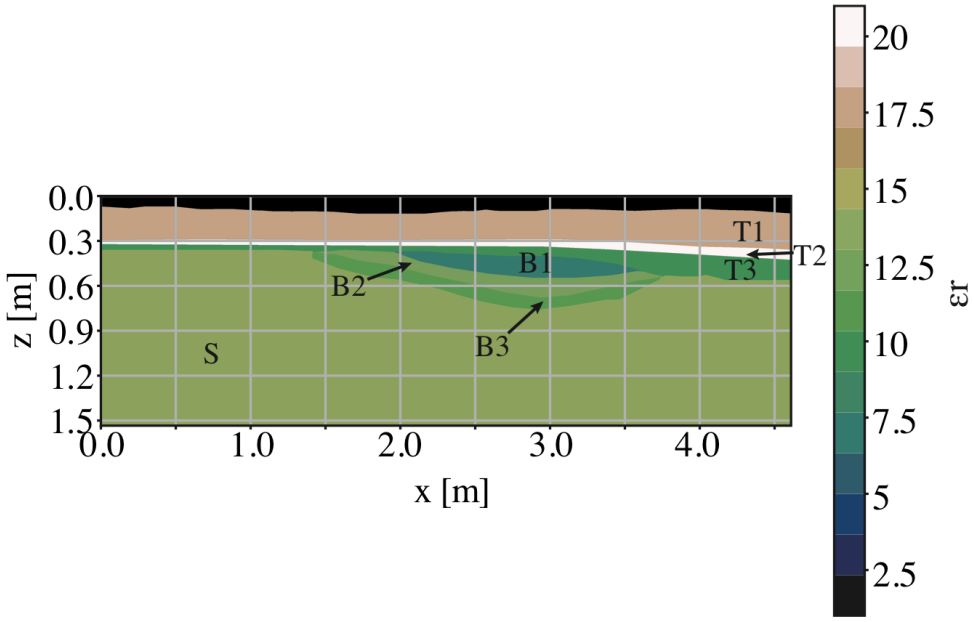

Fig. II.4.19: Permittivity of the best model of the burial. The conductivity is the same as in fig. II.4.17.

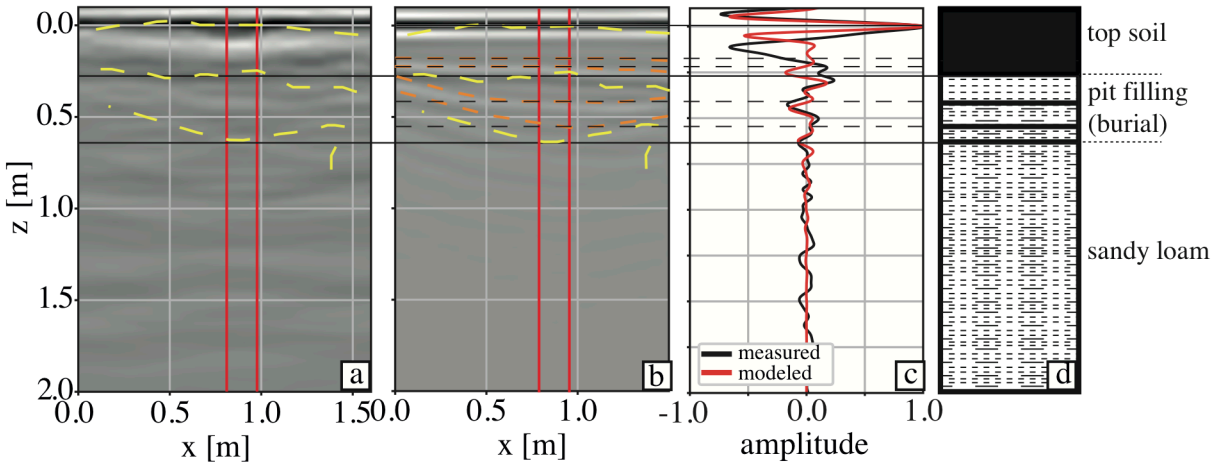

Fig. II.4.20: Comparison of measured and modeled data of the east profile of the burial. a) and b): measured and modeled GPR profile. The red vertical lines present the section, where the mean traces were extracted. The yellow dashed lines represent the archaeological documentation. The orange dashed lines represent the additional layers inserted during the modelling. c): trace comparison of measured and modeled data. All amplitudes are normalized to the largest amplitude of the direct wave. d): schematic stratigraphic column.

The comparison of the measured and modeled trace shows a relatively good fit from 0.26 m to 0.7 m. The largest difference can be found in the uppermost topsoil. The mean permittivity of the topsoil is now 16. This corresponds to a mean porosity of 42 % and a mean water content of 29 %. The mean permittivity of the burial pit is 9.8, which corresponds to a mean porosity of 40 % and a mean water content of 19 %. Table II.4.14 contains the values for the porosity and water content based on the resulting permittivity values.

Again, the porosity values are very similar, whereas the one for the burial pit decreased. Compared with ditch phase 3 the burial pit shows more or less the same water content and porosity.

The subsurface model implies a mean velocity of about 0.083 m/ns. This also confirms the assumed velocity of 0.08 m/ns with which the time-depth conversion was performed.

Table II.4.14: Porosity values and water content for the burial based on the modelling results of the modified model

layer	mean porosity	mean water content	mean relative permittivity
humus layer	42	29	16
burial pit	40	19	9.8
subsoil	42	25	13

II.4.5.2 Magnetic modelling

As mentioned above, soil samples were taken from the ditch profile during the excavation. The analysis provided in-situ values of the volumetric susceptibility. Ditch phases 2 and 3 clearly show the lowest susceptibility values of the profile. This is in a depth between 0.3 and 0.8 m. To verify this observation, the documented situation was modeled exactly. Ditch phases 2 and 3 were constructed as two rectangles, the upper one with about 2 m width and 0.3 m thickness, the lower one has a width of 1.4 m and a thickness of 0.2 m. The measured susceptibility is at about 36.2*1e-5 [SI] and was used for modelling the ditch phases 2 and 3. The surrounding soils have a susceptibility of about 50*1e-5 [SI].The result of this modelling matches the measured amplitude perfectly (check fig. II.4.21).

With regard to soil composition, an explanation for the small susceptibility values was found. Phase 3 has a sand content 7% higher than the humus layer and 12% higher than that of phase 2. The clay content of phase 3 is 27% lower than the humus layer and 23% than of phase 2. Phase 2 shows the highest silt content (see again table II.4.2).

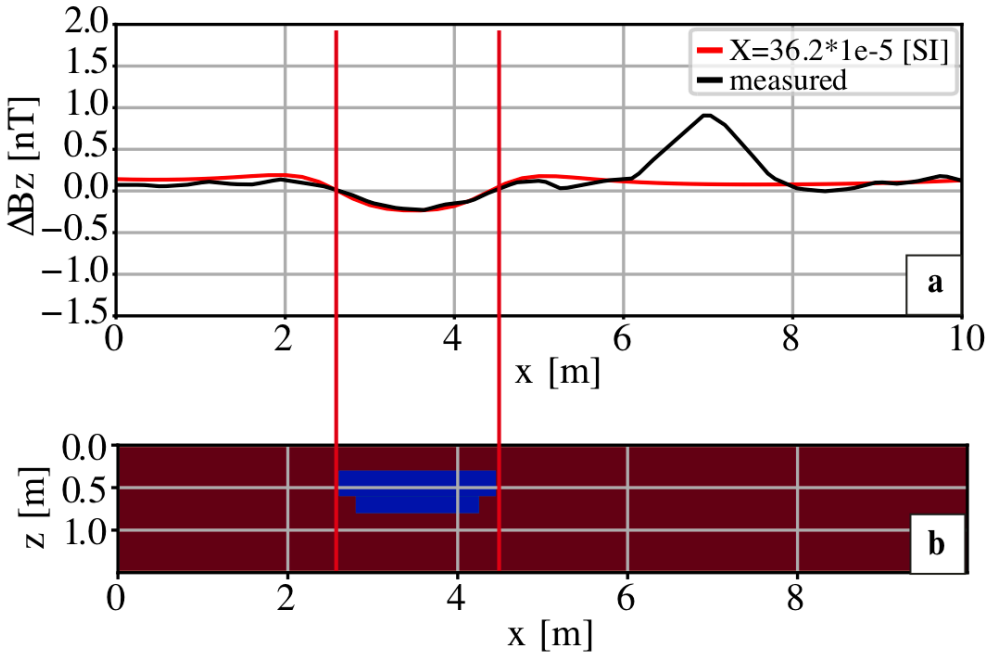

Fig. II.4.21: Result of the magnetic modelling. a) shows the comparison of the modeled (red) and measured (black) magnetic anomaly caused by the ditch. b) shows the input model of the magnetic modelling.

II.4.5.3 Summary

From the soil analyses it is known, that the soil of ditch phase 3, the last ditch phase, contains more sandy material in comparison to the other layers. From the modelling with GPR, it is known, that at least the porosity of the pit directly under the topsoil (either ditch phase 3 or the burial pit) is similar compared to the adjacent layers, but the water content is significantly lower than in the surrounding layers. The modelling highlights that a good initial model leads to a satisfactory result relatively quickly. This starting model was generated under the consideration of the sand content and the porosity and water content values derived from part I of this thesis for the site BH. Magnetics likewise detect the pit directly below the topsoil since the susceptibility is reduced compared to the adjacent layers, resulting in negative amplitudes.

II.5 Discussion

II.5.1 Modelling Pit-Like Features

In the results chapter of this part of the thesis the burial and the ditch were modeled, since they could be detected very well with GPR and magnetics. A simple model based on the archaeological documentation was used at first. Especially when modelling the burial, it became apparent that this model was too simple. The burial was archaeologically documented with only one pit layer. The modelling showed that only the bottom of each pit (burials pit or the bottom of the ditch phases) could be reproduced, if such a simplified model is used.

During the modelling and refining process, it became apparent that pit modelling is challenging. The change of a parameter in one layer can result in serious changes in other depth ranges, so that the modelling was difficult to control. Therefore, a sensitivity analysis was performed using the model shown in figure II.4.20 as the reference model. The root mean square (RMS) between reference and variation was calculated at first. To do this, the permittivity in each layer was varied in the range of $\epsilon_r(layer)$–30 % $< \epsilon_r(layer) <$ $\epsilon_r(layer)$+30 % from the relative permittivity value of the considered layer ($\epsilon_r(layer)$ - see equation II.5.1). In a second step, the moving RMS was calculated to obtain information about the depth or time range on which the respective change has its influence (using equation II.5.3). The following equations were used for this:

$$RMS = \sqrt{\frac{1}{n} * \sum_{i=1}^{n} \frac{(x_{var}(i) - x_{ref}(i))^2}{\sigma^2}} \tag{II.5.1}$$

$$\sigma^2 = \frac{1}{n-1} \sum_{i=1}^{n} (x_{var}(i) - x_{mean})^2 \tag{II.5.2}$$

The first two equations were used to calculate a single misfit value to quantify the misfit between the two traces: the reference trace (ref) and the trace followed by the variation (var) of the permittivity per layer $\epsilon_r(layer)$. The variance σ^2 was used to weight the RMS to get values between 0 and 1. This allows a good visualisation without extreme values. The following equation was used to calculate the moving RMS with a window size of $N = 40$ samples. This represents a time range of about 3 ns.

$$RMS(i) = \sqrt{\frac{1}{N} * \sum_{j=i-N/2}^{i+N/2} (x_{var}(j) - x_{ref}(j))^2} \tag{II.5.3}$$

The resulting figures are fig. II.5.1 showing the RMS and fig. II.5.2 for the moving RMS. Three main aspects can be derived from figure II.5.1. First, the greater the deviation between the permittivity value of the reference and the variation, the greater the misfit. Secondly, if permittivity values smaller as the reference are applied, than a trend can be seen according to which the misfit appears to be larger when the permittivity of the upper layers is varied. One exception is the variation of the first burial pit layer. Thirdly, if one applies permittivity values, that are larger as the reference, than the trend seems to be vice versa, which means if one varies the permittivity values for the deeper layers, than the misfit seems to be larger. A fourth observation is that decreasing the permittivity values of one layer leads to a larger misfit than increasing the permittivity of the same layer. The layer with the greatest influence on the entire trace is the uppermost topsoil layer. Nevertheless, from this figure it is not possible to estimate the influence of the change of a single layer compared to the entire trace or profile respectively. For this, one has to look at figure II.5.2. This shows, broken down by depth range, the influence on the entire trace. The abbreviations T1-3, B1-3 and S represent the layers (check again fig. II.4.19). T1 to T3 represent the three layers of the topsoil, B1-B3 the layers of the burials pit and S the subsoil. The permittivity range that was varied was always $\epsilon_r \pm 30\%$. Therefore, the number of permittivity values per layer is different.

From figure II.5.2, we see that the strongest sensitivity to the trace are parameter variations within the first topsoil layer, as well as the first burial pit layer. If we concentrate on the first topsoil layer (fig. II.5.2b-d), we find that a change in the values in the topsoil affects time ranges of the burial pit itself. The greatest effects, however, remain in the topsoil layer. Let us now look at the effects of changes in the permittivity values of the ditch (fig. II.5.2e-g). The largest effects of the variations of the individual layers also remain in the area of the respective layer. However, effects on the topsoil as well as the subsoil can also be expected. If the permittivity values of the subsoil are varied (fig. II.5.2h), effects on the amplitudes caused by the topsoil are also to be expected and of a similar magnitude as when varying the other layers. In general, the influence of the subsoil is small compared to the variation of the other layers. The observation, that decreasing the permittivity of one layer leads to larger misfit values is supported by all the subfigures shown in fig. II.5.2.

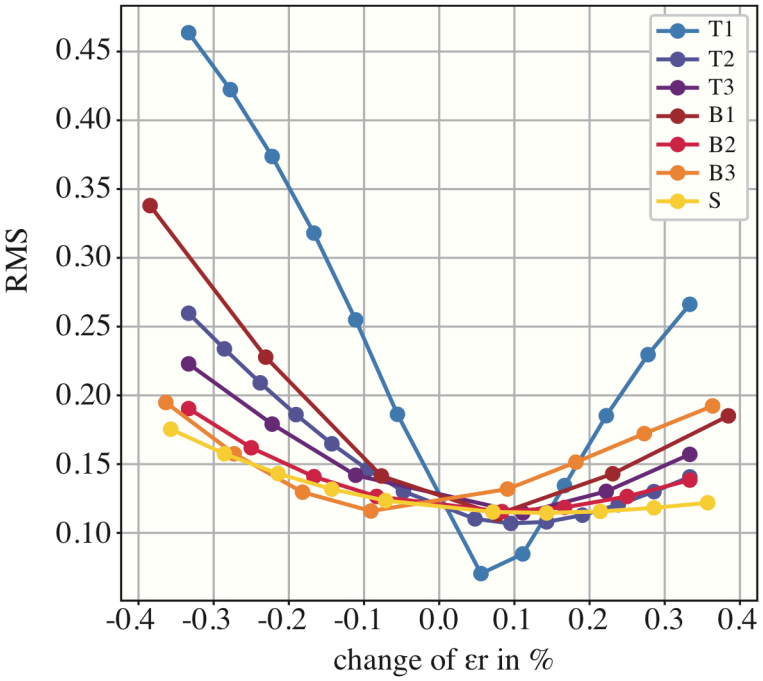

Fig. II.5.1: Misfit represented as RMS for the variation of one layer at a time. The abbreviations can be found in fig. II.4.19.

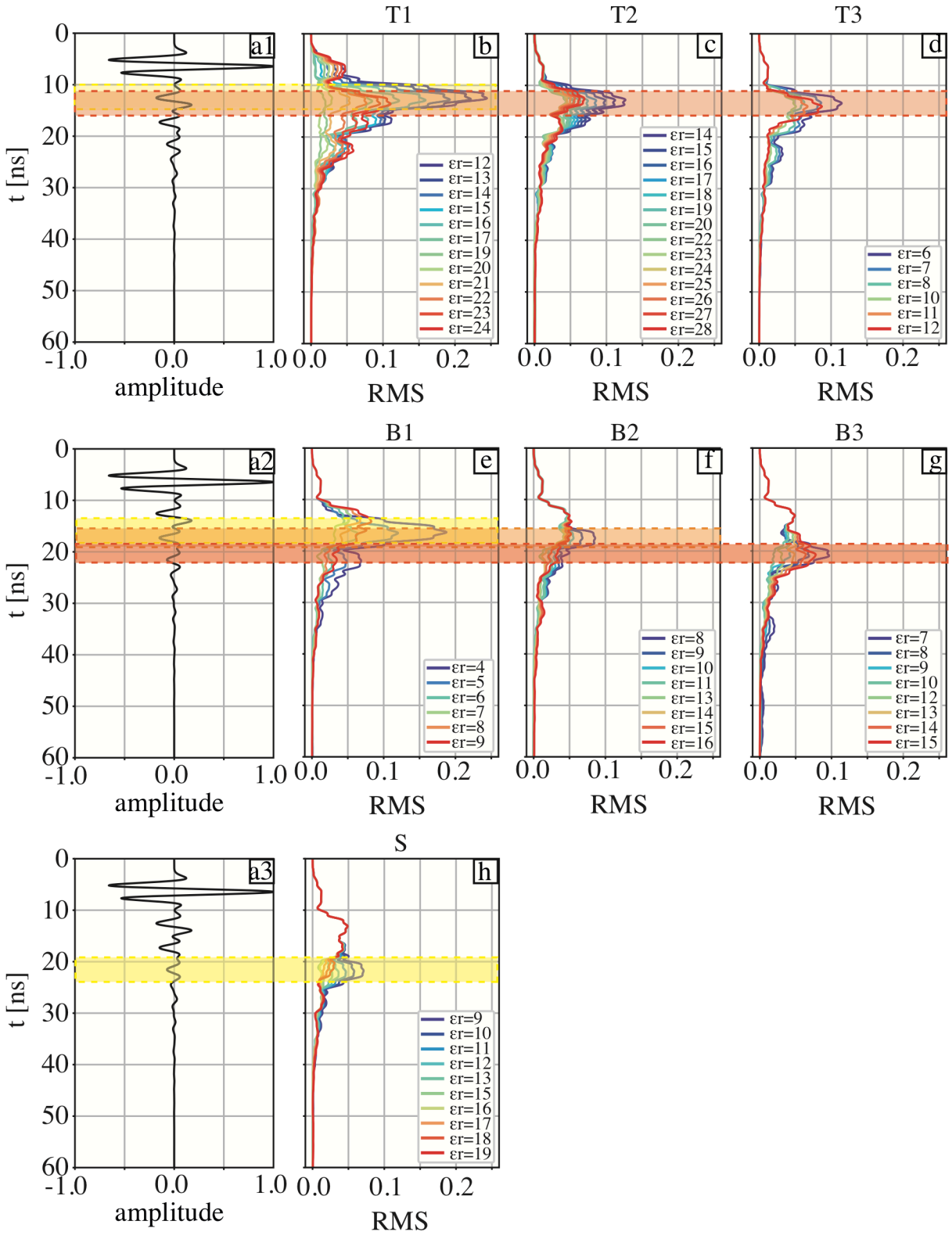

Fig. II.5.2: Moving RMS for each layer and its effect on the whole trace. Here also always one value was varied in one layer at a time. The permittivity range was $\epsilon \pm 30\%$. In a1), a2) and a3) always the reference trace is shown. In b), c) and d) the variation of the three topsoil layers is shown. In e), f) and g) the variation of the three burial layers is shown. h) is showing the variation of the relative permittivity of the subsoil layer. The shaded boxes represent the part with the largest effect in comparison to the time range before and after it. The yellow shaded box is for highlighting the effect of the first layer T1 or B1 or S. The orange shaded box is for highlighting the effect of the second layer T2 or B2. The red box is for highlighting the effect of the third layer T3 or B3.

II.5.2 Evaluation of the Appearance of the Three Ditch Phases in the GPR Profiles

In the results chapter, it was shown, that the ditch walls and bottom of ditch phase 3 can be seen clearly, whereas the walls of phases 2 and 1 could not be detected. There may be several reasons for this. First, the shape of each ditch phase is different, and secondly, the soil properties of each phase are similar to the surrounding subsoil. Both theories shall be reflected here. To quantify the shape of the ditch walls, the angle of incidence of the ditch wall is determined. To investigate the influence of the permittivity contrast between ditch and subsoil, the soil parameters of the subsoil were varied in the modelling.

II.5.2.1 Angle of Incidence of the Ditch's Wall

From the archaeological documentation, it is known, that the ditch of phase 3 is more U-shaped, whereas that of phase 2 is more V-shaped. The ditch walls of phase 1 are sometimes U-shaped and sometimes V-shaped. It can be seen that the ditch walls become steeper with depth. To quantify the observation, the angle of incidence is measured on the basis of the digitized documentation of the archaeologists (table II.5.1). Phase 3 shows an angle of about 24° ± 7°, phase 2 35° ± 10° and phase 1 50° ± 11°. Based on the analysis of the incidence angles of the ditch, one can conclude, that layers with an incidence angle of about 24° are detected in the GPR and it struggles to detect layers with an angle larger than 35°. The angle of incidence is not only the factor of interest, also the soil condition of the layers, first those of the first ditch phase and second, the one of the subsoil.

Table II.5.1: Results of the determined angles of the ditch walls

phase	angle [degrees]	standard deviation
ditch phase 1	49.4	10.9
ditch phase 2	34.6	9.5
ditch phase 3	24.4	6.7

II.5.2.2 Modelling the Ditch

In the results chapter it was found, that the sand content of the ditch filling of phase 3 is higher than that of phases 1 and 2, leading to a higher porosity. A further result is, that the water content of this layer is smaller compared to the topsoil and the layers beneath. Furthermore, it was demonstrated that the sand content decreases with depth. Additionally, the permittivity of phase 3 decrease, as well.

The GPR modelling shows a high contrast in soil properties between the filling of ditch phase 3 and the topsoil or other phases. On the other hand, the soil properties of phases 1 and 2 are very similar to that of the surrounding soil. Consequently, the resolving of the edge is challenging due to the low contrast. To further investigate this, a further modelling case study was carried out.

The model is identical to the model in section II.4.5.1.1. The parameters used can be seen in table II.5.2. The decisive factors are the soil properties of the surrounding subsoil. In the reference model the relative permittivity of all the layers, except of the subsoil, is identical to table II.4.10. In this section the relative permittivity of the subsoil of the reference is $\epsilon_r = 14.4$ (which means no contrast between ditch phase 1 and subsoil). The subsoil permittivity was than varied two times: first with $\epsilon_r(subsoil) = 10$ and second with $\epsilon_r(subsoil) = 18.8$. The difference between the subsoil permittivities is kept fix at $\Delta\epsilon_r(subsoil) = 4.4$. The values of relative permittivity were randomly selected, but high enough to allow the effects of the different parameters to be recognizable. The resulting GPR profiles are shown in fig. II.5.3 together with the trace comparison between measured and modeled data. A larger contrast enhances the appearance of the steeper ditch walls, whereas the recognition is improved, if one assumes a subsoil permittivity, that is smaller, than the one of the pit. Additionally, the moving RMS was calculated (using the equation II.5.3 but weighted by the variance as in equation II.5.1) between the reference and the variation ($\epsilon_r = 10, 18.8$). The result is shown in figure II.5.4. The misfit highlights, that a smaller subsoil permittivity enhances the ditch walls.

To analyse the porosity and water content, one needs to reconsider table A.6. The relative permittivity of 14.4 corresponds to a porosity of $\phi = 45\%$ and a water content of $\theta = 28\%$. The relative permittivity of 10 corresponds to a porosity of $\phi = 46\%$ and a water content of $\theta = 22\%$. The relative permittivity of 18.8 corresponds to a porosity of $\phi = 41\%$ and a water content of $\theta = 32\%$. This means if the subsoil is drier than the ditch filling with nearly the same porosity, than the ditch walls can be seen the best. Table II.5.3 shows the compilation of the corresponding porosity and water content values to the applied relative permittivity values.

Table II.5.2: Dielectric Permittivity and electrical conductivity values used for modelling of the ditch

Layer	Relative Permittivity ($\epsilon_r(subsoil) = 10$)	Relative Permittivity (reference)	Relative Permittivity ($\epsilon_r(subsoil) = 18.8$)
Top soil (1)	17 (layer 1a, [II.4.15a])	17	17
Top soil (2)	12.8 (layer 1b, [II.4.15a])	12.8	12.8
Phase 3 (1)	9.2 (layer 2, [II.4.15a])	9.2	9.2
Phase 3 (2)	11 (layer 3, [II.4.15a])	11	11
Phase 2	14.2 (layer 4, [II.4.15a])	14.2	14.2
Phase 1	14.4 (layer 5, [II.4.15a])	14.4	14.4
Sub soil	10 (layer 6, [II.4.15a])	14.4	18.8

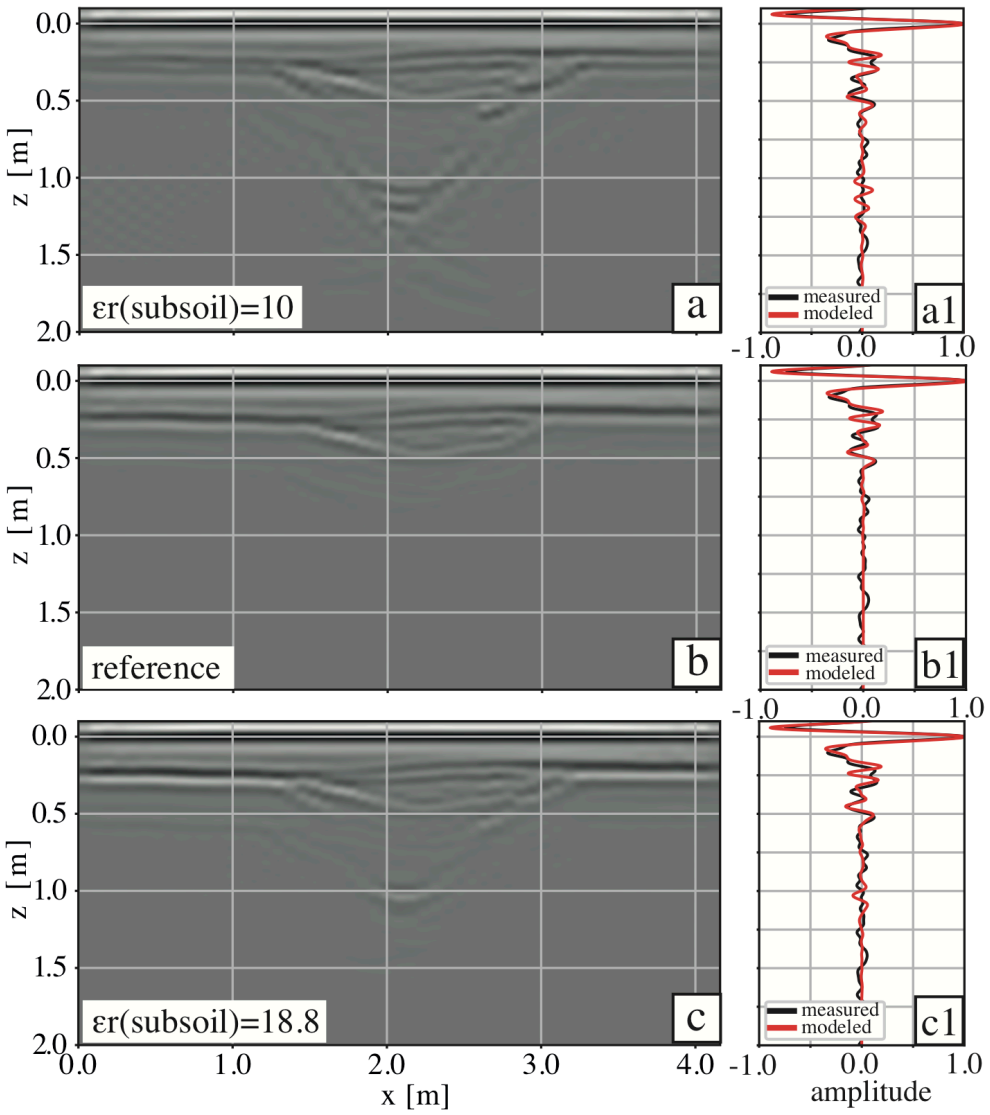

Fig. II.5.3: Comparison of the modeled data of the ditch profile 1 by assuming the subsoils permittivity $\epsilon_r = 10$ (a), $\epsilon_r = 14.4$ of the best fit model (compare fig. II.4.15) (b) and $\epsilon_r = 18.8$ (c). Profile (b) is also the reference profile for the misfit calculation shown in fig. II.5.4. Figures a1), b1) and c1) each show the trace comparisons between the measured and modeled data. The trace shown is in each case the sum trace from the middle area of the ditch over a width of about 30 cm.

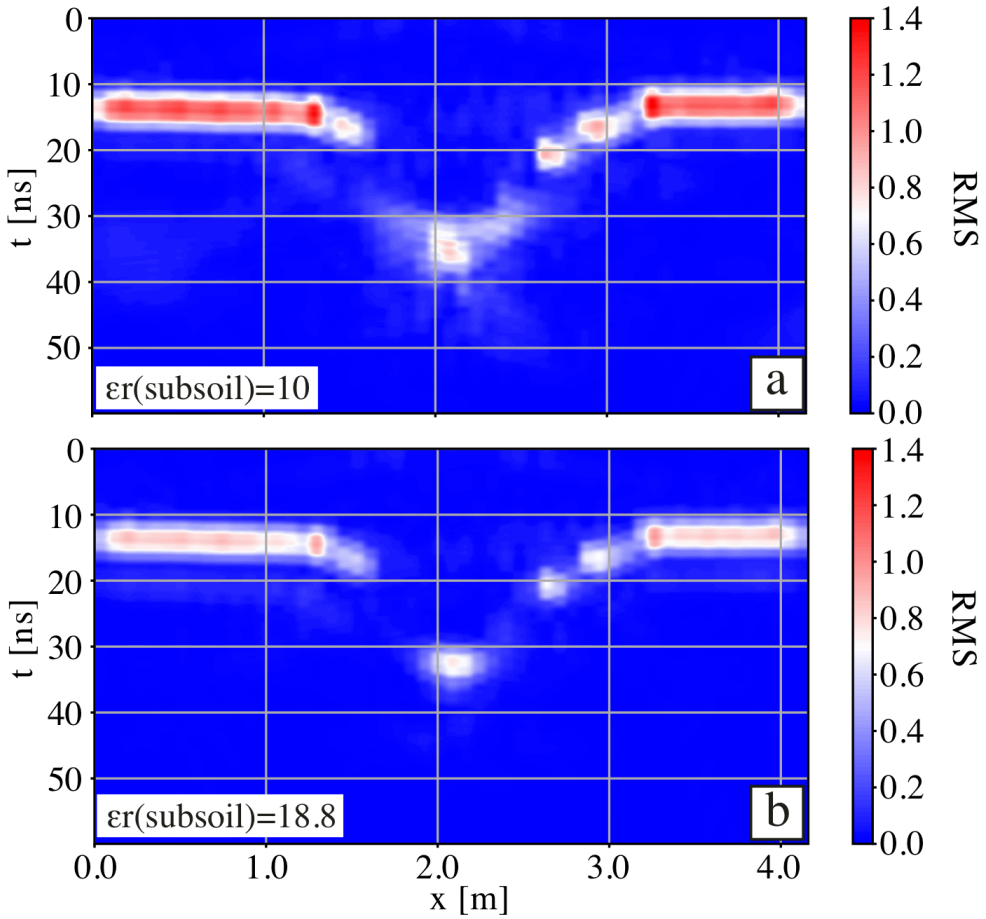

Fig. II.5.4: Moving root mean square (RMS) for the profiles (a) and (c) in fig. II.5.3. In (a) the moving RMS is shown for the profile with $\epsilon_r(subsoil) = 10$. In fig. (b) the moving RMS is shown for the profile with $\epsilon_r(subsoil) = 18.8$

Table II.5.3: Porosity values and water content for the site BH by considering a different sand content

layer	mean porosity	mean water content	mean relative permittivity
ditch phase 1/subsoil	41	26	14.4
subsoil	45	21	10
subsoil	45	33	18.8

Returning to the question posed at the beginning about the nature of the pit filling, the answer is that the bottoms of the pits must be drier than the surrounding soil. In this way, pit walls with a steeper slope can also be detected in the radar. In the example of the ditch, it can also be noted that the ditch phase with the higher sand content is the one that is detected in both radar and magnetics.

II.6 Conclusion

Although pit-like features are difficult to be detected with GPR or even magnetics, a direct comparison with the archaeological documentation gives a clear picture. A requirement of the ground conditions is that the surrounding material is sufficiently different from the pits filling to be detectable by geophysical measurements. After the considerations of pits and their detectability now the question of this part can be answered, namely what the pit filling must be like in order to be detected by radar as well as by magnetics. Soils of pits are different than the surrounding subsoil, since pits were refilled with different material at a later time compared to the formation of the soil. At the site BH, the pits that have been recognised in the geophysical data have a higher sand content. To be detected by GPR the pit filling is also drier than the surrounding soils, whereas the porosity is more or less the same. The modelling studies support this result.

In summary, the following conclusions can be drawn:

1. Ditch phase 3 is detectable with GPR and magnetics due to a higher sand content (about 5 % higher than the surrounding soils).

2. The porosity of the pit fillings directly beneath the subsoil is comparable to the surrounding soils, but the pit filling are about 6 % drier than the surrounding soils.

3. The ditch walls are detectable, if the angle of incidence is $24° \pm 7°$.

4. Neither the ditch walls nor the ditch filling of ditch phases 2 and 1 could be detected with GPR, due to the lack of soil properties contrast compared to the surrounding subsoil. The angle of incidence of ditch phases 2 and 1 are $35° \pm 10°$ and $50° \pm 11°$. The modelling showed that the probability of detecting the steeper ditch walls increases as the surrounding soil dries, for the same porosity.

5. The bottom boundary of ditch phases 2 and 3 are detectable.

6. The pit modelling shows, that decreasing the permittivity values of one layer provides a larger misfit, than increasing the permittivity of the same layer. Furthermore, the change of the permittivity values of the topsoil layers has the largest influence on the whole GPR trace. Also changing the permittivity values of the middle and deeper layers, have an influence on the upper part (means the area, which is caused by the presence of the topsoil layers) of the GPR trace.

The modelling study performed in this part of the thesis is a good example that the soil analyses, which were conducted before a GPR measurement can help to find an adequate starting model. To find the perfect model in particular for pits, a simple starting model is not enough, but nevertheless, the bottom of the pit was always

recovered. Soil analyses can help to create a starting model considering the porosity and water content of the soil type.

The result of part I of this thesis is that archaeological features containing stones can be better recognised when the surrounding soil is moist with about 30 % water content and a porosity of about 42 %. The result of this part of the thesis is that pits filled with dry soil can be detected very well in the geophysical data (GPR and magnetics), but also when the surrounding soil is dry, pits can be detected well (at least) in the GPR. Both results refer to the soil type sandy loam. This means that GPR measurements should take place under more humid conditions with about 30 % water content to detect stony (archaeological) features. To detect pit-like features it is better to wait for drier conditions to measure with GPR, means if the water content of the pit filling is at about 20 % or if the water content of of the soil is at about 5 % lesser than the pit filling. This part of the thesis shows, that soil analyses can help to better assess the soil.

The third part focuses on the ditch as a basis for understanding the use of the burial mound and for estimating the former height of it. For the third part of the thesis, it is helpful to realise that the ditch filling of the last phase of use is well recognisable in the GPR. The transition from phase 2 to phase 1 is also visible in the data, but less pronounced than the transition between topsoil and pit filling of phase 3 or even the transition between the pit filling of ditch phase 3 to ditch phase 2. The bottom of the pit filling of ditch phase 1 is no longer visible a first sight.

Part III

Reconstruction of a Burial Mound based on GPR Measurements

III.1 Introduction

Today it is common practice to carry out a geophysical survey prior to an excavation – in order to be able to excavate with precision, and to include possible further features in the barrow's immediate vicinity in the investigation. In Schleswig-Holstein, barrows are studied to obtain information about Bronze Age society. This desideratum is all the more urgent since, due to their poor preservation, little is known about Bronze Age settlements. Many studies of barrows or tumuli focus on stratigraphy and the investigation of the archaeological features inside. There are different approaches to geophysical investigation, including electrical resistivity tomography (ERT), seismic tomography or GPR. The main aims are localizing the grave, often by using seismic and electrical tomography, and the reconstruction of the stratigraphy using GPR (N. G. Papadopoulos et al. 2010, Tsourlos et al. 2014, Forte & Pipan 2008, Polymenakos et al. 2004, Schneidhofer et al. 2017). Seismic tomography is also applied if GPR is limited in its depth of investigation due to the height of the barrow (Forte & Pipan 2008). Stratigraphic studies are important due to the barrows' long use, since it provides information about the archaeological utilization phases. Nevertheless, to investigate the stratigraphy, the barrows have to be preserved in height. The object of interest situated in Bornhöved (BH in the following) is eroded up to a remaining height of about 0.1 m (this is the artificial part of the barrow), limiting our stratigraphic investigations. One of the archaeological questions when examining an eroded barrow concerns the former height and the amount of material used to create the barrow. The standard assumption is a hemisphere from which the height volume were estimated. From Schaefer-Di Maida it is known, that the shape of well-preserved burial mounds is that of a bell (Schaefer-Di Maida 2019). Here the focus is on the surroundings of the burial mound, by which we mean the ditch surrounding the barrow and the colluvium.

As part of the CRC 1266 "Scales of Transformation" a barrow (LA 117) at the site BH was investigated with geophysics (3D GPR and magnetics), soil analyses and archaeological excavations. LA 117 has a diameter between 12 and 13 m. As explained in part II of this thesis, LA 117 was erected in the late Neolithic Age. The primary burial was a burial pit. Secondary burials from the Bronze Age could not be observed. Bronze Age burials are typically tree coffins set upon the surface and covered by soil to form a barrow. The barrow LA 117 was surrounded by a ditch, which shows three opening or re-filling phases. Furthermore, a colluvium of about 0.7 m thickness could be observed archaeologically in three profiles around the burial mound. Archaeologically, this layer is interpreted as eroded material from the burial mound. Since the archaeological documentation could not provide information about the extent of the colluvium, the comparison of the archaeological documentation with the GPR data is needed in order to identify it in the data set. In part II, it was mentioned that 15 profiles crossing the ditch were archaeologically documented. The information from these profiles was also used in comparison with the GPR data set to identify the ditch in each profile to get

detailed information about width and depth of the ditch per phase.

In this part, our approach is to investigate the vicinity of the barrow to document the colluvium, which will help us estimate the amount of material used to erect the barrow. Another question concerns funeral practices. Since the only burials observed were Neolithic, with no further Bronze Age burials, the question arises whether these burials are already eroded and if the material dug up in each ditch phase could have been used to cover a secondary burial, which necessarily also would raise the barrow. Therefore, the questions, which are addressed in this part are (1) whether it is possible to reconstruct the former height on the basis of the volume of the ditch phases by considering the angle of repose for typical soil materials and (2) whether the ditch material per phase could have been used to cover up a secondary inhumation.

The ditch phases are seen as an indication of the phases of usage of the barrow and give an estimate of its former height. The 3D GPR data set of the site BH is the basis for selecting the layers. In part II, it was found that the last ditch phase (phase 3) could be well detected with the GPR. The bottom of the ditch phase 2 can be seen as well, but not so clear. The edges of the ditch phase 2 could not be detected. Therefore, we analysed some GPR attributes to highlight the ditch. The edges and bottom of ditch phase 1 are not distinguishable from the surrounding soil.

Several approaches to estimate the former height will be applied. First of all, bell-shaped functions are used to estimate the former height based on the ditch phases. By taking into account the angle of repose for the materials typically used in Bornhöved, e.g. sand, gravel and sand-gravel mixtures, the maximum possible height will be determined. In addition, the former height is estimated on the basis of a spherical cap. The hemisphere as a special case is used to assess the plausibility of the determined volume of colluvial layers. Finally, both assumptions (bell shape; spherical shape) were compared with the most stable geometric form of a cone, since this is the typical form for artificial material deposits, e.g. in mining.

In the following, the methods and approach used to answer the questions stated above will be presented and explained. To be discussed are data acquisition and processing, the selection procedure and the equations and functions used for calculations of height and volume. In the section on results, the height based on the determined volume of the ditch phases will be determined by assuming the bell-shape and spherical cap. In addition, the stability criterion was used to determine the maximum possible height of the barrow, based on the bell shape and spherical cap. This will be compared with a cone. There follows a discussion of the height and volume estimates. Finally, the question whether there was only one burial per phase will be answered.

III.2 Methods

III.2.1 Data Acquisition and Processing of Ground-Penetrating Radar (GPR) Data

A 16 channel MALA Mira system was used (Guideline Geo AM [Publ] MALA & ABEM), which can collect a 3D data set due to its channel distance of 8 cm. An RTK-DGPS (Leica) was used for positioning. Processing steps applied are: (a) time zero shift, (b) correction for spherical divergence and attenuation (σ=1.23 mS/m; ϵ_r=14), (c) subtraction of a mean trace to remove horizontal lines, (d) bandpass filtering (from 100 MHz to 700 MHz) (e) topographic migration (Wilken et al. 2016), and (f) time-to-depth conversion. The velocity for migration (v=0.08m/ns) was determined by test migrations.

III.2.2 Picking Process

To pick the reflection horizons, the software Kingdom Suite (version 2018) was used. Along each profile the relating horizons are picked. As already shown, the bottom of ditch phase 3 is recognised very well. Ditch phase 2 is hard to see, that is why the temporal derivative of the envelope of the GPR amplitude was used to pick this phase (in the following called "power" [Bittner & Rabbel 1991]). To create a surface, the picked horizons are interpolated using flex gridding in Kingdom Suite (Markit n.d.). The grid has a mesh width of 0.6 m in both (x and y) directions. Afterwards, the data are again interpolated in Surfer (version 9) to obtain a smoother surface. Here, the "natural neighbor" gridding method was used (mesh width: 0.2 m in x and y-direction for plotting the phases of the mound and 0.6 m in both directions for plotting the colluvium) (Golden Software Inc. 2002).

To reach an estimate of the former height, the ditch phases (fig. III.2.1a-b) and the colluvium (eroded material from the barrow – represented by the red areas in fig. III.2.1c) are picked. This was done by comparing GPR profiles with the archaeological documentation. 15 profiles crossing the ditch were documented during the excavation (Kneisel, Schaefer-Di Maida, et al. (in prep.)). Since ditch phase 2 is not easy to detect, some GPR attributes were analysed to enhance the identification of this phase. The most promising attribute is the temporal derivative of the envelope (called "power" [Bittner & Rabbel 1991] in the following). This decision was based on the comparison between attribute analysis and archaeological documentation.

Considering the colluvial layers, the two crossing profiles (in the north-south and west-east direction), that cover the barrow, are used. In the west, north and east profile sections, colluvial layers could be observed that are compared with the GPR profiles and used to identify them in the whole data set. Always the bottom of

the phases and colluvial layers are picked in order to obtain the volume from top to bottom of the ditch (the volume of the dug material for each opening phase) and from surface to bottom for the colluvial layers.

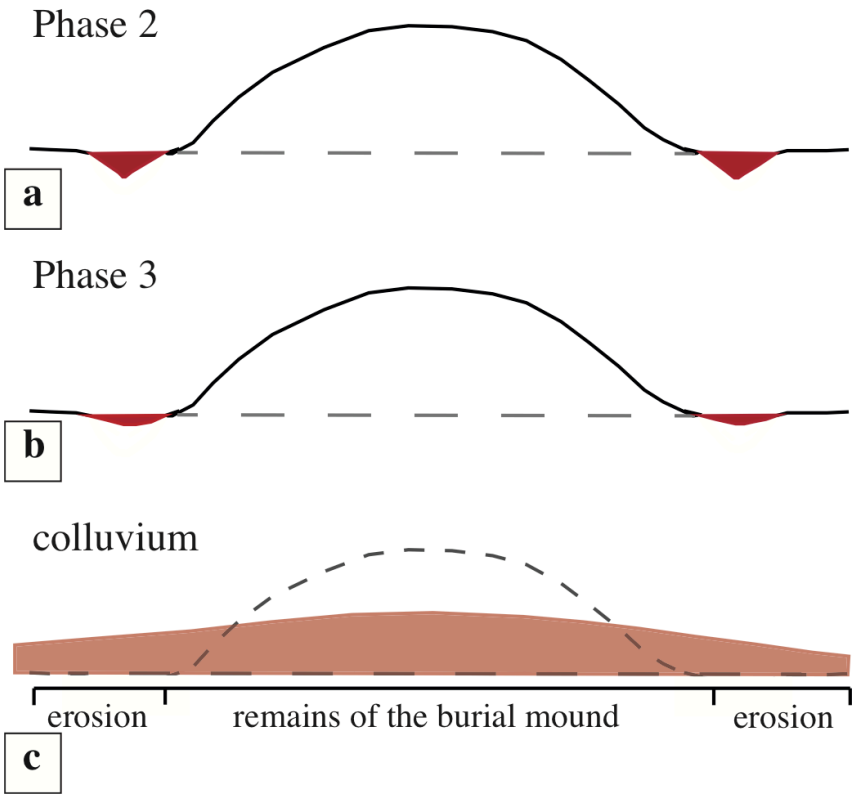

Fig. III.2.1: Schematic presentation of the phases and colluvium of the barrow together with the ditch. (a) shows the ditch phase 2 and (b) phase 3. (c) shows the eroded material of the barrow, which was documented as colluvium. The bottom was consistently selected in the GPR profile.

III.2.3 Estimating the Height and Volume of the Barrow

After picking of the horizons and interpolation over the whole area, the volume was determined using the Surfer (version 9) software. The volume was calculated between two layers. The volume of phase 2 and phase 3 is assumed to consist of the matter between the topsoil and the bottom of the next phase (as it is shown in fig. III.2.1a-b). The volume of the colluvium is the amount of material between the base of the colluvium and the surface (as shown in fig. III.2.1c). To estimate height, four different shapes (fig. III.2.2) are compared: a hemisphere, a spherical cap, three bell-shaped functions (paraboloid, bell-shaped membership function and bump function) and a cone, the shape typical for deposits of material (e.g. sand or gravel) in mining.

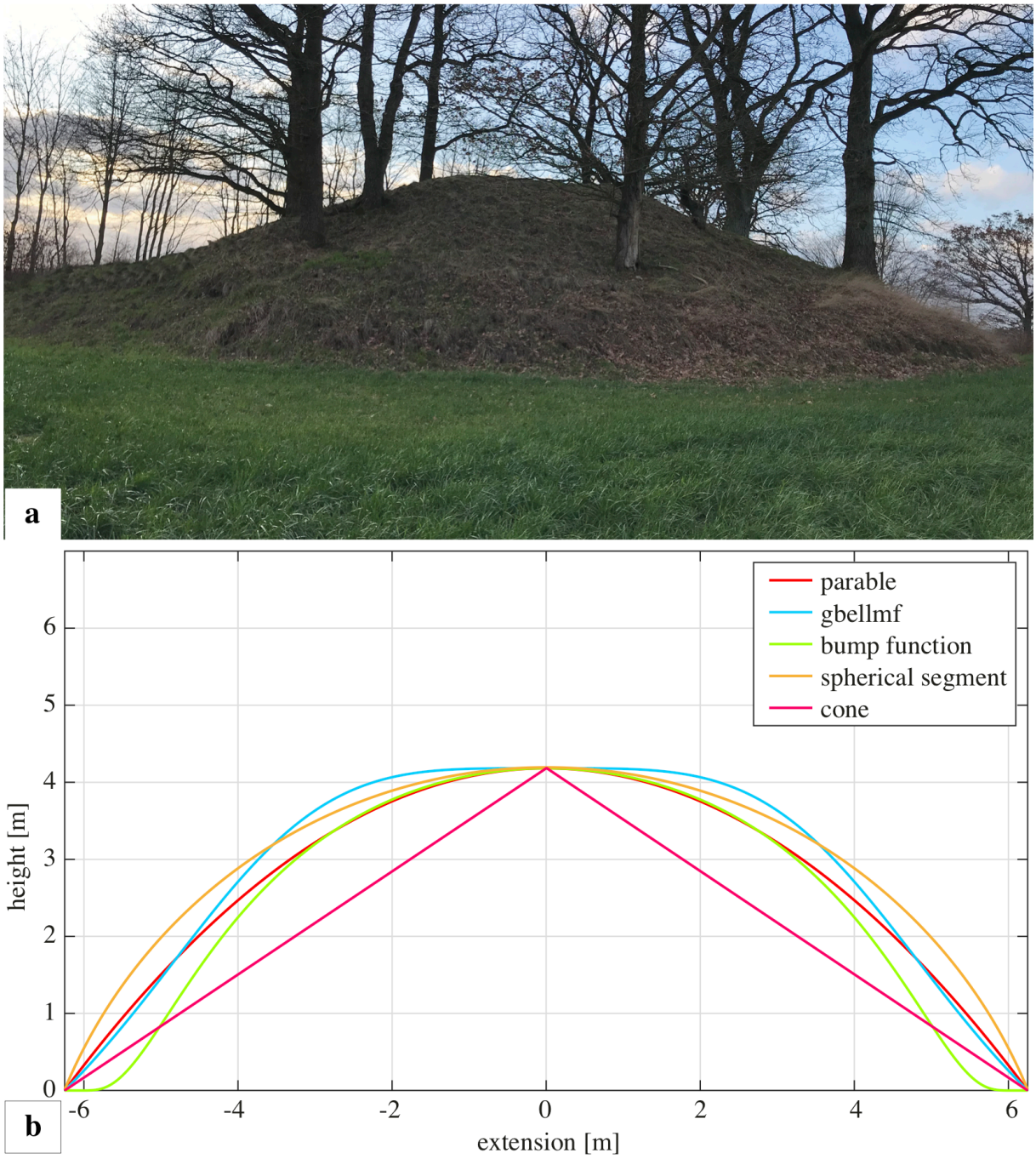

Fig. III.2.2: Photography of a burial mound in Schmalensee, with a height of 4.18m ((a), photograph by Schaefer-Di Maida). (b) shows the bell-shaped functions (parable, generalized bell-shaped membership function (gbellmf) and the bump function), the spherical segment (orange line) and the cross-section of a cone (pink solid line). The maximum point of these functions equals the height of the burial mound shown in (a).

III.2.3.1 Assumption of a Bell-Shaped Form

Three different bell-shaped functions were chosen to represent the former shape of the burial mound: a parable, the generalized bell-shaped membership function and the bump function. The parable is sharper than the more spherical bump function. The generalized bell-shaped membership function has a plateau and

is similar to the photograph in fig. III.2.2a. The mathematical description is listed in table III.2.1.

Table III.2.1: Mathematical description of the used bell-shaped functions. The parameters b, c, d, p and s are explained in the appendix in chapter A.3

Function	2D	3D	parameters
parable/paraboloid	$f(x) = -\frac{1}{a} * x^2$	$f(x,y) = -\frac{1}{a} * (x^2 + y^2)$	
modified generalized bell-shaped membership function	$f(x) = \frac{a}{1+(\frac{x^2-c}{d})^{2b}}$	$f(x,y) = \frac{a}{1+(\frac{(x^2+y^2)-c}{d})^{2b}}$	b=1 c=0 d=30
bump function	$f(x) = a * exp(-\frac{p}{s^2-x^2})$ for -s < x < s; $f(x) = 0$ else	$f(x,y) = a * exp(-\frac{p}{s^2-(x^2+y^2)})$	p=35 s=6.251

As parameterization for the 3D visualization $x = r * cos(\theta)$, $y = r * sin(\theta)$ was used. r represents the radius ($0 \leq r \leq 6.25$ m) of the "barrow's" base and θ the rotation angle (ranging from $0 \leq \theta \leq 2\pi$). The parameter a influences the vertical extension of the function, but is not the height.

The parameters b, c and d for the bell-shaped membership function as well as the parameters p and s were varied and the most suitable regarding the similarity to a burial mound shape was then used and listed in table III.2.1. The most subjectively chosen values are those for parameter d and p.

Volume determination:
The volume of these functions was determined by using the matlab tool "convex hull" (convhull, Mathworks® MATLAB R2019b), which calculates the volume by determining the convex hull of all points of the 3D function (for details see O'Rourke 1998). The condition for varying the shape of the bell-shaped functions was to vary parameter a in table III.2.1. The height is always the maximum point of the function if the base is at 0.

III.2.3.2 Assumption of a Spherical Shape

The spherical cap was used to estimate the former height based on the volume of the ditch phases. The basic principal is an iterative approach to make the volume V of the spherical cap fit the determined volume of the ditch phases V_i by varying the height h of the spherical cap. The volume V of a spherical cap with the height h of the spherical cap and sphere radius R (this is a radius of a theoretical sphere, see fig. III.2.3b) is defined as

$$V = \frac{h^2\pi}{3} * (3R - h). \tag{III.2.1}$$

To calculate the radius R of the sphere the formula

$$R^2 = (R - h)^2 + r^2 \tag{III.2.2}$$

is used, with r being the radius of the spherical cap, in the case of the ditch $r = 6.25$ m (see fig. III.2.3b; Scheid & Schwarz 2017).

Additionally, a hemisphere was used to determine the maximum possible volume that could have been eroded by the barrow. This is then used to assess the amount of the picked colluvium. For calculating the maximum volume, the height h equals the sphere radius R and radius of the spherical cap r: $h = R = r$ (fig. III.2.3a), which is a hemisphere.

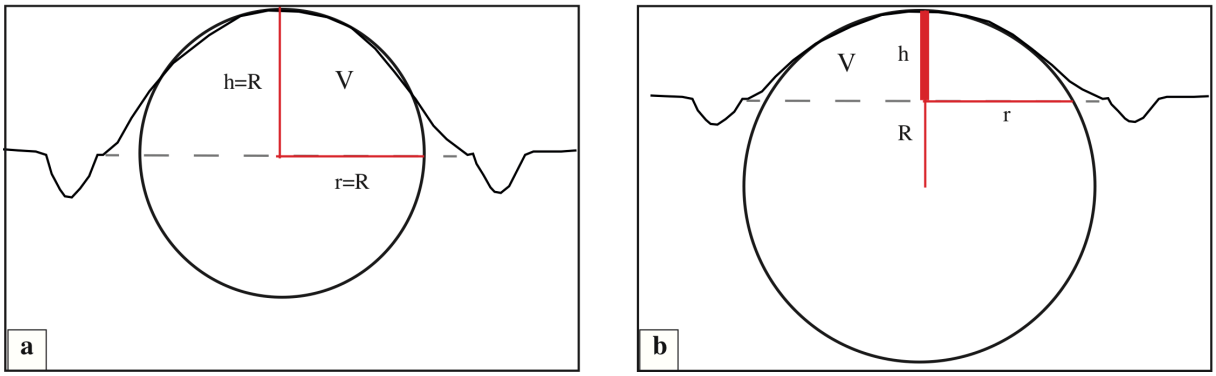

Fig. III.2.3: Scheme of the barrow, assuming a spherical shape. (a) shows the case of the barrow being a hemisphere. R (sphere radius) would be identical with the radius of the barrow base and height of it. The volume of the material would be the largest. (b) shows the case of the barrow being a spherical cap. r is the barrow's base, h the height of the spherical cap and R the radius of the sphere, which is larger, than the barrow's base.

III.2.3.3 Assumption of a Conical Shape

With regard to the angle of repose, a cone is a very stable shape for artificially deposited material. The equation for calculating the volume is $V = \frac{1}{3} * \pi * r^2 * h$. h is the height of the cone and r the radius of its base ($r = 6.25m$).

III.2.3.4 The Angle of Repose as Stability Criterion

To derive the maximum possible heights for the different geometric forms, the angle of repose was used as a stability criterion. Experiments showed that typical angles of repose for sand, clay and gravel are in the range of 30 to 45 degrees (see table III.2.2). In general, experiments show a dependence on particle shape and size, surface friction and the condition of the base (rough or smooth) (Liu 2011, Zhou et al. 2002, Carrigy 1970). With regard to sand-gravel mixtures, it was found that the higher the content of sand, the lower the angle of repose (Liu 2011). Wang et al. were moreover able to establish that the higher the compaction, the larger the angle of repose, which in turn is reduced by larger grain sizes. In laboratory tests they found a maximum angle of repose of 46.2° by considering grain sizes of sand, gravel and the cobble fraction (100 mm) (Wang et al. 2013). In the following, an angle of 45° was assumed as the maximum possible angle.

Table III.2.2: Showing the angle of repose for clay, sand and gravel from different literature

Material	Angle of Repose [°]
Sand-Gravel Mixture (Liu 2011)	24-32
Sand, dry	35 (Carrigy 1970) 15-30 (Glover 1997)
Sand, wet	43 (Carrigy 1970) 45 (Glover 1997)
Sand (Nakashima et al. 2011)	28-31
Clay, dry lump (Glover 1997)	25-40
Earth (Glover 1997)	30-45
Gravel, crushed stone (Glover 1997)	45
Gravel, natural (Glover 1997)	25-30

The angle of repose α is determined by using the equation $tan(\alpha) = m$, with m being the slope of the function at a specific point. This is the first derivative of the function $\frac{df(x)}{dx}$. In the case of the bell-shaped and bump functions $f(x)$ is defined as shown in column 2 of table III.2.1. For the spherical cap $f(x) = \sqrt{(}r^2 - x^2)$. From these functions the first derivative is than determined. The angle of repose for a cone is calculated by $tan(\alpha) = hr$. Assuming a maximum angle of repose of 45°, the height would equal the radius $h_{max} = r$ (Bronstein et al. 2012).

III.3 Results

The identification of all ditch phases is necessary to determine volume and height of the barrow. The archaeological documentation was also the basis for picking the ditch phases and colluvium. In the following the results of the picking process will be presented and the determined volumes and 3D reconstructions of ditch phases 2 and 3. For ditch phase 1 an estimate of the volume can be given only on the basis of the determined volume of ditch phase 2, since it is difficult to identify the ditch's bottom in the radar data. Afterwards the possible heights of the barrow using different geometric shapes are calculated.

III.3.1 Picking of GPR Reflections

III.3.1.1 Ditch Phase 3

Phase 3 was chosen from the reflections of the same intensity because it was easy to identify due to its depression and the negative reflection amplitude caused by the higher porosity of its soil (blue dashed line in fig. III.3.1a). Identification in all profiles was possible by comparing archaeological documentation with the data and extrapolating the information to all relevant GPR profiles.

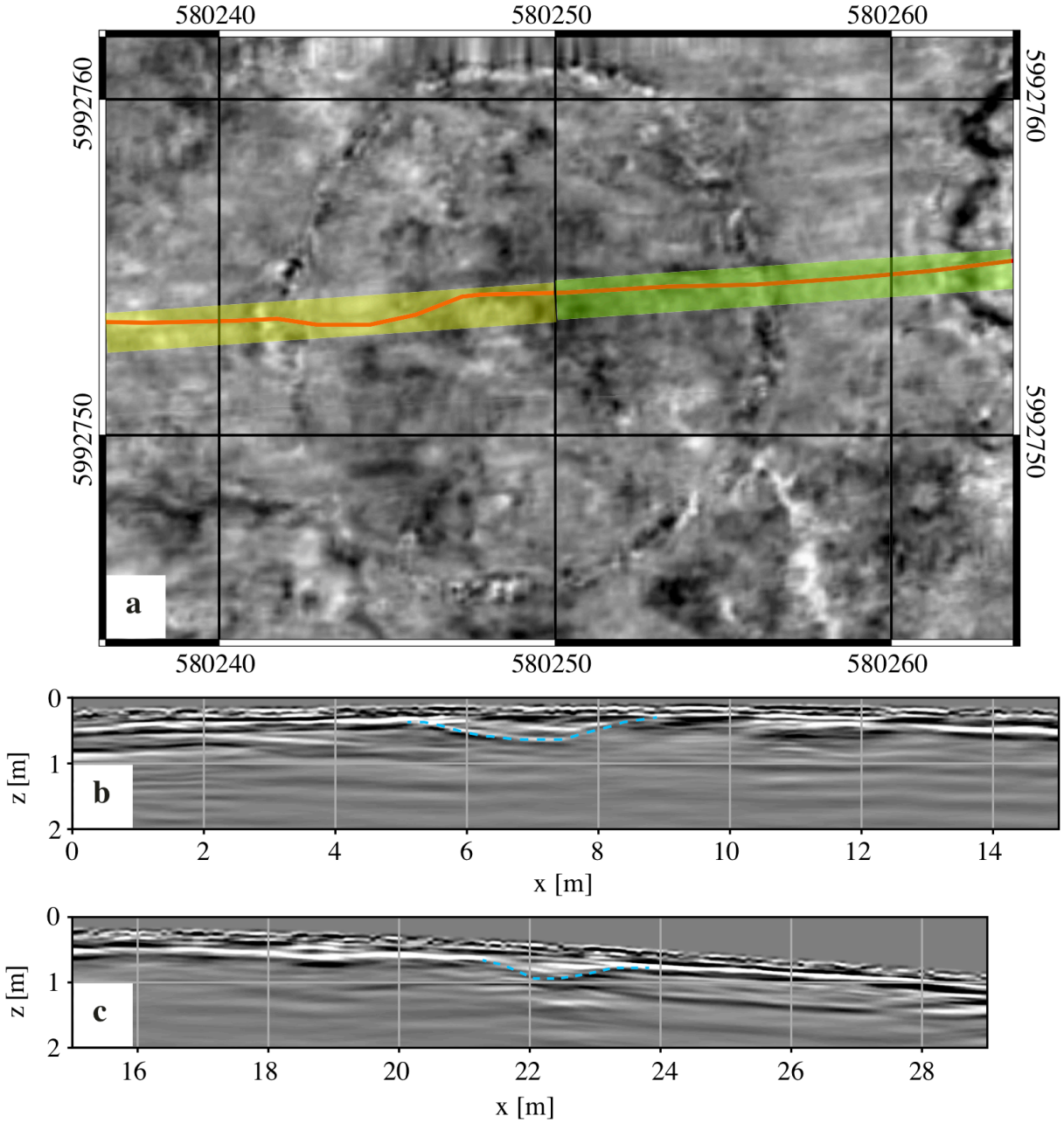

Fig. III.3.1: Example of how phase 3 was picked (blue dashed line in (b) and (c)), divided in the western ((b), yellow rectangle in (a)) and eastern half ((c), green rectangle in (a)), together with its position (a).

III.3.1.2 Ditch Phase 2

To pick phase 2, the temporal derivative of the envelope of the GPR amplitude was used (in the following called "power" [Bittner & Rabbel 1991]). The ditch appears as a local disturbance of the strong reflections in the power profile (fig. III.3.2b,c). In comparison to the archaeological documentation, the local disturbance is smaller than the width of the ditch. It was decided to pick only the local disturbance (fig. III.3.2b,c, blue dashed line).

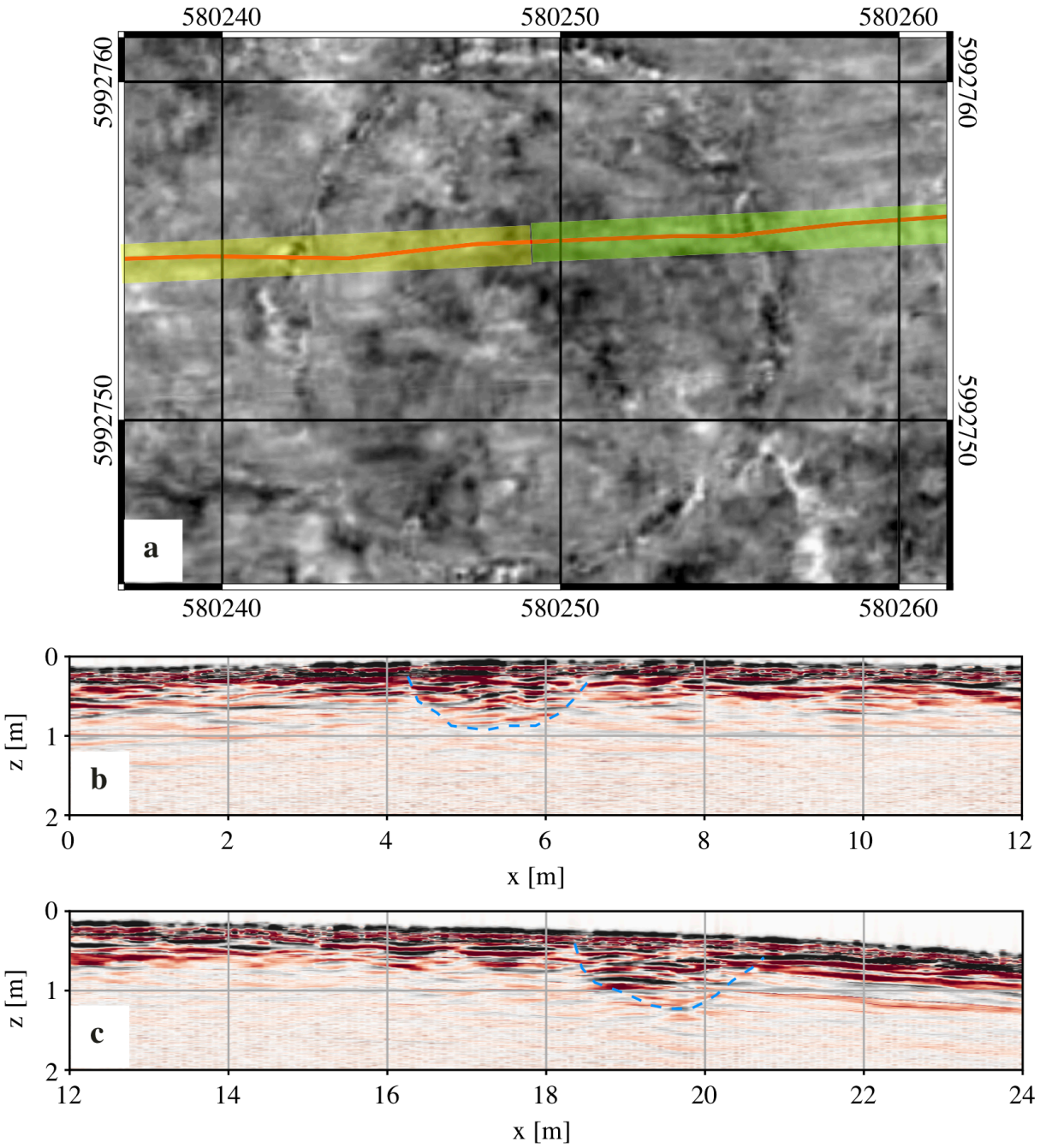

Fig. III.3.2: Example of how phase 2 was selected (blue dashed line in (b) and (c)), divided in the western (b, yellow rectangle in (a)) and eastern half (c, green rectangle in (a)), together with its position (a).

III.3.1.3 Colluvium

Colluvial layers were observed in three of the archaeological cross-profiles, in the west, north and east (highlighted with red lines in fig. III.3.3a). Figure III.3.3b shows the eastern profile as an example, but the information of the other two profiles was used as well. The bottom of the colluvium was chosen for its positive amplitude. The profile in the south was disturbed by the previous excavation from 2017, precluding the archaeological observation of ancient layers. This means that it is not known if colluvial layers might have

been observed here too (black line in fig. III.3.3a).

The analysis of these profiles shows, that the colluvium is the horizon between the topsoil and the geological environment, which consists of gravel layers (orange dashed line in fig. III.3.3c,d) and loamy horizons (lowermost orange line in fig. III.3.4d). The transition between colluvium and geological layers shows strong reflection energy followed by very low reflection energy and could therefore be detected very well in all profiles (fig. III.3.4b,c). Sometimes it was difficult to recognize the beginning of the colluvium on the side facing the hill. In this case, only the layer that could clearly be identified was picked. Additionally, the archaeological profiles cover almost the whole measurement area and show that the colluvial layers do not thin out at the edges (fig. III.3.3b), which means that the extent of the colluvial layers must be larger than the extent of the measurement area. To assess the extent of the colluvial layers beyond the measurement area, it was decided to calculate the thickness of the picked colluvium (fig. III.3.4d).

The colluvial layer could be detected around the barrow with the exception of the southwest. Due to the local topography, it is relatively flat in the west and southwest (see fig. II.4.6a). The colluvial layers thin out very fast in the southwest. During picking it turned out that also the colluvial layers thin out before the excavation trench of 2017. Therefore there is no reason to suppose that the 2017 excavations caused information loss in this section. By comparing fig. III.3.4d one can see that the measurement area is smaller than the extent of the colluvium. The layers of the greatest thickness are expected to be in the northwest and southeast (up to 0.7 m). This is because it correlates with direction of the latest ploughing of this field. Additionally, the eastern half of the measured area shows a relatively strong topography (see fig. II.4.6a) causing a natural erosion in this direction (northeast, east and southeast) too. Considering the flat topography in the west and the ongoing ploughing procedure, one would expect the amount of eroded material outside the measurement area to be larger in the west and northwest than in the eastern half.

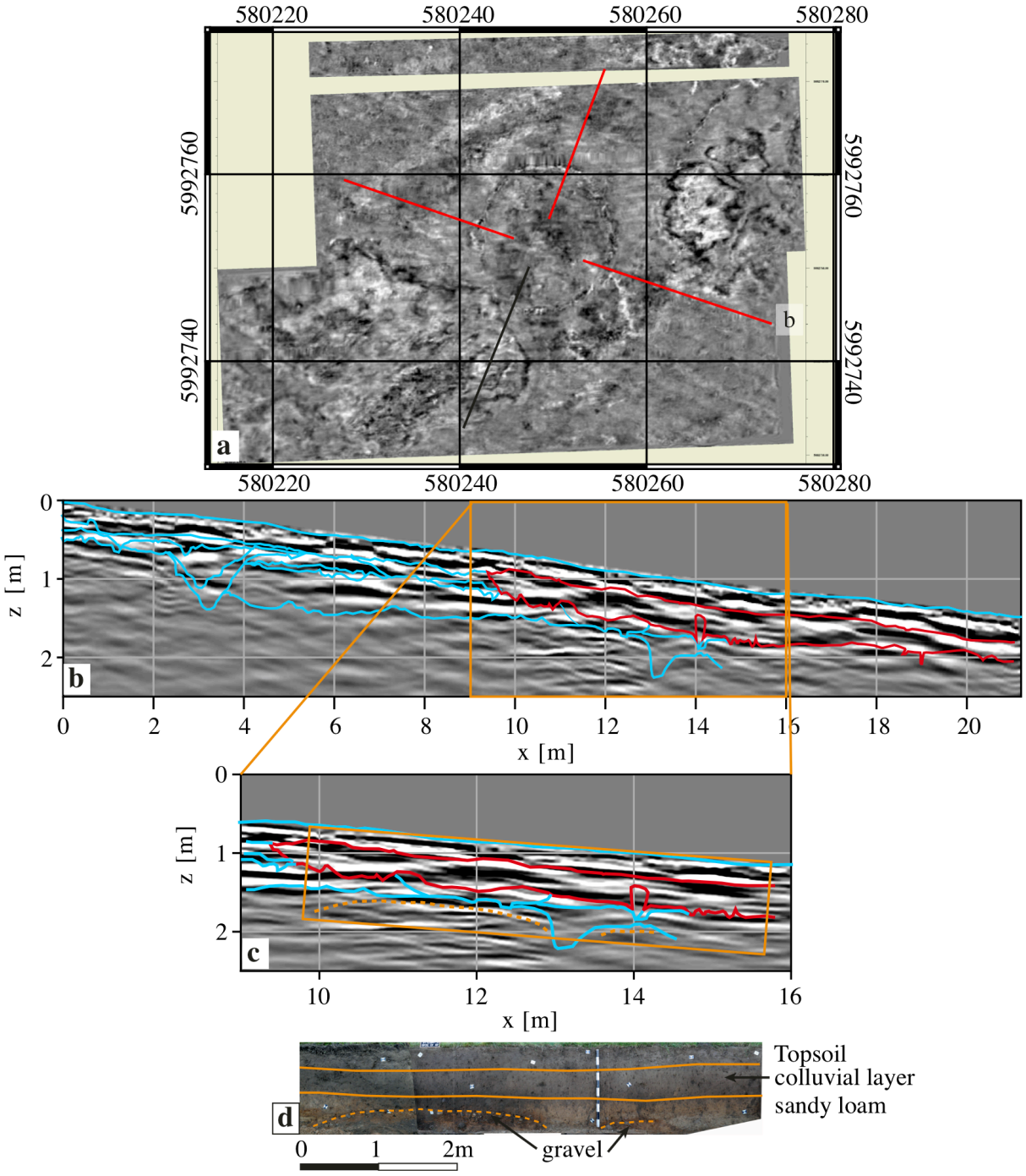

Fig. III.3.3: Position of the cross profiles covering the whole extension of the burial mound (a). Three of the profiles (in the west, north and east – red lines) show the colluvium (eroded material of the barrow). The blue lines in the profile (b) and (c) indicate the archaeological documentation, in red the colluvial layer is highlighted. The profile in (b) and (c) is superelevated by a factor of 1.8. (c) is showing a section of the GPR profile with gravel layers at its base, which can be compared with the photograph taken at this position (photograph by Kneisel) (d). The orange dashed lines in (d) indicate the main layers – topsoil and colluvial layer beneath as well as the sandy loam at the bottom. The orange dashed lines mark the position of the gravel layer. This layer is marked in the GPR profile section of (c) above.

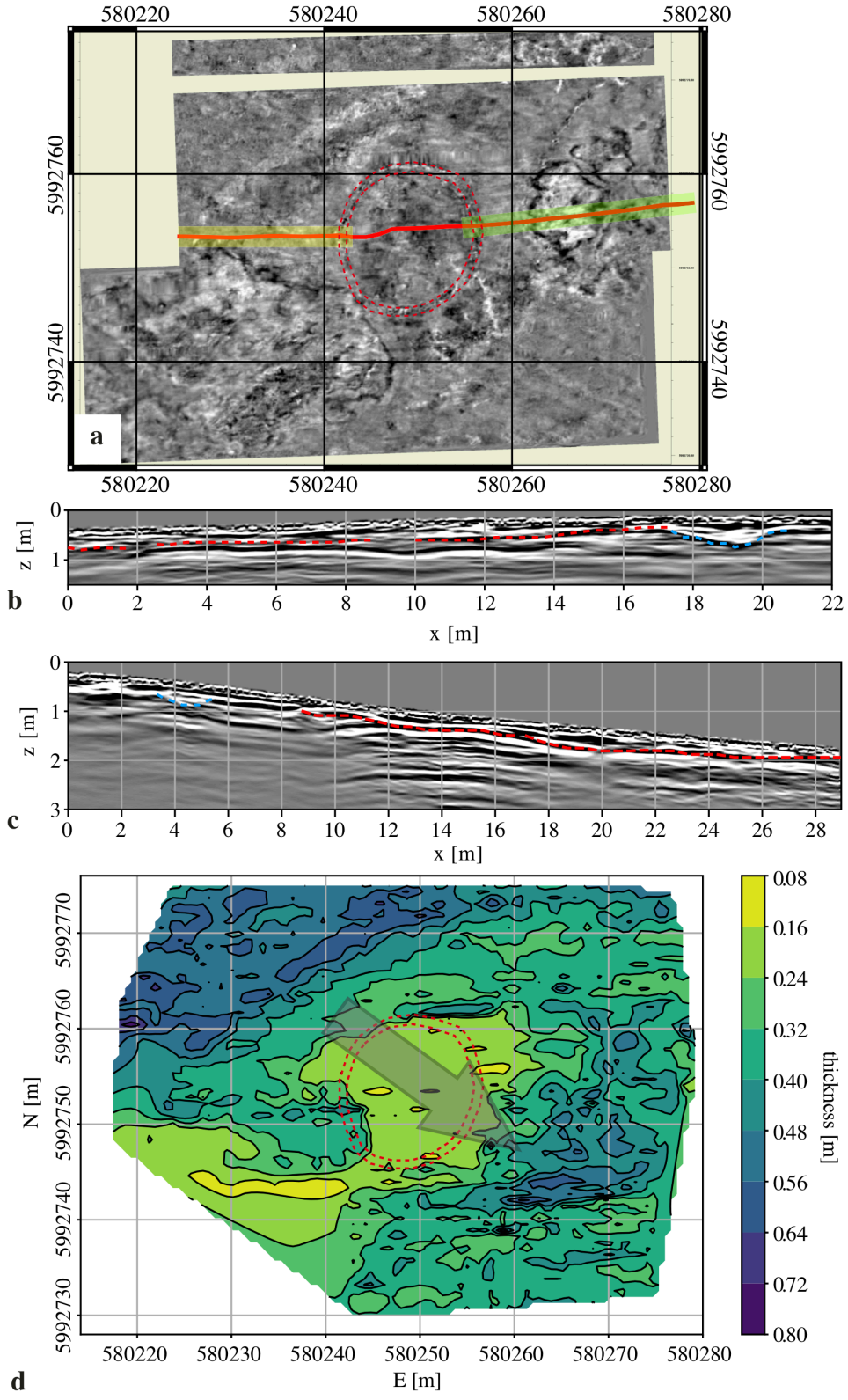

Fig. III.3.4: Example of the picked colluvium divided in the western ((b), yellow shaded rectangle in (a)) and eastern part ((c), green shaded rectangle in (a)), together with its position in the time slice (a). d) shows a map of the colluvium thickness together with the position of the ditch (red dashed line) and the most recent ploughing direction (indicated by a gray shaded arrow NW-SE).

III.3.2 Determining of the Volume on the Basis of Picking the Horizons

III.3.2.1 Ditch

From the picking of phases 2 and 3, a volume of 48 m^3 for phase 2 and 16 m^3 for phase 3 could be determined. Figure III.3.5 shows the 3D reconstruction on the basis of the picking for phase 2 (fig. III.3.5a) and 3 (fig. III.3.5b) together with a depth profile crossing the barrow to obtain a sense of the topography (fig. III.3.5c). The ditch of phase 1 has an average depth of 1.2 m beneath the surface. Assuming the topsoil-ditch boundary to be the upper limit of ditch phase 1 one would have a total depth of 0.9 m, assuming the topsoil to be 0.3 m thick. The ditch of phase 2 has a depth of 0.8 m beneath the surface. Making the same assumptions as was done for phase 1, the ditch of phase 2 had a total depth of 0.5 m. This is at least about 56% more material for phase 1 than for phase 2 and would result in about V=26.6 m^3 more material (starting from V=48 m^3), having in total an estimated volume of V=74 m^3 for phase 1. In total an amount of **V=138 m^3** may have been used to raise the barrow, if one assumes that the ditch was reopened completely before a new phase of usage of the barrow (check table III.3.1).

Table III.3.1: Results of the determined volumes of the ditch phases

	volume [m^3]
ditch phase 1	74
ditch phase 2	48
ditch phase 3	16
total	**138**

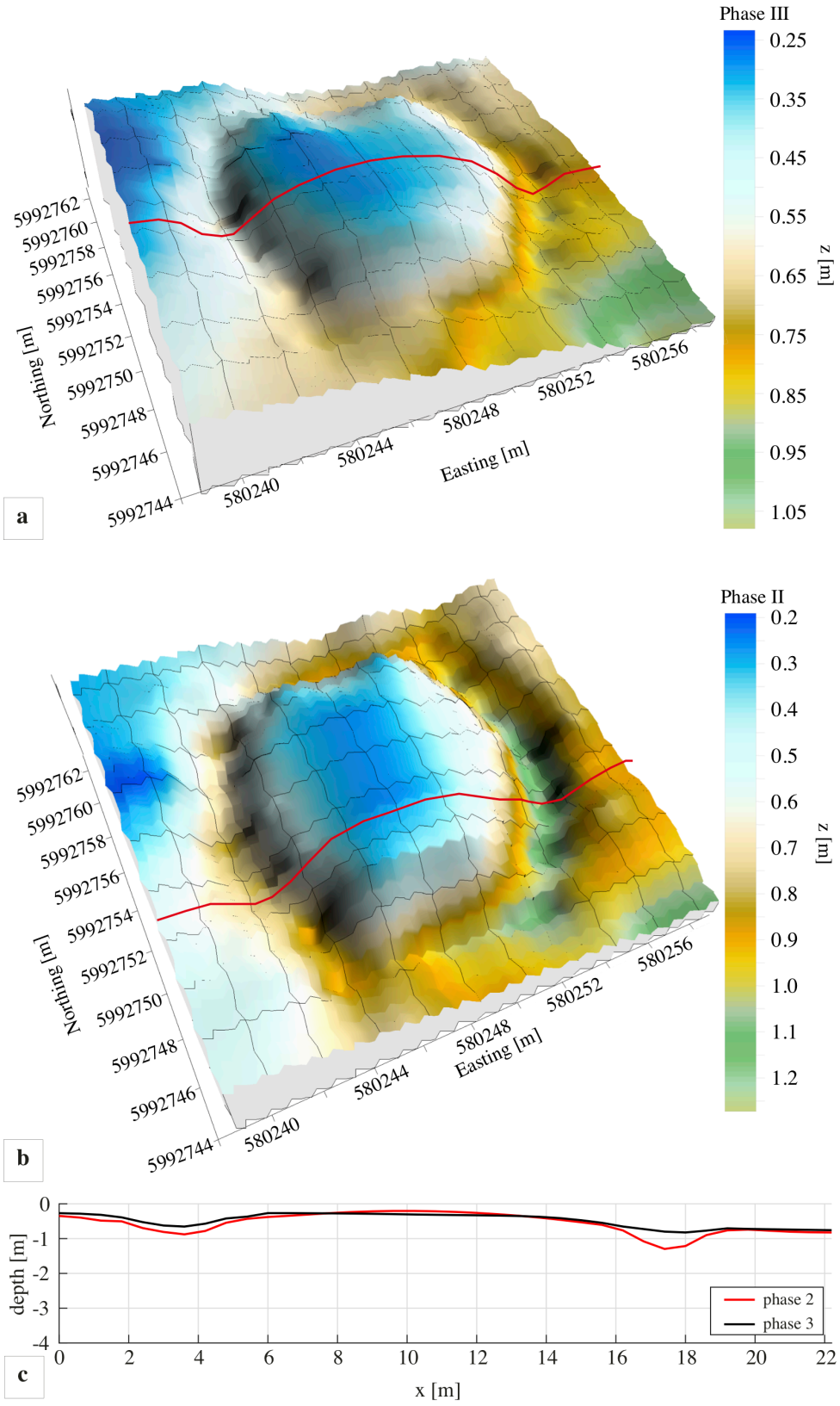

Fig. III.3.5: Resulting 3D reconstruction of phase 3 (a) and 2 (b) (plotted with Surfer 9, Golden Software Inc.) together with the depth profile of both phases ((c); red: phase 2; black: phase 3).

III.3.2.2 Colluvium

As explained above, the detected eroded material is just a part of the whole eroded material. Additionally, the picking of layers in the whole measurement area is based on the archaeological documentation in three cross profiles (see table III.3.2). Therefore the volume calculation is just an estimate. With regard to the picked colluvial layers, a volume of **V=843 m^3** could be determined.

Table III.3.2: Results of the determined volumes of the colluvium

	volume [m^3]
colluvium	843

III.3.3 Mathematical Determination of Volume and Height

III.3.3.1 Bell-Shaped Functions

III.3.3.1.1 Volume and Height on the Basis of the Ditch Phases

By varying the parameter a (see section III.2.3.1 of this part of the thesis) the volume V could be matched (calculated by using the matlab function "convhull") with the already determined volumes V_i per phase (i=1-3) after picking. After matching the volumes, the height could be determined by using the maximum value of each function. The resulting parameters a can be found in table III.3.3.

Table III.3.3: Resulting parameters a

ditch phase	parable	bell-shaped membership function	bump function
1	32.31	1.80	3.14
2	19.69	2.95	2.11
3	17.42	3.33	5.83

In table III.3.4 the resulting heights are listed per ditch phase and bell-shaped function together with an average height and its standard deviation. Accordingly, the barrow would have been 1.20±0.08 m high during phase 1. Subsequently the barrow would be raised about 0.80±0.05 m more and, after the last phase, only another 0.30±0.02 m. If one assumes the ditch to have been completely refilled with material after each phase and needed to be dug up completely for each opening phase, and that no erosion took place, then the burial mound would have reached a total height of **2.3±0.2 m** by using the material dug up from the ditch alone. Figure III.3.6 shows the final shape of the barrow after all phases in 3D (fig. III.3.6a-c) and 2D (fig. III.3.6d) as a cross section by using the bell-shaped functions.

Table III.3.4: Resulting heights [m] by fitting the determined volumes of the ditch phases

ditch phase	parable	bell-shaped membership function	bump function	height [m]
1	1.2	1.1	1.3	1.20±0.08
2	0.8	0.7	0.8	0.80±0.05
3	0.3	0.2	0.3	0.30±0.02
total	**2.3**	**2.1**	**2.4**	**2.3±0.2**

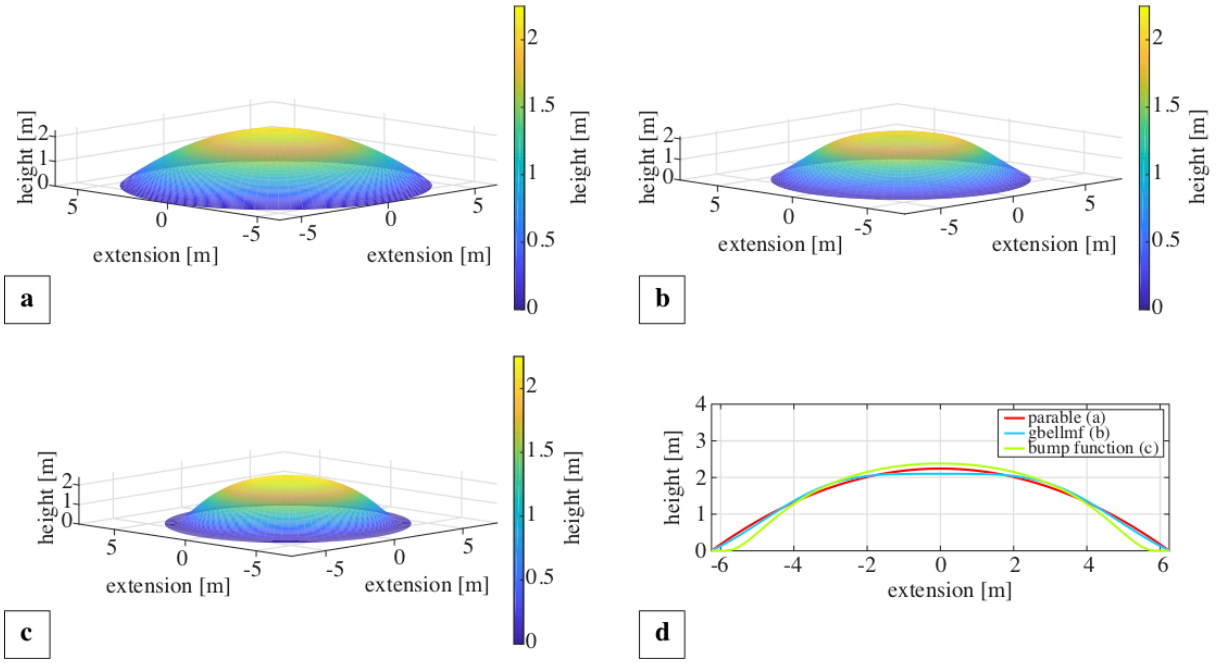

Fig. III.3.6: Reconstruction of the former barrow using bell-shaped functions and assuming the total height. The total height is the sum of all heights resulting after erecting the barrow after each opening phase of the ditch. (a) shows the barrow having a parable shape, (b) is the result by using the generalized bell-shaped membership function (gbellmf) and (c) the bump function. (d) shows a 2D cut through the "barrow" represented by the chosen bell-shaped functions.

To evaluate the stability of the barrow also the slopes of the "theoretical" barrows and its phases were analysed. This is shown in fig. III.3.7. It can be seen that the barrow is very stable after each opening phase (fig. III.3.7a-c). If the total volume at the end of all three phases is used, one can see that the limit of stability is almost reached (fig. III.3.7c). The bump function in particular is critical, since its maximum slope (at the edges) is about 41° after opening phase 1. Nevertheless, the shape of the edges of the bump function is very artificial.

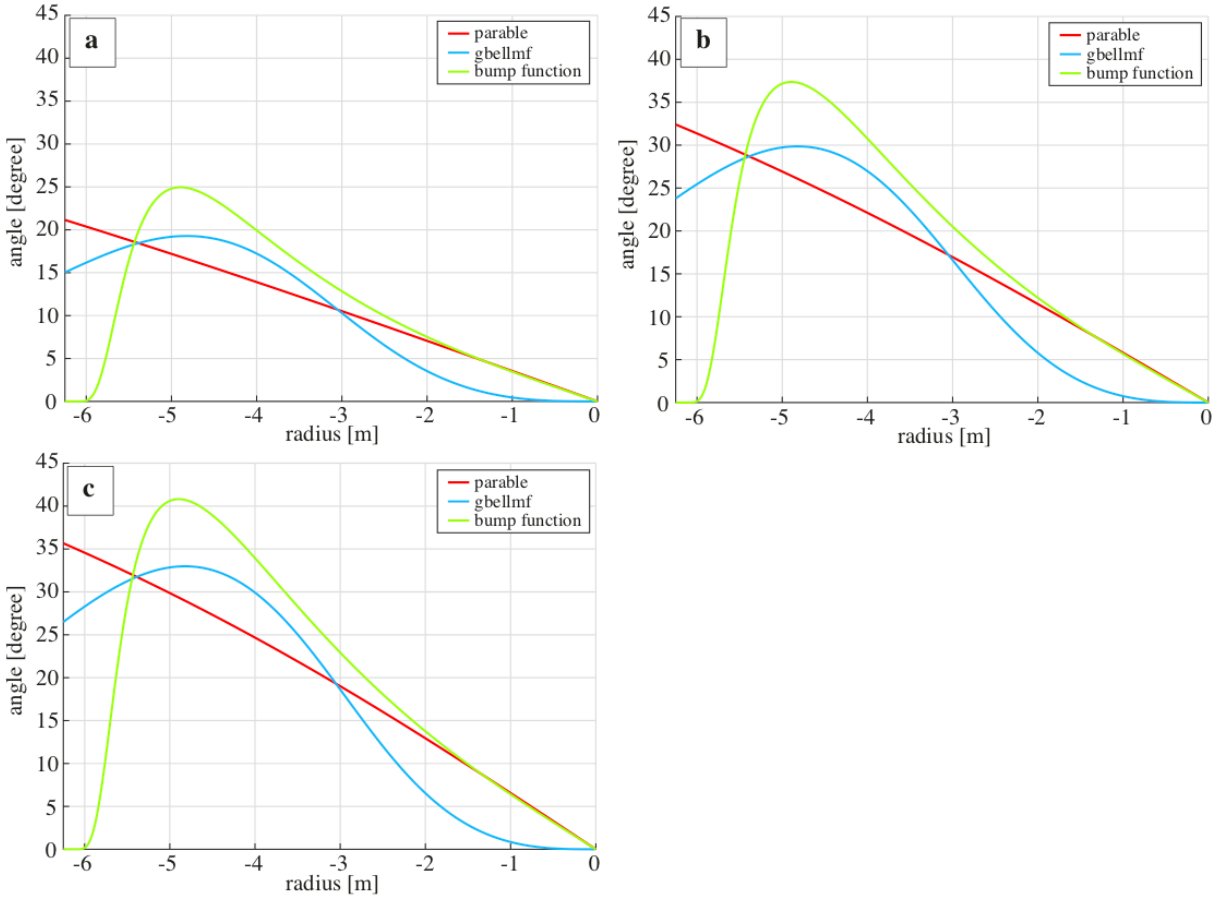

Fig. III.3.7: Slope of each function (parable, generalized bell-shaped membership function (gbellmf), bump function) for each ditch phase. (a) shows the angle of repose of the barrow after erecting the barrow after opening phase 3, (b) after opening phase 2 and (c) after opening phase 1.

III.3.3.1.2 Colluvium

To obtain an impression of the quantity of the picked volume of the colluvium (V=843 m^3), the height that would result from it is determined, assuming the bell-shaped functions. The amount of eroded material that is assumed to originate from the barrow would lead to heights of about **13.8±0.9 m**. The height and parameter a are listed in table III.3.5. In the last section it was found, that a barrow with a material volume of about V=138 m^3 already shows a slope of 41° (see fig. III.3.7c). Therefore one can conclude that a barrow with a height of 13.8 m would be unstable and collapse if one assumes the chosen bell-shaped functions. This would mean that the determined volume based on the picked colluvial layers is probably too high to originate completely from the barrow.

Table III.3.5: Parameter a and height [m] by assuming an eroded amount of material of 842.6 m^3

Parameter	parable	bell-shaped membership function	bump function	average height [m]
a	2.8	20.5	35.8	
height [m]	13.8	12.9	14.6	**13.8±0.9**

III.3.3.2 Spherical Cap

With regard to the spherical cap, one can determine the heights that would result if one were to raise the barrow by using the material dug up in each opening phase of the ditch. According to this calculation, the barrow would be 1.2 m high after opening the ditch in the first phase. After opening the ditch a second time, the barrow would be 0.7 m higher than after phase 1. After the last opening phase, the barrow would be again 0.2 m higher than after phase 2. Ignoring erosion processes the total height after the three opening phases would be **h=2.1 m** (see table III.3.6). In figure III.3.8 the profile of a spherically shaped barrow is shown together with its slope, showing a very stable barrow with an angle of repose smaller than 40°.

Table III.3.6: Height [m] by assuming the barrow having a shape of a spherical cap. Basic assumption are the determined volumes based on the picked horizons

Ditch phase	height [m]
1	1.2
2	0.7
3	0.2
total	**2.1**

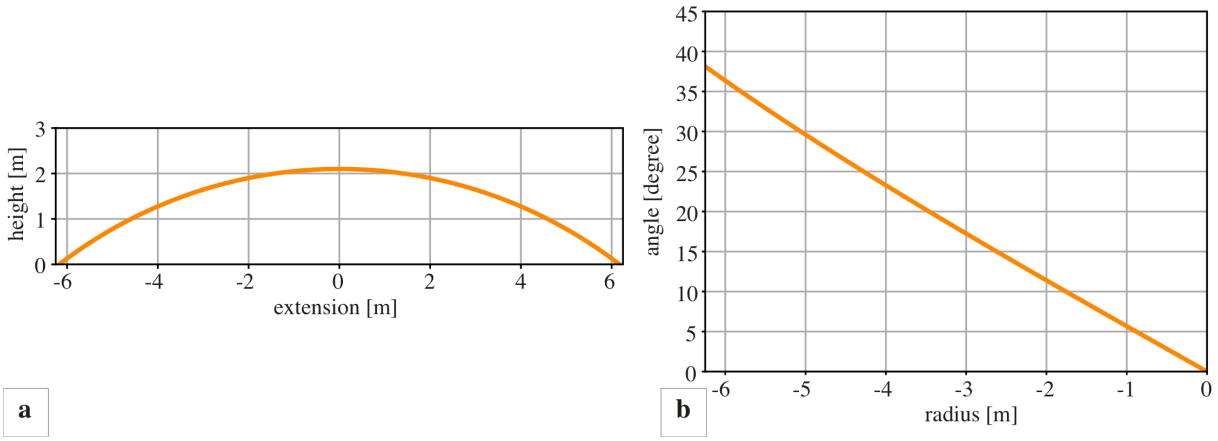

Fig. III.3.8: 2D profile of a "barrow" having the shape as a spherical cap with height h=2.1 m (a) and its stability (b) represented by the angle of repose.

III.3.4 Determining the Maximum Possible Volume and Height

III.3.4.1 Bell-Shaped Functions

Now the maximum possible height shall be determined by assuming a maximum angle of repose of 45° for soil stability (fig. III.3.9a,b). The result of the grid search performed over parameter a shows an averaged height of about 3 m by assuming an amount of material of about **V=186 m^3** (see table III.3.7).

Comparing the total volume that would result by using the ditch material after each opening phase of about V=138 m^3 (section III.3.2.1), one would expect nearly 48 m^3 more material.

Table III.3.7: Resulting parameter a, heights [m] and volume [m^3] in consideration of soil stability by applying the chosen bell-shaped functions

	parable	bell-shaped membership function	bump function	average
a	12.6	5.1	6.7	
height [m]	3.1	3.2	2.7	**3.0±0.3**
volume [m^3]	190	210	158	**186±26**

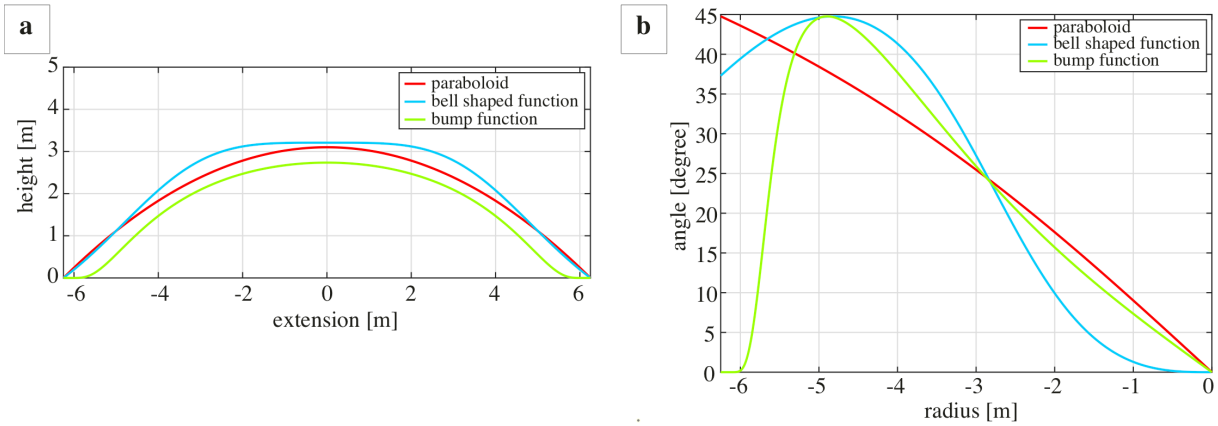

Fig. III.3.9: Maximum possible height if the chosen bell-shaped functions were assumed to be the former shape of the barrow (a) considering the stability in form of the angle of repose (b). (b) is the corresponding angle of repose in degree, showing the maximum stability for sand or sand-gravel mixtures.

III.3.4.2 Hemisphere

A hemisphere would represent a barrow having the maximum possible volume and helps to assess the amount of the picked volume of the colluvium. Assuming r=6.25 m to be the radius of the barrow's base, one would arrive at a maximum volume of **V=511 m^3**. In figure III.3.10 the angle of repose is plotted for a hemisphere. It can be seen that in particular the edges of the barrow are very unstable. Only 2 m towards the interior of

the burial mound does the barrow material become stable. Knowing the volume of the picked colluvium to be V=843 m^3, one can now conclude that the picked material must be a mixture of the barrows material and other soil material.

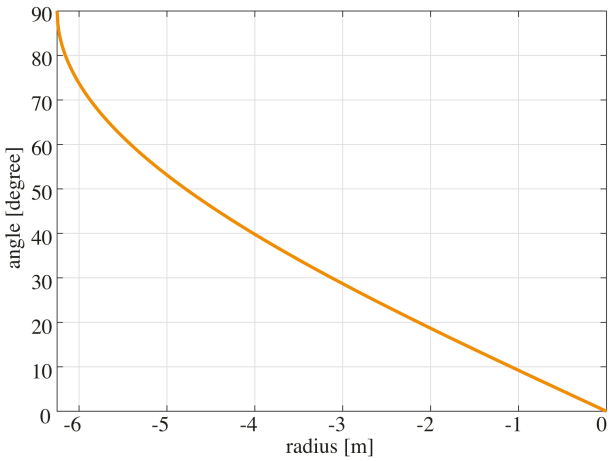

Fig. III.3.10: Angle of repose of a hemisphere as an indicator of the stability of the resulting barrow.

III.3.4.3 Comparison with a Cone

Finally the results can be compared with a more stable geometric form. Assuming a maximum angle of repose of 45°, the resulting height would be 6.25 m and the volume of material would be **V=256 m^3**. This amount of material is larger than the determined volumes of the ditch phases (V=138 m^3) and the maximum possible volume by assuming a bell-shaped form of about V=186 m^3.

The total height resulting from all three phases is about **h=3.4 m**. In table III.3.8 the heights per phase are listed, too. The height of h=3.4 m is slightly larger than the maximum possible height of the bell-shaped form of about 3 m and 1 m larger than the height assuming a spherical shape (see sections III.3.4.1 and III.3.3.2). Finally, possible heights in the range of 2.1 m (based on the spherical cap) and 3.4 m (based on the conical shape) were found. The height of h=2.3 m (see section III.3.3.1.1) resulting from the bell-shaped functions is in between. In this range the material is stable considering the angle of repose.

Table III.3.8: Resulting heights [m] and angle of repose [°] assuming a conical shape

	height [m]	angle of repose [°]
phase 3	0.4	28
phase 2	1.2	25
phase 1	1.8	16
total	**3.4**	

III.4 Discussion

III.4.1 Evaluation of the Geometric Approach

The calculations in the last sections were always based on the assumption that the whole ditch was refilled after each phase of usage and completely reopened for each new phase. Additionally, erosion of the barrow's material is not considered between the phases, which would have caused a reduction in height. Two approaches were applied of getting an estimation of the former height. First, the height was determined based on the estimated volume of the ditch's phases. In a second approach a theoretical height was calculated based on a maximum angle of repose of 45°.

In general, the bell-shaped approach described by a parable, the bell-shaped membership function and bump function do not describe the shape of the barrows very well. Therefore, three different functions were used to extract an average value of height and volume. A comparison with well-preserved barrows does indeed show that our results are appropriate and realistic. While three bell-shaped functions were applied, there are several more. The bell-shaped functions used in this part of the thesis are just examples covering different shapes from the roughly spherical to a parable.

A cone is assumed in order to provide a comparison with a stable form of deposited material and can therefore also only be an estimate. Nevertheless, the maximum height of a cone, assuming an angle of repose of 45°, is 6.25 m (equal to the barrow's base). Regarding the calculations for a cone, one can conclude that the higher the barrow, the more conical its shape must be. This is also shown in fig. III.4.1, where different parameters b were varied to give the bell-shaped membership functions a more conical shape.

By assuming a maximum angle of repose of 45° and varying the parameter b of the generalized bell-shaped membership function, the heights would range between 3.2 m and 4.8 m (fig. III.4.1a), putting them in the range of already observed preserved Bronze Age barrows. The resulting volumes would range between 212 m^3 and 228 m^3, which is smaller than the volume of a cone with a maximum height of 6.25 m (remember V=256 m^3). Compared to the documented Bronze Age burial mounds of Schaefer-Di Maida's (Schaefer-Di Maida 2019) database with the same diameter (12 to 13 m), heights of at least 4.5 m are possible. All the found results are realistic.

Now the first question of this part can be answered: whether it is possible to reconstruct the barrow on the basis of the material of the ditch phases. The answer is no, not directly, but the mathematical approach gives us good estimates of the height and used volume – estimates more precise than could be obtained by assuming a hemisphere.

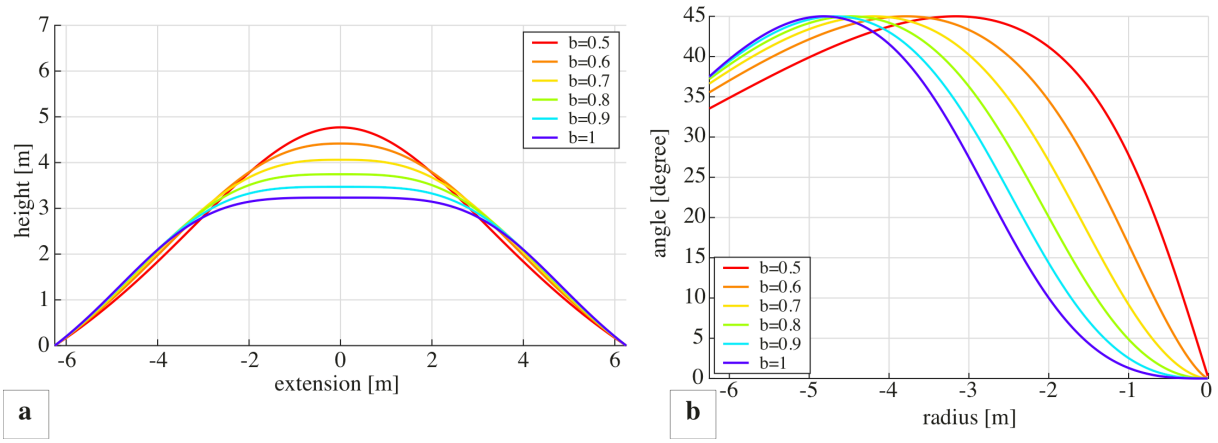

Fig. III.4.1: Different generalized bell-shaped membership function with different b values, to simulate a conical shape (a). These functions have a maximum angle of repose of 45°, which is shown in (b). This assumption allows for heights between h=3m and h=5m.

Nevertheless, assuming a hemisphere helped us to evaluate the amount of the picked colluvium in the vicinity of the barrow. Unfortunately, the measurement area was too small to differentiate the material and determine whether it was eroded by the barrow or by the elevation or new material by agricultural activity (regardless of whether this question could be clarified at all, even if the measurement area had been large enough).

III.4.2 Evaluation of the Function-Based Uncertainty

The assumption of a bell-shaped form is found to be more realistic than that of a spherical shape. It must be borne in mind that there are subjectively determined parameters in the generalized bell-shaped membership and bump functions. To assess the validity of the results concerning the height by using the generalized bell-shaped membership and bump functions, the most subjective parameters d and p were varied and the height was determined by varying parameter a. Figure III.4.2 shows three examples of bell-shaped functions and their different maximum values (fig. III.4.2a for the generalized bell-shaped membership function and fig. III.4.2b for the bump function). Additionally, the dependence of height on the parameters d (bell-shaped membership function) and p (bump function) is shown in fig. III.4.2c.

It can be seen that, depending on parameters d and p, which each determine the shape of the function, the heights differ strongly. For the bell-shaped membership function one can see a decreasing height with an increasing parameter d, while the reverse obtains for the bump function. Furthermore, the smaller d or p are, the larger the changes that can be expected. Additionally, the changes in height are smallest when the generalized bell-shaped membership function is applied. A standard deviation could be found from the dependence of height on the parameters d and p of $\sigma_p(h)$=0.50 m for the bump function and $\sigma_d(h)$=0.38 m for the generalized bell-shaped membership function.

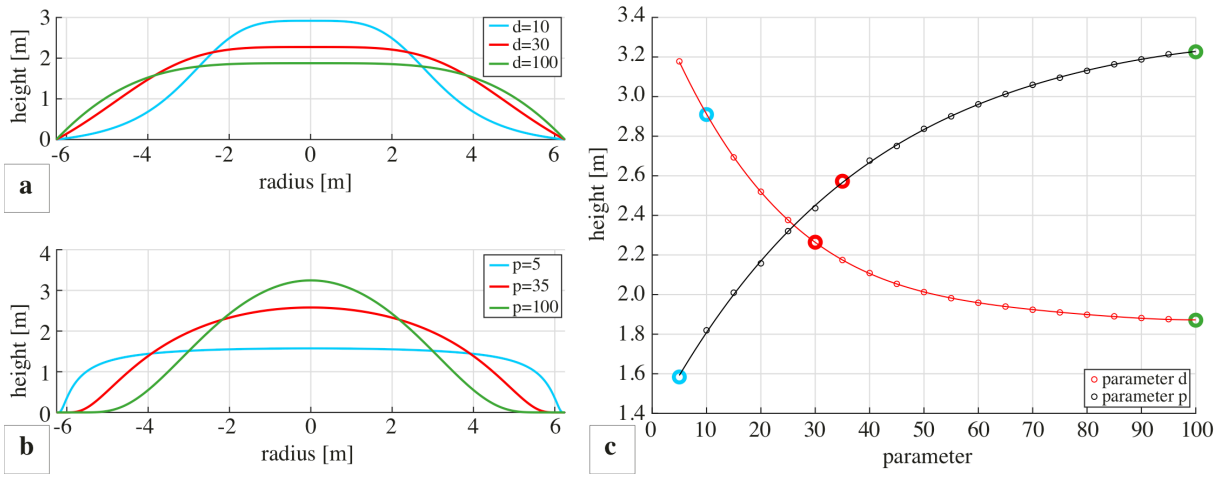

Fig. III.4.2: Resulting shapes of the generalized bell-shaped membership function (a) and bump function (b) by varying the most subjective parameters d and p. (c) shows the dependence of the height on the parameter d for the bell-shaped membership and p for the bump function. The thick blue, red and green dots mark the parameters (d [thin red dots and solid line] or p [thin black dots and solid line]) for the function in (a) and (b). The red and black line are polynomial function of the 4th order h(p) and h(d), to fit the points.

III.4.3 Evidence of a Burial Before each Opening Phase

One of the starting questions was whether it would have been possible to use the material removed from the ditch in each opening phase for the purpose of covering a new grave, raising the burial mound in the process, because it was common practice to put the coffin at the surface and cover it with soil, which would inevitably have raised the barrow during the Bronze Age. Assuming a bell-shaped form, it is possible that the material of the opening phases 1 and 2 may have been used to cover a secondary burial, though it was insufficient material for phase 3. Considering the shape of a cone, the material of phase 3 may have been enough to cover a burial because of an amount of material that would create a barrow with a height of 0.4 m.

Nevertheless, it must be borne in mind that the assumption is always that the ditch needed to be reopened completely. It cannot be reliably ascertained whether the ditch was once more completely filled after the second phase and reopened in the third, at the beginning of which the oak planks were laid down and burned, or whether the ditch was filled by erosion after the second phase, in which case the oak planks were laid down and burned at the beginning of the third phase without the ditch having been reopened beforehand.

III.4.4 Origin of the Material used to Raise the Barrow

Some calculations allow for the possibility of additional material having been used to raise the barrow. With regard to the bell-shaped form and considering the angle of repose, a theoretical maximum height of 3 m would result, with a volume of V=186 m^3. Furthermore, from the calculations above (section III.4.1 of this part) it is known that a more conical form leads to volumes between 212 and 228 m^3. This is ΔV=49 m^3 to ΔV=90 m^3 more than the material of the ditch phases would provide. The difference between the volume of

a cone and the material of the ditch phases is ΔV=117 m^3. This means that theoretically it would have been possible to raise the barrow with 49 m^3 to 117 m^3 of additional material which was not extracted from the ditch.

While a shallow ditch for extracting material was documented during the 2017 excavations, it was not verified during those of the following year. There was a difference in weather conditions, with 2017 wetter than 2018. Kneisel (in prep.) records that a clear identification of features was only possible if they were wet. Therefore it may be that the feature observed of 2017 could not be observed in the following year due to the dry conditions. No further ditch could be detected with GPR either. According to the results from part II of this thesis, pit-like features can be detected very well under dry conditions. It is possible that the structure documented in 2017 was merely a soil discoloration. Nevertheless, studies of other Bronze Age burial mounds have also concluded that material from the vicinity of the barrow was used in their construction (Kneisel, Schaefer-Di Maida, et al. (in prep.) Schaefer-Di Maida 2019).

III.5 Conclusion

The comparison of GPR profiles and archaeological documentation of excavation profiles allowed us to create a 3D model of the ditch surrounding the barrow and its phases. In addition, the volume of the dug material of the ditch could be determined and thus the former height of the barrow could be estimated. The final conclusions are:

General conclusions:

1. The volume of the colluvium of 843 m^3 would suffice to raise the barrow to about 14 m in height. Calculations of stability (angle of repose) and maximum volume, assuming a hemisphere of 511 m^3, indicate that the picked colluvium is a mixture of material eroded by the barrow and local elevation, as well.

2. Considering all investigations, the total volume of the material eroded from the barrow must have been between 186 m^3 and 256 m^3.

3. The former height of the barrow could be determined on the basis of the ditch phases. The minimum height resulting from the usage of the ditch material of the individual phase in total would be between 2.1 m (assuming the spherical cap) and 3.4 m (assuming a cone). This result is in agreement with other documented and well-preserved barrows.

4. Considering the maximum documented angle of repose of 45° and assuming bell-shaped functions, the barrow's maximum height would be 3 m.

5. Furthermore, it was found that the larger the height of the burial mound, the more conical its shape. The assumption of a spherical shape lead to the smallest height of the barrow.

6. Additionally, the direction of modern erosion could be identified as running from northwest to south-east, indicating a high probability of finding archaeological material even in these areas.

Regarding the volume and height, one can conclude the following:

1. Assuming the bell-shaped form, the ditch material of phase 1 would raise the mound by 1.20 ± 0.08 m that of phase 2 by 0.80 ± 0.05 m and that of phase 3 by 0.30 ± 0.02 m. The total height would be 2.3 m. Based on this, the material of the ditch's opening phases 1 and 2 would each be sufficient to cover one burial. These results ignore erosion processes between the opening phases.

2. Assuming a conical shape, the ditch material of phase 1 would raise the barrow by 1.8 m, that of phase 2 by 1.2 m and that of phase 3 by 0.4 m. The total height would be 3.4 m. In this case, the material of each opening phase would be sufficient to cover one burial. These results also ignore erosion processes between the opening phases.

3. The assumption of a spherical cap is the most unstable shape. Nevertheless, the ditch material of phase 1 would raise the barrow by 1.2 m, that of phase 2 by 0.7 m and that of phase 3 by 0.2 m. The total height would be 2.1 m. Here too, the material of the ditch's opening phases 1 and 2 would each be sufficient to cover one burial. These results also ignore erosion processes between the opening phases.

By addressing the two questions at the beginning, (1) whether it is possible to reconstruct the former height on the basis of the volume of the ditch phases by considering the angle of repose for typical soil materials and (2) whether the ditch material per phase could have been used to cover up a secondary inhumation, one can finally conclude the following

1. The mathematical approach gives a good estimation of the former height of the burial mound and the used amount of material used to erect it.

2. If the former shape of the burial mound was bell-shaped, then at least one more burial was possible, which could be covered with ditch material. The more conical the shape the more probable a third burial. Since only one burial has been archaeologically observed, the burial of phase 2 was probably eroded.

3. This multiphase use fits into the picture of the use of other Bronze Age burial mounds.

These results show that, despite erosion by ploughing, the burial mound could be stratigraphically reconstructed using GPR and archaeological excavations for reference. Furthermore, it was possible to identify the direction of erosion processes, which is useful in identifying areas for archaeological surveys. It was also found that areas for future measurement in the ploughed fields ought to cover a wider scope than merely a line perpendicular to ploughing direction. This study shows also the potential for understanding other already eroded burial mounds and their surrounding areas.

iv Summary

The interdisciplinary approach combining geophysics, archaeology and soil sciences aimed at improved detection, easier identification and, in a final step, the reconstruction of archaeological key targets. The main challenge of this investigation was the glacial environment enriched with boulder stones in which the archaeological features – whose components mainly consist of boulder stones as well – were situated. The basis for these investigations were two sites, both situated in Bornhöved, Schleswig-Holstein, in northern Germany.

The first part of this thesis focused on improving the detection rate by combining GPR and magnetics. First the features were classified by their recognition in both GPR and magnetics. To explain the statistics, numerical modelling was used. Furthermore, soil analyses were used to obtain an idea of the soil composition and the permittivity of the soil matrix. Taken together, the soil analysis and numerical modelling helped to give an idea of water content and porosity. In order to explain why archaeological features of the same kind are only sometimes recognised and why, on the other hand, some geological features are misinterpreted as archaeological ones, target features – urns, cooking pits, burials and massive iron oxide concretions – were picked and compared in pairs. Urns and cooking pits were compared in pairs in different soils. Burials and iron oxide concretions caused similar anomalies in GPR and were therefore compared together. The results of the modelling study were then used to classify the signal strength of GPR by assuming a mean porosity and three different water contents.

It was found that the signal strength of the iron oxide concretion is twice as large as those of stony features. Additionally, it was found that the identification of stony archaeological and geological features is not possible using GPR alone. The combination of GPR and magnetics is helpful to identify cooking pits, burials and iron oxide concretions. This information can be combined with the signal strength to develop a pattern recognition tool. The combination also helps to distinguish between stony archaeological features and iron oxide concretions, and between stony archaeological and geological features in the same depth range. It was found the influence of water content on permittivity to be larger than that of porosity. Soil analyses must at least provide direct information about water content directly. Then predictions about the quality of GPR data and the shape of the anomalies in GPR maps are indeed possible. With regard to magnetics, the predictions of archaeological features is made possible by knowing the susceptibility of each component of the feature and soil.

In the second part, the geophysical data of the site BH were presented. In contrast to part I, where the focus was mainly on stone-bearing features, part II is focussed on pit-like features. Due to the soil conditions at this site, less than 20 % of all BH-features could be detected with magnetics or GPR, whereas less than 10 %

of pit- like features could be detected with both methods. The modelling study showcased the complexity of ditch fillings. In contrast to part I, where an improved detectability could be shown if the soils are moist, in part II could be shown, that pits, that are detectable with GPR and magnetics, are more porous and drier, than the surrounding. Those features are detectable with GPR and magnetics. In the second part the derived porosity values and water content were used to find a good initial model for the modelling study. The initial model did not provide a good fit with the measured data but taking into account the sand content and fitting the porosity and water content to it improved the initial model, which provided a very good fit. Thus, it could be shown that it is quite useful to generate good model data based on soil analyses that have been performed in advance to a geophysical measurement in order to estimate the quality of the measured data. Regarding the trench and the detectability of the trench walls, it was demonstrated that the higher the permittivity contrast to the surrounding soil is, the higher the probability is that trench walls steeper than 25° can be detected. The probability increases as well the drier the surrounding soil is with the same porosity.

In the third part, a burial mound was reconstructed by applying a mathematical approach. The burial mound is surrounded by a circular ditch, which shows three phases of usage. Based on the 3D GPR measurements, it was possible to pick the layers of the ditch and the colluvium. Possible volumes of the material could then be calculated on the basis of these picked layers. Different geometrical forms were assumed to describe the shape: a hemisphere, a spherical cap, bell-shape [paraboloid, bell-shape membership function and bump function] and conic form. Additionally, to obtain more realistic estimates of volume and height, the angle of repose was considered. The volumes determined for each picked phase were the basis for estimating a theoretical height of the former barrow.

Based on the volume a height of about h=2.3 m could be determined assuming a bell shape. From an archaeological perspective, taking into account examples of well-preserved barrows, the bell shape is the most realistic. With regard to the conical shape, which is the most stable geometric form, a height of h=3.4 m could be estimated. By considering the angle of repose, the bell-shaped functions and the conical form, we arrived at a volume between V=186 m^3 and V=255 m^3 for the material that must have been eroded from the barrow. The assumption of a hemisphere helped us to evaluate the picked volume of the colluvium. It could be concluded, that the picked volume of the colluvium must consist of a mixture of material from the barrow and additional material from the natural elevation.

To address the archaeological question if a secondary burial would have been possible, we can establish that it would indeed have been possible to cover a secondary burial. To cover a third burial, however, the material from ditch phase 3 would not have been enough.

v Outlook

v.1 Detection and Identification of Archaeological Targets in Glacial Soils

Since the combination of GPR and magnetics has proved useful to improve the identification of archaeological (but also of geological) features, in increased concentration on magnetics shows potential for further insights. This study focussed on GPR, from which more information was available. A subsequent study ought also to include in situ susceptibility measurements on the soil, the stones used and pottery. This can help to solve several problems we have been facing:

1. The modelling showed a very heterogeneous image of the occurring stones, which is typical for glacial soils. The modelling can be improved by knowing the susceptibility of each stone one.
2. The increased measurement of susceptibility in situ can help us learn more about the use of the stones before they came to form part of a stone package of the urn or burial. Probably the susceptibility values of the stones used in cooking pits can provide also more information of the kind and intensity of use. This information is also valuable for archaeological purposes. The problem with the urns is that they were not detected in the magnetics. Here, susceptibility measurements of the pottery can improve the modelling as well. Furthermore, they may help us understand why the urns could not be detected in glacial soils.
3. Better modelling can help in classifying the strength of the magnetic signal. This remains to be done.
4. A last problem that can be solved by measuring susceptibility in situ is that it can help to differentiate between archaeological and geological stony features, since it was found that this is not possible using GPR alone.

If the signal strength of the chosen key targets in both GPR and magnetics is clear, then developing a recognition tool would help to easily identify archaeological and geological features as well. Approaches to analysing GPR time slices are presented by Küçükdemirci & Sarris (2020 and 2019). Comparable recognition tools for analysing magnetic maps can be found e.g. in Hegyi et al. (2020) and Pregesbauer et al. (2014).

Our investigations have so far focused on two sites in close proximity to each other. The glacial soils in which the sites and features were situated are also similar. To obtain an overview of the detection of individual key targets in glacial soils, it is necessary to compare features (archaeological and geological) in different glacial

soils. Considering the geophysical methods applied, it was found GPR and magnetics to be the best choice. Also other geophysical methods were tested to improve the detection and identification of archaeological features. These were electrical resistivity tomography (ERT) and electro-magnetic induction (EMI). They turned out to be unsuitable, since the contrast between feature and surrounding was not good enough. The application of seismics is suitable only for detecting deep (> 3 m) features and therefore not of interest for Bronze Age sites.

v.2 Identification and Reconstruction of Archaeological Targets

The approach to reconstructing an archaeological feature applied in this thesis is something of a pilot project and therefore in need of further validation. It is obvious that none of the bell-shaped functions matches the actual shape of a barrow. Therefore, three different functions were chosen, covering a wide range of shapes from pointed to rounded. Moreover, the conical shape does not correspond to the shapes observed in well-preserved barrows. Nevertheless, a realistic result was achieved. In order to fully verify this approach, one would have to measure a well-preserved barrow with a surrounding ditch with a multichannel GPR antenna or 3D seismic (depending on its height). After picking the bottom of the barrow and the ditch layers, volume and height would be calculated according to the approach presented here. The resulting estimates could then be compared with the volume and height of the real burial mound. This can be done by calculating the volume on the basis of the picked layers directly in the program Kingdom Suite. The result, however, would probably not be precise enough, because of the interpolation between the picked layers per GPR channel. Another way of obtaining the volume of the preserved barrow is measurement with a total station or by aerial photogrammetry (Magnani & Schroder 2015). The volume is then estimated by means of photogrammetric modelling or by applying contour or gridding methods (Magnani & Schroder 2015).

In general, reconstruction is an important task which should be the primary goal of historic preservation. It is important for the preservation of cultural heritage. This issue has also become important in recent times with the destruction of historical monuments in Palmyra and attempts at the digital reconstruction of destroyed cultural heritage (e.g. Denker 2017). The choice of reconstruction method should correspond to the needs of the object. This makes validation of the method developed here all the more important.

vi Appendix

A.1 Appendix for Part I

A.1.1 Comparison of Magnetic Map and GPR Slices

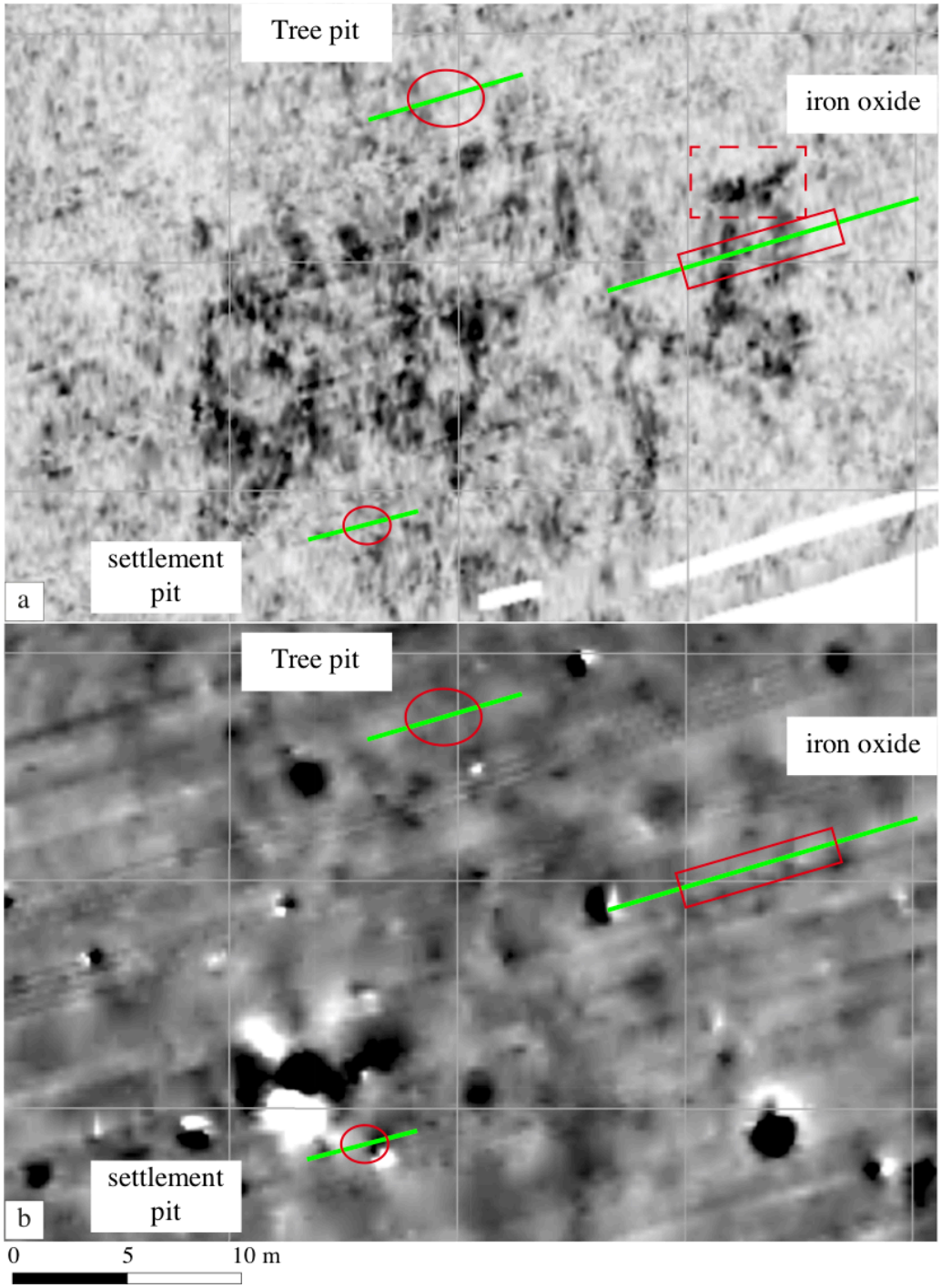

Fig. A.1: GPR (a) and magnetic (b) map showing the profile of one settlement and tree pit as well as the one of an iron oxide concretion. The red dashed rectangle indicates the area that was excavated and photographed. The photograph can be found in fig. I.4.10a. Red circles and rectangle mark the position of the features.

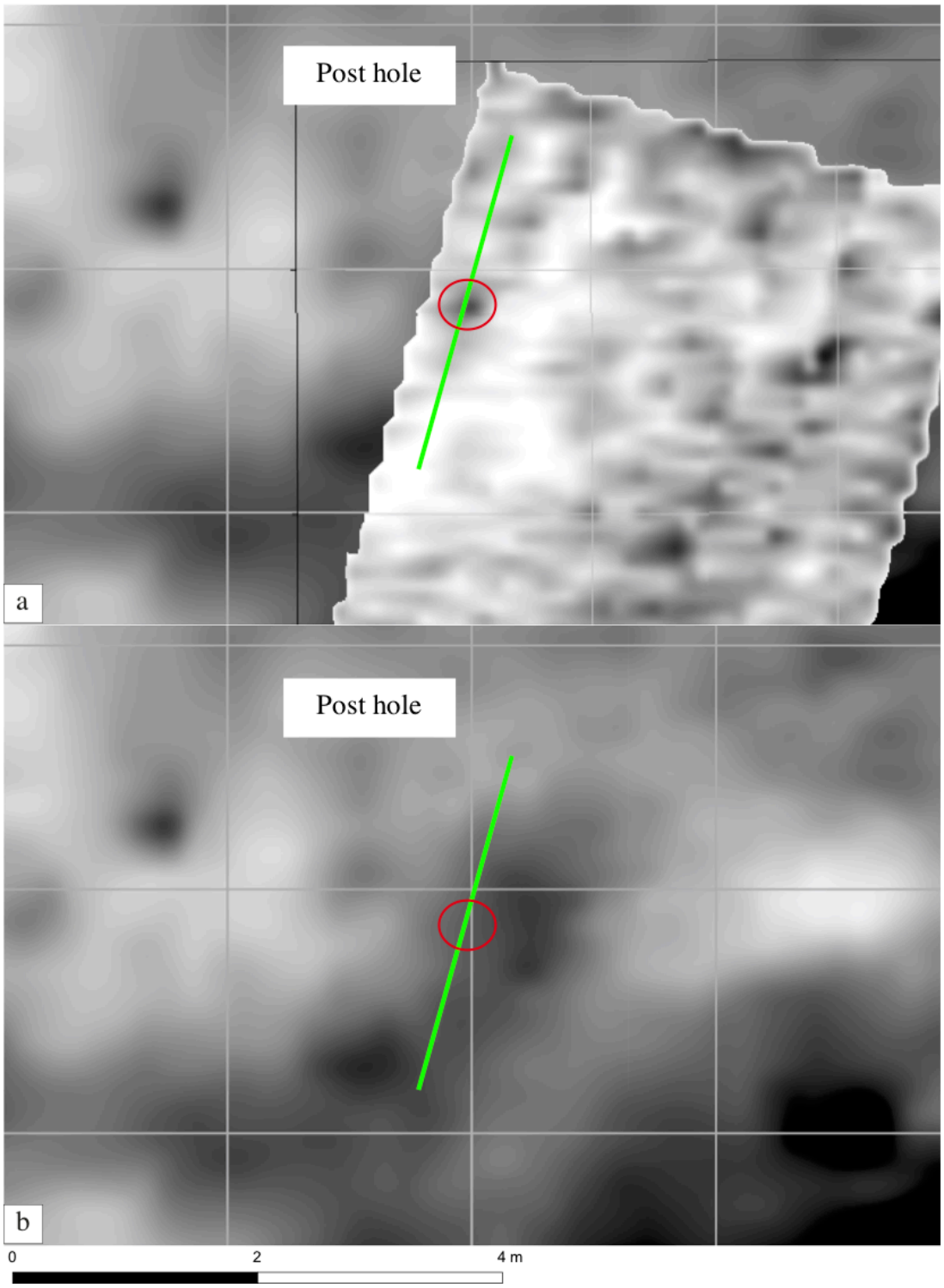

Fig. A.2: GPR (a) and magnetic (b) map showing the profile of one post hole. Red circles mark the position of the features.

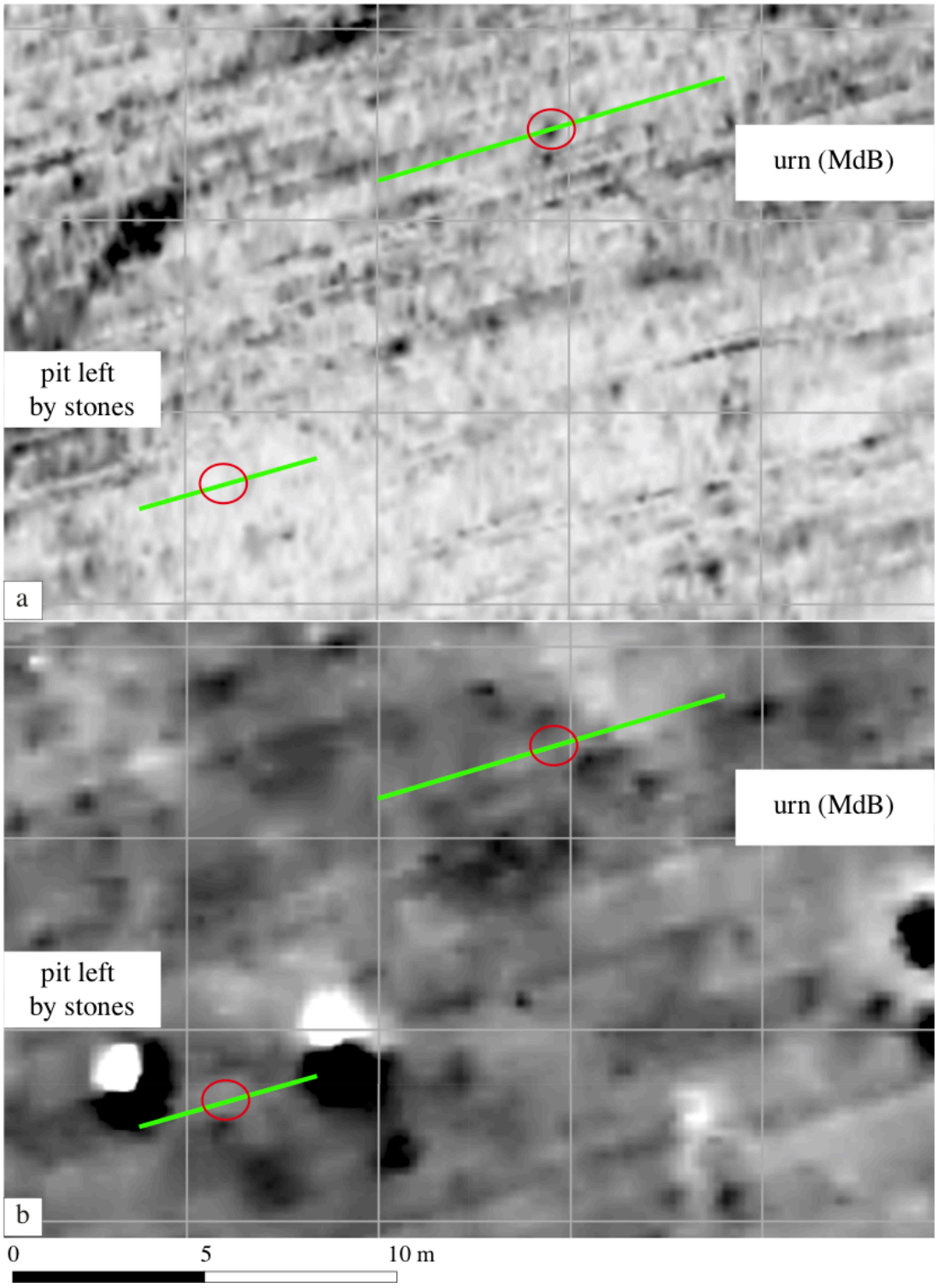

Fig. A.3: GPR (a) and magnetic (b) map showing the profile of one pit left by moved stones and one urn of MdB. Red circles mark the position of the features.

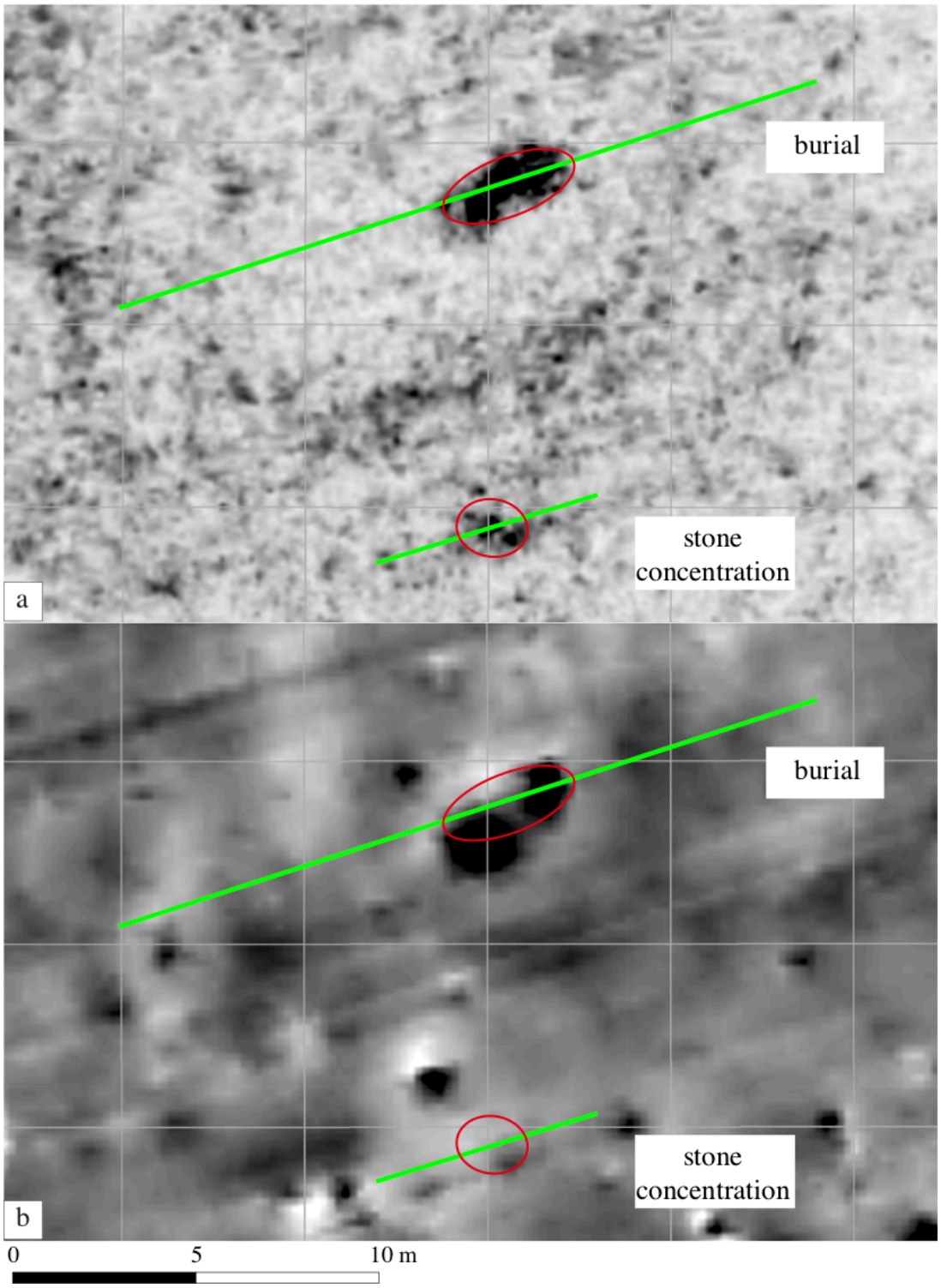

Fig. A.4: GPR (a) and magnetic (b) map showing the profile of one stone concentration and burial. Red circles mark the position of the features.

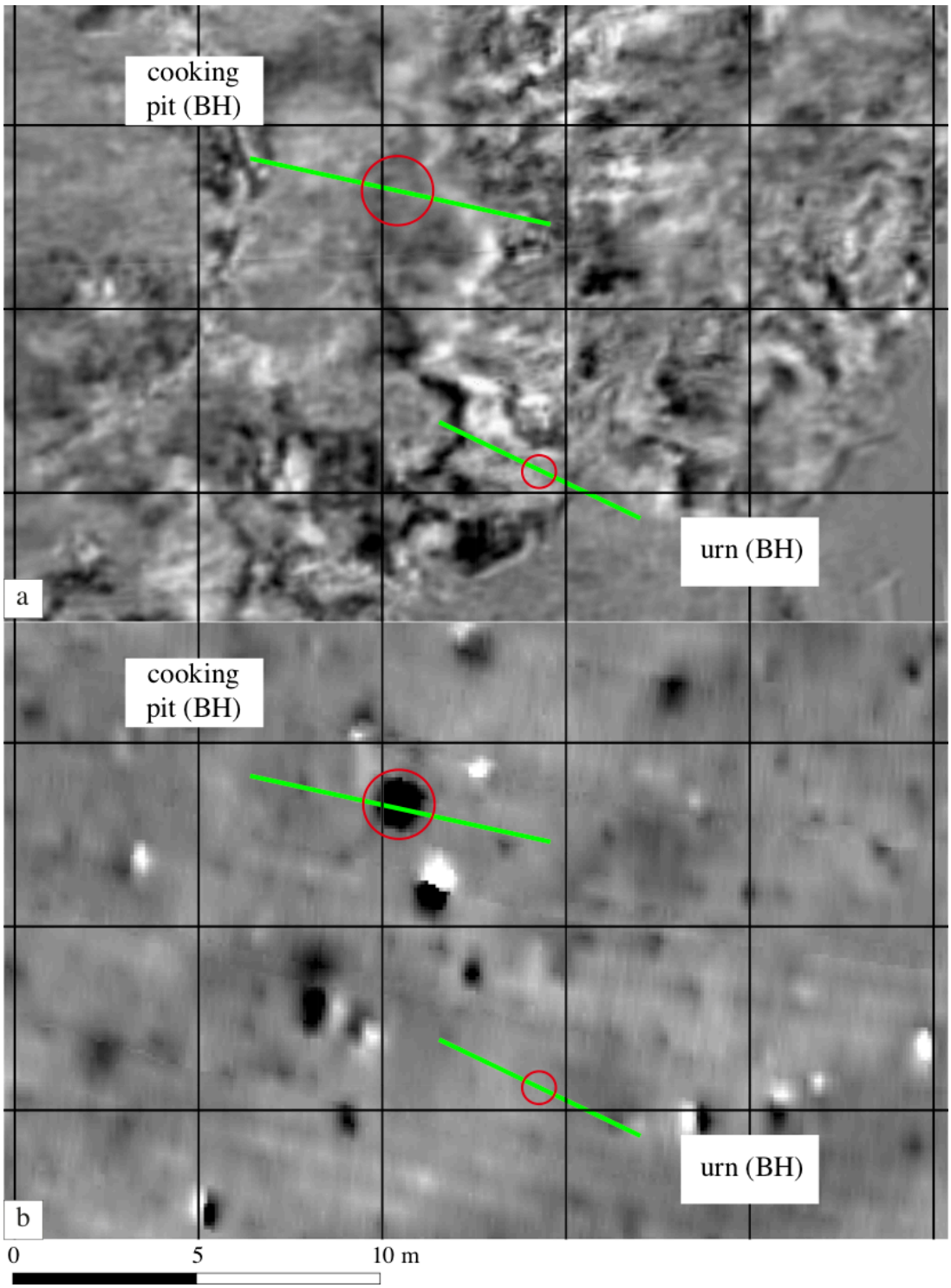

Fig. A.5: GPR (a) and magnetic (b) map showing the profile of one urn and cooking pit of BH. Red circles mark the position of the features.

A.1.2 Raw Data Listed by Type of Feature and Occurrence

Table A.1: Classification of the features and their number as detected or undetected in GPR (U - urn, CP - cooking pit, SC - stone concentration, B - burial, SP - settlement pt, PH - posthole, TP - tree pit, G - geology, PmS - pit left by moved stones)

feature	**area [m^2]**	z_{mean} **[m]**	**Dm [m]**	**number of features**	z_{mean} **[m]**	**Dm [m]**	**number of features**
		detected by GPR			**undetected by GPR**		
U	0.0-0.5	0.41	0.5	14	0.87	0.4	8
	3.0-3.5	0.35	1.8	1			
CP	0.0-0.5	0.63	0.6	4			
	0.5-1.0	0.61	0.9	3			
SC	0.0-1.0	0.35	0.7	2	1.1	1	1
	1.0-2.0	0.35	1.4	2	0.72	1.3	2
	3.0-4.0				1.15	2	1
	4.0-5.0	0.35	2.4	2			
	6.0-7.0	0.35	2.8	1			
	>200	0.4	14.4	1			
B	0.0-2.0	0.35	1.2	1	0.82	0.8	1
	2.0-4.0	0.7	2.0	2			
	4.0-6.0	0.35	2.5	2			
	6.0-7.0	0.35	2.8	1			
SP	0.0-1.0	0.35	0.6	8	0.35	0.7	24
	1.0-2.0	0.35	1.2	6	0.35	1.4	1
	2.0-3.0	0.35	1.7	3	0.35	1.7	1
	7.0-10.0	0.59	3.0	2			
PH	0.0-0.3	0.35	0.4	8	0.46	0.3	60
	0.3-0.6	0.35	0.6	8	0.35	0.7	3
	.06-1.0	0.35	0.9	2	0.35	0.9	1
	1.0-2.0	0.35	1.5	1			
TP	0.0-1.0	0.35	0.6	2	0.35	0.9	2
	1.0-2.0	0.35	1.5	3			
	2.0-3.0	0.35	1.9	3			
	4.0-5.0	0.35	2.2	1			
G	0.0-150.0	1.22	8.8	4			
	250.0-350.0	0.65	18.8	3			

Continued on next page

Table A.1 – Continuation of table A.1

feature	area [m^2]	z_{mean} [m]	Dm [m]	number of features	z_{mean} [m]	Dm [m]	number of features
	1000.0-1500.0	0.32	32	1			
PmS	0.0-0.2	0.35	0.3	6	0.5	0.3	78
	0.2-0.4	0.35	0.7	2	0.45	0.5	10
	0.4-0.6	0.35	1	1	0.35	1.1	1
	1.0-2.5				0.35	1.3	2

Table A.2: Classification of the features and their number as detected or undetected in magnetics (U - urn, CP - cooking pit, SC - stone concentration, B - burial, SP - settlement pt, PH - posthole, TP - tree pit, G - geology, PmS - pit left by moved stones)

feature	area [m^2]	z_{mean} [m]	Dm [m]	number of features	z_{mean} [m]	Dm [m]	number of features
		detected by magnetics			undetected by magnetics		
U	0.0-0.5	0.35	0.6	5	0.62	0.4	17
	3.0-3.5				0.35	1.8	1
CP	0.0-0.5	0.63	0.6	4			
	0.5-1.0	0.61	0.9	5			
SC	0.0-1.0	0.35	0.5	1	0.73	1	2
	1.0-2.0	0.35	1.4	2	1.09	1.3	2
	3.0-4.0				1.15	2	1
	4.0-5.0				0.35	2.4	2
	6.0-7.0				0.35	2.8	1
	>200	0.4	14.4	1			
B	0.0-2.0	0.35	1.2	1	0.82	0.8	1
	2.0-4.0	0.7	2.0	2			
	4.0-6.0	0.35	2.6	2			
	6.0-7.0				0.35	2.8	1
SP	0.0-1.0	0.35	0.7	2	0.35	0.7	30
	1.0-2.0	0.35	1.2	1	0.35	1.2	6
	2.0-3.0				0.35	1.8	4
	7.0-10.0	0.35	1.7	1	0.82	2.7	1
PH	0.0-0.3				0.44	0.3	60
	0.3-0.6				0.35	0.6	11

Continued on next page

Table A.2 – Continuation of table A.2

feature	**area [m^2]**	z_{mean} **[m]**	**Dm [m]**	**number of features**	z_{mean} **[m]**	**Dm [m]**	**number of features**
	0.6-1.0				0.35	0.9	3
	1.0-2.0				0.35	1.5	1
TP	0.0-1.0				0.35	0.7	4
	1.0-2.0				0.35	1.5	3
	2.0-3.0				0.35	1.9	3
	4.0-5.0				0.35	2.2	1
G	0.0-150.0	1	10.5	2	1.44	7.2	2
	250.0-350.0	0.68	18.7	1	0.64	18.9	2
	1000.0-1500.0				0.32	32	1
PmS	0.0-0.2				0.49	0.3	84
	0.2-0.4				0.44	0.5	12
	0.4-0.6				0.35	1.1	2
	1.0-2.5				0.35	1.3	2

Table A.3: Depth, size and number of features detected (columns 2-5) and undetected (columns 6-9) in GPR

feature	depth [m]	area [m^2]	Dm [m]	number [%]	depth [m]	area [m^2]	Dm [m]	number [%]
urns	0.38	0.43	1.15	65	0.87	0.15	0.4	35
cooking pit	0.62	0.52	0.75	100				
stone concen-tration	0.36	28.16	4.3	67	0.99	1.93	1.43	33
burial	0.44	3.96	2.1	6	0.82	0.56	0.8	14
geology	0.73	288.24	19.9	100				
settlement pit	0.41	3.96	1.6	42	0.35	0.58	1.3	58
posthole	0.35	0.39	0.85	23	0.39	0.12	0.63	77
tree pit	0.35	2.1	1.5	82	0.35	0.63	0.9	18
pit left by moved stones	0.35	0.23	0.67	9	0.41	0.14	0.8	91

Table A.4: Depth, size and number of features detected (columns 2-5) and undetected (columns 6-9) in magnetics

feature	depth [m]	area [m^2]	Dm [m]	number [%]	depth [m]	area [m^2]	Dm [m]	number [%]
urns	0.35	0.31	0.6	22	0.49	0.36	1.1	78
cooking pit	0.62	0.63	0.75	100				
stone concen-tration	0.38	42.22	5.4	33	0.65	2.89	1.9	67
burial	0.47	3.5	1.9	71	0.59	3.48	1.8	29
geology	0.84	181.58	14.6	38	0.8	352.24	19.4	63
settlement pit	0.35	3.05	1.7	9	0.47	0.96	1.6	91
posthole					0.37	0.18	0.8	100
tree pit					0.35	1.84	1.6	100
pit left by moved stones					0.41	0.15	0.8	100

A.2 Appendix for Part I and II

A.2.1 Soil Conditions - MdB

Table A.5: Soil conditions of MdB assuming a permittivity of the soil matrix of ϵ_r=6.9

Permittivity	**Porosity [%]**	**Water Content [%]**
7.061	54	20
7.073	32	12
7.160	48	18
7.261	42	16
7.362	36	14
7.451	52	20
7.464	30	12
7.554	46	18
7.657	40	16
7.761	34	14
7.853	50	20
7.958	44	18
8.064	38	16
8.157	54	22
8.171	32	14
8.264	48	20
8.372	42	18
8.481	36	16
8.577	52	22
8.590	30	14
8.687	46	20
8.797	40	18
8.909	34	16
9.007	50	22
9.120	44	20
9.233	38	18
9.333	54	24
9.347	32	16
9.447	48	22
9.563	42	20
9.679	36	18

Continued on next page

Table A.5 – Continuation of table A.5

Permittivity	**Porosity [%]**	**Water Content [%]**
9.781	52	24
9.796	30	16
9.899	46	22
10.017	40	20
10.136	34	18
10.240	50	24
10.360	44	22
10.481	38	20
10.587	54	26
10.603	32	18
10.710	48	24
10.832	42	22
10.956	36	20
11.065	52	26
11.080	30	18
11.190	46	24
11.315	40	22
11.442	34	20
11.553	50	26
11.680	44	24
11.808	38	22
11.921	54	28
11.937	32	20
12.051	48	26
12.181	42	24
12.312	36	22
12.427	52	28
12.444	30	20
12.560	46	26
12.693	40	24
12.827	34	22
12.944	50	28
13.079	44	26
13.215	38	24
13.334	54	30

Continued on next page

Table A.5 – Continuation of table A.5

Permittivity	Porosity [%]	Water Content [%]
13.351	32	22
13.471	48	28
13.609	42	26
13.748	36	24
13.869	52	30
13.887	30	22
14.009	46	28
14.149	40	26
14.291	34	24
14.415	50	30
14.557	44	28
14.700	38	26
14.826	54	32
14.844	32	24
14.971	48	30
15.116	42	28
15.262	36	26
15.390	52	32
15.409	30	24
15.537	46	30
15.685	40	28
15.834	34	26
15.964	50	32
16.114	44	30
16.265	38	28
16.397	54	34
16.416	32	26
16.549	48	32
16.702	42	30
16.855	36	28
16.990	52	34
17.010	30	26
17.145	46	32
17.300	40	30
17.456	34	28

Continued on next page

Table A.5 – Continuation of table A.5

Permittivity	Porosity [%]	Water Content [%]
17.593	50	34
17.751	44	32
17.909	38	30
18.048	54	36
18.068	32	28
18.207	48	34
18.367	42	32
18.528	36	30
18.669	52	36
18.690	30	28
18.831	46	34
18.994	40	32
19.158	34	30
19.301	50	36
19.466	44	34
19.632	38	32
19.777	54	38
19.798	32	30
19.944	48	36

A.2.2 Soil Conditions - BH

Table A.6: Soil conditions of BH assuming a permittivity of the soil matrix of ϵ_r=7.5

Permittivity	Porosity [%]	Water Content [%]
7.072	50	18
7.080	34	12
7.208	44	16
7.337	54	20
7.345	38	14
7.475	48	18
7.483	32	12
7.615	42	16
7.747	52	20
7.756	36	14
7.889	46	18

Continued on next page

Table A.6 – Continuation of table A.6

Permittivity	Porosity [%]	Water Content [%]
7.898	30	12
8.033	40	16
8.169	50	20
8.178	34	14
8.315	44	18
8.454	54	22
8.462	38	16
8.602	48	20
8.611	32	14
8.752	42	18
8.894	52	22
8.903	36	16
9.046	46	20
9.055	30	14
9.200	40	18
9.346	50	22
9.355	34	16
9.502	44	20
9.650	54	24
9.659	38	18
9.808	48	22
9.813	40	19
9.818	32	16
9.968	42	20
9.973	34	17
10.039	55	25
10.044	47	22
10.054	31	16
10.120	52	24
10.125	44	21
10.129	36	18
10.201	49	23
10.206	41	20
10.211	33	17
10.282	46	22

Continued on next page

Table A.6 – Continuation of table A.6

Permittivity	**Porosity [%]**	**Water Content [%]**
10.292	30	16
10.446	40	20
10.601	50	24
10.611	34	18
10.767	44	22
10.925	54	26
10.935	38	20
11.094	48	24
11.104	32	18
11.264	42	22
11.425	52	26
11.435	36	20
11.597	46	24
11.608	30	18
11.771	40	22
11.936	50	26
11.946	34	20
12.112	44	24
12.279	54	28
12.290	38	22
12.458	48	26
12.469	32	20
12.638	42	24
12.809	52	28
12.820	36	22
12.986	54	29
12.991	46	26
12.997	38	23
13.002	30	20
13.175	40	24
13.350	50	28
13.361	34	22
13.536	44	26
13.713	54	30
13.724	38	24

Continued on next page

Table A.6 – Continuation of table A.6

Permittivity	Porosity [%]	Water Content [%]
13.902	48	28
13.913	32	22
14.092	42	26
14.182	47	28
14.187	39	25
14.193	31	22
14.272	52	30
14.283	36	24
14.368	49	29
14.374	41	26
14.380	33	23
14.465	46	28
14.476	30	22
14.659	40	26
14.842	50	30
14.854	34	24
14.854	34	24
14.935	55	32
14.941	47	29
14.946	39	26
15.039	44	28
15.225	54	32
15.237	38	26
15.424	48	30
15.436	32	24
15.625	42	28
15.814	52	32
15.826	36	26
16.011	54	33
16.017	46	30
16.023	38	27
16.029	30	24
16.221	40	28
16.414	50	32
16.427	34	26

Continued on next page

Table A.6 – Continuation of table A.6

Permittivity	**Porosity [%]**	**Water Content [%]**
16.621	44	30
16.817	54	34
16.829	38	28
16.921	51	33
16.927	43	30
16.934	35	27
17.026	48	32
17.032	40	29
17.038	32	26
17.236	42	30
17.436	52	34
17.448	36	28
17.649	46	32
17.661	30	26
17.863	40	30
18.066	50	34
18.078	34	28
18.282	44	32
18.487	54	36
18.501	38	30
18.707	48	34
18.720	32	28
18.810	53	36
18.817	45	33
18.824	37	30
18.927	42	32
19.136	52	36
19.149	36	30
19.359	46	34
19.373	30	28
19.584	40	32
19.796	50	36
19.809	34	30
20.023	44	34

A.3 Appendix for Part III

A.3.1 Parametrization of the bell-shaped functions

Parametrization of the generalized bell-shaped membership function:
Factor c of the generalized bell-shaped membership function represents the midpoint of the function, d describes the half-width and b the width of the plateau. The smaller b, the sharper its plateau. With the growth of b, the function gets closer to a rectangular function. These parameters were varied and the most suitable regarding the similarity to a burial mound shape was then used and listed in table III.2.1. They were kept constant for determining the height.

For the generalized bell-shaped membership function we decided to use a relative narrow plateau, choosing $b = 1m$. For comparison with the other functions, we set the midpoint to be zero ($c = 0$) and the last parameter determines the width and the shape of the edges of the function. $d = 30$ was found by comparison with the shape of the barrow from fig. III.2.2a. This is the most subjectively chosen parameter.

Parametrization of the bump function:
The bump function is described by the parameter p, which determines how much of the function's edges is close to zero. This parameter determines also the shape of the function. Parameter s determines the width or the range in which the function works. If larger, the function is wider, if smaller, the function becomes numerically unstable. Therefore, s is slightly larger than the radius of the barrow's bottom, because otherwise it causes numerical instability due to division by zero if $x = s$ (Hossain et al. 2018, Johnson 2007). These parameters were varied and the most suitable regarding the similarity to a burial mound shape was then used and listed in table III.2.1. They were kept constant for determining the height.

Parameter s was set to $s = 6.25$ m. With reference to the photograph of fig. III.2.2a we decided the parameter p to be 35. This is again a subjectively chosen value.

Bibliography

Barsch, D. (1978a). Erläuterungen zur Geomorphologischen Karte 1:25000 der Bundesrepublik Deutschland. Vol. GMK 25. Blatt 1.

— (1978b). Geomorphologische Karte der Bundesrepublik Deutschland 1:25000. Vol. GMK 25. Blatt 1.

Birchak, J. R. et al. (1974). High dielectric constant microwave probes for sensing soil moisture. Proceedings of the IEEE 62.1, pp. 93–98.

Bittner, R. & W. Rabbel (1991). Energy- and Power-Sections in Seismic Interpretation.. Continental Lithosphere: Deep Seismic Reflections 22, pp. 409–415.

Blakely, R. J. (1996). Potential theory in gravity and magnetic applications. Cambridge university press.

Blume, H.-P. et al. (2016). Scheffer/schachtschabel: Lehrbuch der bodenkunde. Springer-Verlag.

Boeniger, U. & J. Tronicke (2010). Improving the interpretability of 3D GPR data using target–specific attributes: application to tomb detection. Journal of Archaeological Science 37.2, pp. 360–367.

Bronstein, I. N. et al. (2012). Taschenbuch der Mathematik. Vol. 1. Springer.

Carmichael, R. S. (2017). "Magnetic properties of minerals and rocks". *Handbook of Physical Properties of Rocks (1982)*. CRC Press, pp. 229–288.

Carrigy, M. A. (1970). Experiments on the angles of repose of granular materials. Sedimentology 14.3-4, pp. 147–158.

Cassidy, N. J. & H. Jol (2009). Electrical and magnetic properties of rocks, soils and fluids. Vol. 2. chapter.

Chapman, J. et al. (2014). The second phase of the Trypillia mega-site methodological revolution: A new research agenda. European Journal of Archaeology 17.3, pp. 369–406.

Chesworth, W. et al. (2008). "Iron oxides". *Encyclopedia of Soil Science. Encyclopedia of Earth Sciences Series.* Chesworth, W.

Clark, O. A. & A. Clark (1996). Seeing beneath the soil: prospecting methods in archaeology. Routledge.

Corradini, E., S. Dreibrodt, et al. (2020). Understanding wetlands stratigraphy: geophysics and soil parameters for investigating ancient basin development at lake Duvensee. Geosciences 10.8, p. 314.

Corradini, E., B. V. Eriksen, et al. (2020). Investigating lake sediments and peat deposits with geophysical methods-A case study from a kettle hole at the Late Palaeolithic site of Tyrsted, Denmark. Quaternary International 558, pp. 89–106.

Corradini, E., D. Wilken, et al. (2020). Reconstructing the palaeoenvironment at the early Mesolithic site of Lake Duvensee: Ground-penetrating radar and geoarchaeology for 3D facies mapping. The Holocene 30.6, pp. 820–833.

Daniels, D. & E. Utsi (2013). "GPR case histories and known physical principles". *2013 7th International Workshop on Advanced Ground Penetrating Radar*. IEEE, pp. 1–9.

Danielson, R. & P. Sutherland (1986). Porosity. Methods of soil analysis: Part 1 physical and mineralogical methods 5, pp. 443–461.

Davis, J. & A. P. Annan (1989). Ground-penetrating radar for high-resolution mapping of soil and rock stratigraphy. Geophysical prospecting 37.5, pp. 531–551.

Dean, W. E. (1974). Determination of carbonate and organic matter in calcareous sediments and sedimentary rocks by loss on ignition; comparison with other methods. Journal of Sedimentary Research 44.1, pp. 242–248.

Dearing, J. A. et al. (1996). Frequency-dependent susceptibility measurements of environmental materials. Geophysical Journal International 124.1, pp. 228–240.

Denker, A. (2017). Rebuilding Palmyra virtually: Recreation of its former glory in digital space. Virtual Archaeology Review 8.17, pp. 20–30.

Dreibrodt, S., O. Nelle, et al. (2009). Investigations on buried soils and colluvial layers around Bronze Age burial mounds at Bornhöved (northern Germany): an approach to test the hypothesis oflandscape openness' by the incidence of colluviation. The Holocene 19.3, pp. 487–497.

Dreibrodt, S. & J. Wiethold (2015). Lake Belau and its catchment (northern Germany): A key archive of environmental history in northern central Europe since the onset of agriculture. The Holocene 25.2, pp. 296–322.

Eder-Hinterleitner, A., W. Neubauer, & P. Melichar (1999). Magnetic modelling for the 3D reconstruction of the neolithic circular ditch system of Steinabrunn/Austria. ICOMOS – Hefte des Deutschen Nationalkomitees 33, pp. 32–33.

Faßbinder, J. W. (1994). Die magnetischen Eigenschaften und die Genese ferrimagnetischer Minerale in Böden im Hinblick auf die magnetische Prospektion archäologischer Bodendenkmäler. Verlag Leidorf.

Feeser, I. et al. (2022). On-site to off-site: A multidisciplinary and multiscale consideration of the 13th to 11th century BCE transformation in northern Germany. MILLET AND WHAT ELSE?, p. 185.

Forte, E. & M. Pipan (2008). Integrated seismic tomography and ground-penetrating radar (GPR) for the high-resolution study of burial mounds (tumuli). Journal of Archaeological Science 35.9, pp. 2614–2623.

Gardner, W. H. (1986). Water content. Methods of Soil Analysis: Part 1 Physical and Mineralogical Methods 5, pp. 493–544.

Glover, T. (1997). Pocket Reference. 2nd. Sequoia Publishing, Inc.

Green, A. & P. Cheetham (2019). "Rise of the Machines: Improving the identification of possible graves in GPR data with interactive survey guidance and machine learning". *New Global Perspectives on Archaeological Prospection*. Ed. by J. Bonsall. 13th International Conference on Archaeological Prospection 28 August – 1 September 2019.

Groß, D. et al. (2019). Adaptations and transformations of hunter-gatherers in forest environments: New archaeological and anthropological insights. The Holocene 29.10, pp. 1531–1544.

Guidi, G., M. Russo, & D. Angheleddu (2013). Digital reconstruction of an archaeological site based on the integration of 3D data and historical sources. International Archives of the Photogrammetry, Remote Sensing and Spatial Information Sciences 5.

Guo, H. & A. S. Barnard (2013). Naturally occurring iron oxide nanoparticles: morphology, surface chemistry and environmental stability. Journal of Materials Chemistry A 1.1, pp. 27–42.

Guskos, N. et al. (2002). Photoacoustic, EPR and electrical conductivity investigations of three synthetic mineral pigments: hematite, goethite and magnetite. Materials Research Bulletin 37.6, pp. 1051–1061.

Gustavsen, L. et al. (2018). Archaeological prospection of a specialized cooking-pit site at Lunde in Vestfold, Norway. Archaeological Prospection 25.1, pp. 17–31.

Hanson, M. A. et al. (2015). Provenance and deposition of glacial Lake Missoula lacustrine and flood sediments determined from rock magnetic properties. Quaternary Research 83.1, pp. 166–177.

Hargrave, M. L. (2006). "Ground Truthing the Results of Geophysical Survey". *Remote Sensing in Archaeology: An Explicitly North American Perspective*. Ed. by M. Giardano et al. University of Alabama Press. Chap. 12, pp. 269–304.

Hegyi, A., M.-M. Vernica, & L. Drăguț (2020). An object-based approach to support the automatic delineation of magnetic anomalies. Archaeological Prospection 27.1, pp. 3–12.

Hingst, H. (1976). Grabhügelfelder der jüngeren Bronze-und der frühen Eisenzeit aus Schleswig-Holstein. Offa 33.66–122.

Hingst, H. (1979). "Die vorrömische Eisenzeit". *Geschichte Schleswig-Holsteins. Band 2. Von der Bronzezeit bis zur Völkerwanderungszeit.* Ed. by O. Klose, pp. 147–247.

Hirata, Y., M. Kawabata, & Y. Ishihara (1993). Electrical properties of silica-alumina ceramics in nitrogen atmosphere. Journal of materials research 8.5, pp. 1116–1121.

Holst, M. K., H. Breuning-Madsen, & M. Rasmussen (2001). The South Scandinavian barrows with well-preserved oak-log coffins. Antiquity 75.287, pp. 126–136.

Hossain, M. et al. (2018). Application of the hybrid ANFIS models for long term wind power density prediction with extrapolation capability. PloS one 13.4, pp. 1–31.

Hunt, C. P., B. M. Moskowitz, & S. K. Banerjee (1995). Magnetic properties of rocks and minerals. Rock physics and phase relations: A handbook of physical constants 3, pp. 189–204.

Irving, J. & R. Knight (2006). Numerical modeling of ground-penetrating radar in 2-D using MATLAB. Computers & Geosciences 32.9, pp. 1247–1258.

Johnson, S. G. (2007). *Saddle-point integration of C∞ "bump" functions*.

KG, V. G. (n.d.). List of dielectric constants. https://www.vega.com, last checked: 7th october 2019.

Kirsch, R. et al. (2006). Groundwater resources in buried valleys: a challenge for geosciences. Leibniz Institute for Applied Geosciences (GGA-Institut).

Klein, C. (2006). Die Problematik der Datenkombination bei Messungen mit unterschiedlichen Georadarantennen. PhD thesis. CAU Kiel.

Kneisel, J., J. Brinkmann, et al. (2018). Mang de Bargen bei Bornhöved Kleine Region, große Fragen. Archäologische Nachrichten Schleswig-Holstein 23 (2017), pp. 48–55.

Kneisel, J., S. Schaefer-Di Maida, et al. ((in prep.)). Leben und Ansichten von LA 117 und LA 57, Grabhügel. Vorbericht über die Ausgrabungen bronzezeitlicher Grabhügel bei Bornhöved, Kr. Segeberg.

Koenigsberger, J. G. (1930). Größenverhältnis von remanentem zu induziertem Magnetismus in Gesteinen; Größe und Richtung des remanenten Magnetismus. Zeitschrift für Geophysik 6.190–207.

— (1934). Magnetische Eigenschaften der ferromagnetischen Mineralien in den Gesteinen. Beiträge Zur Angewandten Geophysik 4, pp. 385–394.

— (1936). Die Abhängigkeit der natürlichen remanenten Magnetisierung bei Eruptivgesteinen von deren Alter und Zusammensetzung. Beiträge Zur Angewandten Geophysik 5, pp. 193–246.

Krosigk, S. v. (1976). Untersuchungen zum vor- und frühgeschichtlichen Siedlungsablauf am Fundbild der Gemarkungen Bornhöved – Gönnebek – Groß-Kummerfeld – Schmalensee, Kreis Segeberg/Holstein. Offa 1.

Küçükdemirci, M. & A. Sarris (2019). "Automated segmentation of Archaeo-Geophysical Images by Convolutional Neural Networks". *New Global Perspectives on Archaeological Prospection*. Ed. by J. Bonsall. 13th International Conference on Archaeological Prospection 28 August – 1 September 2019.

Küçükdemirci, M. & A. Sarris (2020). Deep learning based automated analysis of archaeo-geophysical images. Archaeological Prospection 27.2, pp. 107–118.

Landesamt für Landwirtschaft, U. u. l. R., ed. (2012). Geologische Übersichtskarte von Schleswig-Holstein 1:250000.

Liu, Z. (2011). Measuring the angle of repose of granular systems using hollow cylinders. PhD thesis. University of Pittsburgh.

Lütjens, I. (2013a). *Bornhöved, Kreis Segeberg, LA 17 – Bericht über die archäologische Hauptuntersuchung 2005*. Tech. rep. Archäologisches Landesamt von Schleswig-Holstein.

— (2013b). *Bornhöved, Kreis Segeberg, LA 18 – Bericht über die archäologische Hauptuntersuchung 2005*. Tech. rep. Archäologisches Landesamt von Schleswig-Holstein.

— (2013c). *Bornhöved, Kreis Segeberg, LA 58 – Bericht über die archäologische Hauptuntersuchung 2005*. Tech. rep. Archäologisches Landesamt von Schleswig-Holstein.

— (2013d). *Bornhöved, Kreis Segeberg, LA 59 – Bericht über die archäologische Hauptuntersuchung 2005*. Tech. rep. Archäologisches Landesamt von Schleswig-Holstein.

— (2013e). *Bornhöved, Kreis Segeberg, LA 60 – Bericht über die archäologische Hauptuntersuchung 2005*. Tech. rep. Archäologisches Landesamt von Schleswig-Holstein.

Magnani, M. & W. Schroder (2015). New approaches to modeling the volume of earthen archaeological features: a case-study from the Hopewell culture mound. Journal of Archaeological Science 64, pp. 12–21.

Mariotti Lippi, M., C. Bellini, & M. Mori Secci (2010). Palaeovegetational reconstruction based on pollen and seeds/fruits from a Bronze Age archaeological site in Tuscany (Italy). Plant Biosystems 144.4, pp. 902–908.

Markit, I. (n.d.). Kingdom Suite - Flex Gridding Algorithm. http://onlinehelp.ihs.com, last checked: 31th Jan. 2020.

Nakashima, H. et al. (2011). Determining the angle of repose of sand under low-gravity conditions using discrete element method. Journal of Terramechanics 48.1, pp. 17–26.

Neal, A. (2004). Ground-penetrating radar and its use in sedimentology: principles, problems and progress. Earth-science reviews 66.3-4, pp. 261–330.

Neubauer, W. & A. Eder-Hinterleitner (1997). 3D-interpretation of postprocessed archaeological magnetic prospection data. Archaeological Prospection 4.4, pp. 191–205.

Neubauer, W., P. Melichar, & A. Eder-Hinterleitner (1996). Collection, visualization and simulation of magnetic prospection data. ANALECTA PRAEHISTORICA LEIDENSIA 28, pp. 121–128.

Nowaczinski, E. et al. (2015). A multidimensional research strategy for the evaluation of settlement pits: 3d electrical resistivity tomography, magnetic prospection and soil chemistry. Archaeological Prospection 22.4, pp. 233–253.

O'Rourke, J. (1998). Computational geometry in C. 2nd. Cambridge university press.

Papadopoulos, N. G. et al. (2010). Geophysical investigation of tumuli by means of surface 3D electrical resistivity tomography. Journal of Applied Geophysics 70.3, pp. 192–205.

Parry, W. (2011). Composition, nucleation, and growth of iron oxide concretions. Sedimentary Geology 233.1-4, pp. 53–68.

Pašteka, R. et al. (2012). REGCONT: A Matlab based program for stable downward continuation of geophysical potential fields using Tikhonov regularization. Computers & Geosciences 49, pp. 278–289.

Pickartz, N., E. Corradini, et al. (2020). "Extending archaeological documentation from 2D to 3D: The benefits of geophysical on-site measurements in excavations." *Archaeology in the Žitava valley I - The LBK and Želiezovce settlement site of Vráble*. Ed. by M. Furholt et al. Sidestone Press.

Pickartz, N., W. Rabbel, et al. (2020). What over 100 drillings tell us: a new method for determining the Koenigsberger ratio of soils from magnetic mapping and susceptibility logging. Archaeological Prospection 27.4, pp. 393–414.

Piotrowski, J. A. (1991). Quartär-und hydrogeologische Untersuchungen im Bereich der Bornhöveder Seenkette, Schleswig-Holstein: Quaternary geological and hydrogeological investigations of the Bornhöved Lakes area, Schleswig-Holstein, Northern Germany. PhD thesis. Geologisch-Paläontologisches Inst. und Museum, Univ. Kiel.

Polymenakos, L. et al. (2004). Investigation of a monumental Macedonian tumulus by three-dimensional seismic tomography. Archaeological Prospection 11.3, pp. 145–158.

Pregesbauer, M., I. Trinks, & W. Neubauer (2014). An object oriented approach to automatic classification of archaeological features in magnetic prospection data. Near Surface Geophysics 12.5, pp. 651–656.

Rasmussen, K. L. et al. (2012). Pottery firing temperatures: a new method for determining the firing temperature of ceramics and burnt clay. Journal of Archaeological Science 39.6, pp. 1705–1716.

Roderick, G. L. (1972). Review of particle-size classifications of soils. Highway Research Record 405.

Schaefer-Di Maida, S. (2019). Bronzezeitliche Transformationsprozesse in Schleswig-Holstein am Beispiel vom Fundplatz von Mang de Bargen, Bornhöved (Kr. Segeberg). PhD thesis. CAU Kiel.

Schaefer, S. (2017). *Bornhöved, Kreis Segeberg, LA 57 – Bericht über die archäologische Hauptuntersuchung 2017*. Tech. rep. Institut für Ur- und Frühgeschichte, CAU Kiel.

Scheid, H. & W. Schwarz (2017). Elemente der Geometrie. Springer.

Schneidhofer, P. et al. (2017). Geoarchaeological evaluation of ground penetrating radar and magnetometry surveys at the Iron Age burial mound Rom in Norway. Archaeological Prospection 24.4, pp. 425–443.

Schnepp, E. et al. (2004). A German catalogue of archaeomagnetic data. Geophysical Journal International 157.1, pp. 64–78.

Seguin, J. et al. (2019). 2500 years of anthropogenic and climatic landscape transformation in the Stymphalia polje, Greece. Quaternary Science Reviews 213, pp. 133–154.

Smed, P. & J. Ehlers (2002). Steine aus dem Norden.

Šperl, J. & J. Trčková (2008). Permeability and porosity of rocks and their relationship based on laboratory testing. Acta Geodyn Geomater 5.149, pp. 41–47.

Thompson, R. (2012). Environmental magnetism. Springer Science & Business Media.

Trinks, I. (2015). Advancing large-scale high-resolution near-surface geophysical prospection. PhD thesis. TU Wien.

Tsourlos, P. et al. (2014). Comparison of measuring strategies for the 3-D electrical resistivity imaging of tumuli. Journal of Applied Geophysics 101, pp. 77–85.

Uieda, L. (2010-2016). Gravity and magnetics (fatiando.gravmag). https://legacy.fatiando.org/api/gravmag.html, last checked: 26th Feb. 2020.

Uieda, L., V. C. Oliveira J., & V. Barbosa (2013). "Modeling the earth with fatiando a terra". *Proceedings of the 12th Python in Science Conference*, pp. 96–103.

Viberg, A., I. Trinks, & K. Lidén (2011). A review of the use of geophysical archaeological prospection in Sweden. Archaeological prospection 18.1, pp. 43–56.

Wang, J. J. et al. (2013). Angle of repose of landslide debris deposits induced by 2008 Sichuan Earthquake. Engineering Geology 156, pp. 103–110.

Warren, C. & A. Giannopoulos (2012). Simulating Commercial GPR antennas: How close can we get?.

Wessel, P. & W. H. Smith (1991). Free software helps map and display data. Eos, Transactions American Geophysical Union 72.41, pp. 441–446.

Wilken, D. et al. (2016). Integrated GPR and archaeological investigations reveal internal structure of man-made Skiphóll mound in Leiruvogur, Iceland. Journal of Archaeological Science: Reports 9, pp. 64–72.

Williams, P. A. & S. Saha (1996). The electrical and dielectric properties of human bone tissue and their relationship with density and bone mineral content. Annals of biomedical engineering 24.2, pp. 222–233.

Zanon, M. et al. (2018). European forest cover during the past 12,000 years: a palynological reconstruction based on modern analogs and remote sensing. Frontiers in plant science 9.253.

Zhao, W., E. Forte, S. T. Levi, et al. (2015). Improved high-resolution GPR imaging and characterization of prehistoric archaeological features by means of attribute analysis. Journal of Archaeological Science 54, pp. 77–85.

Zhao, W., E. Forte, M. Pipan, et al. (2013). Ground penetrating radar (GPR) attribute analysis for archaeological prospection. Journal of Applied Geophysics 97, pp. 107–117.

Zhou, Y. et al. (2002). An experimental and numerical study of the angle of repose of coarse spheres. Powder Technology 125.1, pp. 45–54.

Acknowledgements

The presented study was funded by the German Research Foundation (DFG) grant 2901391021 (SFB 1266/ CRC 1266). I wish to thank my colleagues in the CRC 1266 for the fantastic opportunity to be part of such a big interdisciplinary project.

I would like to thank Prof. Dr. W. Rabbel for his constant support and suggestions, and for the professional exchange of ideas. Thanks also go to Assoc. Prof. Dr. Immo Trinks for taking the time to work on my dissertation as a co-referee, and to all the other members of the committee. Special thanks go to Dr. T. Wunderlich, whose programming work facilitated the evaluation of the 3D GPR data sets and who made helpful suggestions concerning the formal aspect of this thesis. I would also like to thank Dr. D. Wilken as well as Dr. A. Steinberg, who were my contact persons on the subject of inversion.

For a good working atmosphere and good cheer, both in the office and during the measurements, but also for fruitful professional exchanges I would like to thank Dr. E. Corradini, who became a friend in the course of our work together. From archaeological perspective I would like to thank Dr. J. Kneisel as well as Dr. S. Schaefer-Di Maida, who discussed findings and further-ranging ideas as well as helping in the interpretation of geophysical data. They were always available in the office and during the measurements. Dr. Schaefer-Di Maida was also responsible for the magnetic measurements and their evaluation, on which this thesis relies.

A further thank you goes to Dr. S. Dreibrodt, who took and evaluated all the soil samples taken the excavations. His data were the basis for the investigations in this thesis.

Special thanks go to all the helping hands during the measurements: Helene-Sophie Hilbert, Simon Fischer, Ercan Erkul, Detlef Schulte-Kortnack, Laura Rose, Sebastian Wilhelm, Henning Andresen, Anna-Lena Heyn, Hermann Gorbahn, Dr. Clara Drummer, and Dr. Nathalie Pickartz.

Erklärung

Hiermit erkläre ich, dass die vorliegende Arbeit mit dem Titel: 'Geophysical Measurements on Glacial Soils - A Challenge in the Detection, Identification and Reconstruction of Archaeological Targets' von mir selbstständig angefertigt wurde. Bis auf zitierte bzw. angegebene Referenzen und Beratung meiner Betreuer wurden keine weiteren Quellen verwendet. Diese Arbeit ist unter Einhaltung der Regeln guter wissenschaftlicher Praxis der Deutschen Forschungsgemeinschaft entstanden. Sie wurde weder im Rahmen eines Prüfungsverfahrens an anderer Stelle vorgelegt noch veröffentlicht oder zur Veröffentlichung eingereicht. Ich versichere darüber hinaus, dass mir nie ein akademischer Grad entzogen wurde.

Salzgitter, March 2023

D. Panning